Synthesis and Self-Assembly of Metal Carbonyl Organometallic Macromolecules Prepared *via* Migration Insertion Polymerization

by

Kai Cao

A thesis

presented to the University of Waterloo

in fulfillment of the

thesis requirement for the degree of

Doctor of Philosophy

in

Chemistry

Waterloo, Ontario, Canada, 2016

AUTHOR'S DECLARATION

This thesis consists of material all of which I authored or co-authored: see Statement of Contributions included in the thesis. This is a true copy of the thesis, including any required final revisions, as accepted by my examiners.

I understand that my thesis may be made electronically available to the public.

Statement of Contributions

Part of Chapter 1 was published in *Macromolecular Rapid Communications*. **2015**, 36(7), 586-596.

The research work discussed in Chapter 2 was published in *Organometallics*. **2014**, 33(2), 531-539.

The preparation of single crystals of the 5-membered ring and NMR analysis of the 5-membered and 6-membered ring were done by Yibo Liu.

The research work discussed in Chapter 3 was published in *Chemical Communications*. **2014**, 50(70), 10062-10065.

The research work discussed in Chapter 4 was published in *Macromolecular Rapid Communications.* **2016**, 37(3), 246-250.

The research work discussed in Chapter 6 has been published in *Macromolecules*. **2015**, 48, 7968-7977.

The cell viability (MTT) study was done by Anand Lopez.

I am the first author of all these journal publications.

Abstract

   Migration insertion polymerization (MIP) has been developed for the synthesis of air-stable metal carbonyl polymers. $CpFe(CO)_2(CH_2)_3PPh_2$ (FpP) was synthesized as a monomer. The solution polymerization of FpP at a monomer concentration of 20 wt% generated PFpP oligomers with a DP_n of 11, cyclic molecules, and a fraction of THF-insoluble material. On the other hand, bulk polymerization of FpP resulted in soluble macromolecules and no THF-insoluble material was produced. PFpP with a relatively high molecular weight (M_n = 257,00 g/mol was obtained when FpP was polymerized in bulk at 105 ^{o}C in the presence of 5 wt% DMSO. The PFpPs are thermally stable up to 180 ^{o}C and have a T_g of 99 ^{o}C as indicated by TGA and DSC analysis, respectively. End group analysis suggests that PFpPs possess Fp and phosphine end groups. Taking advantage of the reactivity of the Fp end groups, three PFpP amphiphiles, Ph_2PCn-PFpP (n = 6, 10, 18), were synthesized *via* migration insertion reactions (MIR) of the Fp end groups with alkyldiphenylphosphines. Moreover, $[\eta^5\text{-}Ph_2P(CH_2)_3C_5H_4]Fe(CO)_2(CH_2)_5CH_3$ (FpP^{Cp}) with an alkylphosphine group tethered on the Cp ring was synthesized. Bulk MIP of FpP^{Cp} resulted in PFpP^{Cp} oligomers with a M_n of 4200 g/mol and a PDI of 1.73. Preliminary studies indicated that PFpP was able to self-assemble into uniform and stable vesicles in water. Hydration of the carbonyl groups was deemed to be responsible for the stability of the colloids. Using a nano-precipitation technique, the efficient encapsulation of hydrophilic molecules, e.g., PEG, within PFpP vesicles was achieved.

Acknowledgements

First and foremost, I would like to thank my supervisor Prof. Xiaosong Wang for providing me the opportunity to work as a PhD student under his supervision. Prof. Wang gave me a lot of constructive suggestions and helpful discussions toward the experiment design, data analysis and academic writing during the four years PhD program. The thesis could not be completed without his guidance and supervision. In addition, I really appreciate that Prof. Wang always helped me to develop the ability of critical thinking, leadership and communication, which will be beneficial for my whole life.

I would like to thank my committee member Prof. Mario Gauthier, Prof. Sonny Lee and Prof. Boxin Zhao for their helpful discussion and kind support toward the research project and thesis writing.

I would like to express my gratitude to Prof. Mario Gauthier, Prof. Graham Murphy, Prof. Micheal K.C Tam, Prof. Juewen Liu's group for providing access to their instruments and facilities. Janet Venne and Dr. Jalil Assoud are also acknowledged for their patient technical support. I also would like to thank Catherine Van Esch for her kind help during my PhD program.

Next, I want to thank all the graduate and undergraduate students from Prof. Xiaosong Wang's group: Nicholas Lanigan, Nimer Murshid, Dapeng Liu, Na Zhou, Shaowei Shi, Diya Geng, Lulu

Table of Contents

Chapter 3. Bulk Polymerization of CpFe(CO)$_2$(CH$_2$)$_3$PPh$_2$ (FpP) and Physical Properties

Chapter 5. Synthesis of [η^5-Ph$_2$P(CH$_2$)$_3$C$_5$H$_4$]Fe(CO)$_2$[(CH$_2$)$_5$CH$_3$] for Migration Insertion

Polymerization (MIP) 95

List of Figures

List of Tables

List of Schemes

List of Abbreviations

A	Absorption
AIBN	Azobisisobutyronitrile
ADMET	Acyclic diene methathesis polymerization
ATR	Attenuated total reflectance
ATRP	Atom transfer radical polymerization
AFM	Atomic force microscopy
bpy	Bipyridine
Cp	Cyclopentadiene
COSY	Correlation spectroscopy
CHC	Critical hexane content
DCM	Dichloromethane
DMSO	Dimethyl sulfoxide
DBSA	Dodecylbenzenesulfonic acid
DCC	*N*, *N*-Dicyclohexylcarbodiimide
DPPN	1,2-Bis(diphenylphosphino)ethane
D_h	Hydrodynamic diameter
DFT	Density Functional Theory
DLS	Dynamic light scattering
DSC	Differential scanning calorimetry
ε	Molar extinction coefficient
EA	Energy analysis
EBL	Electron beam lithography
EDA	Energy decomposition analysis
EE	Encapsulation efficiency
ESI	Electrospray ionization
FpR	Alkyldicarbonylcyclopentadienyliron

FpK	Cyclopentadienyl dicarbonyliron potassium
FpP	Cyclopentadienyldicarbonyldiphenylphosphinopropyliron
FpMe	$CpFe(CO)_2CH_3$
Fp anion	η^5-Cyclopentadienyl dicarbonyl iron anion
FpP^{Cp}	$[\eta^5\text{-}PPh_2(CH_2)_3C_5H_4]Fe(CO)_2(CH_2)_5CH_3$
Fp_2	Cyclopentadienyl iron dicarbonyl dimer
FT-IR	Fourier transform infrared spectroscopy
GPC	Gel permeation chromatography
HOMO	Highest occupied molecular orbital
HMQC	Heteronuclear multiple quantum coherence
HMBC	Heteronuclear multiple bond correlation
HMDI	Hexamethylene diisocyanate
ICP	Inductively coupled plasma atomic emission spectroscopy
LDA	Lithium diisopropylamide
LUMO	Lowest unoccupied molecular orbital
LC	Loading capacity
l	Path length
MCPs	Metal-containing polymers
MCMCOMs	Main-chain metal carbonyl organometallic macromolecules
MIR	Migration insertion reaction
MIP	Migration insertion polymerization
MC	Metal carbonyl
M_n	Number average molecular weight
M_w	Weight average molecular weight
	N-[3-Cobaltoceniumcarboxyl
MPF6	propyl]-cis-5-norbornene-exo-2,3-dicarboximide
	hexafluorophosphate

MALDI	Matrix-assisted laser desorption/ionization
MFM	Magnetic force microscopy
MS	Mass spectroscopy
MS/MS	Tandem mass spectroscopy
NMR	Nuclear magnetic resonance
NMP	Nitroxide mediated radical polymerization
OES	Optical emission spectroscopy
PMMA	Poly(methyl methacrylate)
PMAEFc	Poly(2-(methacrylolyoxy)ethyl ferrocenecarboxylate
PEG	Poly(ethylene glycol)
PVBC	Poly(p-chloromethyl styrene)
PMDETA	N,N,N',N'',N''-Pentamethyldiethylenetriamine
PHEA	Poly(2-hydroxyethyl acrylate)
PXRD	Powder X-ray diffraction
PS	Polystyrene
PDCH	Poly[benzoic acid N'-(4-vinyl benzoyl)hydrazide]
PFS	Polyferrocenylsilanes
PDMS	Polydimethylsiloxane
PFDMG	Polyferrocenyldimethylgermane
PPES	Poly(4-(phenylethynyl)styrene)
POrn	Poly(ornithine acrylamide)
PnBu	Poly(n-butylacrylamide)
PCL	Poly(ε-caprolactone)
PDMA	Poly(dimethylaminoethyl methacrylate)
PNIPAM	Poly(N-isopropylacrylamide)
PtBA	Poly(*tert*-butyl acrylate)
PMPC	Poly[2-(methacryloyloxy)ethyl phosphorylcholine]

PMAECoPF6	Poly(2-(methacrylolyoxy)ethyl cobaltoceniumcarboxylate hexafluorophosphate)
PDI	Polydispersity index
R_h	Hydrodynamic radius
R_g	Radius of gyration
RCM	Ring-closing metathesis
ROP	Ring-opening polymerization
ROMP	Ring-opening metathesis polymerization
RAFT	Reversible addition fragmentation chain transfer polymerization
SLS	Static light scattering
SEM	Scanning electron microscopy
THF	Tetrahydrofuran
TMEDA	Tetramethylethylenediamine
TGA	Thermogravimetric analysis
TOF	Time of flight
TLC	Thin layer chromatography
TEM	Transmission electron microscopy
UCST	Upper critical solution temperature
UV	Ultraviolet
WCI	Water carbonyl interaction
WAXS	Wide angle X-ray diffraction
ZPE	Zero point energy

Chapter 1. Literature Review

Metal-containing macromolecules exhibit a wide range of interesting properties due to the presence of various metal coordination structures, resulting in many applications such as solar cells,[1] self-healing materials,[2] electronic and optical devices.[3] According to the location of the metal complex in the polymer chains, metal-containing polymers can be divided into two categories, which are the side-chain metal containing polymers and the main-chain metal containing polymers, respectively.

1.1 Synthesis of ferrocene-based side-chain metal-containing polymers

Ferrocene is an organometallic sandwich compound consisting of two cyclopentadienyl rings attached to the central iron. The compound is extremely stable and is therefore commonly used for the synthesis of organometallic polymers. Macromolecules containing ferrocene side groups have been intensively studied since the 1960s. Various polymerization techniques have been utilized to incorporate the ferrocene group into the side chain of polymers, e.g., the free radical,[4] cationic[5] and anionic[6] polymerization of vinyl, acrylate, or acrylamide ferrocene-containing monomers. In 1995, polypyrrole and polythiophene containing ferrocene as a pendant group were synthesized *via* electrochemical polymerization.[7] Early efforts on the polymerization of ferrocene-containing monomers generally led to polymers with low molecular weights and high polydispersities.[7] In addition, the polymer structures were poorly characterized.[7] In 1992, ring-opening metathesis polymerization (ROMP) was used for the polymerization of *trans*-(*exo*,*endo*)-2-carbomethoxy-(*endo*, *exo*)-3-ferrocenyl-5-norbornene, resulting in well-defined polymer with ferrocene side groups.[8] The M_n of the resulting polymers

was 5090 g/mol with a polydispersity index (PDI) of 1.2. Due to the living nature of the polymerization, block copolymers containing a norbornene block with a degree of polymerization (DP) of up to 80 were prepared.[8, 9] Starting in the 1990's, controlled radical polymerization techniques, including atom transfer radical polymerization (ATRP)[10] and reversible addition fragmentation chain transfer polymerization (RAFT) [11] have been used for the preparation of metallopolymers with ferrocene side groups. The preparation of side-chain metal containing polymers using living and controlled polymerization has been summarized in a recent review paper.[12]

1.2 Synthesis of non-ferrocene-based side-chain metal-containing polymers

A few examples of metallopolymers with non-iron metal species, such as Co and Ru, as side groups, have been explored recently. In 2010, Tang et al. successfully introduced cobaltocenium moieties into the side chains of poly(*tert*-butyl acrylate)-*b*-poly(2-hydroxyethyl acrylate) (PtBA-*b*-PHEA) block copolymers *via* esterification of cobaltocenium acyl chloride with the hydroxyl groups.[13] Wan et al. synthesized a series of well-defined diblock copolymers of polystyrene-*b*-poly[benzoic acid *N*'-(4-vinyl benzoyl)hydrazide]) (PS-*b*-PDCH) *via* nitroxide-mediated radical polymerization, and *cis*-Ru(bpy)$_2$Cl$_2$ 2H$_2$O was subsequently attached to the side chain of PS-*b*-PDCH.[14] Due to the steric hindrance and electrostatic repulsion between the adjacent bulky Ru complex in the polymer side chain, the maximum Ru content in the modified PS-*b*-PDCH was limited to 11 %, as revealed by inductively coupled plasma atomic emission spectroscopy (ICP) analysis.[14] In addition to post-polymerization modification, the direct polymerization of Co and Ru containing monomers was also possible.

Tang et al. successfully polymerized methacrylate cobaltocenium-containing monomers *via* RAFT. Hompolymers of poly(2-(methacrylolyoxy)ethyl cobaltoceniumcarboxylate hexafluorophosphate) (PMAECoPF6) with a molecular weight of up to 31700 g/mol and a PDI of 1.24 were obtained.[15] Using the homopolymers as macro raft agents, diblock copolymers of PMAECoPF6-*b*-PtBA and PMAECoPF6-*b*-PMMA, as well as a heterobimetallic diblock copolymer PMAECoPF6-*b*-PMAEFc (PMAEFc: poly(2-(methacrylolyoxy)ethyl ferrocenecarboxylate) were synthesized.[15] In addition to RAFT, ROMP was also employed to prepare high molecular weight cobaltocenium-containing polymers using Grubbs' 3rd generation catalysts at room temperature in an open air atmosphere.[16] For example, ROMP of norbornene-based *N*-[3-cobaltoceniumcarboxyl propyl]-*cis*-5-norbornene-*exo*-2,3-dicarboximide hexafluorophosphate (MPF6) generated homopolymers with a DP of up to 282. This polymer has the highest molecular weight among all reported cobaltocenium polymers. A kinetic study revealed that the polymerization proceeded in a living fashion.[16]

In the case of Ru-containing side-chain metallopolymers, free radical polymerization[17] and ring-opening polymerization (ROP)[18] have been attempted. However, all these polymerization techniques provided no control over the molecular weight. In 1995, Schrock and coworkers reported the living polymerization of ethynylruthenocene using $Mo(N-2,6-Me_2C_6H_3)(CHCMe_2Ph)[OCMe(CF_3)_2]_2$ as the initiator, and the resulting polymers exhibited molecular weights ranging from 6700 to 16,400 g/mol with a PDI of 1.2.[19]

1.3 Synthesis of ferrocene-based main-chain metal-containing polymers

Between 1950 and 1970, some efforts have been made to prepare main-chain

metal-containing polymer using step-growth polymerization, which often generated polymer with low molecular weights.[20] Soluble, stable and processible main chain metal-containing polymers were rarely reported except for polyferrocenylsilane (PFS).[21] The polymerization techniques reported for the synthesis of PFS are summarized below.

1.3.1 Thermal ring-opening polymerization

In 1992, the first high molecular weight PFS was reported by Manners et al. *via* the thermal ring-opening polymerization of strained, silicon-bridged[1]ferrocenophane $Fe(\eta-C_5H_4)_2Si(CH_3)_2$ **1** at 130 ^{o}C in bulk.[21] **1** was prepared *via* a reaction of dilithioferrocene·TMEDA (TMEDA: tetramethylethylenediamine) with dimethyldichlorosilane,[22] as shown in Figure 1.1. GPC analysis revealed that polymer **2** had a M_n of 34,000 g/mol and a PDI of 1.5. However, when two phenyls or two hydrogens instead of two methyl groups were substituted on the silicon, thermal ring-opening polymerization of these two monomers led to polymers which were insoluble in organic solvents.[21, 23]
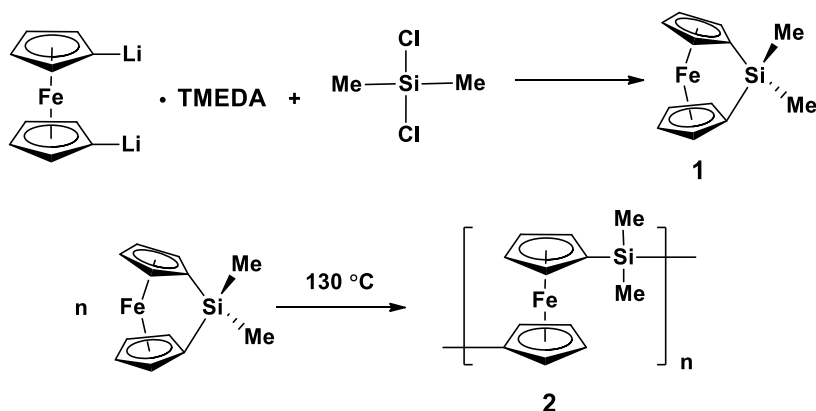
Figure 1.1 Synthesis and thermal ring-opening polymerization of $(\eta^5-C_5H_4)_2FeSi(CH_3)_2$.

1.3.2 Living anionic ring-opening polymerization

In 1994, living anionic polymerization of **1** at room temperature was achieved using PhLi or *n*-BuLi as initiator,[24] as shown in Figure 1.2. By adjusting the ratio between the initiator and monomer, a series of PFS **3** with molecular weights ranging from 4000 to 34,000 g/mol and a low polydispersity (1.02-1.26) were obtained. By sequential addition of a second strained monomer, cyclotrisiloxane $[Me_2SiO_3]_2$, to the intermediate PFS homopolymer before quenching, block copolymer **4,** polyferrocenylsilane-*b*-polydimethylsiloxane (PFS-*b*-PDMS), with a low polydispersity was prepared (Figure 1.3).
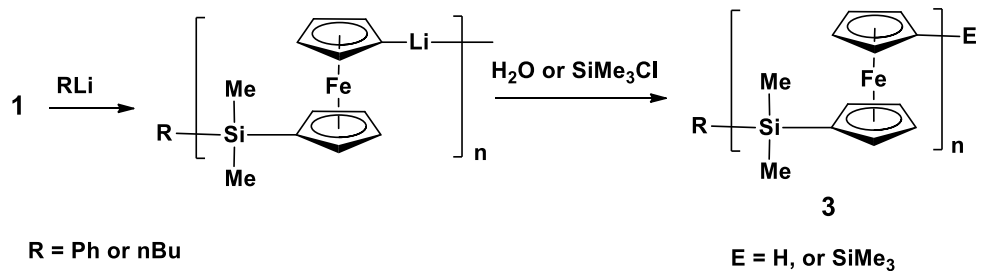
Figure 1.2 Anionic ring-opening polymerization of $(\eta^5\text{-}C_5H_4)_2FeSi(CH_3)_2$ using PhLi or *n*-BuLi as initiator.
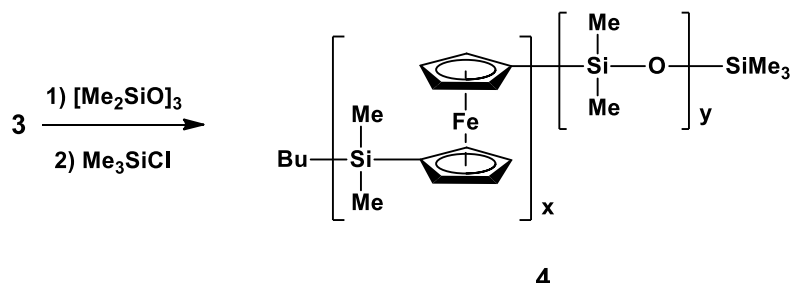
Figure 1.3 Preparation of PFS-*b*-PDMS diblock copolymer by anionic ring-opening polymerization.

1.3.3 Transition metal-catalyzed polymerization

In 1995, ring-opening polymerization of silicon-bridged[1]ferrocenophane in solution at ambient temperature catalyzed by a transition metal complex was reported.[25][26] It was found that PFS with molecular weight of 122,500 g/mol was obtained when $PtCl_2$ or $PdCl_2$ was used as the catalyst for the ring-opening polymerization of **1**.[25]

1.3.4 Photo-controlled anionic ring-opening polymerization

In 2004, Tanabe and Manners et al. reported the photo-controlled living anionic polymerization of **1** *via* an iron-cyclopentadienyl bond cleavage mechanism.[27] It was found that when $Na[C_5H_5]$ was used as initiator under UV irradiation, anionic ROP of **1** was successfully accomplished, resulting in the formation of polymer **5** (Figure 1.4). By varying the ratio between the monomer and initiator, a series of PFS with controlled molecular weights ranging from 9300 to 70,000 g/mol and a low PDI were synthesized.[27] In contrast to BuLi initiated anionic polymerization, the propagation center for the photo-controlled anionic polymerization was a silyl substituted Cp anion. Block copolymers were prepared by sequential addition of a second monomer.[28]
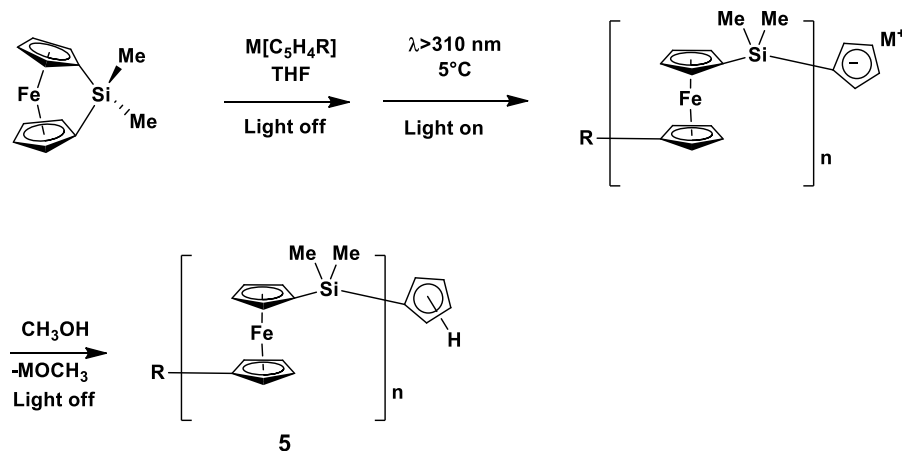
Figure 1.4 Photo-controlled living ROP of **1**.

In contrast, when labile Lewis base 4,4'-dimethyl-2,2'-bipyrinde (Me$_2$bpy) instead of Na[C$_5$H$_5$] was used as initiator, a series of oligomeric cyclic PFS **6** were obtained (Figure 1.5).[29] The cyclic species were separated by column chromatography and characterized by single crystal X-ray diffraction. The formation of cyclic oligo-PFS, instead of linear species, was attributed to the substitutional lability of the Me$_2$bpy ligand as compared to Na[C$_5$H$_5$] on the end group of a growing PFS chain, which made the backbiting intramolecular cyclization reaction relatively easy to happen.[29] Meanwhile, by adjusting the reaction temperature and concentration, cyclic PFS with a molecular weight of more than 100 KDa can be obtained.[29]
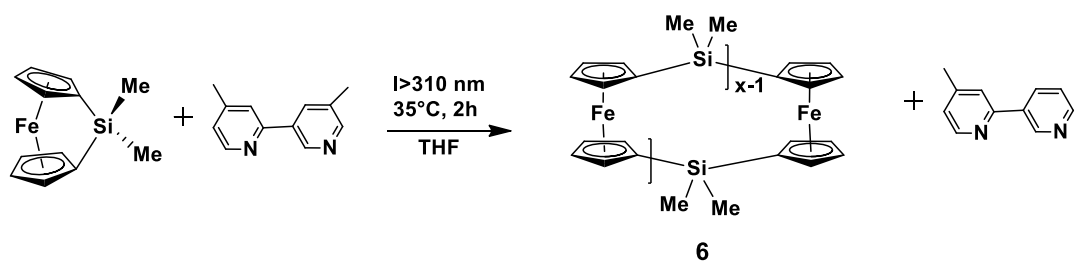
Figure 1.5 Ring-expansion of macrocyclization of **1**.

1.3.5 Metallocene-based polymer with different ligands and substituents on Cp ring

Thermal ROP of ruthenocenophane **7**[30] and transition-metal catalyzed ROP of chromarenophane **8**[31] has also been attempted, but led to either insoluble polymeric materials or soluble oligomeric species.

7

(a) R = H
(b) R = Me

7

(a) R = R '= Me
(b) R = Me, R' = Et

8
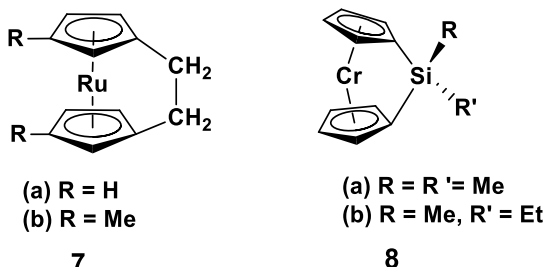
Figure 1.6 Chemical structure of ruthenocenophane (**7**) and chromarenophane (**8**) for ROP.

In 2009, germanium-bridged[1]ferrocenophane **9** was synthesized and used for the anionic ring-opening polymerization. Well-defined polyferrocenyldimethylgermane (PFDMG) homopolymer **10** with DP_n ranging from 66-117 was obtained (Figure 1.7). All the resulting polymers displayed a low PDI (1.02-1.05).[32]

9

1. ^{n}BuLi, THF, 25 °C
2. MeOH

10
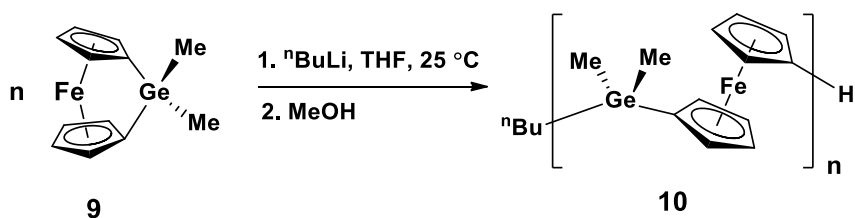
Figure 1.7 Anionic ROP of germanium-bridged [1]ferrocenophane.

In 2014, tricarba[3]nickelocenophane **11** was prepared.[33] Thermal ring opening polymerization of **11** led to insoluble materials.[33] However, when **11** was stirred in pyridine, polymeric materials were obtained. MALDI-TOF and light scattering results indicate that the resulting material was a mixture of cyclic and linear polymers. The cyclic materials had a DP of 33, while the linear polymers had a DP of 175 (Figure 1.8).[33] The formation of cyclic species may be attributed to the lability of the pyridine initiator, which can be replaced by the Cp end group.[33]

8
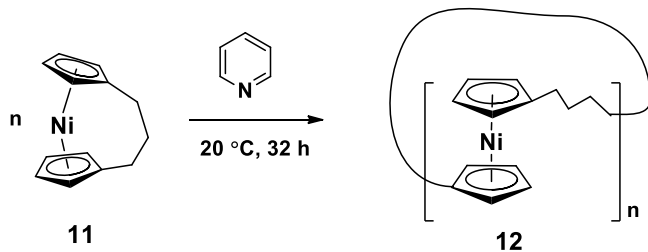
Figure 1.8 ROP of tricarba[3]nickelocenophane in pyridine.

1.4 Synthesis of metal carbonyl polymers

1.4.1 Metal carbonyl complex

Metal carbonyl (MC) coordination involves two types of interactions, sigma and pi bonds. Sigma bonds are formed *via* electron donation from a CO ligand to an appropriate metal orbital (such as unfilled *p*, *d*, or hybrid orbital) (Figure 1.9a).[34] Meanwhile, the metal atoms that have electrons in the *d* orbitals with appropriate symmetry, can directly back donate electrons to the empty π^* orbitals of CO (Figure 1.9b), forming π bonds.[34] The σ and π bonds are synergistic and reinforce each other.[34]
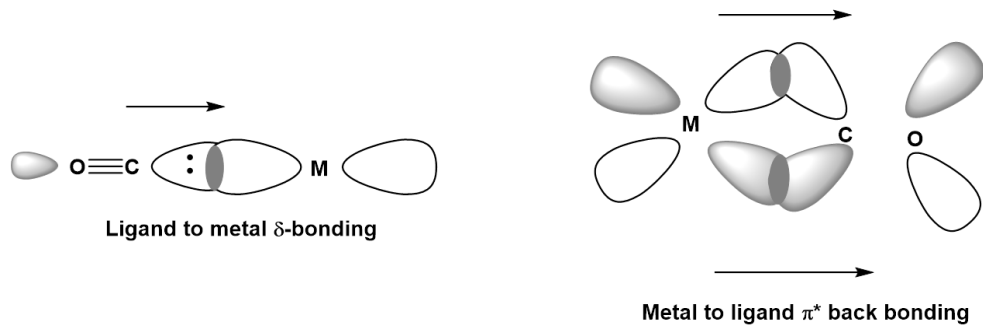
Figure 1.9 Orbital overlap in metal carbonyl bonding.[35] (arrows in the picture indicate the direction of electron flow)

Carbon monoxide (CO) ligands in MC compounds may terminally coordinate to one metal center (terminal mode) (Figure 1.10a), or bridge two or three metal atoms (bridging mode)

(Figure 1.10b, c). The latter are designated using the Greek letter μ, followed by a subscript specifying the number of metal atoms bridged. C and O atoms both coordinated to metal centers are also possible. In this case, the carbonyl ligands are defined as η^2 (Figure 1.10d). MC complexes can be homoleptic, which means that the compound contains only CO ligands such as $Ni(CO)_4$. Most of the metal carbonyl complexes are, however, heteroleptic and have different kinds of ligands coordinated to the metal atom.
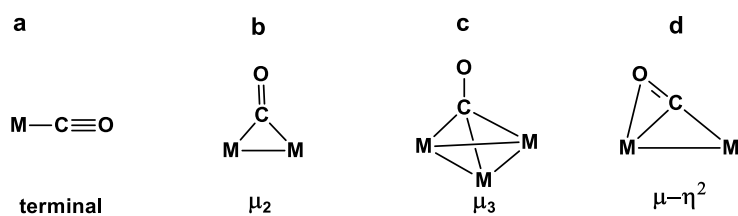
Figure 1.10 (a) Terminal, (b, c) bridging mode of metal carbonyl complexes and (d) carbonyl ligand with carbon and oxygen both coordinated to metal center.

In contrast to the noteworthy progress in ferrocene-based polymers, the synthesis of metal carbonyl (MC) organometallic macromolecules has been less explored. The major issue involved is the instability of MC complexes, which renders the metal carbonyl complexes incompatible with many conventional polymerization techniques, e.g., radical,[36] anionic.[37] The early exploration focused on the synthesis of side-chain MC organometallic macromolecules by taking advantage of the synthetic and polymer chemistry. These efforts involved the direct polymerization of organometallic monomers containing MC moieties or post-polymerization modification of prepared polymers.

1.4.2 Synthesis of side-chain metal carbonyl organometallic macromolecules

1.4.2.1 Direct polymerization of organometallic monomers containing metal carbonyl group

Polymerization techniques developed for organic polymers have been used for the preparation of MC macromolecules. For example, **13**[38] and **14**[39, 40] were prepared *via* free radical and oxidative polymerization (Figure 1.11), respectively. **15**[41] was synthesized *via* the polycondensation of cyclopentadienyl dicarbonyl iron functionalized diol and diacyl chloride. These efforts usually generate oligomeric species or polymers with low solubility. For example, the resulting **13** has a low molecular weight of 2800 g/mol and the yield is merely 12 %.[38] Partly insoluble material was generated during the polymerization for **15**.[41] **14** cannot be dissolved in organic solvent and only becomes moderately soluble upon addition of dodecylbenzenesulfonic acid (DBSA).[40]
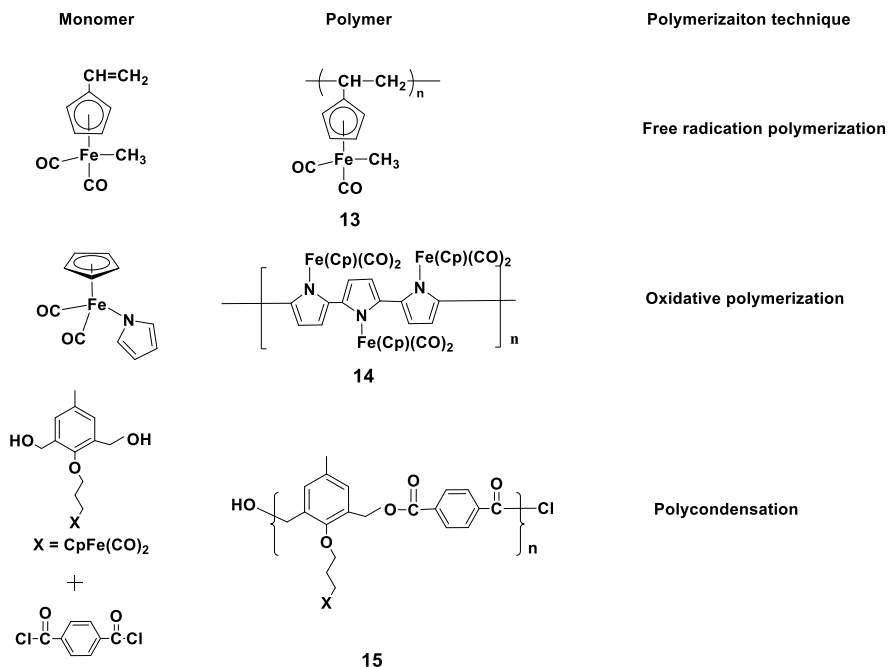
Figure 1.11 Direct polymerization of monomers containing cyclopentadienyl dicarbonyl iron moieties.

In 2002, conjugated copolymers containing chromium tricarbonyl moieties were synthesized by Chujo et al. *via* Pt-catalyzed polycondensation of η^6-(1,4-diethynylbenzene)tricarbonylchromium with 3-alkyl-2,5-dibromothiophene (Figure 1.12).[42] The resulting **16** had a M_n ranging from 13,500 to 22,400 g/mol and was soluble in common solvents such as THF, CH_2Cl_2, $CHCl_3$ and toluene.[42]
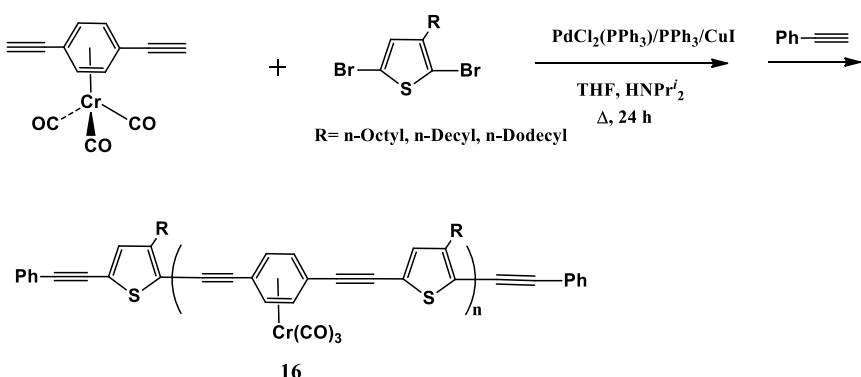
Figure 1.12 Synthesis of conjugated copolymers containing chrominum tricarbonyl.

Ring-opening metathesis polymerization (ROMP) of strained bicyclic norbornene monomers using Grubbs' catalyst is compatible with various types of functional groups.[43] Taking this advantage, Tew et al. discovered that the ROMP of **18** can be achieved in a living fashion using the 3rd generation Grubbs' catalyst (Figure 1.13).[43] **18** was prepared by reacting **17** with dicobalt hexacarbonyl (Figure 1.13). The molecular weight of the resulting **19** ranged from 20 to 100 kDa with PDI of less than 1.2.[43] By sequential polymerization of **20** and **18**, block copolymer **21** was synthesized (Figure 1.14).[44]
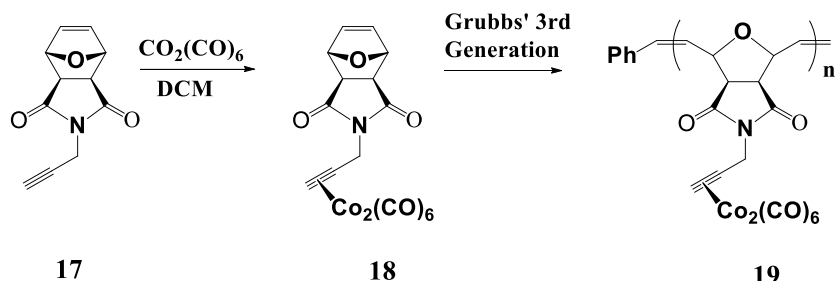
Figure 1.13 Protection of acetylene with dicobalt hexacarbonyl and ring opening metathesis polymerization of monomer **18**
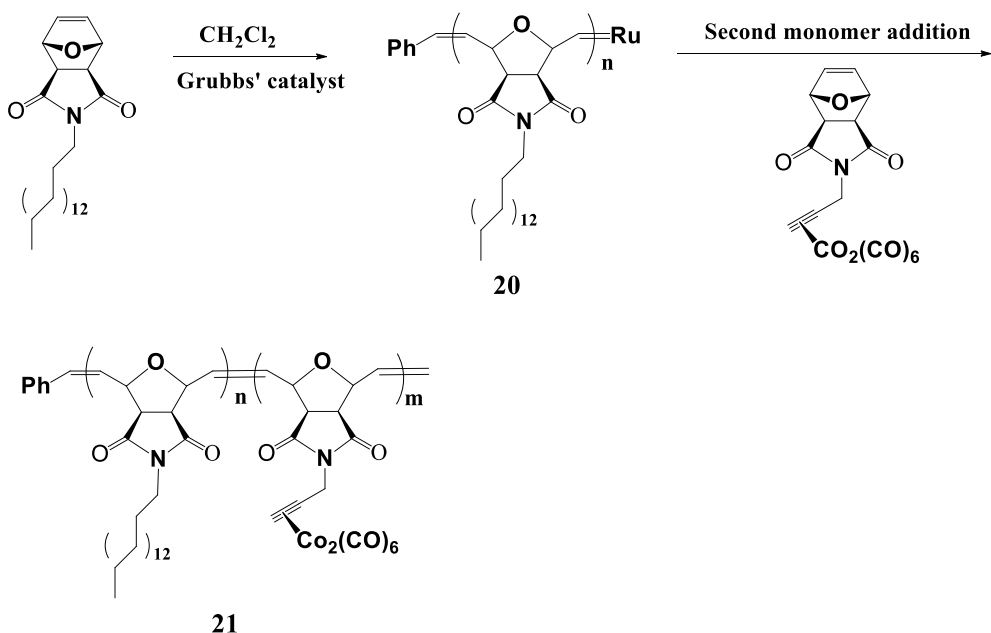
Figure 1.14 Synthesis of cobalt carbonyl containing block copolymers *via* ROMP using Grubbs' 3rd generation catalyst.

1.4.2.2 Synthesis of metal carbonyl polymers *via* post-polymerization modification

A salt-elimination reaction of the η^5-cyclopentadienyl dicarbonyl iron anion (Fp anion) for the prepared polymers is a major method of post-polymerization modification (Figure 1.15) for the preparation of MC macromolecules. Poly(*p*-chloromethyl styrene) (PVBC)

homopolymer, prepared *via* free radical polymerization, was reacted with Fp anion, yielding **22**.[45] When the ratio of phenyl to Fe fell in the range of 0.15-0.30, **22** was soluble in common organic solvents such as benzene, THF, CH_2Cl_2. After 25 % of the chloromethyl groups reacted with the Fp anion, the molecular weight distribution of the resulting polymer slightly increased to 1.32, as compared to the starting PVBC homopolymer with a PDI of 1.17. CS_2 solution of **22** was repeatedly filtered through aluminum oxide column to obtain the pure product; however, the yield for **22** was only 65 % due to difficulties in purification.[45]
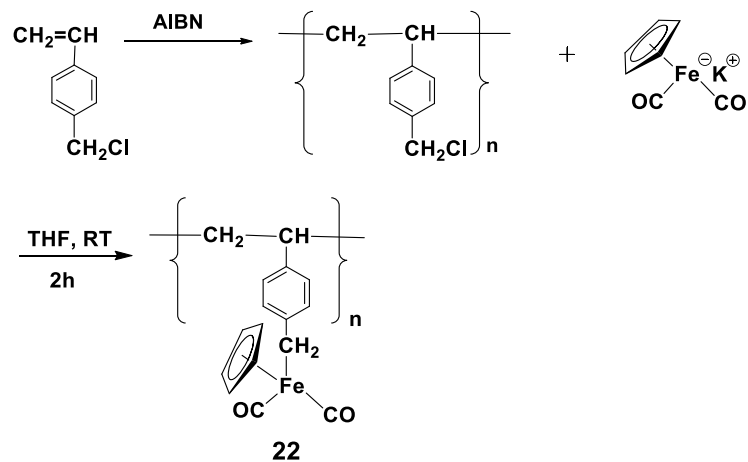
Figure 1.15 Synthesis of homopolymer **22** *via* the salt-elimination reaction between Fp anion and PVBC.

Taking the same strategy, Fp groups were also introduced into polydichlorophophazene, yielding **23**[46]. However, **23** was not characterized due to its low solubility. By adding sodium trifluoroethoxide THF solution to **23**, all the remaining chlorides were replaced by trifluoroethoxide, yielding **23a**. **23a** is soluble in acetone and THF. GPC results revealed that **23a** exhibited a lower molecular weight as compared to polydichlorophophazene, probably because chain cleavage occurred during the reaction of polydichlorophophazene with the Fp anion.
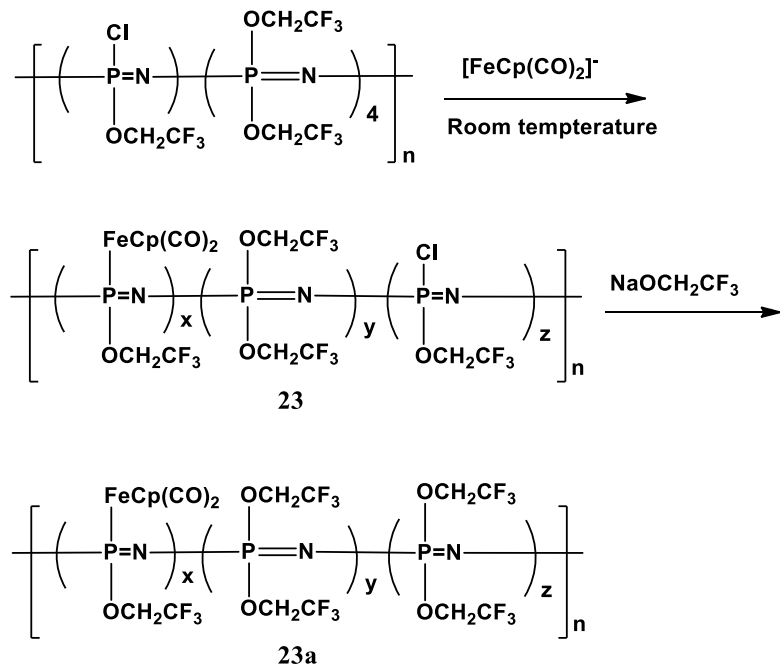
Figure 1.16 Reaction of polydichlorophophazene with Fp anion.

The reaction of the Fp anion with poly[*p*-(chloromethylsilylene)phenylene] generated **24**.[47] The counterion of Fp anion seems to affect the reaction. For example, GPC results revealed a bimodal molecular weight distribution when [Cp(CO)$_2$Fe]Na was used. The high molecular weight fraction was probably caused by partial cross-linking in the backbone. However, in the case of [Cp(CO)$_2$Fe]K, the reaction resulted in a monomodal molecular weight distribution with a PDI of 4.1. The ^{29}Si NMR spectrum displayed a single peak at 33.9 ppm, which is characteristic for metal-substituted silicon.
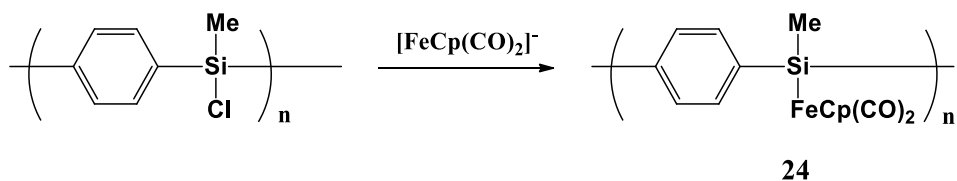
Figure 1.17 Reaction of poly[p-(chloromethylsilylene)phenylene] with Fp anion.

In addition to the salt-elimination reaction, Fp groups can also be introduced into block

copolymer side chains *via* a hydrosilylation reaction. As shown in Figure 1.18, **25** was

prepared *via* the reaction of Fp anions with $Cl(CH_3)_2SiCH=CH_2$, and subsequently **25** was

reacted with the Si-H group for the post-polymerization modification of **26,** generating **27.**[48]
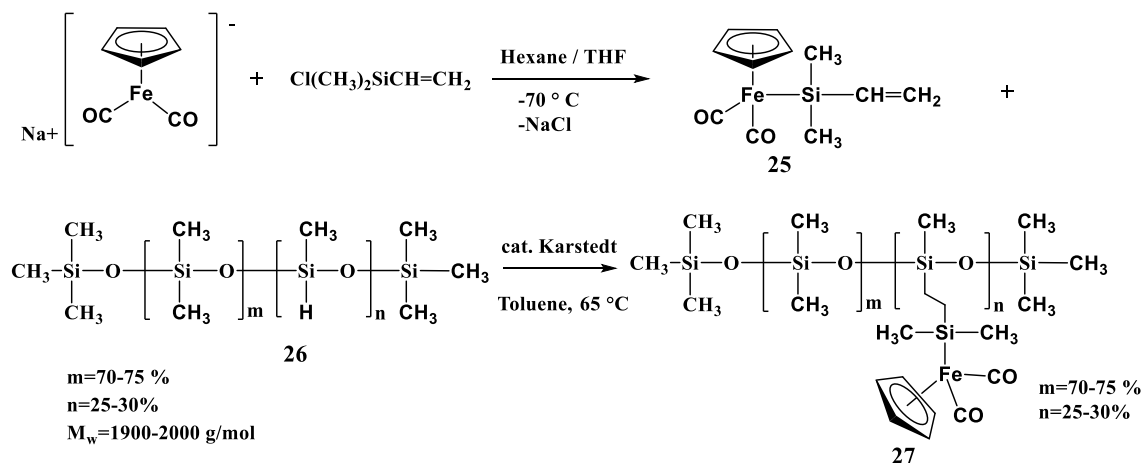
Figure 1.18 Post-polymerization modification of poly[p-(chloromethylsilylene)phenylene] *via* a

hydrosilylation reaction.

Coordination of $[Co_2(CO)_8]$ and $[MoCp(CO)_2]_2$ with alkynes has been used for the

post-polymerization modification of PFS.[49] The metal carbonyl cluster $[Co_2(CO)_8]$ readily

reacted with acetylide-substituted PFS at 25 ^{o}C, generating **28**. ^{1}H NMR analysis revealed that

$[Co_2(CO)_8]$-PFS has a clusterization extent of ca. 75 %. In the case of polymer **29**, the reaction

was carried out at 75 ^{o}C and ^{1}H NMR analysis indicated that triple bonds were 69 %

clusterized.[49]
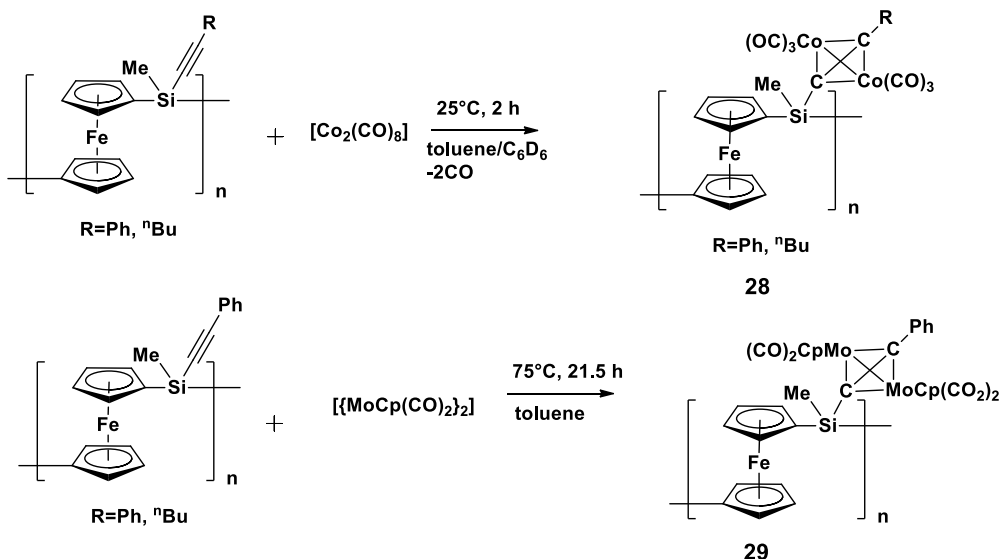
Figure 1.19 Reactions of acetylide-substituted PFS with [Co$_2$(CO)$_8$] and [MoCp(CO)$_2$]$_2$.

Cobalt-carbonyl containing diblock copolymer **30** was synthesized by reacting block copolymer of polystyrene-*b*-poly(4-(phenylethynyl)styrene) (PS-*b*-PPES) with [Co$_2$(CO)$_8$] (Figure 1.20). Elemental analysis revealed that 80-90 % of the alkyne groups were reacted.[50] When the molar ratio between [Co$_2$(CO)$_8$] and alkyne group increased from 1 to 2, a product with a low solubility in toluene was generated, suggesting the presence of cross-linking.[50]
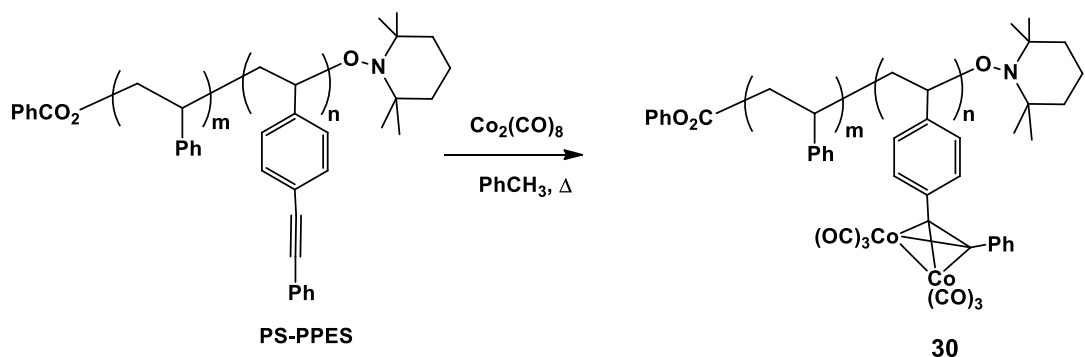
Figure 1.20 Reactions of acetylide-substituted PS-*b*-PPES with [Co$_2$(CO)$_8$].

Ruthenium carbonyl groups were attached to the side chain of poly(ethylene glycol)-*b*-poly(ornithine acrylamide)-*b*-poly(*n*-butylacrylamide) (PEG-*b*-POrnNa-*b*-PnBu) *via* complexation of [Ru(CO)$_3$Cl$_2$]$_2$ with the middle segment OrnNa of the block copolymer, yielding **31**[51] (Figure 1.21). Inductively coupled plasma optical emission spectroscopy

(ICP-OES) revealed that 58-75 % of the OrnNa units were complexed with ruthenium carbonyl groups;[51] the lack of full complexation was possibly caused by the bulkiness of the Ru carbonyl group.[51]
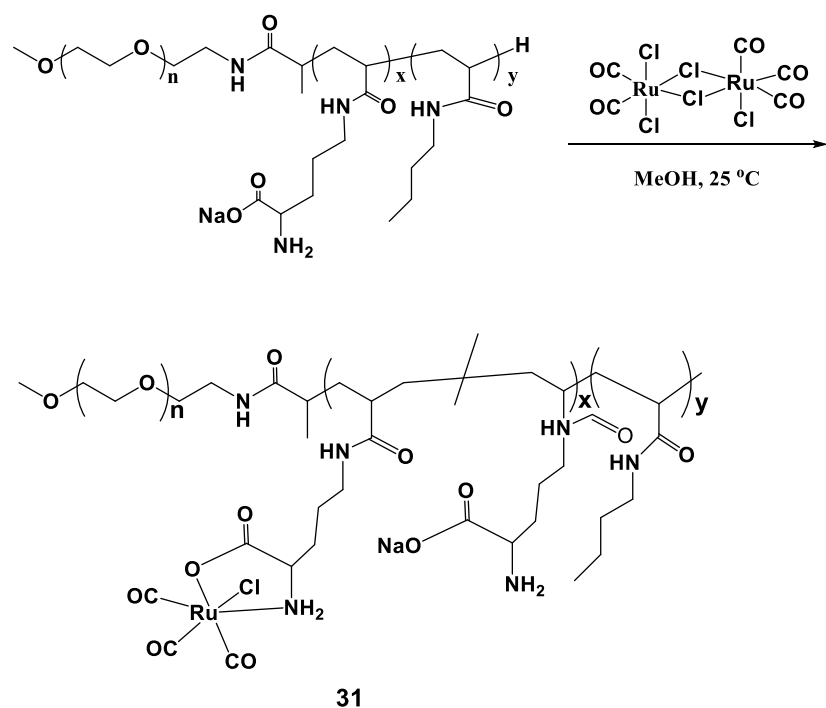
Figure 1.21 Reactions of [Ru(CO)$_3$Cl$_2$]$_2$ with PEG-*b*-POrnNa-*b*-PnBu.

1.4.3 Synthesis of main-chain metal carbonyl organometallic macromolecules (MCMCOMs)

The synthesis of main-chain metal carbonyl organometallic macromolecules (MCMCOMs) is challenging and rarely reported, due to the instability of metal carbonyl complexes. The groups of Tyler and Pannell have made great effort to address this challenge and created a number of MCMCOMs by strategically using organometallic, organic and polymer synthetic chemistry. These polymers are classified into two types: MCMCOMs containing metal-metal bonds; MCMCOMs with main group elements, e.g., Si, Ge. The synthesis of these monomers and their corresponding polymers are summarized in the following.

18

1.4.3.1 MCMCOMs containing metal-metal bonds

Tyler et al. have contributed significantly to develop the chemistry for the synthesis of MCMCOMs with metal-metal bonds along the polymer backbone.[52] This type of polymer is photochemically degradable due to the relatively weak metal-metal bonds that can be cleaved by visible light.[53, 54]

Based on the chemistry for the preparation of cyclopentadiene (Cp) functionalized metal-metal bonded dimers, monomers were designed to introduce polymerizable groups into dimers. However, the labile metal-metal bond imposes a challenge for the synthesis.[55] To address this challenge, two synthetic routes have been developed.[52] As shown in Figure 1.22, the dimers can be prepared starting from the functionalization of the Cp ring prior to the creation of the metal-metal bond (route a in Figure 1.22). Alternatively, phosphine ligands containing polymerizable groups R can be introduced to the existing metal-metal bonded dimers *via* mild ligand substitution reactions (route b in Figure 1.22). Using these two approaches, a number of monomers containing metal-metal bonds have been prepared[52] and some of them are illustrated in Figure 1.23.
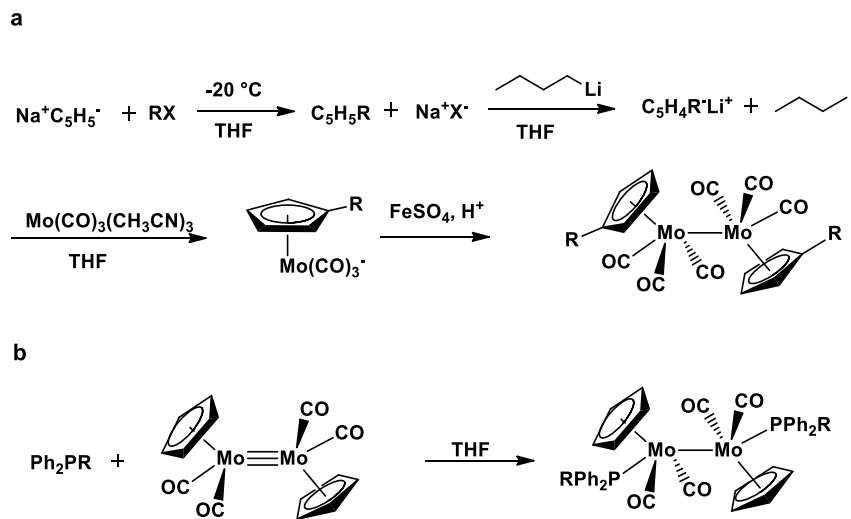
Figure 1.22 Synthetic routes for the preparation of $(\eta^5\text{-}C_5H_4R)_2Mo_2(CO)_6$ and $(\eta^5\text{-}C_5H_5)_2Mo_2(CO)_4(PPh_2R)_2$ containing Mo-Mo bond with functional group R on (a) Cp ring and (b) coordinated phosphine group.
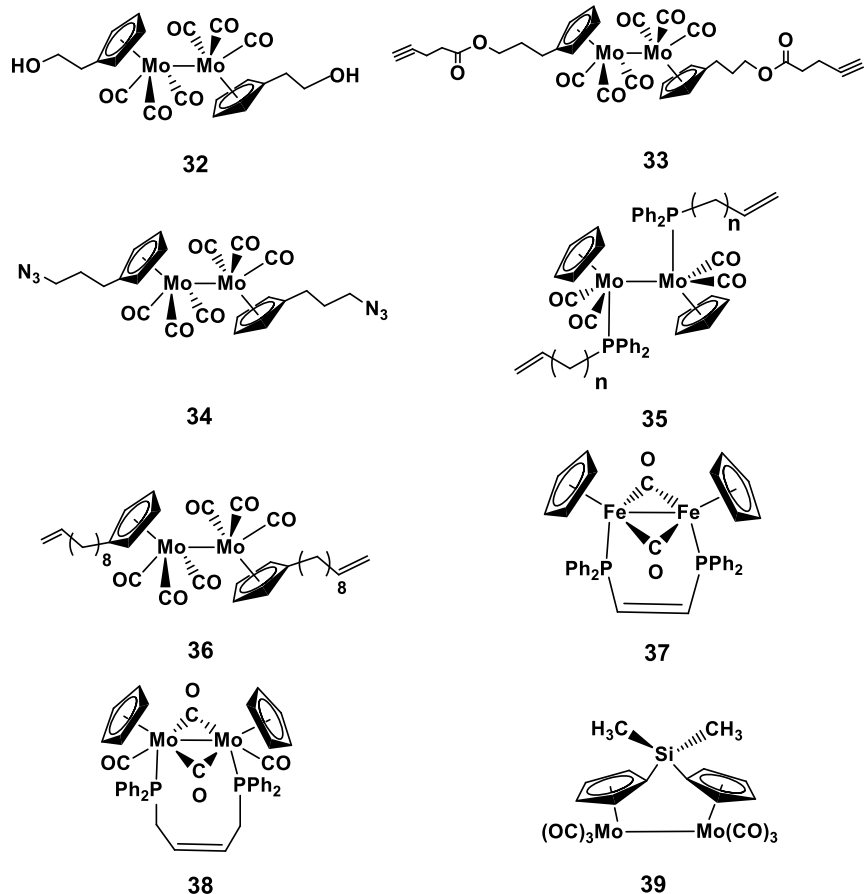
Figure 1.23 Chemical structure of functionalized monomers containing metal-metal bond.

Different polymerization methodologies including step-growth polymerization, ROMP and thermal ROP have been explored for the preparation of MCMCOMs. Since this work has been well summarized in the literature,[52] only representative examples of each polymerization technique will be briefly highlighted.

Step-growth polymerization of a bifunctional dimer has enabled the preparation of MCMCOMs with either $Cp_2Mo_2(CO)_6$ or $Cp_2Fe_2(CO)_4$[56] in the polymer backbone. Figure 1.24 shows an example of the synthesis of polyurethanes with Mo-Mo bonds by reacting a metal-metal bonded diol complex **32** with hexamethylene diisocyanate (HMDI). Based on this same strategy other types of polyurethanes,[57] polyureas and polyamides with Mo-Mo bonds in the polymer backbone have been prepared.[54] The molecular weight of the synthesized polymers usually falls within the range of 5000-20,000 g/mol (DP = 7-25). As stated in a previous review,[55] no efforts have been made to increase the molecular weight, since the photodegradable properties of the macromolecules rather than the polymerization process itself was the focus of the research. Cleavage of the metal-metal bond during the polymerization process was also observed under specific conditions. For example, polycondensation of **32** and diacyl chloride resulted in the formation of metal halide complex instead of the targeted polyesters (Figure 1.25).[52, 58]
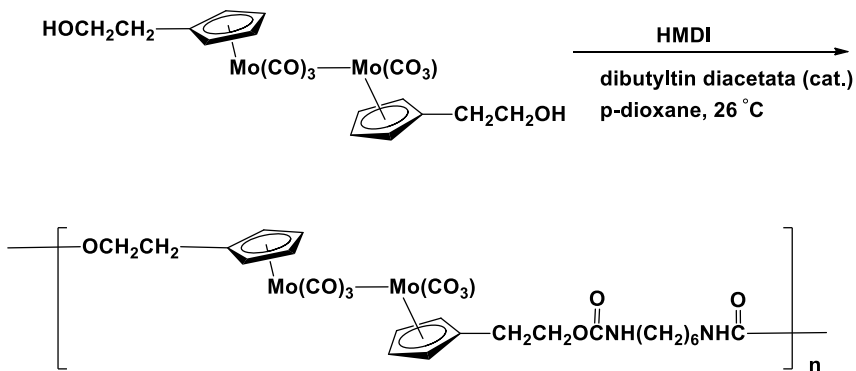
Figure 1.24 Synthesis of polyurethane with Mo-Mo bond in the polymer backbone *via* polycondensation.
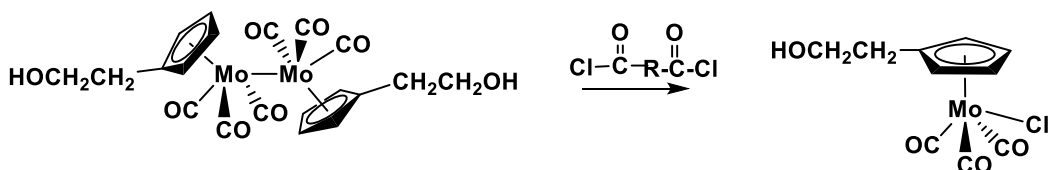
Figure 1.25 Reaction of **32** with diacyl chloride.

Alkyne and azide click reactions can be performed under mild conditions and have therefore been explored for the synthesis of MCMCOM with metal-metal bonds. Monomer **33** containing alkyne groups were prepared *via* N,N-dicyclohexylcarbodiimide (DCC) mediated esterification of $[(\eta^5\text{-}C_5H_4(CH_2)_3OH)Mo(CO_3)]_2$. Copolymerization of **33** with azide-functionalized polystyrene oligomers was performed using $CpRu(PPh_3)_2Cl$ as catalyst (Figure 1.26).[59] GPC results revealed that the product had a bimodal molecular weight distribution, with $M_n = 120000$ g/mol and $M_n = 8900$ g/mol, respectively. The reaction of complex **33** with azide-functionalized polyethylene glycol (PEG) with M_n of 300 g/mol was also performed. After 15 h, the GPC trace also displayed two peaks with $M_n = 73000$ g/mol and $M_n = 9700$ g/mol. However, extending the polymerization time to 33 h, to increase the extent of reaction, lead to the decomposition of the $Cp_2Mo_2(CO)_6$ units.[59] Commonly used catalysts such as Cu complexes with either N,N,N',N'',N''-pentamethyldiethylenetriamine (PMDETA) or bipyridine (bpy) led to

disproportionation of the metal-metal bond. Control experiments indicated that PMDETA and

bpy in the copper/ligand systems caused the disproportionation of the dimer.[59]
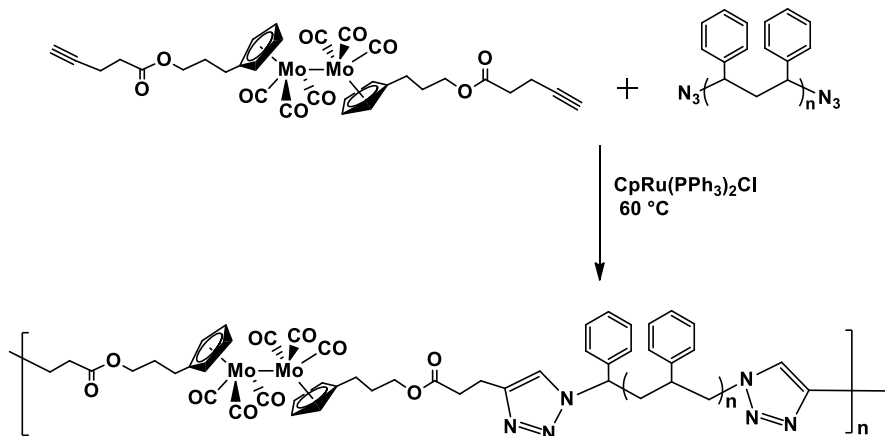
Figure 1.26 Polymerization of **33** with azide functionalized polystyrene oligomers *via* click

reactions.

Monomer **34**, that contains an azide group instead of an alkyne group, was used to react with

1,3,5-triethynylbenzene.[60] However, no click reaction occurred when CpRu(PPh$_3$)$_2$Cl was

employed as the catalyst. It was found that the azide can react with the phosphine ligand

forming aza-ylide (Staudinger reaction).[61] To avoid this problem, CpRu(COD)Cl was used for

the polymerization. In this case a polymer was obtained, but without a Mo-Mo backbone. A

control experiment revealed that this polymer was probably produced by the cyclotrimerization

of the alkyne groups in 1,3,5-triethynylbenzene. Finally, when Cu(IMes)Cl was used as the

catalyst, a polymer with Mo-Mo backbone was produced but with a low yield (<10 %). This

polymer had a molecular weight of 77,000 g/mol.[60]

Acyclic diene methathesis polymerization (ADMET) is a newly developed polymerization

technique used for the polymerization of divinyl monomers. The catalysts utilized in the

polymerization are tolerant to a number of functional groups. As a result, it was explored in the

polymerization of metal-metal dimers. Attempts to polymerize complex **35**, in which the C=C

23

unit is part of the phosphine, *via* ADMET using different catalysts were not successful[62] and only an oligomer with a DP of ca. 3 was produced.[63] This inability of polymerization was attributed to the steric effect caused by the short alkyl chain connecting the metal and the C=C group.[62] In the case of complex **36** the alkene substituents were located on the Cp ligand, ADMET of **36**, under concentrated solution condition using Schrock's catalyst, led to the formation of oligomer **40** with a molecular weight of 2300 g/mol and a high PDI of 4.3 (Figure 1.27).[64] The molecular weight slightly increased to 3400 g/mol when complex **36** was copolymerized with 1,9-decadiene using Grubb's 2nd generation catalyst, resulting in the formation of **41** (Figure 1.27). In a dilute solution ring-closing metathesis (RCM) was preferred, leading to cyclization product **42** (Figure 1.27).[64]
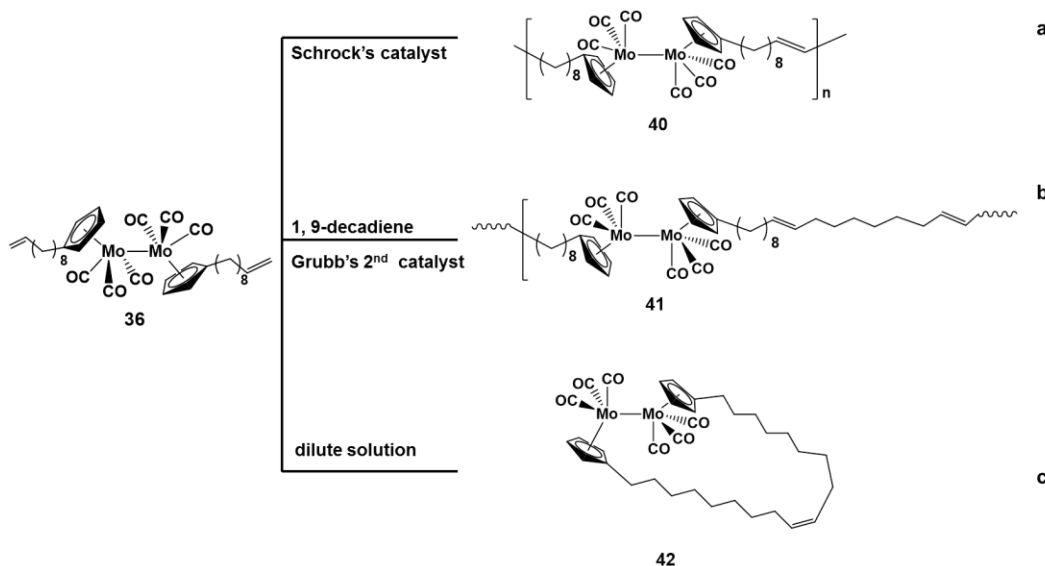
Figure 1.27 (a) ADMET hompolymerization of complex **36**; (b) copolymerization of complex **36** with 1,9-decadiene and (c) ring-closing metathesis of complex **36**.

Ring-opening metathesis polymerization (ROMP) is a living chain growth polymerization,[65] which offers the possibility to prepare MCMCOM in a designed fashion. Several cyclic

metal-metal bonded complexes with C=C were prepared and used for ROMP. The polymerization of complex **37** with up to 10 % loading of Grubbs' 1st generation catalyst did not yield any polymeric species.[66] This was probably due to the bulky phenyl groups on 1,2-bis(diphenylphosphino)ethane (DPPN). Consequently, the C=C in **37** could not coordinate to the catalyst, which prevented the polymerization. In order to overcome this steric effect posed by the phenyl groups, complex **38** with a longer butenyl spacer was designed. However, similarly to complex **37**, the polymerization of complex **38** did not give any polymeric materials regardless of which catalyst was used,[52] indicating that the extra methylene in the phosphine ligand is not sufficient to alleviate the steric effect caused by the bulky phenyl group.[49]

Ring-opening polymerization of silicon-bridged metal-metal bonded cyclic molecules **39** was also attempted.[37] Both anionic polymerization using *n*-BuLi as an initiator and a transition metal-mediated polymerization using $PtCl_2$ as catalyst also did not produce polymeric materials. The unsuccessful polymerization was attributed to insufficient ring strain. However, when the monomer was heated to 150 ^{o}C for 3 h, polymeric species with a M_n of 140,000 g/mol and a PDI of 1.5 were obtained.[37] FT-IR analysis of the polymer revealed that the product was actually a mixture containing both Mo-Mo and Mo≡Mo units. The Mo≡Mo units resulted from the loss of two CO groups.[57] Extending the reaction time to 6 h led to degradation of the polymer product.

1.4.3.2 MCMCOMs containing main group elements

1.4.3.2.1 Ring-opening polymerization of sila-matallacyclobutantes and germa derivative

By treating $(\eta^5$-$C_5H_5)Fe(CO_2)SiR_2CH_2Cl$ **43** or its isomer, $(\eta^5$-$C_5H_5)Fe(CO_2)CH_2SiR_2Cl$ **44,**

with lithium diisopropylamide (LDA) in THF, Pannell et al. synthesized 1-sila-3-metallacyclobutanes clobutanes with different R groups connected to Si (**45**) (Figure 1.28).[67] The stability of the metallacycles **45** (**a-d**) depends on the R groups on the silicon. When $R_2 = Bu_2$, the di-*n*-butyl complex **45c** is thermally stable and can be isolated; but it could not be polymerized by either thermal, anionic or transition metal-catalyzed polymerization methods.[67] Instead, photo-chemical treatment of **45c** lead to a phosphine substituted-metallacycle, which was characterized by single-crystal X-ray diffraction.[67]

When $R_2 = Me_2$, MeBu, MePh (**45a**, **45b**, **45d**)**,** polymerization occurred even at room temperature upon solvent evaporation; thus isolation and characterization of the monomers could not be executed. The resulting polymers **46a** and **46b** were soluble in THF, while **46d** became insoluble after precipitating in hexane. The signal for the methylene carbon in the ^{13}C NMR spectrum downfield shifted from -53 ppm in **45a** to -26.1 ppm in **46a**, indicating the occurrence of the polymerization. Polymer **46a** had a M_n of 72,000 g/mol with a PDI of 2.4. Polymer **46b** had a M_n of 1500 g/mol with a high PDI of 6.3. The resulting polymer **46a** was further reacted with mono or diphosphine *via* migration insertion reaction, resulting in the formation of phosphine coordinated linear polymers, $[(\eta^5\text{-}C_5H_4)Fe(CO)(PR_3)C(O)CH_2SiMe_2]_n$ ($R_3 = Me_2Ph$, Ph_3), or diphosphine bridged polymers.[68]
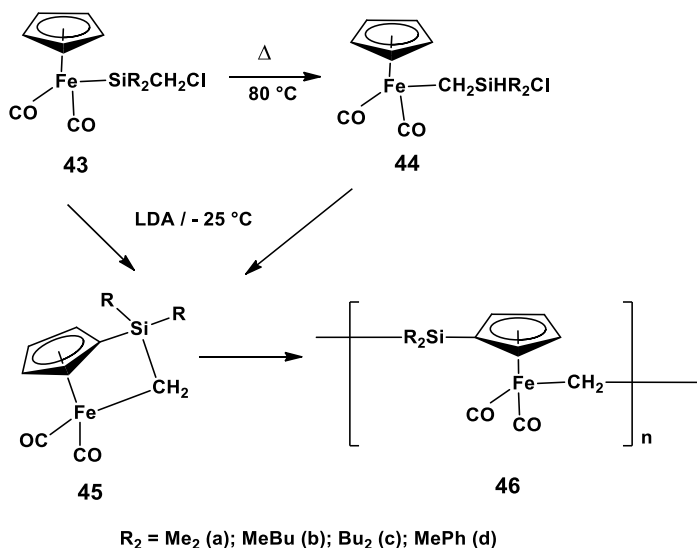
Figure 1.28 Synthesis and ring-opening polymerization of sila-metallacyclobutanes.

Following the synthetic strategy developed for sila-metallacyclobutanes, germa-matallacyclobutanes were obtained by treating **47-52**, **47a**, **48a** and **52a** with LDA (Figure 1.29).[36] Whether the resulting cyclobutane compounds could be isolated or not depended on the metal involved. When the cyclobutanes contained Mo and W as metal centers **55-58**, the compounds could be isolated as stable, crystalline materials. The molecular structures of **55** and **57** were subsequently characterized by single crystal X-ray diffraction.[36] Although their crystal structures revealed the presence of ring strain in M-C-Ge-C, these complexes could not be polymerized. For instance, the ring opening polymerization of **55** was attempted by a number of reagents, including radical initiator (AIBN), anionic and base species (*n*-BuLi, LDA, Et$_3$N) and transition metal complexes ((PPh$_3$)$_4$Pd), yet no polymerization was detected.[36] Instead, the thermal reaction of **55** and **57** with PPh$_3$ in THF yielded phosphine substituted products.[36] Compared to the Mo and W complexes, cyclobutanes with Fe as the metal center are less stable. Dimethylgermane complex **53** could not be isolated, but transformed into polymer **53a** in a short period of time. GPC analysis revealed that **53a** had a M$_n$ of 2200 g/mol with a PDI of 1.13.[36] In

27

contrast, butylgermane iron complex **54** was more stable and could be purified *via* silica gel chromatography. This complex, different from its silicon analogue, **45c**, underwent a ring-opening polymerization when it was left for a long period of time (one month), even at 0 $^{\circ}$C, generating the corresponding polymer **54a** with a M_n of 2500 g/mol and a PDI of 2.1.

M = Fe, R = Me **(47)**, n-Bu **(48)**, n = 2
M = Mo, R = Me **(49)**, n-Bu **(50)**, n = 3
M = W, R = Me **(51)**, n-Bu **(52)**, n = 3

M = Fe, R = Me **(47a)**, n-Bu **(48a)**, n = 2
M = W, R = n-Bu **(52a)**, n = 3

M= Fe, R = Me **(53)**, n-Bu **(54)**, n = 2
M= Mo, R = Me **(55)**, n-Bu **(56)**, n = 3
M= W, R = Me **(57)**, n-Bu **(58)**, n= 3

M = Fe, R = Me **(53a)**, n-Bu **(54a)**, n = 2
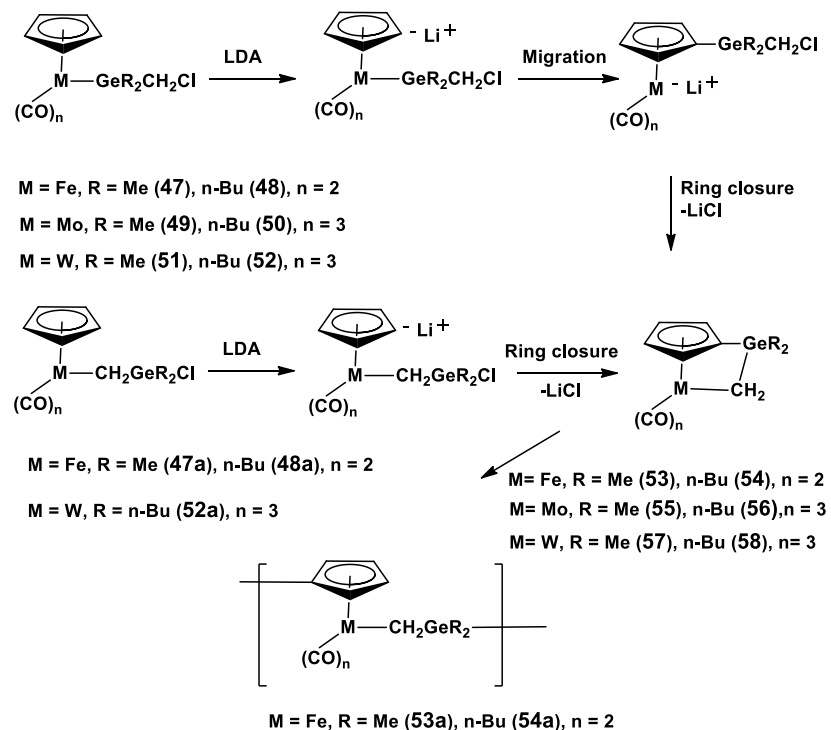
Figure 1.29 Synthesis and polymerization of germa-matallacyclobutanes.

1.4.3.2.2 Ring-opening polymerization of disila-metallacyclobutanes.

In addition to sila-matallacyclobutanes, disila-metallacyclobutanes are also appealing candidates for ring-opening polymerization. When $(\eta^5\text{-}C_5H_5)Fe(CO_2)\text{-}SiR_2SiR'_2Cl$, **59** ($R_2 = Bu_2$, $R_2' = Bu_2$) and **60** ($R_2 = Me_2$, $R_2'= Bu_2$) were treated with LDA, analytically pure 1,2-disila-3-ferracycles **59a** ($R_2 = Bu_2$, $R_2' = Bu_2$) and **60a** ($R_2 = Me_2$, $R_2' = Bu_2$) were obtained (Figure 1.30).[69] However, the ring-opening polymerization of these two complexes did not occur. Alternatively, when $R_2 = R_2' = Me_2$, polymer **62** was quantitatively formed by treating $(\eta^5\text{-}C_5H_5)Fe(CO_2)\text{-}SiR_2SiR_2'Cl$ **61** with LDA at -5 $^{\circ}$C, but the exact monomer structure could

not be confirmed. There was no evidence indicating the formation of 1,2-disila-ferracyclobutane.[69]
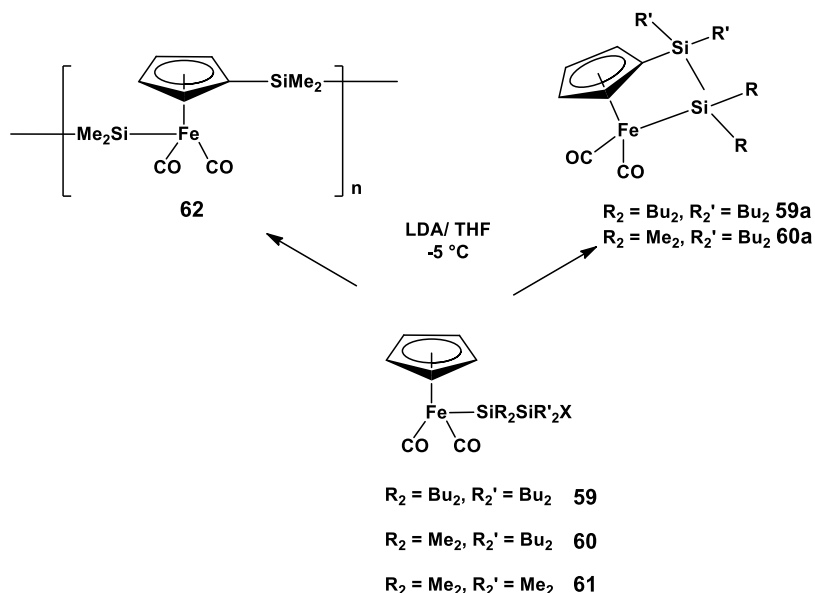
Figure 1.30 Synthesis and ring-opening polymerization of disila-metallacyclobutanes.

Polymer **62** was soluble in hot THF and had a M_n of 3200 g/mol with a PDI of 2.[69] The solid state ^{29}Si NMR spectrum of the polymer displayed two peaks at 22.0 ppm, due to Fe-Si, and at -8.2 ppm, resulting from Cp-Si, implying a regular alternating arrangement of the building blocks in the polymer backbone. Wide angle X-ray diffraction (WAXS) results suggested that the polymer was partially crystalline, as distinct peaks at 13.3^o and 14.2^o were observed in the scattering pattern.[69]
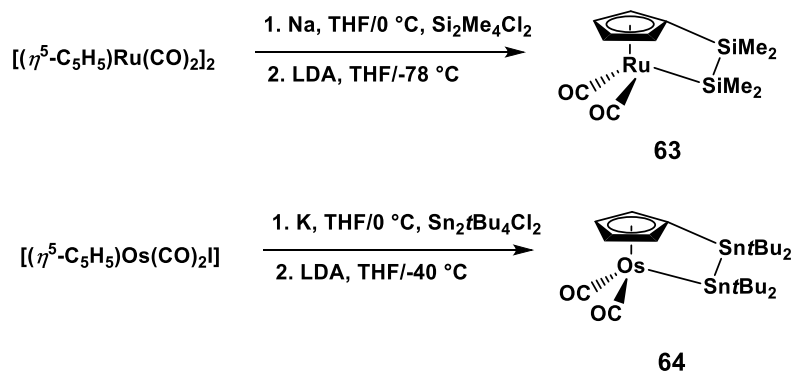
Figure 1.31 Synthesis of non-iron disila-metallacyclobutanes.

Non-iron cyclobutanes complexes **63** and **64** were prepared by treating anionic complexes, generated in situ from $[(\eta^5\text{-}C_5H_5)Ru(CO)_2]_2$ and $[(\eta^5\text{-}C_5H_5)Os(CO)_2I]$ *via* reduction reactions, with $SiMe_4Cl_2$ and $Sn_2tBu_4Cl_2$, respectively (Figure 1.31).[70] Unlike the related iron derivative, **61**, **63** and **64** were thermally stable up to 150 ^{o}C. Single crystals of **63** and **64** suitable for X-ray diffraction were obtained. The bond angle analysis of **63** revealed the existence of ring strain in the structure. Ring-opening polymerization of **63** at 150 ^{o}C was achieved, resulting in polymer **65**, which has limited solubility in hot THF (Figure 1.32).[70] GPC analysis revealed that the M_n of the polymer was 7430 g/mol, relative to polystyrene (PS) standards, with a PDI of 1.6. The chain structure for the polymer was characterized by ^1H NMR and ^{29}Si NMR spectroscopies.[70] In contrast, **64** did not exhibit a ring-opening polymerization behavior under similar reaction condition.
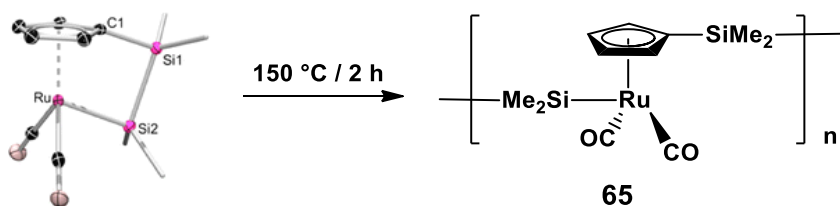
Figure 1.32 Ring-opening polymerization of **63**. Reprinted with permission from reference 70, Copyright 2014, American Chemical Society.

30

Comparing **63** with **61**, it was found that the type of metal center determines the stability of the complexes. Energy decomposition analysis (EDA) has been used to investigate this phenomenon.[70] Calculation results show that both the Si2-Si1 and Si2-Ru bonds in complex **63** are stronger than the corresponding Si2-Si1 and Si2-Fe in Fe complex **61**. As a result, the Si-Si bond in **61** is more prone to be cleaved as compared to that in **63**.[70] This calculation also explained why **61** could not be isolated and underwent polymerization upon solvent evaporation, even at low temperature. Furthermore, atomic charge analysis revealed that the weaker Si-Si bond in **61** was caused by greater charge transfer from Si2 to Fe in complex **61** as compared to that from Si2 to Ru in complex **63**.[70]

1.5 Materials exploration of metal carbonyl organometallic macromolecules

1.5.1 Metal carbonyl organometallic macromolecules used for the release of carbon monoxide

Carbon monoxide plays a versatile role in tissue protection *via* its anti-inflammatory effect,[51] although direct inhalation of CO causes undesirable adverse effects due its toxicity at higher concentrations.[51] Therefore, a safe and controllable method for the release of CO is required.[51] Small photoactive metal carbonyl complexes have been investigated as agents for CO delivery. However, the controlled release of CO molecules *via* these small molecular metal carbonyl complex still exhibits challenges because of their raid diffusion, and the CO molecules may be liberated before they actually reach their target tissues.[51] In 2010, Hubbell et al. synthesized a triblock copolymer named PEG-*b*-POrnNa-*b*-PnBu, containing ruthenium carbonyl groups.[51]
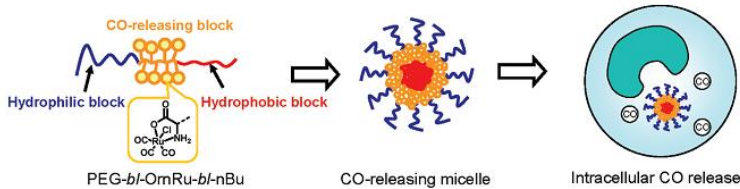
Figure 1.33 Schematic illustration of micelle formation of PEG-*b*-POrnRu-*b*-PnBu triblock copolymer and CO release after cellular uptake. Reprinted with permission from reference 51, Copyright 2010, American Chemical Society.

The block copolymer self-assembled in water into monodisperse, spherical micelles with an average diameter of 40 nm.[51] The release of CO could be induced by a thiol compound such as cysteine, which is abundant within cells. Compared to $Ru(CO)_3Cl$ (glycinate), the polymeric micelles showed a slow release rate which may be attributed to the hindrance of PEG corona.[51]

1.5.2 Metal carbonyl organometallic macromolecules used as resists for electron-beam lithography and UV-photolithography

Electron beam lithography (EBL) is a maskless lithography technique in which a resist material is exposed to an electron beam at a controlled dosage in a predetermined pattern. Due to the presence of the metal element, metal-containing polymers have a higher resistance as compared to commonly used organic polymer resists such as poly(methyl methacrylate) (PMMA). Both Co-PFS (**28** in Figure 1.19) and Mo-PFS (**29** in Figure 1.19) can function as negative resists.[49] For Co-PFS resists, various shapes including dots, bars and curved lines were successfully fabricated[71] (Figure 1.34). Before pyrolysis, magnetic force microscopy (MFM) revealed no appreciable magnetic field gradient above the bars.[71] In order to improve the magnetism of the patterned bars, the array of bars was pyrolyzed at 900 $^{\circ}$C. Subsequent

MFM imaging revealed that the bars after pyrolysis were composed of heterogeneous ferromagnetic clusters whose magnetic dipoles appeared to be randomly oriented.[71]
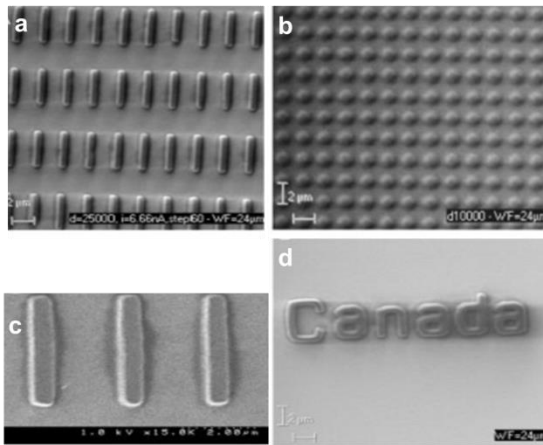
Figure 1.34 SEM images of (a) bars; (b) dot; (c) lines and (d) curved lines fashioned by EBL using a Co-PFS resist. Reprinted with permission from reference 71, Copyright 2004, Wiley.

In addition to electron beam lithography (EBL), photolithography is also routinely used for parallel patterning over large areas in the microelectronics industry.[72] Co-PFS has also shown to behave as a negative resist for UV photolithography. Patterning of Co-PFS films with features in a size range of ca. 50-500 μm was generated using a metal foil shadow (Figure 1.35a). Small features in a size range of ca. 10-20 μm could be obtained using a chrome contact mask (Figure 1.35b). In both cases, the unexposed polymers were dissolved during development using THF.[72] In contrast, thin films of unclusterized PFS remained completely soluble in THF after UV exposure, indicating that the metal carbonyl is a necessary component in the cross-linking mechanism.[72]
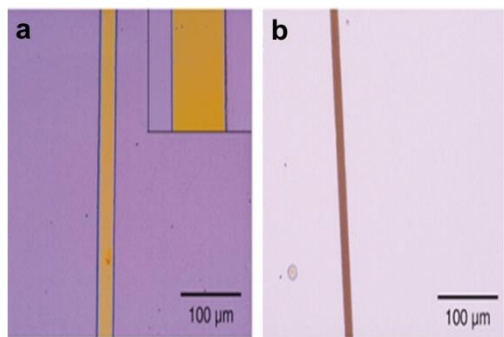
Figure 1.35 Optical micrographs of lines of **30** fabricated by UV photolithography using a (a) shadow mask and (b) chrome contact mask. The insert shows the surface morphology of the patterned polymer under high magnification. Reprinted with permission from reference 72, Copyright 2004, Royal Society of Chemistry.

Upon pyrolysis of the patterned Co-PFS at 900 $^{\circ}$C under N_2 atmosphere for 5 h, magnetic ceramic lines were obtained (Figure 1.36a). The resulting ceramic lines showed good shape retention with respect to their polymer precursors. At higher magnifications, collections of small ceramic islands were observed (Figure 1.36b). The composition of the ceramic islands were probably Co/Fe alloy nanoparticles embedded in a SiC/C matrix.[72] Atom force microscopy (AFM) analysis of the pyrolyzed Co-PFS pattern indicated that the height of the islands ranged from 5 to 87 nm, with an average value of 30 nm (Figure 1.37a). Lastly, MFM analysis revealed that the magnetic dipoles probably resulted from the Co/Fe alloy nanoparticles, and the orientation of the magnetic dipoles appeared to be random.[72]
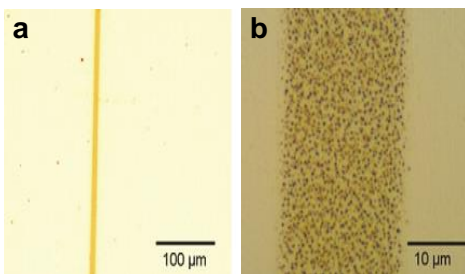
Figure 1.36 Optical micrograph of patterns at (a) low magnification and (b) high magnification after Co-PFS was pyrolyzed at 900 ^{o}C. Reprinted with permission from reference 72, Copyright 2004, Royal Society of Chemistry.
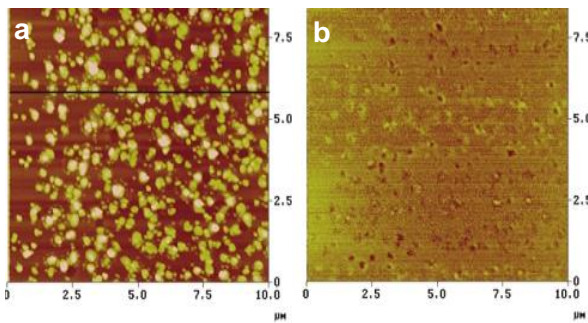
Figure 1.37 (a) Tapping mode AFM image of a region on a pyrolyzed pattern of **29** (height scale: 200 nm) and (b) the corresponding MFM image of the same region. Reprinted with permission from reference 72, Copyright 2004, Royal Society of Chemistry.

1.5.3 Metal carbonyl organometallic macromolecules used as precursors for magnetic materials

Cobalt carbonyl containing diblock copolymers can self-assemble into MC cylindrical domains with a diameter of 20 nm within the matrix of the organic continuous phase.[44] CO ligands can be detached at an elevated temperature (ca. 110 ^{o}C), resulting in the aggregation of Co atoms within nanocylindrical domains (Figure 1.38a). These materials were found to be ferromagnetic at room temperature and could be strongly attach to a permanent magnet[44] (Figure 1.39a). In contrast, the resulting materials generated by the thermal treatment of

35

homopolymers under the same conditions were paramagnetic (Figure 1.39b), and only a

random distribution of Co nanoparticles was observed[44] (Figure 1.38b).
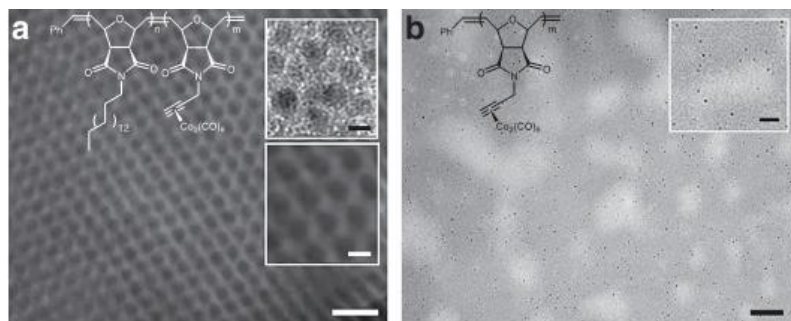
Figure 1.38 TEM images of an unstained, microtomed cross-section of a thermally annealed, Co

containing (a) block copolymer (scale bar, 100 nm) and (b) homopolymer (scale bar, 100 nm).

Reprinted with permission from reference 44, Copyright 2011, Nature Publishing Group.
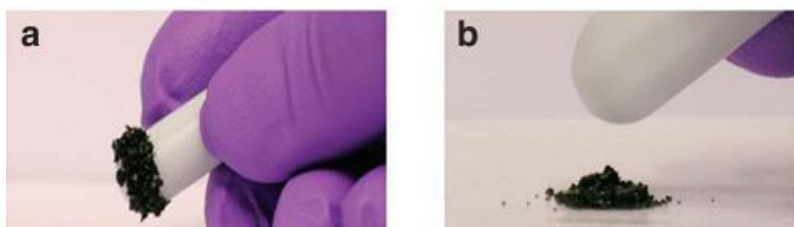
Figure 1.39 The room temperature response of the thermally annealed Co containing (a) block

copolymer and (b) homopolymer, to a permanent magnet. Reprinted with permission from

reference 44, Copyright 2011, Nature Publishing Group.

Chapter 2. Synthesis, cyclization and migration insertion oligomerization of $CpFe(CO)_2(CH_2)_3PPh_2$ in solution

2.1 Introduction

The convergence of organometallic and polymer chemistry has led to the emergence of an interdisciplinary research field of metal-containing polymers (MCPs).[1-5] Many MCPs exhibit interesting functions and self-assembly behavior, which makes them very promising as building blocks for modern technologies.[6-16] Taking advantage of the well-developed organometallic chemistry, a number of organometallic monomers have been synthesized for the preparation of processible MCPs.[17-23] However, it is still demanding to synthesize new organometallic monomers and develop new polymerization techniques in order to extend the scope of MCPs.[24]

It is well known that the reaction of alkyldicarbonylcyclopentadienyliron (FpR) with nucleophilic ligands, e.g., phosphine (PR$_3$), leads to air-stable phosphine-coordinated acyl complexes as a result of a migration insertion reaction (MIR).[25, 26] Therefore, we envision that MIR can be used to link organometallic units together into a macromolecular chain structure through the rational design of organometallic monomers. For example, A-B type bifunctional monomers can be designed with organometallic groups capable of MIR acting as (A) and phosphine ligands acting as (B). To explore the possibility of this new polymerization concept, cyclopentadienylironcarbonyl (Fp) chemistry is used for monomer and MCP synthesis. In this Chapter, an A-B type bifunctional monomer $CpFe(CO)_2(CH_2)_3PPh_2$ (FpP) was synthesized for the construction of macromolecular chain structures. In an effort to explore solution migration insertion polymerization, the reaction behavior of FpP in solution was investigated. The effects

of temperature and concentration on the FpP solution reaction were studied. The experimental results indicated that FpP in solution undergoes both intramolecular cyclization reactions and intermolecular MIR depending on the reaction conditions. At a low concentration, intramolecular cyclization reactions are preferred, generating two cyclic molecules either at 25°C or 70 ^{o}C, On the other hand, at relatively higher monomer concentration, intermolecular reactions of FpP are predominant. As a result of this investigation, solution polymerization of FpP at a monomer concentration of 20 % by weight was conducted at 70 ^{o}C, resulting in both THF-soluble and insoluble PFpP.

2.2 Experimental

2.2.1 Materials and Instrumentation

All experiments were performed under an atmosphere of dry nitrogen using either standard Schlenk techniques or in a glovebox unless otherwise indicated. THF was freshly distilled under nitrogen from Na/benzophenone. *n*-Hexane was degassed with dry nitrogen before use. Toluene was dried with molecular sieves before use. Sodium (Na), 1-bromo-3-chloropropane and potassium (K) were purchased from Sigma-Aldrich. Cyclopentadienyl iron dicarbonyl dimer (Fp$_2$) was purchased from Strem Chemicals Inc. Chlorodiphenylphosphine was purchased from Tokyo Chemical Industry (TCI). Benzophenone was purchased from Fisher Scientific. All chemicals were used as received unless otherwise indicated.

2.2.2 Nuclear magnetic resonance (NMR) spectroscopy

^{1}H, ^{31}P, ^{13}C NMR and heteronuclear multiple quantum coherence (HMQC) and correlation spectroscopy (COSY) were performed on a Bruker Avance 300 (^{1}H: 300 MHz, ^{31}P: 120 MHz, ^{13}C: 75 MHz) spectrometer at ambient temperature using appropriate solvents. NMR samples were prepared under an atmosphere of dry nitrogen unless otherwise indicated.

2.2.3 Solid state nuclear magnetic resonance spectroscopy

Solid state ^{13}C NMR spectroscopy was performed on Bruker Avance 500 (^{13}C: 125 MHz) spectrometer at ambient temperature with cross polarization and magic angle spinning. The contact time and spinning rate were 2 ms and 6.1 KHz, respectively. The pulse program cpramp was used. A total of 2K scans were collected. The low frequency ^{13}C signal at 29.5 ppm from admantane was used as external reference to determine the chemical shifts.

Solid state ^{31}P NMR spectroscopy was performed on Bruker Avance 500 (^{31}P: 202 MHz) spectrometer at ambient temperature. High power decoupling with magic angle spinning was employed. The relaxation time and spinning rate were 20 s and 5.2 KHz, respectively. Hpdec program was used. A total of 2K scans were accumulated. Chemical shifts were determined with respect to external signal for ammonium dihydrogen phosphate at 0.81 ppm.

2.2.4 FT-IR

Fourier transform infrared spectroscopy (FT-IR) spectra for FpP and PFpP solid samples were recorded on a Bruker Tensor 27 spectrophotometer with a resolution of 1 cm^{-1}. Test pellets were prepared by grinding and compressing FpP or PFpP (2 wt%) in KBr.

2.2.5 Gel permeation chromatography (GPC)

Molecular weights and molecular weight distributions, M_w/M_n, were characterized using GPC analysis at room temperature with THF as eluent at a flow rate of 1.00 mL/min. The Viscotek GPC max unit used was equipped with a VE 2001 GPC, three PolyAnalytik organic mixed bed columns, PAS-103-L, PAS-104-L, and PAS-105-L with dimensions of 8 mm (i.d.)×300 mm (L) each, and a Viscotek triple detector array including refractive index, viscosity, and dual-angle light scattering detectors. Polystyrene standards were used as references.

2.2.6 Single crystal X-ray diffraction

Single crystals suitable for X-ray diffraction analysis were mounted onto the tips of glass fibers with thick oil and transferred immediately into the cold nitrogen gas stream of the diffractometer cryostat. X-ray data were collected using Mo Kα radiation at 200 K on a Bruker Kappa APEX II System (Madison, WI, USA).

2.2.7 Powder X-ray diffraction

Powder X-ray diffraction (PXRD) pattern were acquired on a Bruker Kappa APEX II System (Madison, WI, USA), using Mo Kα radiation with a wavelength of 0.71073 Å

2.2.8 Synthesis of cyclopentadienyl dicarbonyliron potassium (FpK)

Potassium benzophenone ketyl was prepared by stirring benzophenone (4.9 g, 27 mmol) and potassium (0.975 g, 25 mmol) in dry THF (50.0 mL). Upon mixing potassium and benzophenone, the solution turned to dark blue immediately. The reaction mixture was stirred overnight to ensure the complete solubilization of the potassium. Afterwards, cyclopentadienyl

dicarbonyl iron dimer (4.6 g, 13 mmol) dissolved in dry THF (20.0 mL) was added under vigorous stirring. The deep blue color of the potassium benzophenone disappeared within several minutes, and a red brown solution and an orange precipitate were formed. The reaction mixture was stirred for ca. 2 h at room temperature under a static nitrogen atmosphere. After the reaction, THF was removed under vacuum and the resulting crude product was washed with toluene several times in order to remove benzophenone and unreacted dimer until the supernatant was colorless. Afterwards, the supernatant was removed *via* cannula; the product was dried under vacuum at room temperature, yielding an orange powder (3.52 g, 65 %).

2.2.9 Synthesis of sodium diphenylphosphide (Ph$_2$PNa)

Ph$_2$PNa was prepared by heating sodium and ClPPh$_2$ at 40 ^{o}C for three days. The resulting orange solution was directly used for further reactions. ^{31}P NMR (THF): -23 ppm.

2.2.10 Synthesis of 3-chloropropyldiphenylphosphine

A 250 mL Schlenk flask was charged with a solution of BrCH$_2$CH$_2$CH$_2$Cl (7.87 g, 5.0×10^{-2} mol) in 50.0 mL THF. Then the solution was cooled to 0 ^{o}C using an ice bath, and Ph$_2$PNa (60 mL, 0.5 mol/L) was added drop-wise. Afterwards, the ice bath was removed and the reaction mixture was allowed to warm to room temperature and left stirring overnight. After the reaction, THF and excess BrCH$_2$CH$_2$CH$_2$Cl were removed under vacuum at 60 ℃ for ca. 2 h. The crude product was dissolved in minimum amount of hexane and filtered through a silica gel column. Hexane was then removed under vacuum at room temperature, yielding a colorless oil. (5.52 g, 70 %). ^{1}H NMR (CDCl$_3$): 7.45 ppm and 7.35 ppm (*d*, 10H, C$_6$**H**$_6$), 3.60 ppm (*t*, 2H, C**H**$_2$Cl), 2.20 ppm (*t*, 2H, C**H**$_2$P) and 1.92 (*m*, CH$_2$C**H**$_2$CH$_2$).^{31}P NMR (CDCl$_3$): -14.7 ppm.

2.2.11 Synthesis of FpP

A solution of $Ph_2PCH_2CH_2CH_2Cl$ (1.01 g, 3.8×10^{-3} mol) in 5.0 mL THF was added drop-wise to an orange suspension of FpK[27] (1.00 g, 4.6×10^{-3} mol) in 25.0 mL THF at 0 ℃. The reaction flask was wrapped by aluminum foil in order to avoid the light. The reaction mixture was stirred for 2 h at room temperature. The THF was then removed under vacuum; degassed hexane was added to dissolve the crude product. The hexane solution was transferred using cannula into another schlenk flask. After removal of solvent, oil-like crude product was obtained. The crude product was purified by filtering the solution on a short silica gel column to remove dimers which was formed during the reaction using hexane/DCM (4 : 1, v/v) as eluent. The bright yellow solution was collected and solvent was subsequently removed under vacuum, generating a bright yellow powder (1.1 g, 60 %). The yellow powder was recrystallized from hexane at -49 ℃, yielding yellow crystals. ^{1}H NMR (DMSO-d_6): 7.35 (t, 4H, ortho-C_6H_5), 7.32 ppm (m, 6H, para, meta-C_6H_5), 4.87 ppm (s, 5H, C_5H_5), 2.07 ppm (2H, PCH_2), 1.46 ppm (4H, $FeCH_2CH_2$). ^{1}H NMR (C_6D_6): 7.61 ppm (t, 4H, ortho- C_6H_5), 7.20 (m, 6H, para, meta-C_6H_5), 4.03 ppm (s, 5H, C_5H_5),[28] 2.25 ppm (t, 2H, PCH_2), 1.80 ppm (m, 2H, $CH_2CH_2CH_2$), 1.64 ppm (t, 2H, $FeCH_2$). ^{31}P NMR (DMSO-d_6): -14.7 ppm. ^{31}P NMR (C_6D_6): -14.4 ppm. ^{13}C NMR (DMSO-d_6): 5 ppm (FpCH$_2$, $^{3}J_{P-C}$=11.4 Hz), 32.5 ppm (CH$_2$CH$_2$P(Ph)$_2$, $^{2}J_{P-C}$=15.3 Hz), 34.3 ppm (CH$_2$PPh$_2$, $^{1}J_{P-C}$=14 Hz), 87 ppm (C_5H_4), 129 ppm, 132 ppm, 139 ppm (C_6H_5), 218 ppm (Fe$C\equiv$O).[29] FT-IR: 2004 cm^{-1} and 1952 cm^{-1} (terminal CO stretching).

2.2.12 Synthesis of species (1) with a 5-membered ring from FpP

FpP was dissolved in THF (conc. 10.0 mg/mL). The solution was stirred at room temperature for 7 days. THF was subsequently removed under vacuum, yielding an orange oil. The orange oil was chromatographed on a silica gel column using hexane/ethyl acetate (10 : 1 v/v) as eluent. The yellow band was collected and solvent was removed under vacuum, yielding an orange oil (70 %). The resulting oil was recrystallized from hexane at -49 °C. ^{1}H NMR (CDCl$_3$): 7.76 ppm, 7.49 ppm, 7.33 ppm and 7.15 ppm (10H, C$_6$**H**$_5$), 4.21 ppm (s, 5H, C$_5$**H**$_5$), 2.50 ppm (m, 1H, PC**H**$_2$), 2.30 ppm (m, 1H, PC**H**$_2$), 2.10 ppm (m, 1H, CH$_2$C**H**$_2$CH$_2$), 1.30 ppm (m, 1H, CH$_2$C**H**$_2$CH$_2$), 2.0 ppm (m, 2H, FeC**H**$_2$). ^{13}C NMR (CDCl$_3$): 36 ppm (d, P**C**H$_2$, $^1J_{\text{P-C}}$=31.2 Hz), 31 ppm (d, CH$_2$**C**H$_2$CH$_2$, $^2J_{\text{P-C}}$=12.8 Hz), 12 ppm (d, Fe**C**H$_2$, $^3J_{\text{P-C}}$=10.9 Hz), 82.6 ppm (s, **C**$_5$H$_5$), 134 ppm, 130 ppm and 128 ppm (**C**$_6$H$_5$). ^{31}P NMR (CDCl$_3$): 109 ppm.

2.2.13 Synthesis of species (2) with a 6-membered ring from FpP

FpP was dissolved in THF (conc. 10.0 mg/mL), and the solution was heated at 70 °C for 2 h in the dark (the reaction flask was covered with aluminum foil). Afterwards, the reaction flask was cooled to room temperature and THF was removed under vacuum, yielding a yellow oil. The yellow oil was further purified using chromatography on a silica gel column. Hexane/ethyl acetate (2.5 : 1, v/v) was used as eluent, yielding a yellow oil (55 %). The resulting oil was recrystallized from DCM/hexane (1 : 5, v/v) at -49 ℃, yielding yellow crystals. ^{1}H NMR (CDCl$_3$): 7.62 ppm, 7.48 ppm (10H, C$_6$**H**$_5$), 4.52 ppm (*s*, 5H, C$_5$**H**$_5$), 2.84 ppm (*t*, 1H, COC**H**$_2$), 2.33 ppm (*m*, 1H, COC**H**$_2$), 2.50 ppm (*m*, 1H, PC**H**$_2$), 2.33 ppm (*m*, 1H, PC**H**$_2$), 1.91 ppm (*m*, 1H, CH$_2$C**H**$_2$CH$_2$), 1.30 ppm (*m*, 1H, CH$_2$C**H**$_2$CH$_2$). ^{13}C NMR (Dept-135, CDCl$_3$): 68 ppm (s,

COCH_2), 29 ppm (d, PCH_2, $^1J_{\text{P-C}}$=32.4 Hz), 21 ppm (b, CH$_2$CH_2CH$_2$), 82.6 ppm (s, C_5H$_5$), 134 ppm, 130 ppm and 128 ppm (C_6H$_5$). ^{31}P NMR (CDCl$_3$): 70 ppm.

2.2.14 Solution polymerization of FpP

FpP was dissolved in THF (20 wt%) and the solution was heated at 70 $^{\circ}$C. At certain time intervals, samples were withdrawn for ^{31}P NMR analysis. After 19 h, the polymerization was terminated by cooling the solution to room temperature, and the suspended solid was separated by centrifuge. The clear yellow supernatant was added drop-wise to hexane to precipitate PFpP. Both THF-insoluble product and the precipitate were collected and dried under vacuum at room temperature overnight. The resulting polymers (THF-insoluble and -soluble fractions) are both bright yellow powders. The weight ratio for the two fractions was ca. 3 : 7. THF-insoluble fraction: solid state ^{13}C NMR: 20 ppm (CH$_2$CH_2CH$_2$) 32, 36 ppm (PCH_2), 67 ppm (CH$_2$C=O), 85-88 ppm (C_5H$_5$), 125-130 ppm (C_6H$_5$). Solid state ^{31}P NMR: 73.0 ppm and 37.8 ppm. FT-IR: 1898 cm^{-1} (terminal CO stretch), 1597 cm^{-1} (ketonic CO stretch). THF-soluble fraction: ^{1}H NMR (DMSO-d_6): 7.8-7.1 ppm (b, 10H, C$_6$$H_5$), 4.4-4.2 ppm (b, 5H, C$_5$$H_5$), 2.78-2.60 ppm (b, 1H, COCH_2), 2.47-2.17 ppm (b, 1H, COCH_2), 2.13-1.89 ppm (b, 2H, CH_2P) and 1.32-0.74 ppm (b, 2H, CH$_2$CH_2CH$_2$).^{13}C NMR (DMSO-d_6): 20 ppm (s, CH$_2$CH_2CH$_2$), 29 ppm (d, PCH_2, $^1J_{\text{P-C}}$=29.4 Hz), 66 ppm (s, CH$_2$C=O), 84 ppm, 86 ppm (C_5H$_5$), 127 ppm, 128 ppm, 129 ppm, 130 ppm, 132 ppm (C_6H$_5$), 220 ppm, 217 ppm (d, s, C≡O) and 274 ppm (s, CH$_2$$C$=O). ^{31}P NMR (CDCl$_3$): 73.4 ppm, 72.3 ppm and -13.6 ppm. FT-IR: 1910 cm^{-1} (terminal CO stretch), 1600 cm^{-1} (ketonic CO stretch).

2.3 Results and Discussion

2.3.1 Synthesis of cyclopentadienyl dicarbonyliron potassium (FpK)
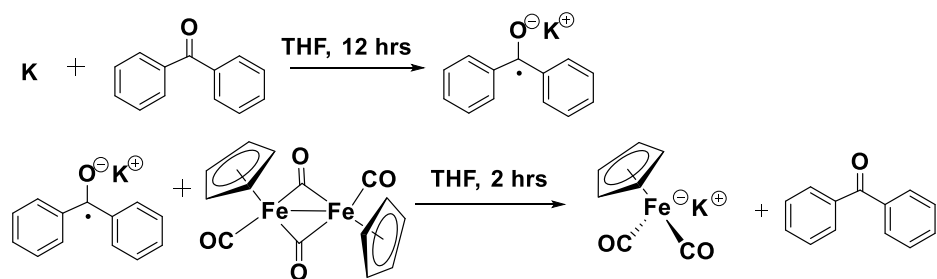
Scheme 2.1 Synthesis of FpK.

The FpK was reduced from cyclopentadienyl dicarbonyl iron dimer (Fp$_2$) using potassium

benzophenone ketyl as a reduction agent (Scheme 2.1). FpK was an air-sensitive orange powder

and stored in a glovebox for further reaction.

2.3.2 Synthesis of sodium diphenylphosphide (Ph$_2$PNa)

Ph$_2$PNa was synthesized by the reaction of PPh$_2$Cl with Na in THF. After stirring at 40 $^\circ$C for

three days, the solution turned to a red color and Ph$_2$PNa was formed. The ^{31}P NMR spectrum

for the resulting solution revealed a single peak at -23 ppm.

2.3.3 Synthesis of 3-chloropropyldiphenylphosphine
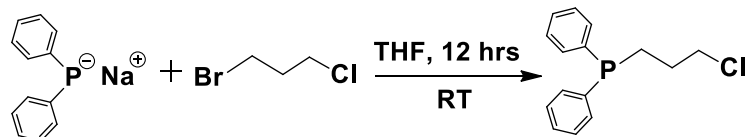
Scheme 2.2 Synthesis of 3-chloropropyldiphenylphosphine (Ph$_2$P(CH$_2$)$_3$Cl).

The 3-chloropropyldiphenylphosphine was synthesized by the reaction of NaPPh$_2$ and

Br(CH$_2$)$_3$Cl. The final product was characterized by ^{1}H NMR and ^{31}P NMR spectroscopy. As

shown in Figure 2.1, the peak at 1.9 ppm (c in Figure 2.1) is attributed to the middle CH$_2$ in the

propyl spacer. The chemical shift due to the CH$_2$ connected to the chloride appears at 3.6 ppm (a

in Figure 2.1). The resonance signal at 2.2 ppm (b in Figure 2.1) is assigned to the CH$_2$

coordinated to the phosphorus atom. The integration ratio of the three peaks (a, b, c) is 1 : 1 : 1, which is in agreement with the proposed structure. In addition, the peak at 7.55-7.28 ppm is assigned to the protons in the phenyl group. The integration ratio of the peaks at 7.55-7.28 ppm and the peak at 3.6 ppm (a in Figure 2.1) is 5 : 1, which matches the theoretical value. In the ^{31}P NMR spectrum, a single peak at -15 ppm is observed (Figure 2.2), indicating the presence of phosphine group. In conclusion, the NMR analysis results suggest that $Ph_2P(CH_2)_3Cl$ was successfully synthesized.
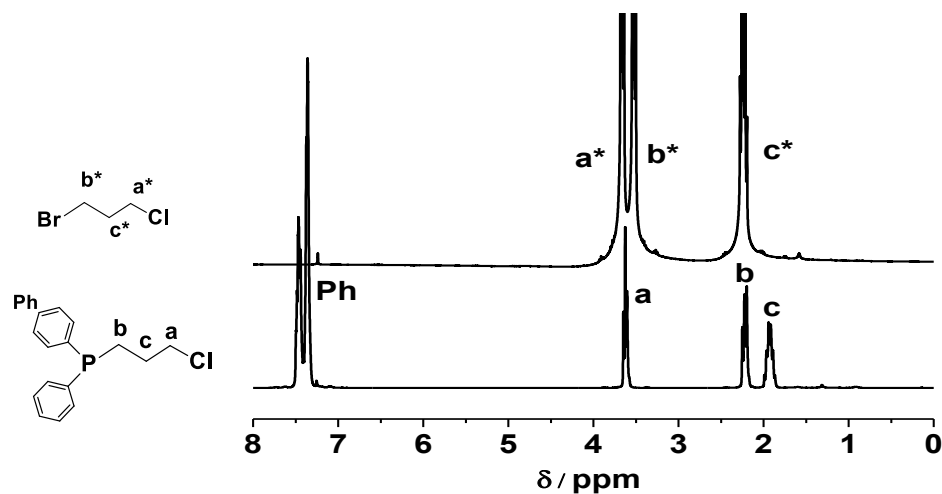
Figure 2.1 ^{1}H NMR spectra for $Ph_2P(CH_2)_3Cl$ (bottom) and $Br(CH_2)_3Cl$ (top) in $CDCl_3$.
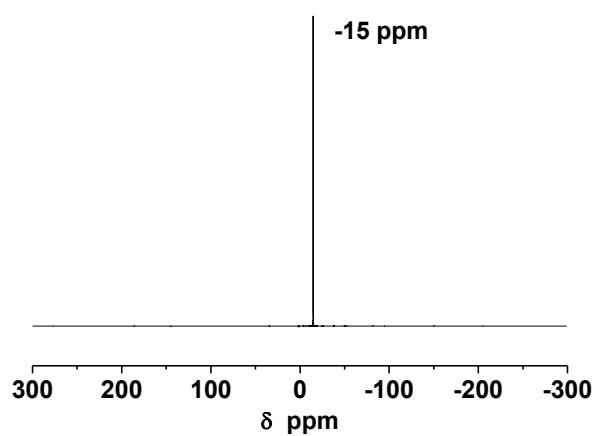
Figure 2.2 ^{31}P NMR spectrum for $Ph_2P(CH_2)_3Cl$ in $CDCl_3$.

2.3.4 Synthesis of FpP

Cyclopentadienyldicarbonyldiphenylphophinopropyliron (FpP) was synthesized by the reaction of (3-chloropropyldiphenyl)phosphine with potassium cyclopentadienyldicarbonyliron, as shown in Scheme 2.3.
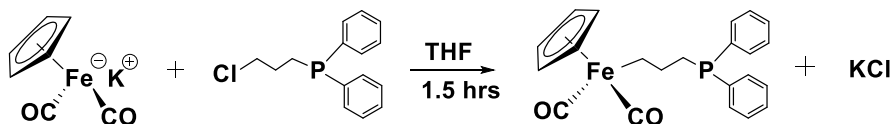
Scheme 2.3 Synthesis of FpP.

A yellow oil-like substance was produced most of the time, which rendered the recrystallization of FpP difficult. Possible reasons for this are the light sensitivity of Fp derivatives,[30] and trace amounts of impurities that may be produced during the purification process. We therefore performed the reaction and purification in the dark. As a result, a yellow powder FpP was obtained upon solvent evaporation. The yellow powder could be recrystallized from hexane solutions at -49 °C, resulting in single crystals suitable for x-ray diffraction. X-ray diffraction analysis showed that the molecules crystallized into a monoclinic crystal system with a space group of $P2_1/c$ (Table S2.1). As shown in Figure 2.3a, the Fe is coordinated in pseudo-octahedral three-legged piano-stool fashion. The bond distance for Fe-C8 was 2.066 Å, and the bond angles for C6-Fe-C7, C6-Fe-C8 and C7-Fe-C8 were 93.64 °(14), 85.84 °(12) and 87.29°(12), respectively. These crystal structure parameters are similar to other Fp derivatives reported in literature such as $[(\eta^5\text{-}C_5H_5)Fe(CO)_2]_2(CH_2)_4$ (Table S2.2).[31]

The FT-IR spectrum for FpP shows two peaks at 1952 cm^{-1} and 2004 cm^{-1} (Figure 2.3b), which are characteristic for the terminal CO groups in Fp derivatives.[32] The ^{31}P NMR spectrum reveals a signal at -14.7 ppm, confirming the presence of the phosphine group (Figure 2.3c).
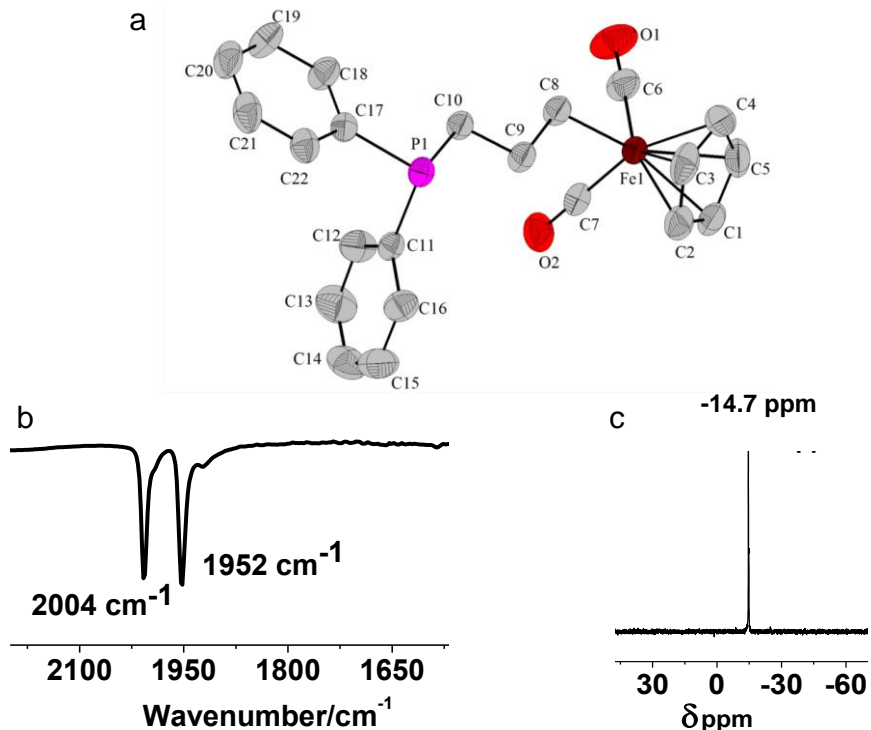
Figure 2.3 (a) Crystal structure with thermal ellipsoids (50 % probability level), (b) FT-IR spectrum and (c) ^{31}P NMR spectrum for FpP in DMSO-d_6.

The ^{1}H NMR spectrum for FpP in DMSO-d_6 (Figure 2.4a) exhibits a strong resonance signal at 4.8 ppm due to the Cp ring. The broad resonance signal at 7.40–7.30 ppm is attributed to the phenyl group. The chemical shifts due to the protons α and β to Fe overlapped and appear at 1.46 ppm (a+b in Figure 2.4a). The resonance signal at 2.1 ppm (c in Figure 2.4a) is due to the protons adjacent to the phosphorus atom. The integration ratio of the peak at 1.46 ppm and the peak at 2.1 ppm is 2 : 1 (Figure 2.4a), which supports the above peak assignment. The ^{1}H-^{1}H 2D COSY NMR spectrum for FpP in C$_6$D$_6$ was also performed and is illustrated in Figure 2.4b. As shown in the Figure, the chemical shifts for the propyl spacer are well separated in C$_6$D$_6$. The chemical shift at 1.6 ppm (a in Figure 2.4b) represents the protons α to Fe. The triplet peak at 2.2 ppm (c in Figure 2.4b) is due to the protons adjacent to phosphorus. The multiple peaks at

1.8 ppm (b in Figure 2.4b) can be assigned to the protons β to Fe. This assignment is confirmed

by the 2D chemical shift correlation map (Figure 2.4b). No cross peaks are observed for the

signals at 1.6 ppm and 2.2 ppm, suggesting that they are separated by the methylene in the

middle of the propyl spacer.
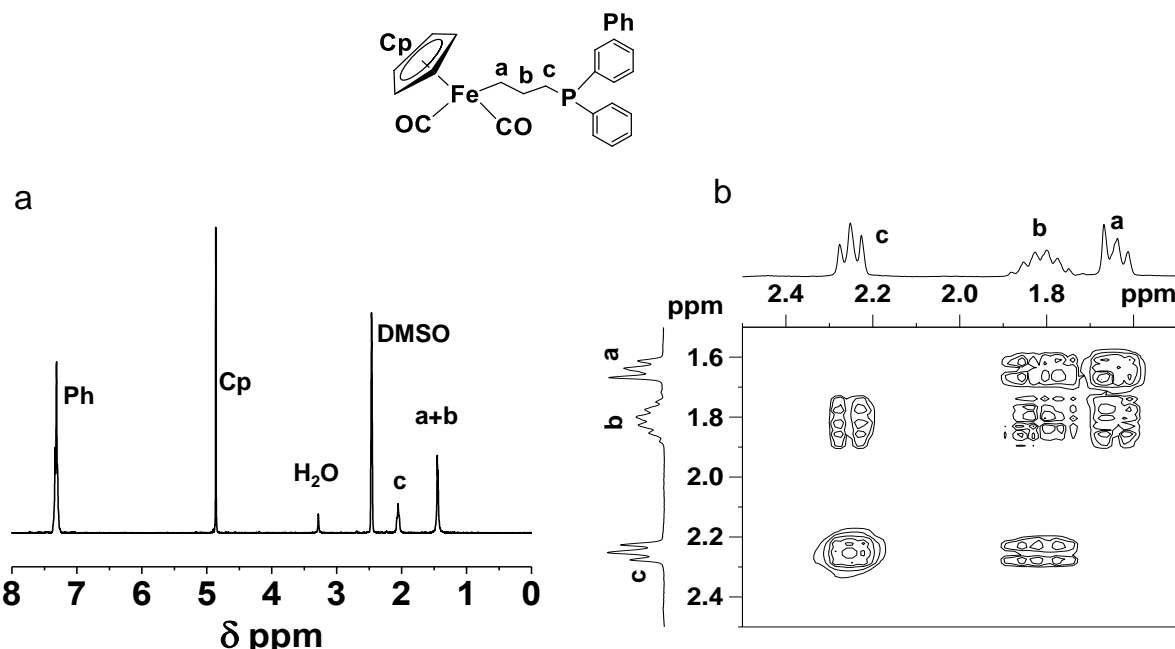
Figure 2.4 (a) ^{1}H NMR spectrum for FpP in DMSO-d_6 and (b) ^{1}H-^{1}H COSY 2D NMR spectrum

for FpP in C_6D_6.

The ^{13}C NMR spectrum for FpP in DMSO-d_6 shows one peak at 217 ppm, representing the

terminal CO group. The resonance signals due to the phenyl and the Cp group appear at 128-139

and 85-86 ppm, respectively (Figure 2.5a). The chemical shifts due to the three carbons in the

propyl spacer (a, b, c in Figure 2.5a) are observed upfield at 34.3, 32.5 and 5.1 ppm, respectively.

The ^{13}C-^{1}H HMQC 2D NMR spectrum for FpP in C_6D_6 was performed to assign these signals

(Figure 2.5b). As shown in the Figure, the cross-peaks indicate that the signals at 5.1, 34.3 and

32.5 ppm in the ^{13}C NMR spectrum are connected to a, b and c protons in the ^{1}H NMR spectrum,

respectively. Based on this assignment, the one, two and three-bond ^{13}C-^{31}P coupling constants for these three carbons ($^1J_{pc}$, $^2J_{pc}$ and $^3J_{pc}$) are 14 Hz, 15.3 Hz and 11.4 Hz, respectively (Inset in Figure 2.5a). We noticed that $^2J_{pc}$ is larger than $^1J_{pc}$, which is peculiar but commonly observed for phosphine compounds.[33]
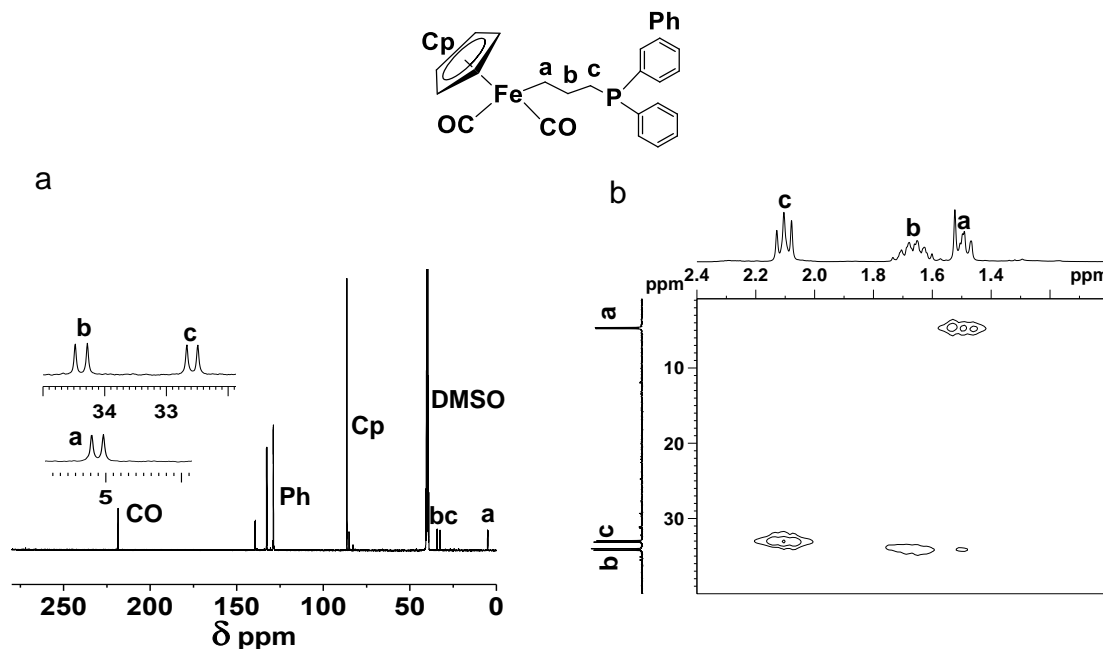
Figure 2.5 (a) ^{13}C NMR spectrum for FpP in DMSO-d_6 and (b) ^{13}C-^{1}H HMQC 2D NMR spectrum for FpP in C$_6$D$_6$.

2.3.5 Cyclization reaction of FpP

Fp derivatives usually undergo two types of reactions in the presence of phosphine: 1) CO release followed by phosphine coordination;[30] 2) MIR at an elevated temperature.[25] FpP containing both Fp and phosphine groups is therefore expected to undergo cyclization reactions under both conditions. When a THF solution of FpP with concentration of 1 wt% was exposed to light and left at room temperature for 7 days, over 99 % of FpP was converted to a 5-membered ring (**1** in Scheme 2.4). On the other hand, if the solution was heated at 70 °C in

dark, the majority products (ca. 70 %) are 6-membered rings (**2** in Scheme 2.4) *via* an intramolecular MIR, as shown in Scheme 2.4.
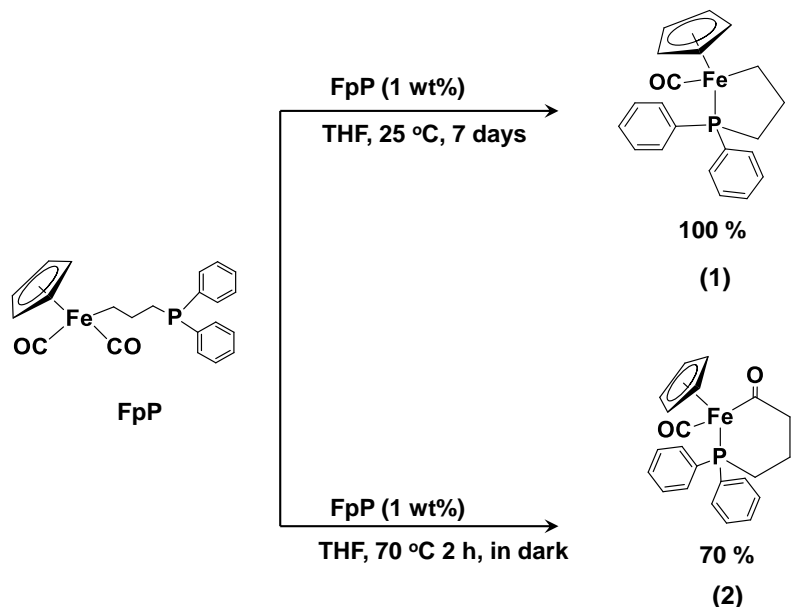
Scheme 2.4 Cyclization reactions of FpP in THF.

To characterize **1** and **2**, single crystals suitable for X-ray crystallography were grown in hexane for **1** and in hexane : DCM (v/v = 4 : 1) mixed solvents for **2** at -49 ℃, respectively. The X-ray analysis shows that both molecules crystallized into a monoclinic crystal system with space group of P2$_1$/c (Table S2.1). Both Fe atoms in **1** and **2** contain pseudo-octahedral coordination geometry with the Cp ring occupying three coordination sites (piano-stool configuration). The listed torsion angles (Table S2.3 and Table S2.4) indicate that all elements in the ring structures are not on the same plane. The six membered ring **2** adopts a cyclohexane-like chair conformation, suggesting that the strain energy involved is low in the compound.
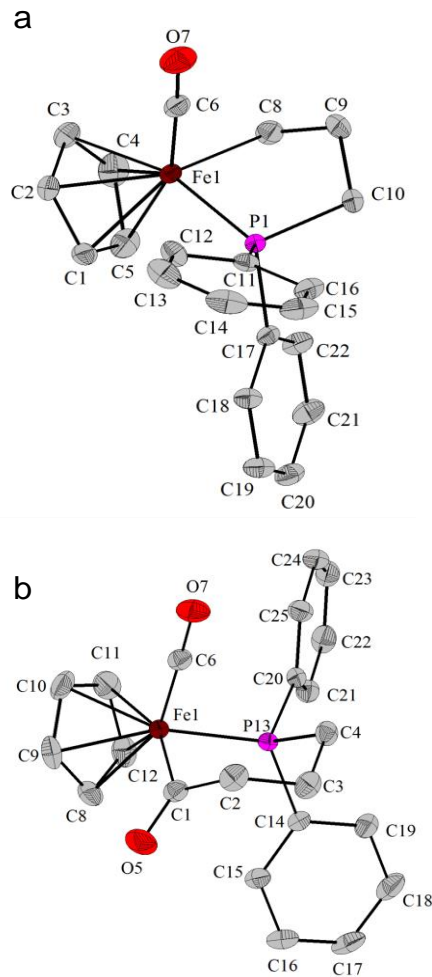
Figure 2.6 Crystal structure for (a) 5-membered and (b) 6-membered rings with thermal ellipsoids (50 % probability level).

Through comparison with previously reported data for acyclic analogues,[34] we determined that the formation of the cyclic structures appears to counteract the steric effect of phosphine ligands, leading to a shorter P-Fe bond. For Fp derivatives, Fe offers limited space to accommodate CO, phosphine and one anionic ligand of R^- on the three coordination sites. The size of phosphine and R groups will therefore influence their bonding distances to Fe and the bond angles. For example, as shown in Table 2.1, the compounds with an R of bulky carborane cage $(C_2B_{10}H_{11})$,[34] the P-Fe-C angles are much larger than those for the compound with R = Et (Table 2.1). Also as a result of steric effects, the Fe-P bond distance (2.271 Å) is much longer as

compared to 2.1699(4) for the Et-substituted analogue (Table 2.1).[30] For the five membered ring **1**, C(8)-Fe-P angle (81.98(4) °) is obviously smaller than the acyclic analogues (Table 2.1), which may generate certain degree of ring strain. However, as a result of the ring constraints, we can see that the P-Fe bond (2.1581(3) Å) becomes much smaller as compared to acyclic compounds (Table 2.1). This result suggests that the cyclic bidentate ligand is able to introduce a strong P-Fe bond by overcoming phosphine steric effects. The distances of Fe to the other ligands are comparable for both cyclic and acyclic compounds (Table 2.1).

Table 2.1 Comparison of bond angles and distances in the 5-membered ring and its acyclic analogues

Bond Angles and Distances	Ring	Acyclic $(\eta^5\text{-}C_5H_5)Fe(CO)(PPh_3)R$	
	(1)	R =Et[30, 35]	R = $C_2B_{10}H_{11}$[34]
C(8)-Fe-C(6)	89.81(6)	92.76(7)	92.3(4)
C(6)-Fe-P	93.60(5)	90.61(5)	96.4(3)
C(8)-Fe-P	81.98(4)	87.86 (5)	99.68(1)
Fe-P	2.1581(3)	2.1699(4)	2.271(2)
Fe-CO	1.729(4)	1.7291(17)	1.729(8)
Fe-C(R)	2.057(1)	1.9601(16)	2.093(6)

For Fp acetyl derivatives, it has been systemically studied and demonstrated that the Fe-P bond length is related to steric effects of the alkylphosphine ligand.[36] As shown in Table 2.2, using dimethyl phenyl phosphine to replace commonly used triphenylphosphine, the shortest

Fe-P bond (2.180(1) Å) for this type of compound had been reported (Table 2.2),[36] while *via* the formation of cyclic Fp acyl derivatives **2**, the bond can be further strengthened, leading to an even shorter P-Fe bond length of 2.1699(4) Å. A similar bond length was also reported for a five-membered ring of Fp acetyl derivatives.[37]

Table 2.2 Comparison of bond angles and distances in the 6-membered ring and its acyclic analogues

Bond Angles and Distances	Ring (2)	Acyclic $(\eta^5\text{-}C_5H_5)Fe(CO)(PPhRR')C(O)R'$	
		R = Ph; R' = Bu [38]	R = Me; R' = Me [36]
C(1)-Fe-C(6)	92.76(7)	92.1(4)	94.6(2)
C(6)-Fe-P	90.61(5)	95.9(3)	92.9(1)
C(1)-Fe-P	87.89(5)	91.3(3)	88.2(1)
Fe-P	2.1699(4)	2.198(2)	2.180(1)
Fe-CO	1.7291(17)	1.723(9)	1.725(4)
Fe-C(O)R	1.9601(16)	1.992(8)	1.948(4)

The ^{31}P NMR spectra for (1) and (2) are shown in Figure 2.7. As shown in the figure, compound **1** and **2** exhibit a single peak at 109 ppm and 70 ppm, respectively. These peaks can therefore be used as indicative for the formation of the rings.
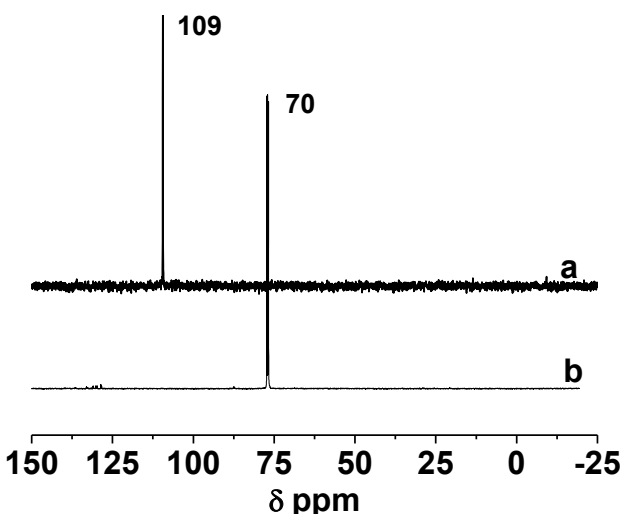
Figure 2.7 ^{31}P NMR spectra for (a) 5-membered and (b) 6-membered ring in CDCl$_3$.

The ^{1}H NMR spectrum for **1** is illustrated in Figure 2.8a. The chemical shift due to the Cp ring appears at 4.2 ppm. This peak undergoes 0.6 ppm upfield shift as compared to that in FpP as a result of the coordination of phosphorus to Fe. The occurrence of the coordination created an asymmetric Fe unit, which significantly complicated the ^{1}H NMR spectrum of the molecule (Figure 2.8a). As shown in the figure, multiple chemical shifts are observed at 7.8-7.1 and 2.50-1.30 ppm accounting for the phenyl group and the propyl spacer, respectively. To resolve the upfield peaks, ^{13}C NMR and ^{13}C-^{1}H HMQC 2D NMR spectroscopies were performed. In the ^{13}C NMR spectrum, the signals due to the three propyl carbons appear at 36 ppm, 31 ppm and 12 ppm, which can be assigned to the carbon adjacent to phosphorus,[32] β and α to Fe, respectively based on the degree of C-P coupling effect. Hydrogen to carbon connectivity is subsequently determined from the cross peaks in the 2D NMR spectrum. Consequently, the chemical shifts at 2.5 and 2.3 ppm can be assigned to the protons α to the phosphorus atom (c in Figure 2.8b); the peaks at 2.0 ppm are due to protons α to iron (a in Figure 2.8b). The chemical shift for the protons β to iron appears at 2.1 and 1.3 ppm (b in Figure 2.8b).

55
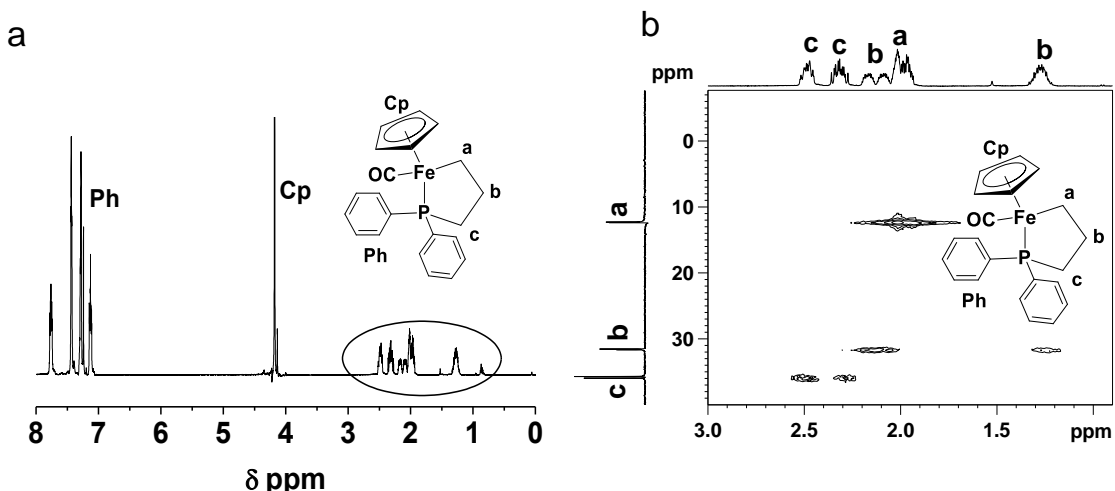
Figure 2.8 (a) ^{1}H NMR spectrum and (b) ^{13}C-^{1}H HMQC 2D NMR spectrum for 5-membered ring in CDCl$_3$.

Similarly to **1**, the ^{1}H NMR spectrum for compound **2** also displays multiple peaks for the propyl spacer, which appear upfield. From the ^{13}C NMR spectrum, the C-P coupling with J_{p-c} of 32.4 Hz was only observed for the resonance signal at 29 ppm, and no coupling effect was observed for other two signals. Therefore, the chemical shift at 29 ppm is assigned to the carbon adjacent to phosphorus (c in Figure 2.9b). The chemical shift for the carbon α to the acyl group appears at 68 ppm (a in Figure 2.9b), which is consistent with value as reported in previous literature[25]. The resonance signal at 21 ppm (c in Figure 2.9b) is attributed to the carbon β to the acyl group. Subsequently, the chemical shifts for protons are assigned *via* the cross peaks appeared in the 2D NMR spectrum (Figure 2.9b).
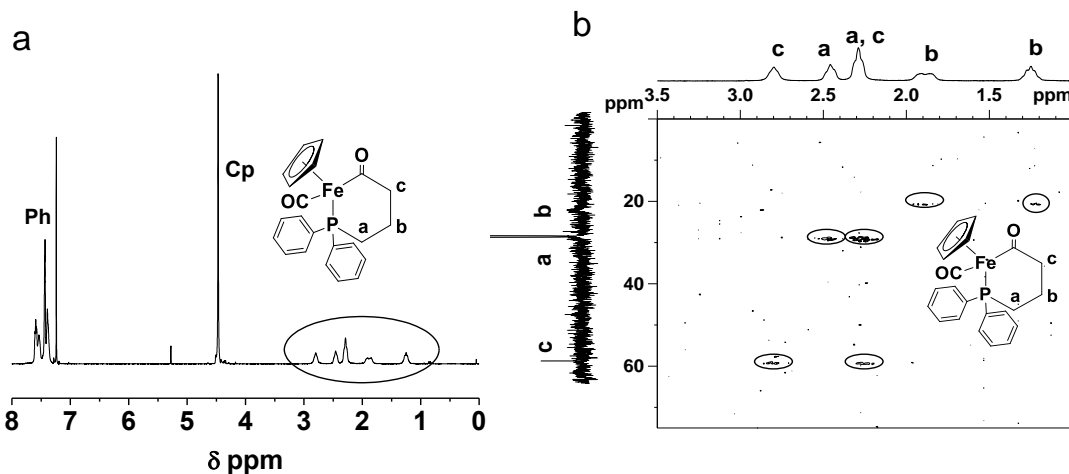
Figure 2.9 (a) ^{1}H NMR spectrum and (b) ^{13}C-^{1}H HMQC 2D NMR spectrum for 6-membered ring in CDCl$_3$.

2.3.6 Effects of concentration and temperature on the reaction of FpP in solution

Based on the above investigation, the products produced from FpP solution reaction can be analyzed using ^{31}P NMR spectroscopy. A representative spectrum is illustrated in Figure 2.10. As shown in the figure, after the solution was heated at 40 ^{o}C for 6 h, both **1** and **2** were formed as indicated by the resonance signals at 109 and 70 ppm. The chemical shift at -14.7 ppm is attributed to the unreacted FpP. In addition, two signals at 72.8 and -13.6 ppm due to the coordinated[32] and uncoordinated phosphorus are observed. The appearance of these two peaks with intensity ratio close to 1 : 1 suggests the formation of FpP dimers. Taking advantage of well-resolved chemical shifts for the products resulting from intra- and intermolecular reactions, solution reactions of FpP were further investigated at various concentrations and temperatures.
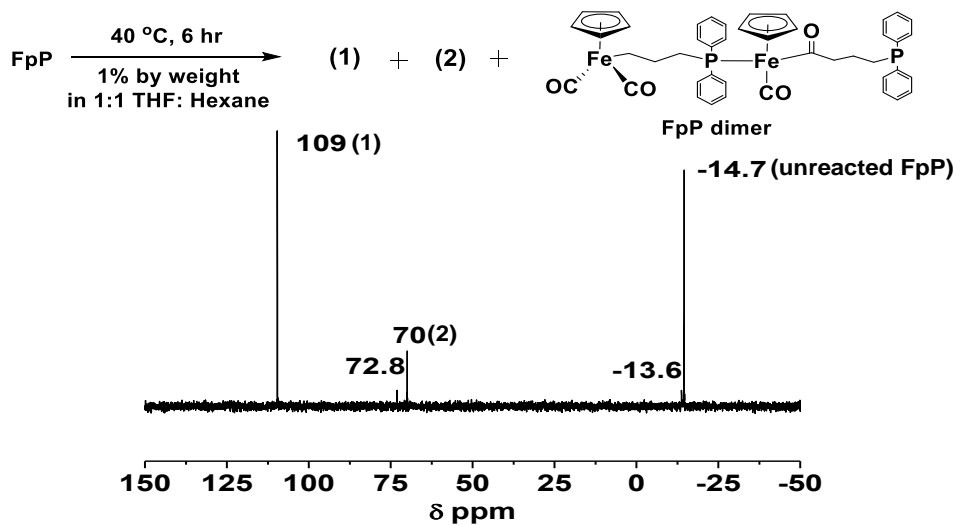
Figure 2.10 ^{31}P NMR spectrum for the reaction solution of FpP in THF: Hexane (1 : 1, v/v) (1 wt%, 40 °C, 6 h)

Table 2.3 ^{31}P NMR analysis of reaction mixtures of FpP solutions

Entry	Solvent	Temp.	Concentration (wt%)	Time	Relative Conversion[a] (1)	(2)	(3)
1	Hexane	25 °C	1.0 %	7 days	93.5 %	2.8 %	3.7 %
2	THF	25 °C	1.0 %	7 days	99.8 %	0.1 %	0.08 %
3	THF	40 °C	1.0 %	6 h	76.0 %	12.8 %	11.2 %
4	THF	70 °C	1.0 %	4 h	51.8 %	36.8 %	11.40 %
5	THF	70 °C	2.0 %	4 h	13%	40.7 %	46.3 %
6	THF	70 °C	5.0 %	4 h	8.6 %	21 %	70.4 %
7	THF	70 °C	10 %	4 h	5.0 %	5.4 %	89.6 %

[a] **1** and **2** represent intramolecular cyclic complexes while **3** represents intermolecular MIP product.

58

By comparing the integration ratios, the relative conversions of FpP to each species can be extracted. The resulting data for all reaction conditions are illustrated in Table 2.3. It is well known that Fp derivatives can readily release CO ligands at room temperature and that the reaction is light sensitive.[30] On the other hand, MIR requires a relatively higher temperature.[25] As a result, intramolecular cyclization *via* CO release is the major reaction when the reaction was performed at room temperature, leading to the formation of **1** with a yield of over 90 %. (entry 1 and 2 in Table 2.3). Particularly, when THF was used as the solvent (entry 2 in Table 2.3), **1** was produced almost exclusively. In contrast, by increasing the temperature to 40 ^{o}C and 70 ^{o}C, MIR was promoted, leading to significant amount of products produced from either intra or inter molecular MIR (entry 3, 4 in Table 2.3). The higher the temperature, the more MIR products; while keeping the reaction temperature at 70 ^{o}C, the percentage of intermolecular products increased from 46.3 to 89.6 % (entry 5, 7 in Table 2.3) by carrying out the reaction with the concentration of FpP at 2 % and 10 %, respectively. Based on this investigation, migration insertion polymerization of FpP is possible if a solution of FpP with a high concentration is heated to an elevated temperature.

2.3.7 Solution polymerization

Solution polymerization of FpP in THF at a concentration of ca. 20 wt% was performed at 70 ^{o}C. After the solution was heated for 1 h, insoluble material was observed and was suspended in the solution. The insoluble fraction was separated from the THF solution *via* centrifugation at the end of the polymerization. The clear supernatant was then added drop-wise into hexane, yielding a pale yellow precipitate. The weight ratio of the soluble and insoluble fraction was ca.

7 : 3. The THF-insoluble fraction has the same color and appearance as the THF-soluble product. The insoluble polymers were first characterized using solid-state ^{31}P NMR and ^{13}C NMR spectroscopy. As shown in Figure 2.11(a), the ^{31}P NMR spectrum reveals two peaks at 73 ppm and 37.8 ppm along with multiple spinning side bands. These two peaks can be assigned to the main-chain coordinated phosphorus and oxidized phosphine end group, respectively. The solid-state ^{13}C NMR spectrum is illustrated in Figure 2.11(b). As shown in the figure, the signals for the phenyl group appear at 125-130 ppm; the peaks between 85 and 88 ppm are assigned to the Cp ring. The resonance signal at 67 ppm is due to the carbon next to the acyl group. Due to C-P coupling, two peaks at 32 and 36 ppm were observed for the carbon adjacent to the phosphorus atom. The chemical shift for the middle carbon in the propyl spacer appears at 20 ppm. However, the chemical shift for the carbonyl groups is invisible due to the weak ^{1}H-^{13}C cross polarization for carbonyl carbon. In order to verify the presence of carbonyl groups, FT-IR was employed. As shown in Figure 2.11(c), two peaks at 1898 cm^{-1} and 1597 cm^{-1} are observed, which are corresponding to the terminal carbonyl and the migrated carbonyl groups, respectively.[39] The existence of these two types of carbonyl groups suggests that the insoluble material also resulted from migration insertion reactions. Powder X-ray diffraction of the THF insoluble material was also performed and the result indicated that the insoluble material was crystalline (Figure S2.1). The crystalline feature was probably the reason for the poor solubility.
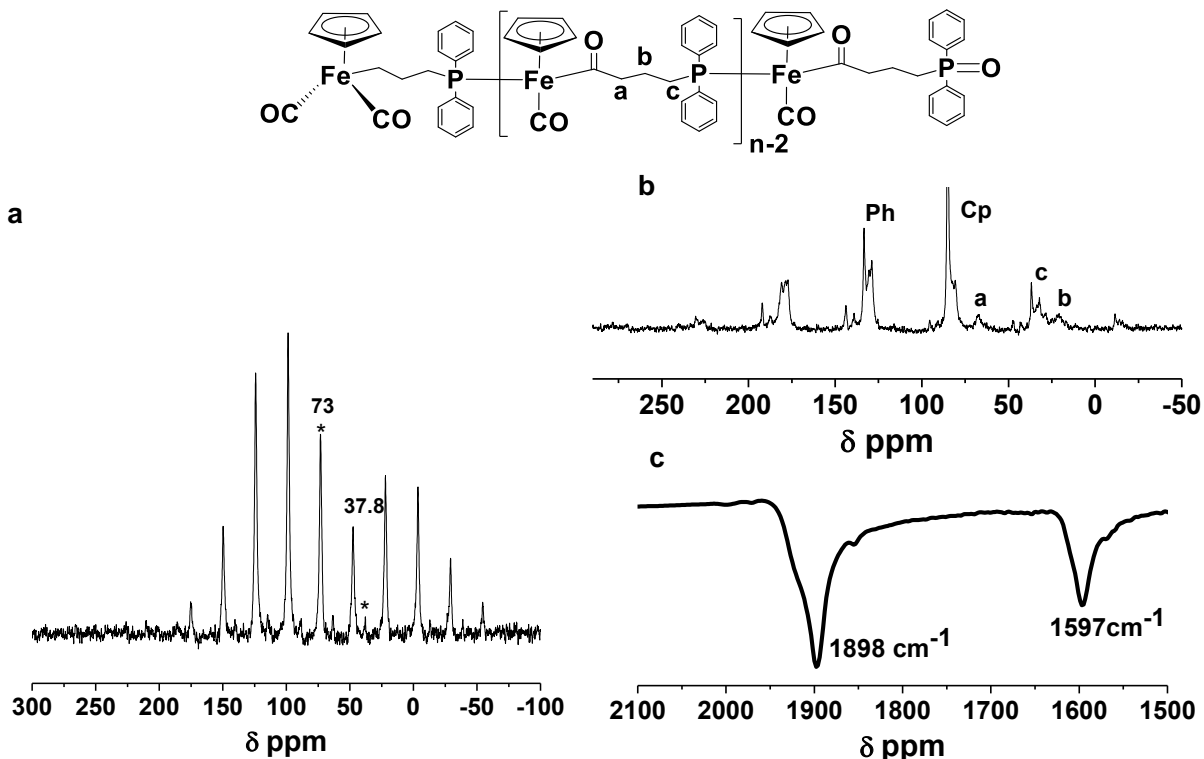
Figure 2.11 (a) Solid state ^{31}P NMR spectrum; (b) solid state ^{13}C NMR spectrum and (c) FT-IR spectrum for the insoluble materials produced from solution MIP of FpP.

GPC results reveal that the THF-soluble material has a M_n of 4200 g/mol with a PDI of 1.24, indicating that oligomeric species were generated. The chemical structure of the PFpP oligomer was characterized using ^{1}H NMR spectroscopy (Figure 2.12b). In the ^{1}H NMR spectrum, the chemical shifts at 7.8-7.1 ppm and 4.3 ppm represent the phenyl groups and the Cp rings in each Fp acyl repeat unit, respectively. The integration ratio of these two peaks is 2 : 1, which is in agreement with the expected value. The signal at 4.8 ppm represents Cp ring for the Fp end group of the oligomer. Intensities of the chemical shifts for the peak at 4.3 and 4.8 ppm are compared for end group analysis, suggesting that the oligomer has a DP_n of 11. The molecular weight estimated from the ^{1}H NMR analysis is ca. 4400 g/mol, which is in agreement with the GPC results. Chemical shifts for the propyl spacer appear upfield between 0.8–2.7 ppm.

61
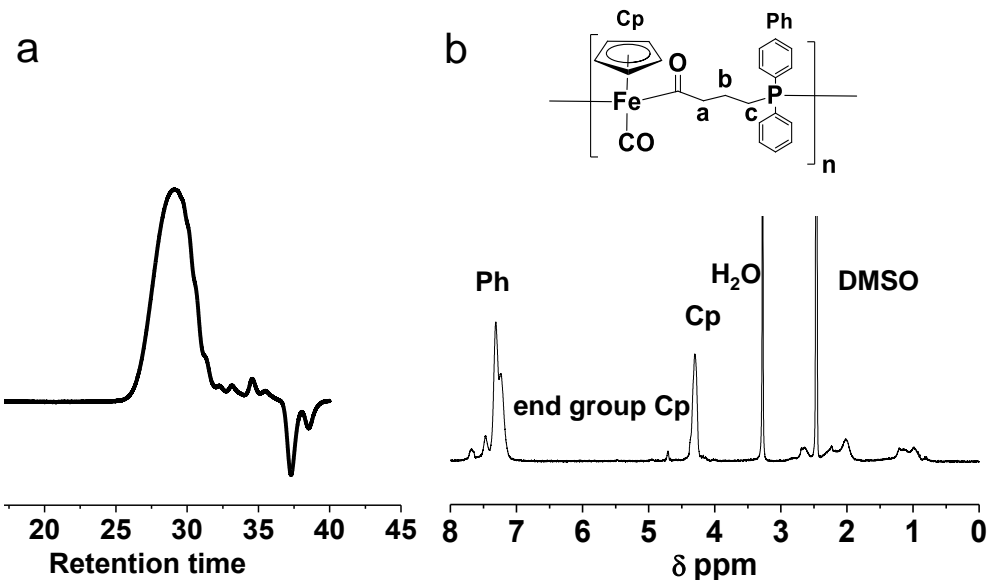
Figure 2.12 (a) GPC curve for PFpP oligomer and (b) ^{1}H NMR spectrum for oligo-PFpP in DMSO-d_6 produced *via* solution polymerization of FpP in THF.

^{13}C-^{1}H HMQC 2D NMR spectroscopy was performed to assign the signals for the propyl spacer. The correlation map shows that the signals at 2.8 and 2.3 ppm in the ^{1}H NMR spectrum both correlate to the peak at 66 ppm due to the carbon α to the acyl group in the ^{13}C NMR spectrum (a in Figure 2.13), suggesting that the two protons from C(O)CH$_2$ are diastereotopic. The expanded ^{13}C NMR spectrum displays two peaks for the chemical shift at 29 ppm (c in Figure 2.13) due to C-P coupling, suggesting that this carbon is adjacent to the phosphorus atom. In contrast, the peak at 20 ppm (b in Figure 2.13) is a singlet, indicating a weak C-P coupling effect. Therefore, the peak at 20 ppm can be assigned to the carbon β to iron center. From the cross peaks observed in Figure 2.13, the signal at 1.9-2.2 ppm (c in Figure 2.13) in the ^{1}H NMR spectrum is assigned to the proton on the carbon adjacent to PPh$_2$, while the peak at 0.9-1.3 ppm (b in Figure 2.13) is due to the protons β to the iron center.
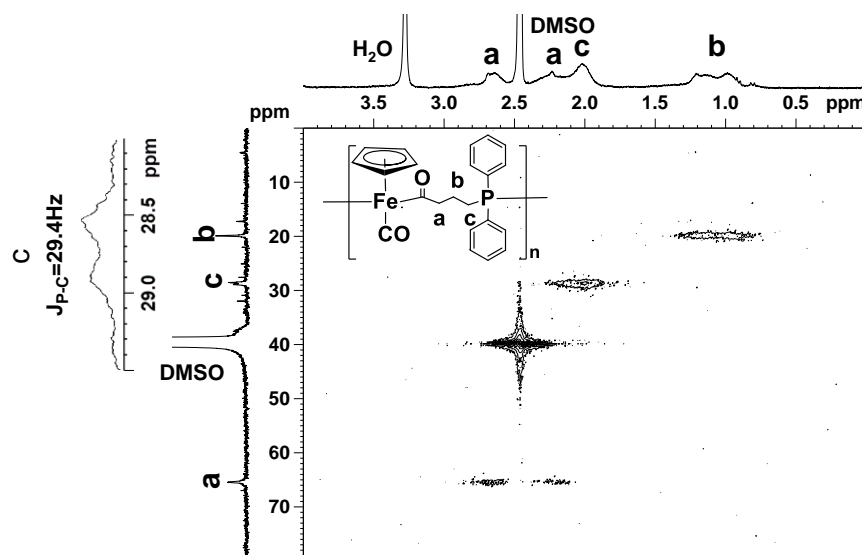
Figure 2.13 ^{13}C-^{1}H HMQC 2D NMR spectrum for PFpP oligomer in DMSO-d_6.

During the polymerization, samples were withdrawn at certain time intervals from the reaction mixture and subsequently examined using ^{31}P NMR spectroscopy in THF. As shown in Figure 2.14, with the progress of the polymerization, the peak at 109 and 69.5 ppm gradually increased, indicating that the formation of the 5- and 6-membered ring.
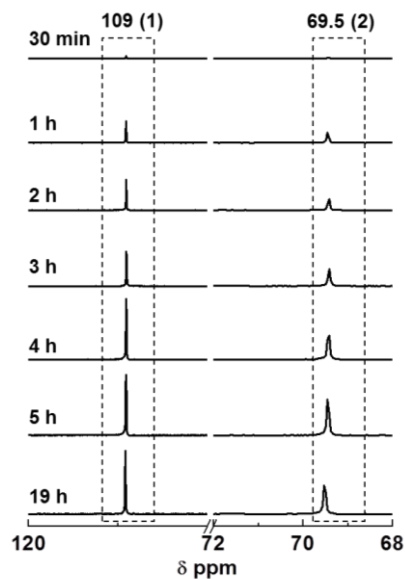
Figure 2.14 ^{31}P NMR spectra for the 5-membered ring (1) and 6-membered ring (2) generated in the solution polymerization of FpP (20 wt%) in THF at 70 ^{o}C.

63
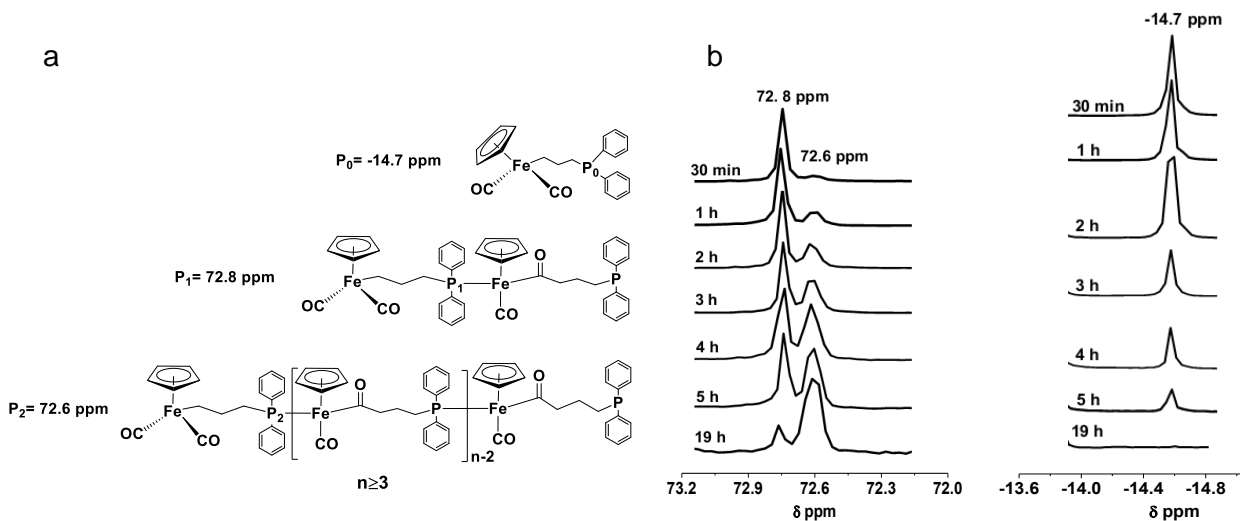
Figure 2.15 (a) Chemical structures for FpP, FpP dimer and PFpP with DP larger than 2 (P_0, P_1 and P_2 represents phosphorus in FpP, coordinated phosphorus in FpP dimer and terminal repeat unit of PFpP with DP larger than 2, respectively) and (b) Intensities for the ^{31}P NMR signals at -14.7 ppm (P_0), 72.6 ppm (P_1) and 72.8 ppm (P_2) as function of polymerization time.

In addition, as illustrated in Figure 2.15, the signal at -14.7 ppm is due to the monomers (P_0 in Figure 2.15a).[39] The chain end coordinated phosphorus for dimers and other species with a DP greater than 2 can be distinguished in the ^{31}P NMR spectra. As illustrated in the figure, the signal at 72.8 ppm is assigned to the dimers (P_1 in Figure 2.15a) and at 72.6 ppm is due to the PFpP with DP larger than 2 (P_2 in Figure 2.15a). As shown in the figure, with the progress of the polymerization, the peak at -14.7 ppm gradually decreased, which is accompanied by the increased intensities for the peaks due to coordinated backbone phosphorus, suggesting that polymerization occurred, as shown in Figure 2.16. The peaks that appear at 73.4-75.0 ppm are attributed to the main chain coordinated phosphorus. The intensity for these peaks increased during the polymerization, suggesting the growth of PFpP chains. The multiple peaks probably are caused by PFpP with different DP or different repeat units in the same PFpP chains. This

result suggests that the chemical shifts for these phosphoruses are sensitive to the length of PFpP and their positions in the same polymers when THF is used as the solvent.
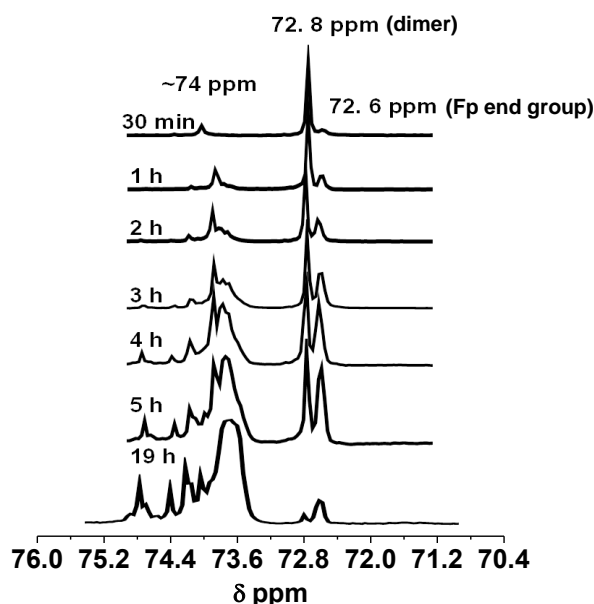
Figure 2.16 ^{31}P NMR spectra for the main chain coordinated phosphorus in THF.

As shown in Figure 2.14b, dimers were preferentially formed, as indicated by the appearance of the signal at 72.8 ppm when the solution was heated for 30 min. These dimers converted to longer chains over time, as indicated by the increased intensities for the peaks at 72.6 ppm (Figure 2.14b) and the peaks around 74 ppm due to the backbone phosphorus (Figure 2.15). As expected, the monomer consumption was much faster than the step-growth of the dimers. After polymerization for 5 h, although over 90 % of FpP was consumed, 50 % of the coordinated products are dimers, as estimated from the integration ratio between the signals at 72.8 and 72.6 ppm. Small amount of dimers (16.6 %) still remained in the solution, even after all monomers were consumed after 19 h (Figure 2.14b). The NMR analysis indicates that the polymerization follows a typical step-growth mechanism.

2.4 Conclusions

$CpFe(CO)_2(CH_2)_3PPh_2$ (FpP) was synthesized and fully characterized. In solution, FpP undergoes both intra- and intermolecular reactions depending on the reaction conditions. The reactions of FpP at lower concentration (ca. 1 wt%) at 25 ^{o}C favors the formation of five membered rings *via* CO release, while at a higher temperature (70 ^{o}C) MIR was promoted, generating six membered rings as the major product when FpP concentration was low. Intermolecular MIR was promoted by increasing the concentration of FpP. Polymerization of FpP at a high concentration solution (20 wt%) was therefore performed at 70 ^{o}C, leading to both THF-soluble and insoluble polymers. Both the soluble and insoluble polymers appeared similar in color. The soluble materials had a M_n of ca. 4200 g/mol with a PDI of 1.24 as determined by GPC analysis. FT-IR and solid-state NMR analysis of the insoluble product indicated that they were also generated *via* the migration insertion reaction. These comprehensive studies of FpP chemical reactions in solution offers valuable fundamental knowledge required for further exploration of the newly developed MIP.

Chapter 3. Bulk Polymerization of CpFe(CO)$_2$(CH$_2$)$_3$PPh$_2$ (FpP) and Physical Properties of PFpP

3.1 Introduction

As discussed in Chapter 2, we studied the reaction behaviour of CpFe(CO)$_2$(CH$_2$)$_3$PPh$_2$ (FpP) in solution. A PFpP oligomer with DP$_n$ = 11 was generated in the solution polymerization of FpP. However, cyclics and a fraction of THF-insoluble material were also produced during the polymerization.

In this Chapter, bulk MIP of FpP (Scheme 3.1) is conducted in an attempt to supress cyclization reactions and to produce PFpP with a higher molecular weight. The effects of temperature and DMSO on the polymerization were investigated. The chemical structure for the resulting polymers was characterized. In addition, the thermal behavior and solution properties of PFpP were also briefly studied. At the end, density functional theory (DFT) calculations indicated that PFpP adopts a linear chain configuration.
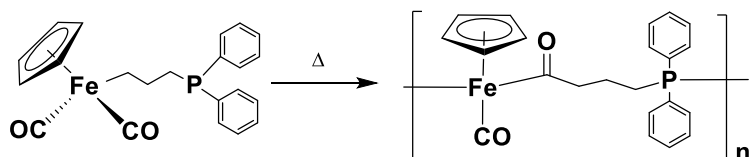
Scheme 3.1 Migration insertion polymerization (MIP) of CpFe(CO)$_2$(CH$_2$)$_3$PPh$_2$ (FpP).

3.2 Experimental

3.2.1 Materials and Instrumentation

All experiments were performed under dry nitrogen atmosphere using either standard Schlenk techniques or in a glovebox unless otherwise indicated. Tetrahydrofuran (THF) was freshly distilled under nitrogen from Na/benzophenone. *n*-Hexane was degassed with dry nitrogen before use. Toluene was dried with molecular sieves before use. Sodium (Na), 1-bromo-3-chloropropane and potassium (K) were purchased from Sigma-Aldrich. Cyclopentadienyl iron dicarbonyl dimer (Fp$_2$) was purchased from Strem Chemicals Inc. Chlorodiphenylphosphine was purchased from Tokyo Chemical Industry (TCI). Benzophenone was purchased from Fisher Scientific. All the chemicals were used as received unless otherwise indicated.

^{1}H and ^{31}P NMR spectra were obtained on a Bruker Avance 300 (^{1}H NMR: 300 MHz, ^{31}P NMR: 120 MHz) spectrometer at ambient temperature using appropriate deuterated solvents. The NMR samples were prepared under dry nitrogen atmosphere unless otherwise indicated.

The molecular weights and molecular weight distributions, M_w/M_n, were characterized using GPC analysis at room temperature with THF as eluent at a flow rate of 1.0 mL/min. The Viscotek GPC max unit used was equipped with a VE 2001 GPC, three PolyAnalytik organic mixed bed columns, PAS-103-L, PAS-104-L, and PAS-105-L with dimension of 8 mm (ID)$\times$ 300 mm (L) each, and a viscotek triple detector array, including refractive index, viscosity, and dual-angle light scattering detectors.

UV-vis absorption spectra for the samples with four different concentrations in DCM were conducted on a Varian (Carey 100 Bio) UV visible spectrophotometer using a quartz cuvette with a path length of 1 cm. DCM was used as blank. The absorption intensity at a wavelength of 350 nm was plotted against solution concentration, leading to a straight line. The molar extinction coefficient was determined from the slope of the line.

Fourier transform infrared spectroscopy (FT-IR) spectra for the PFpP solid samples were recorded on a Bruker Tensor 27 spectrophotometer with a resolution of 1 cm^{-1}. Test pellets were prepared by grinding and compressing PFpP (2 wt%) in KBr.

Turbidity measurements were performed on a Varian (Carey 100 Bio) UV-visible spectrophotometer equipped with a temperature controller. The heating program started at 25 ^{o}C at a constant rate of 1.0 ^{o}C/min, followed by cooling back to 25 ^{o}C at the same rate. The wavelength was fixed at 600 nm. The transmittance curve was obtained by plotting the transmittance as a function of temperature. The inflection point in the transmittance curve was taken as the cloud point; this point was graphically determined by the maximum of the first derivative of the heating or cooling curve.

3.2.2 Synthesis of FpP

The synthesis of FpP was described in Chapter 2.

3.2.3 Polymerization of FpP

The polymerization of FpP was carried out in bulk at elevated temperature without or with DMSO (5 wt%). The polymerization time and temperature are indicated in Table 3.1. After the desired polymerization time, the polymerization was terminated by cooling the reaction flask to

room temperature. The crude product was dissolved in a minimum amount of THF and subsequently precipitated in hexane. The precipitate was collected by filtration and dried under vacuum at room temperature overnight. The resulting polymer was a bright yellow powder. For PFpP produced at 70 $^{\circ}$C, NMR spectroscopy of the resulting PFpP was performed in DMSO-d_6. ^{1}H NMR (DMSO-d_6): 7.8-7.1 ppm (b, 10H, C$_6$**H**$_5$), 4.4-4.2 ppm (b, 5H, C$_5$**H**$_5$), 2.78-2.60 ppm (b, 1H, COC**H**$_2$), 2.47-2.17 ppm (b, 1H, COC**H**$_2$), 2.13-1.89 ppm (b, 2H, C**H**$_2$P), 1.32-0.74 ppm (b, 2H, CH$_2$C**H**$_2$CH$_2$). ^{31}P NMR (DMSO-d_6): 73.5 ppm (main chain coordinated phosphorus), 72.7 ppm (chain end coordinated phosphorus), -14.7 ppm (chain end uncoordinated phosphorus). FT-IR: 1910 cm^{-1} (terminal carbonyl groups), 1600 cm^{-1}. (migrated carbonyl group). For PFpP produced at 105 $^{\circ}$C, NMR spectroscopy of the resulting PFpP was performed in CDCl$_3$. ^{1}H NMR (CDCl$_3$): 7.6-7.1 ppm (b, 10H, C$_6$**H**$_5$), 4.4-4.0 ppm (b, 5H, C$_5$**H**$_5$), 2.8-2.60 ppm (b, 1H, COC**H**$_2$), 2.4-2.1 ppm (b, 1H, COC**H**$_2$), 2.1-1.8 ppm (b, 2H, C**H**$_2$P), and 1.4-0.8 ppm (b, 2H, CH$_2$C**H**$_2$CH$_2$). ^{31}P NMR (CDCl$_3$): 73 ppm (main chain coordinated phosphorus), 35 ppm (chain end oxidized phosphorus). FT-IR: 1911 cm^{-1} (terminal carbonyl groups), 1600 cm^{-1} (migrated carbonyl group)

3.2.4 Migration insertion reaction of PFpP oligomer with hexyldiphenylphosphine (Ph$_2$PC6)

20.0 mg PFpP (DP$_n$ = 7) was dissolved in 4.0 mL of DMSO in a NMR tube and the solution was heated to 50 $^{\circ}$C in the presence of one equivalent of Ph$_2$P(CH$_2$)$_5$CH$_3$. The reaction mixture was analyzed using ^{31}P NMR spectroscopy before and after heating for 44 h. Afterwards, the reaction solution was precipitated in hexane, yielding a yellow powder; the powder was collected by centrifugation and dried under vacuum overnight. The resulting product was then

characterized by ^{1}H NMR, ^{31}P NMR and ^{13}C NMR spectroscopies. ^{31}P NMR (DMSO-d_6): 73.6 ppm. ^{1}H NMR (DMSO-d_6): 7.8-7.1 ppm (b, 10H, C$_6$**H**$_5$), 4.3 ppm (b, 5H, C$_5$**H**$_5$), 2.8-2.60 ppm (b, 1H, COC**H**$_2$), 2.47-1.87 ppm (b, 1H, COC**H**$_2$), 2.47-1.87 ppm (b, 2H, C**H**$_2$P), 2.47-1.87 ppm (b, 2H, C**H**$_2$PPh$_2$(CH$_2$)$_5$CH$_3$), 1.35-0.87 ppm (b, 2H, CH$_2$C**H**$_2$CH$_2$), 1.35-0.87 ppm (b, 2H, C**H**$_2$(CH$_2$)$_4$CH$_3$), 0.87-0.63 ppm (b, 3H, CH$_2$(CH$_2$)$_4$C**H**$_3$). ^{13}C NMR (DMSO-d_6): 13.7 ppm (**C**H$_3$(CH$_2$)$_4$CH$_2$PPh$_2$), 21.7 ppm (CH$_3$(**C**H$_2$)$_4$CH$_2$PPh$_2$), 30.5 ppm (CH$_3$(CH$_2$)$_4$**C**H$_2$PPh$_2$), 65 ppm (**C**H$_2$C=O), 20 ppm (CH$_2$**C**H$_2$CH$_2$), 29 ppm (**C**H$_2$PPh$_2$), 84 ppm, 86 ppm (**C**$_5$H$_5$), 127 ppm, 128 ppm, 129 ppm, 130 ppm, 132 ppm (**C**$_6$H$_5$), 274 ppm (CH$_2$**C**=O), 220 ppm (**C**≡O).

3.2.5 Reaction of PFpP oligomer with FpMe

The reactivity of the phosphine end group in the PFpP oligomer was investigated. The PFpP oligomer (20.0 mg) and CpFe(CO)$_2$CH$_3$ (FpMe) (5 equivalents relatively to PFpP oligomer) were dissolved in 4.0 mL of DMSO-d_6 in an NMR tube and the solution was heated at 50 $^{\rm o}$C. FpMe was prepared according to literature.[1] The reaction mixture was analyzed by ^{1}H NMR spectroscopy before and after heating for 3 days.

3.3 Results and Discussion

3.3.1 Bulk polymerization of FpP

In order to supress the formation of cyclic species, bulk polymerization of FpP was conducted at 70 $^{\rm o}$C. During the polymerization, we observed that the system became vitrified and the orignally orange oil-like monomer gradually changed to a transparent reddish-brown solid. After 20 h, the polymerization was terminated by cooling the reaction flask to room temperature. A

small amount of THF was added to dissolve the crude product, yielding a clear red solution. The

red solution was then precipitated into a large amount of hexane, yielding a yellow precipitate.

No THF-insoluble material was produced.

The yellow powder was first characterized by FT-IR spectroscopy (Figure 3.1). As shown in

Figure 3.1, upon polymerization, two peaks at 2007 cm^{-1} and 1953^{-1} corresponding to the terminal

CO in FpP monomer shifted to lower frequencies. Particularly, one CO signal appeared at 1600

cm^{-1}, suggesting that acyl CO was formed as a result of the migration insertion reaction.
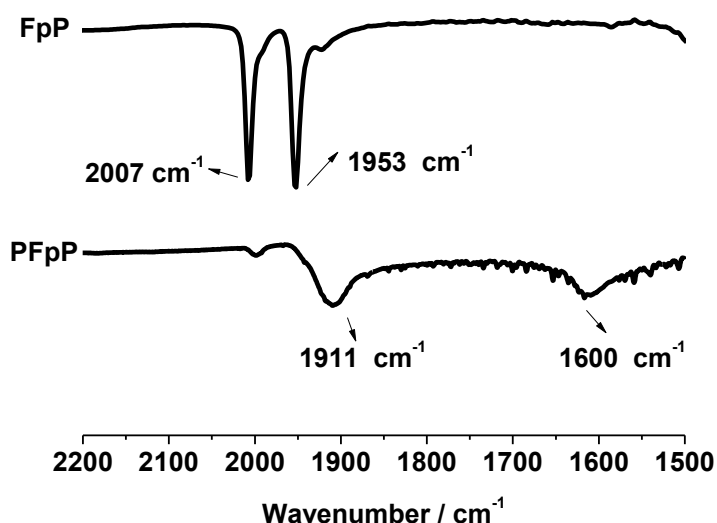
Figure 3.1 FT-IR spectra for FpP and PFpP produced from bulk polymerization of FpP at 70 $^{\circ}$C.

The resulting product was also characterized by ^{31}P and ^{1}H NMR spectroscopy. As shown in

Figure 3.2a, three peaks at 73.5 ppm (P$_1$), 72.7 ppm (P$_2$) and -14.7 ppm (P$_3$) were observed in

the ^{31}P NMR spectrum, which can be assigned to the main chain coordinated phosphorus (P$_1$),

the chain end coordinated phosphorus (P$_2$) and the uncoordinated phosphine end group (P$_3$),

respectively. The presence of the phosphine end groups suggests that the resulting polymers

may be linear. The ^{1}H NMR spectrum for PFpP was displayed in Figure 3.2b, the chemical shift

at 7.8-7.1 ppm is attributed to the protons from the phenyl group. The resonance signals at 4.7

ppm and 4.3 ppm represent the Cp ring in the chain end group (Cp_2 in Figure 3.2b) and the Cp ring in the Fp acyl repeat unit (Cp_1 in Figure 3.2b), respectively. The integration ratio between the resonance signals at 4.3 ppm (Cp_1) and at 4.7 ppm (Cp_2) is 6 : 1. From this integration ratio, we can estimate that the DP_n of the product is 7. The chemical shifts due to the propyl spacer appear upfield. To be specific, the peak at 2.78-2.6 ppm (a in Figure 3.2b) and 2.47-2.17 ppm (a in Figure 3.2b) is assigned to the two diastereotopic protons from the CH_2 α to the acyl group; the chemical shift due to the CH_2 β to the acyl group appears at 1.32-0.74 ppm (b in Figure 3.2b). The resonance signal at 2.13-1.89 ppm (c in Figure 3.2b) represents the CH_2 coordinated to phosphorus.
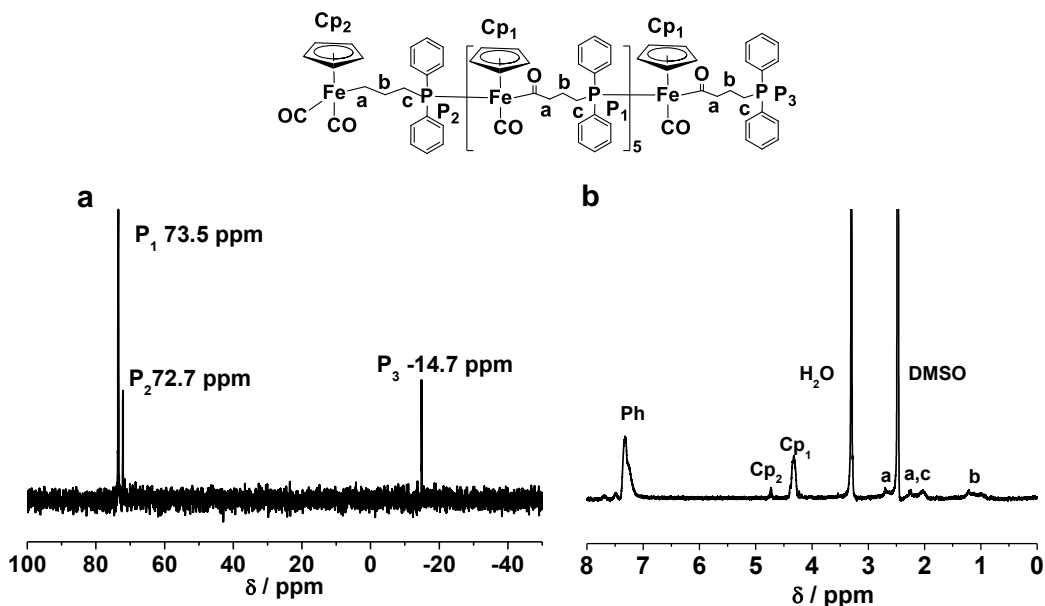
Figure 3.2 (a) ^{31}P and (b) ^{1}H NMR spectra for PFpP produced from bulk polymerization of FpP at 70 °C in DMSO-d_6.

Table 3.1 Effects of temperature and added DMSO on the polymerization of FpP in bulk[a]

Entry	Temp. ($^{\circ}$C)	DMSO[b]	M_n (g/mol)	PDI
1	70	--	2800[c]	--
2	105	--	8200[d]	1.35
3	70	DMSO	3000[d]	3.15
4	105	DMSO	25700[d]	1.73

[a] Polymerization time was 20 h. [b] DMSO (ca. 5 wt%) was added. [c] end group analysis. [d] GPC results: conventional calibration using PS standards for entries 2 and 3, as the samples did not scatter sufficient light to yield reliable light scattering data; triple detection used for entry 4. Note: The *dn/dc* value for PFpP measured from the differential refractometer is 0.2

The effects of temperature and DMSO on bulk MIP were investigated and the results are summarized in Table 3.1. As shown in the table, under all conditions, the PFpP molecular weights are relatively low. In order to understand the reason for the production of low molecular weight polymers, the reactivity of the two terminal groups (Fp and phosphine) in the PFpP oligomers was examined. PFpP (DP_n = 7) was first reacted with one equivalent of hexyldiphenylphosphine (PPh_2C_6). The reactants and products were examined using ^{31}P NMR spectroscopy. As shown in Figure 3.3a, the chemical shift at 72.7 ppm (P_1 in Figure 3.3a), due to the coordinated phosphorus for terminal FpP repeat unit, disappeared upon reaction, suggesting that the Fp end group is reactive.[2] Figure 3.3b shows that the signals for the uncoordinated phosphorus from PPh_2C_6 and PFpP's phosphine chain end are distinguishable, appearing at -14.6 (P_0 in Figure 3.3b) and -14.7 ppm (P_3 in Figure 3.3b), respectively. After the reaction, the intensity for the peak at -14.6 ppm resulting from PPh_2C_6 disappeared, while the peak at -14.7 ppm due to PFpP phosphine end group remained unchanged. This result suggests that PFpP phosphine end group is less reactive as compared to PPh_2C_6. The reactivity of the Fp

end group is also verified *via* the ^{1}H NMR spectrum for the oligomers. As illustrated in Figure 3.3c, the signal at 4.7 ppm (Cp$_1$ in Figure 3.3c) due to the Cp ring in the Fp end group upfield shifted to 4.3 ppm (Cp$_2$ in Figure 3.3c) as a result of the PFpP end group MIR.[3]
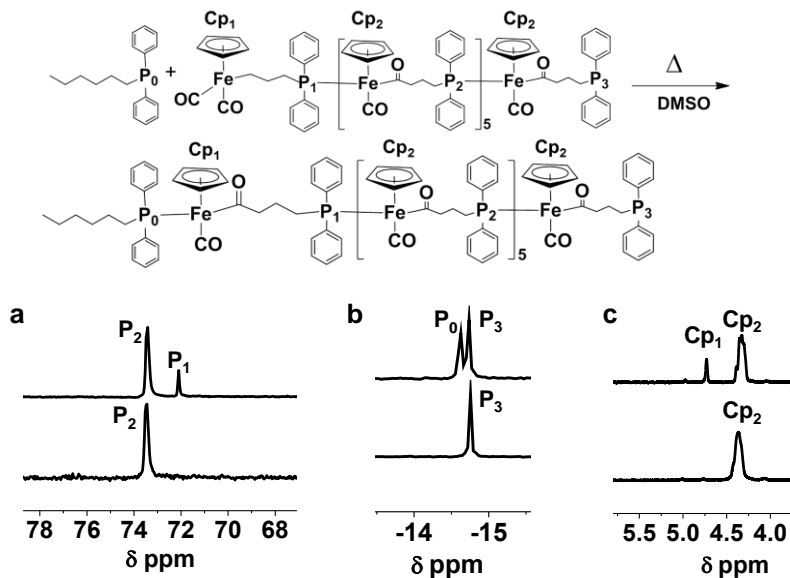
Figure 3.3 (a, b) ^{31}P NMR spectra for PFpP solution in the presence of hexyldiphenylphosphine before heating (above) and after heating for 44 h (below); (c) ^{1}H NMR spectra for PFpP oligomer (above) and the hexyldiphenylphosphine functionalized PFpP (below) in DMSO-d_6.

On the other hand, the lack of reactivity for the phosphine end group was further verified *via* the reaction of PFpP with FpMe in DMSO-d_6. As shown in Figure 3.4, the chemical shift at 4.95 ppm (Cp$_3$) represents the Cp ring in FpMe, the resonance signals for the chain end and main chain Cp ring appear at 4.72 ppm (Cp$_1$) and 4.3 ppm (Cp$_2$), respectively. The integration ratio for these three peaks remains the same after heating, indicating that no MIR occurred for the Fp end group both in PFpP and FpMe.
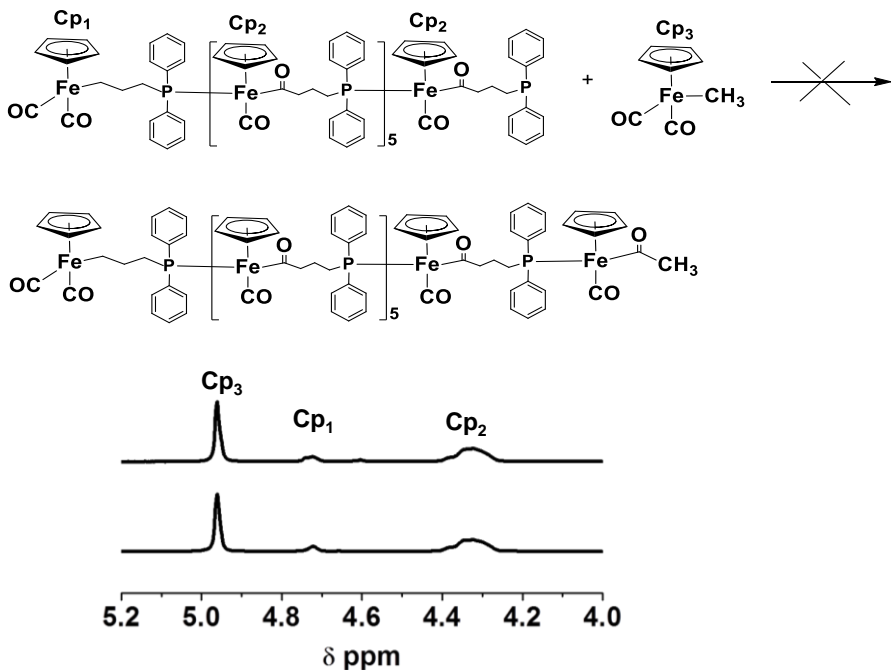
Figure 3.4 ^{1}H NMR spectra for PFpP ($DP_n = 7$) DMSO-d_6 solution in the presence of FpMe before (above) and after (below) heating at 50 °C.

The above NMR analysis suggested that the PFpP phosphine end groups are not reactive toward either Fp end groups in PFpP oligomer or FpMe small molecules under the conditions of the experiment. The attenuated reactivity of phosphine end groups can therefore be a reason accounting for the difficulty in preparing high molecular weight PFpP.

The temperature effect on MIP was investigated using ^{31}P NMR spectroscopy. The ^{31}P NMR spectra for the crude products produced at 70 and 105 °C were performed and compared. As shown in Figure 3.5, the peak at 72.8 ppm (P_1 in Figure 3.5) is assigned to the coordinated phosphorus in the FpP dimer.[4] For the oligomer with DP larger than 2, this chemical shift for the chain end coordinated phosphorus appears at 72.6 ppm (P_2 in Figure 3.5).[4] As shown in Figure 3.5, the disappearance of the peak at 72.8 ppm and the decreased intensity of the peak at 72.6 ppm suggest that step-growth reaction of the FpP dimers and other oligomers with DP larger than 2 are both enhanced at higher temperature.[4] It was therefore concluded that higher

76

molecular weight polymers resulted from enhanced step growth reactions of FpP dimers and oligomers at the higher polymerization temperature, due to the increased mobility of the molecules.
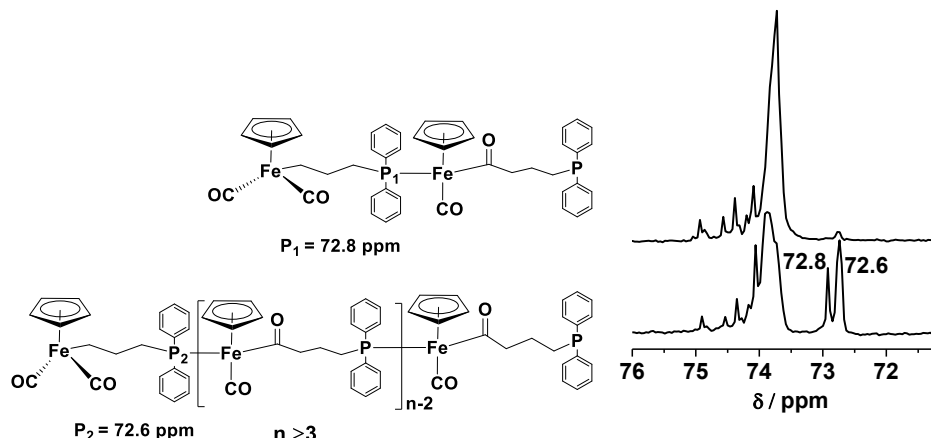
Figure 3.5 ^{31}P NMR spectra for the PFpP crude products produced from MIP of FpP at 105 ^{o}C (above) and 70 ^{o}C (below) in bulk.

It has been reported that DMSO can induce MIR *via* coordination to Fe, and a solvent-coordinated intermediate was revealed by ^{1}H NMR analysis in a previous report.[5] We therefore performed MIP of FpP in the presence of a small amount of DMSO (ca. 5 wt%). When the polymerization was performed at 70 ^{o}C (entry 3 in Table 3.1), the molecular weight of the resulting polymers remained low. However the molecular weight distribution was broad (PDI = 3.15) and the weight-average molecular weight (M_w) was 9400 g/mol, suggesting that a small amount of higher molecular weight polymer was produced. This result suggests that DMSO is exerting an influence on MIP, but this effect is limited due to the lower chain mobility at 70 ^{o}C. To overcome this limitation, polymerization of FpP in the presence of DMSO was performed at 105 ^{o}C. GPC analysis revealed that the resulting polymer had a M_n of 25,700 g/mol with a PDI of 1.73 (entry 4 in Table 3.1). Comparing the molecular weight for the polymers produced at 105 ^{o}C with and without DMSO (Table 3.1), it becomes obvious that DMSO can promote step

growth coupling, leading to PFpP with relatively higher molecular weight (Entry 4 in Table 3.1).

3.3.2 Physical properties of PFpP

3.3.2.1 Thermal behavior of PFpP

Thermal properties of the polymer were studied using DSC and TGA. DSC result indicates that the glass transition temperature T_g for the PFpP oligomer with $DP_n = 7$ is 99 $^\circ$C (Figure 3.6)
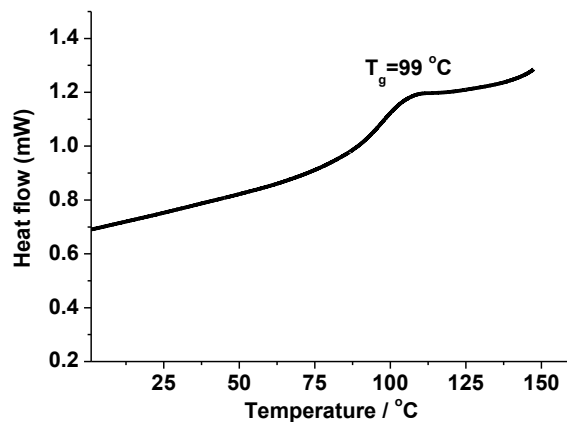
Figure 3.6 DSC curve of PFpP oligomer with $DP_n = 7$.
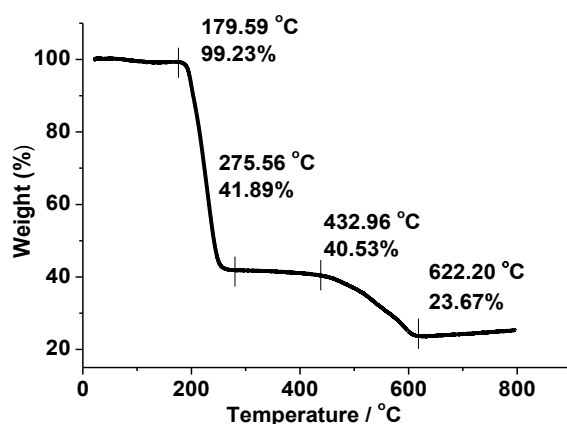
Figure 3.7 TGA curve of PFpP.

TGA revealed that PFpP starts to lose weight at 180 $^\circ$C. The second stage of weight loss starts at 432 $^\circ$C. Finally, the polymer loses ca. 77 % of its original weight at 622 $^\circ$C, with a char yield of ca. 23 %. This TGA result indicates that PFpP has improved thermal stability when compared to FpP, that starts to decompose at 130 $^\circ$C.[6]

3.3.2.2 Solution properties of PFpP

Triple detection GPC analysis (entry 4 in Table 3.1) reveals that the α-value of PFpP for the Mark–Houwink equation is 0.53, suggesting that the polymers are approaching theta conditions in THF at 35 °C.

UV-vis of the polymer in DCM (Figure 3.8) reveals that PFpP solution absorbs light at wavelength of 350 nm with a molar extinction coefficient ε of 1.13×10^4 L mol^{-1} cm^{-1} (Figure 3.8).
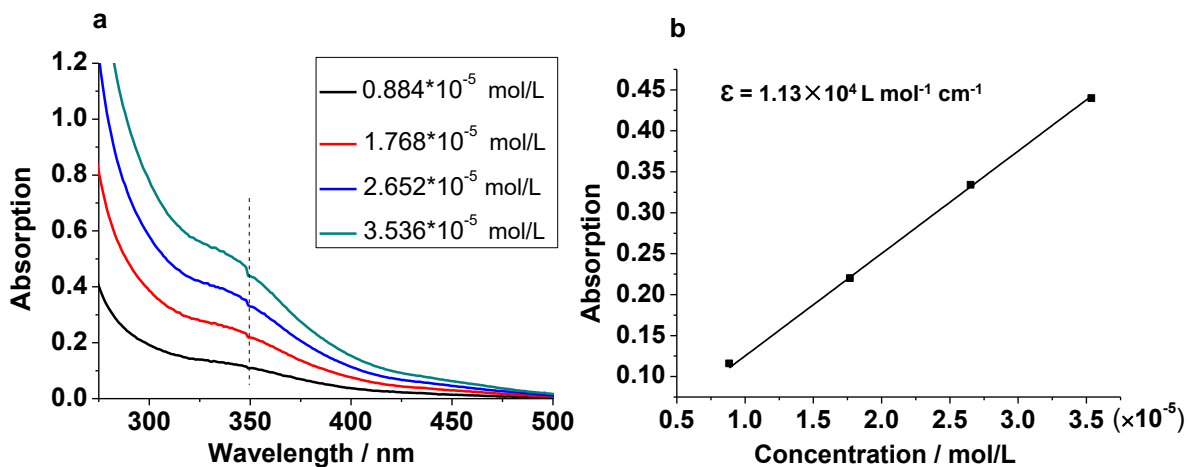
Figure 3.8 (a) UV-vis absorption spectra for PFpP in DCM and (b) plot of the absorption at 350 nm as a function of solution concentration.

Interestingly, we discovered that PFpP exhibits a molecular weight-dependent solution behaviour in DMSO. Although the PFpP oligomer (M_n = 2800 g/mol) is readily soluble, the higher molecular weight PFpP (M_n = 25700 g/mol) is almost completely insoluble in DMSO at 25 °C, but solubilizes above 50 °C. Figure 3.9 shows that this temperature-dependent solubility is reversible, with an upper critical solution temperature (UCST) appearing at 40.3 °C upon heating and at 34.9 °C upon cooling. In contrast, such thermoresponsive solution behavior was

not observed for the PFpP oligomer (Figure 3.9). It is worth noting that polymers, especially organometallic macromolecules, exhibiting molecular weight-dependent UCST in organic solvents are rarely reported.[7] Further research into this property will open up new opportunities for functional materials.
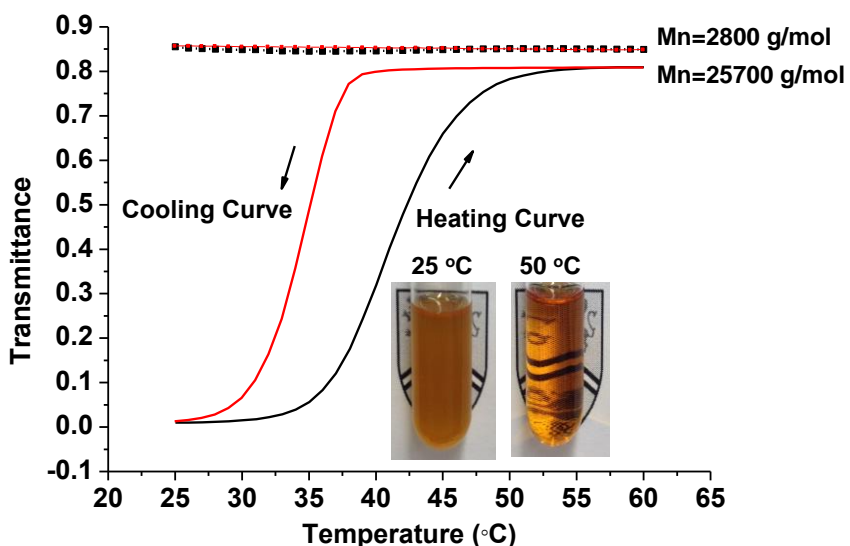
Figure 3.9 Turbidity curve of PFpP solution in DMSO (4 wt%) at heating and cooling rates of 1 ^{o}C/min (wavelength: 600 nm).

3.4 Conclusions

In this Chapter, bulk polymerization of FpP was performed and the effects of temperature and DMSO on the polymerization were investigated. High molecular weight polymers with M_n up to 25,700 g/mol were produced by conducting the MIP at 105 ^{o}C in the presence of DMSO. TGA and DSC analysis revealed that the polymer was thermally stable up to 180 ℃ and has a T_g of ca. 99 ℃, respectively. DFT calculation results suggested that PFpP adopted a linear structure, which is supported by the NMR analysis of the polymer structure. PFpP displayed molecular

weight-dependent solubility and exhibited reversible temperature-dependent solubility in DMSO for higher molecular weight samples. This solution behaviour may render these polymers interesting for materials application such as positive electron beam resists for lithography[8] and temperature-stimulated supramolecular organometallic materials.[9]

Chapter 4. End Group Functionalization of PFpP Macromolecules *via* the Fp Migration Insertion Reaction

4.1 Introduction

The synthesis of metal-containing amphiphilies, including surfactants[1] and block copolymers,[2] provides supramolecular building blocks.[3-7] Particularly, metal carbonyl-containing amphiphiles have been found useful for effective CO delivery[8] and as precursors for magnetic materials.[9]

As described in Chapter 3, bulk polymerization of FpP was carried out in order to supress intramolecular cyclic reactions. ^{1}H and ^{31}P NMR analysis revealed that the PFpP oligomer with $DP_n = 7$ has two end groups, which are the Fp and phosphine group, respectively.[10] In addition, we have experimentally demonstrated that the Fp end group is reactive for MIR, while the reactivity of the terminal phosphine group is low.[11]

In this Chapter, we further studied the reaction conditions for the end group functionalization of PFpP. A number of alkyl diphenylphosphines (Ph$_2$PCn: n = 6, 10, 18) with varying chain lengths are used to react with PFpP *via* Fp end group MIR. The steric effects on the extent of reaction were investigated.

4.2 Experimental

4.2.1 Materials and Instrumentation

All experiments were performed under dry nitrogen atmosphere using either standard Schlenk techniques or in a glovebox unless otherwise indicated. THF was freshly distilled under nitrogen from Na/benzophenone. *n*-Hexane was degassed with dry nitrogen before use. Toluene was dried with molecular sieves before use. Sodium (Na), 1-bromo-3-chloropropane and potassium (K) were purchased from Sigma-Aldrich. Cyclopentadienyl iron dicarbonyl dimer (Fp$_2$) was purchased from Strem Chemicals Inc. Chlorodiphenylphosphine was purchased from Tokyo Chemical Industry (TCI). Benzophenone was purchased from Fisher Scientific. 1-bromohexane, 1-Bromodecane and 1-bromooctadecane were purchased from Sigma-Aldrich. All chemicals were used as received unless otherwise indicated.

^{1}H, ^{31}P and ^{13}C NMR spectra were obtained on a Bruker Avance 300 (^{1}H: 300 MHz, ^{31}P: 120 MHz, ^{13}C: 75 MHz) spectrometer at ambient temperature using appropriate solvents.

Fourier transform infrared spectroscopy (FT-IR) spectra for PFpP-PPh$_2$Cn (n = 6, 10, 18) solid samples were recorded on a Bruker Tensor 27 spectrophotometer with a resolution of 1 cm^{-1}. Test pellets were prepared by grinding and compressing PFpP-PPh$_2$Cn (2 % by weight) in KBr.

Dynamic light scattering (DLS) was carried out at 25 ^{o}C using Malevern Zetasizer Nano90.

4.2.2 Synthesis of oligo-PFpP

The synthesis and characterization of oligo-PFpP with DP$_n$ = 7 were described in Chapter 3.

4.2.3 Synthesis of Ph$_2$PCn (n = 6, 10, 18)

NaPPh$_2$ (50.0 mL, 25.0 mmol) was added drop-wise to a THF solution of Br-Cn (n = 6, 10, 18) (27.0 mmol) at 0 $^{\circ}$C in an ice bath. After addition, the ice bath was removed and the solution was allowed to warm to room temperature and left to stir overnight. Afterwards, THF and the starting material Br-Cn (n = 6, 10, 18) was removed under vacuum at an elevated temperature. The product was then dissolved in hexane and filtered through a silica gel column. Hexane was then removed under vacuum, yielding a colorless oil or white powder. PPh$_2$C6: ^{31}P NMR (CDCl$_3$): -14.0 ppm. ^{1}H NMR (CDCl$_3$): 7.6-7.2 ppm (b, 10H, C$_6$$\boldsymbol{H}$$_5$), 2.1 ppm (t, 2H, Ph$_2PC\boldsymbol{H}$$_2$), 1.5-1.3 ppm (b, 8H, Ph$_2$PCH$_2$(C$\boldsymbol{H}$$_2$)$_4CH_3$), 0.9 ppm (t, 3H, Ph$_2PCH_2$(CH$_2$)$_4C\boldsymbol{H}$$_3$). PPh$_2$C10: ^{31}P NMR (CDCl$_3$): -14.0 ppm. ^{1}H NMR (CDCl$_3$): 7.6-7.2 ppm (b, 10H, C$_6$$\boldsymbol{H}$$_5$), 2.1 ppm (t, 2H, Ph$_2PC\boldsymbol{H}$$_2$), 1.5-1.3 ppm (b, 16H, Ph$_2$PCH$_2$(C$\boldsymbol{H}$$_2$)$_8CH_3$), 0.9 ppm (t, 3H, Ph$_2PCH_2$(CH$_2$)$_4C\boldsymbol{H}$$_3$). PPh$_2$C18: ^{31}P NMR (CDCl$_3$): -14.0 ppm. ^{1}H NMR (CDCl$_3$): 7.6-7.2 ppm (b, 10H, C$_6$$\boldsymbol{H}$$_5$), 2.1 ppm (t, 2H, Ph$_2PC\boldsymbol{H}$$_2$), 1.5-1.3 ppm (b, 32H, Ph$_2$PCH$_2$(C$\boldsymbol{H}$$_2$)$_{16}CH_3$), 0.9 ppm (t, 3H, Ph$_2PCH_2$(CH$_2$)$_4C\boldsymbol{H}$$_3$).

4.2.4 End group functionalization of PFpP with Ph$_2$PCn (n = 6, 10, 18)

PFpP with DP$_n$ = 7 (700.0 mg, 0.25 mmol) and excess amounts of alkyldiphenylphosphines were dissolved in 30.0 mL THF. 1.5 equivalents of Ph$_2$PC6 and 3.0 equivalents of Ph$_2$PC10 and Ph$_2$PC18, relatively to PFpP, were added for the reactions. The reaction mixture was then refluxed at 70 $^{\circ}$C under N$_2$ atmosphere. After the desired reaction time, the reaction mixture was cooled to 25 $^{\circ}$C and the solutions were subsequently concentrated under vacuum. The concentrated solution was precipitated in a large amount of hexane and the precipitate was

collected *via* filtration. For the reaction system with Ph$_2$PC18, the precipitate was further washed with 2.0 mL methanol three times in order to remove the remaining Ph$_2$PC18. The yellow precipitate was dried under vacuum at 25 ^{o}C. PFpP-PPh$_2$C6: ^{31}P NMR (DMSO-d_6): 73.5 ppm, 32.5 ppm. ^{1}H NMR (DMSO-d_6): 7.8-7.1 ppm (b, 10H, C$_6$**H**$_5$), 4.4-4.2 ppm (b, 5H, C$_5$**H**$_5$), 2.78-2.60 ppm (b, 1H, COC**H**$_2$), 2.47-2.17 ppm (b, 1H, COC**H**$_2$), 2.13-1.89 ppm (b, 2H C**H**$_2$P + 2H CH$_3$(CH$_2$)$_4$C**H**$_2$), 1.32-0.74 ppm (b, 2H CH$_2$C**H**$_2$CH$_2$ + 8H CH$_3$(C**H**$_2$)$_4$CH$_2$), 0.7-0.6 ppm (b, 3H, C**H**$_3$(CH$_2$)$_4$CH$_2$). ^{13}C NMR (DMSO-d_6): 274 ppm (**C**=O), 220 ppm (**C**≡O), 132-127 ppm (**C**$_6$H$_6$), 86, 84 ppm (**C**$_5$H$_5$), 66 ppm (**C**H$_2$CH$_2$CH$_2$PPh$_2$), 30.5 ppm (CH$_3$(CH$_2$)$_4$**C**H$_2$PPh$_2$), 29 ppm (CH$_2$CH$_2$**C**H$_2$PPh$_2$), 21.7 ppm (CH$_3$(**C**H$_2$)$_4$CH$_2$PPh$_2$), 20 ppm (CH$_2$**C**H$_2$CH$_2$PPh$_2$), 13.7 ppm (**C**H$_3$(CH$_2$)$_4$CH$_2$PPh$_2$). IR: 2010 cm^{-1}, 1910 cm^{-1}, 1600 cm^{-1}. PFpP-PPh$_2$C10: ^{31}P NMR (DMSO-d_6): 73.5 ppm, 32.5 ppm. ^{1}H NMR (DMSO-d_6): 7.8-7.1 ppm (b, 10H, C$_6$**H**$_5$), 4.4-4.2 ppm (b, 5H, C$_5$**H**$_5$), 2.78-2.60 ppm (b, 1H, COC**H**$_2$), 2.47-2.17 ppm (b, 1H, COC**H**$_2$), 2.13-1.89 ppm (b, 2H C**H**$_2$P + 2H CH$_3$(CH$_2$)$_8$C**H**$_2$), 1.32-0.74 ppm (b, 2H CH$_2$C**H**$_2$CH$_2$ + 16H CH$_3$(C**H**$_2$)$_8$CH$_2$), 0.7-0.6 ppm (b, 3H, C**H**$_3$(CH$_2$)$_8$CH$_2$). IR: 2010 cm^{-1}, 1910 cm^{-1}, 1600 cm^{-1}. PFpP-PPh$_2$C18: ^{31}P NMR (CDCl$_3$): 73.5 ppm, 32.5 ppm. ^{1}H NMR (CDCl$_3$): 7.8-7.1 ppm (b, 10H, C$_6$**H**$_5$), 4.3 ppm (b, 5H, C$_5$**H**$_5$), 2.78-2.60 ppm (b, 1H, COC**H**$_2$), 2.47-2.15 ppm (b, 1H, COC**H**$_2$), 2.13-1.89 ppm (b, 2H C**H**$_2$P + 2H CH$_3$(CH$_2$)$_{16}$C**H**$_2$), 1.28-0.99 ppm (b, 2H CH$_2$C**H**$_2$CH$_2$ + 32H CH$_3$(C**H**$_2$)$_{16}$CH$_2$), 0.7-0.6 ppm (b, 3H, C**H**$_3$(CH$_2$)$_{16}$CH$_2$). IR: 2010 cm^{-1}, 1910 cm^{-1}, 1600 cm^{-1}.

4.2.5 Measurement of critical amount of hexane for the aggregation of amphiphiles

A solution with 0.1 mg/mL PFpP-PPh$_2$Cn (n = 6, 10 and 18) in THF was prepared. The solution was then filtered through a PTFE membrane with a pore size of 0.22 μm. Afterwards, various amounts of hexane were slowly added (1 drop/s) to the above THF solution under stirring. The counting rate of the resulting solution was measured at 25 $^\circ$C by DLS. The counting rate was then plotted against the volume of added hexane to determine the critical amount of hexane for the aggregation of amphiphiles.

4.2 Results and Discussion

4.2.1 Synthesis of alkyl diphenylphosphine

$$\text{NaPPh}_2 \ + \ \text{Br}-\text{CH}_2\!\!\left(\!\text{CH}_2\!\right)_{\!n}\!\text{CH}_3 \ \xrightarrow{\text{THF, RT}} \ \text{PPh}_2-\text{CH}_2\!\!\left(\!\text{CH}_2\!\right)_{\!n}\!\text{CH}_2 + \ \text{NaBr}$$

$$(n = 4, 8, 16)$$

Scheme 4.1 Synthesis of alkyldiphenylphosphines (n = 4, 8, 16).

The alkyldiphenylphosphines (Ph$_2$PCn, n = 6, 10, 18) were prepared through a salt-elimination reaction of sodium diphenylphophine with alkyl bromide (Scheme 4.1). Figure 4.1 illustrates the ^{31}P NMR and ^{1}H NMR spectra for Ph$_2$PC6 in CDCl$_3$. A single peak at -14 ppm is observed in the ^{31}P NMR spectrum (Figure 4.1a), indicating the presence of phosphine. In the ^{1}H NMR spectrum, the chemical shift due to the phenyl groups appears at 7.5-7.4 ppm; the peak at 2.1 ppm (c in Figure 4.1b) is assigned to the CH$_2$ α to phosphorus. The chemical shifts at 1.5-1.3 ppm (b in Figure 4.1b) and 0.9 ppm (a in Figure 4.1b) are attributed to the four CH$_2$ and the methyl group in the hexyl group, respectively. The integration ratio of *Ph* : Ph$_2$P*CH$_2$* : *(CH$_2$)$_4$* : *CH$_3$* is 10 : 2 : 8 : 3, which is in agreement with the theoretical values.

Therefore, the ^{31}P NMR and ^{1}H NMR results suggest that Ph$_2$PC6 was successfully synthesized. Ph$_2$PCn (n = 10, 18) were also prepared and characterized in the same manner (Figure S4.1, S4.2).
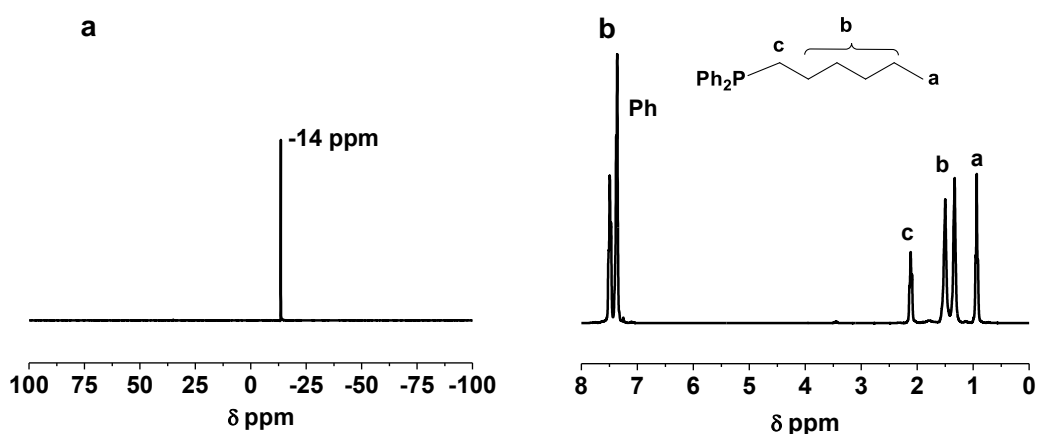
Figure 4.1 (a) ^{31}P and (b) ^{1}H NMR spectra for Ph$_2$PC6 in CDCl$_3$.

4.2.2 End group functionalization of PFpP
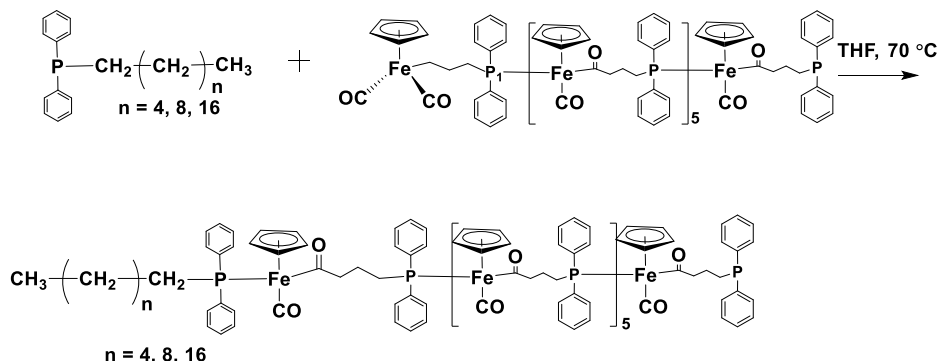
Scheme 4.2 Preparation of alkyldiphenylphosphine functionalized PFpP amphiphiles.

The Fp end group migration insertion reaction (MIR) was performed *via* refluxing a THF solution of PFpP and PPh$_2$Cn at 70 °C (Scheme 4.2).[11] The molar ratio between PFpP and Ph$_2$PC$_6$ was 1 : 1.5. The reaction was monitored using ^{31}P NMR spectroscopy. As discussed in our previous work,[11] the chemical shift due to the coordinated phosphorus in the repeating unit containing an unreacted Fp end group was at 72.5 ppm, which shifted 1.0 ppm upfield as

compared to the rest of the coordinated phosphorus in the polymer backbone (73.5 ppm). During the reaction, we found that the intensity for the peak at 72.5 ppm gradually dropped, suggesting that the Fp end groups in PFpPs have coupled with Ph$_2$PC6 *via* end group MIR.[11] After 31 h the signal at 72.5 ppm disappeared, suggesting that the reaction was completed. The completion of the reaction was also verified *via* ^{1}H NMR analysis of the final product, in which the chemical shift due to Cp ring in Fp end group shifted from 4.7 ppm to 4.3 ppm as a result of MIR.[13]

However, when Ph$_2$PC10 and Ph$_2$PC18 were used for the reactions, we observed that the chemical shift at 72.5 ppm remained even though the reaction solutions had been heated to 70 ^{o}C for 48 and 72 h, respectively. This result suggests that MIR of Fp end group in the presence of Ph$_2$PCn with longer alkyl chains has slower reaction rates, probably due to steric effects.[14-16] In order to promote the reaction, we changed the molar ratio of PFpP and Ph$_2$PCn from 1 : 1.5 to 1 : 3. Under this condition, we observed that the chemical shift at 72.5 ppm vanished after the solution containing Ph$_2$PC10 was heated for 54 h (Figure 4.2a); while the reaction of PPh$_2$C18 with PFpP took a longer time and was completed after 72 h (Figure 4.2a). The completion of the reactions was confirmed *via* ^{1}H NMR characterization of the final products. As shown in Figure 4.2b, the chemical shift for the Cp ring in Fp end group of starting PFpP appears at 4.7 ppm (DMSO-d_6). After MIR, this peak upfiled shifts to 4.3 ppm, indicating that all Fp end groups are coordinated with Ph$_2$PC10 *via* MIR.[13] In the case of PFpP-Ph$_2$PC18, because the product has poor solubility in DMSO, ^{1}H NMR spectroscopy was performed in CDCl$_3$. As shown in Figure 4.2c, the chemical shift representing Fp end group (4.5 ppm) disappeared upon MIR, implying that all Fp end groups coupled with PPh$_2$C18.[13]
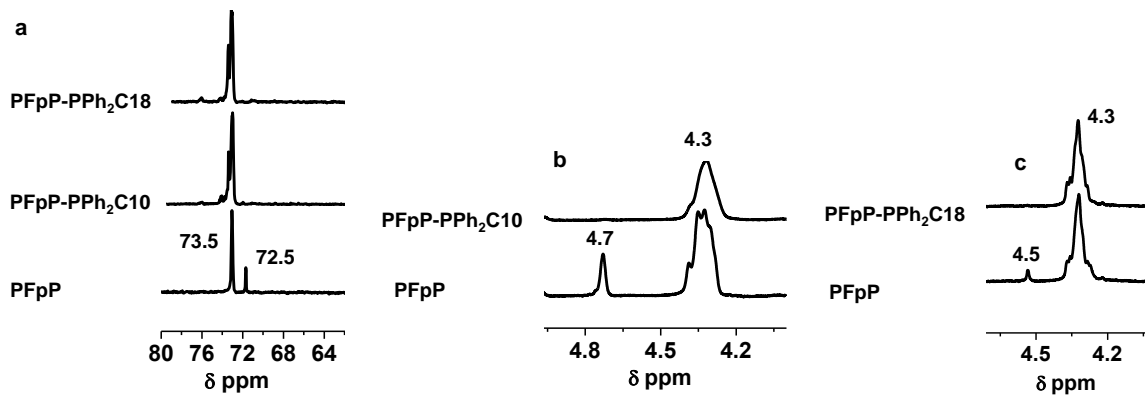
Figure 4.2 (a) ^{31}P NMR spectra for PFpP in DMSO-d_6 (bottom), PFpP/Ph$_2$PC10 (middle) and PFpP/PPh$_2$C18 (top) reaction mixture in THF. The solutions were heated for 54 h and 72 h, respectively; (b) ^{1}H NMR spectra for PFpP (bottom) and purified PFpP-PPh$_2$C10 (top) in DMSO-d_6; (c) ^{1}H NMR spectra for PFpP (bottom) and purified PFpP-PPh$_2$C18 (top) in CDCl$_3$.

In order to purify the final product, the solution was concentrated under vacuum and subsequently precipitated in an excess amount of hexane, yielding a yellow powder. For the PPh$_2$C$_6$ and PPh$_2$C$_{10}$ systems, the supernatants were colorless, suggesting that all end group functionalized products were precipitated. For the reaction system containing PPh$_2$C$_{18}$, the supernatant was yellow and turbid, implying that a part of the end group-functionalized product formed micelles in the THF/hexane solution. The ^{31}P NMR spectrum of the precipitates indicated that there were some PPh$_2$C18 mixed with PFpP-PPh$_2$C18, so we washed the precipitate with 2.0 mL methanol three times in order to remove the remaining PPh$_2$C18. The resulting product was characterized using ^{31}P NMR, ^{1}H NMR and IR spectroscopies. The NMR results are illustrated in Figure 4.3. The ^{31}P NMR spectrum shows two peaks at 73.5 ppm (P$_1$ in Figure 4.3a) and at 32.5 ppm (P$_2$ in Figure 4.3a), which can be assigned to the coordinated phosphorus and the oxidized phosphine end group, respectively.[17, 18] The ^{1}H NMR spectrum of

the molecules (Figure 4.3b) shows that the signal at 4.5 ppm, due to the Cp ring for the Fp end group, upfield shifted as a result of MIR and merged with the rest of Cp rings in the main chain (4.3 ppm). The chemical shifts for the alkyl group from PPh_2C18 appear upfield and partially overlap with those for the propyl spacers from the repeat units of PFpP oligomers. To be specific, the chemical shift for the CH_2 spacer (e in Figure 4.3b) in the PPh_2C18 alkyl chain is merged with the middle CH_2 of the propyl spacer in PFpP, which is at 0.99-1.28 ppm (b+e in Figure 4.3b). The signals due to the CH_2 α to phosphorus (c + d in Figure 4.3b) and α to the acyl groups (a in Figure 4.3b) appear at 1.8-2.5 ppm; while the chemical shift for the methyl group in the alkyl chain of PPh_2C18 (f in Figure 4.3b) appears independently at 0.88 ppm. The integration ratio for the peaks at 0.99-1.28 ppm, 1.8-2.5 ppm, and 0.88 ppm with that for Cp ring at 4.3 ppm is 1.2, 0.8 and 0.08, which is close to theoretical value of 1.3, 0.86 and 0.086. $PFpP-PPh_2C6$ and $PFpP-PPh_2C10$ amphiphiles were prepared and characterized in the same manner. Their ^{31}P and ^{1}H NMR spectra are illustrated in Figures S4.3, S4.4.
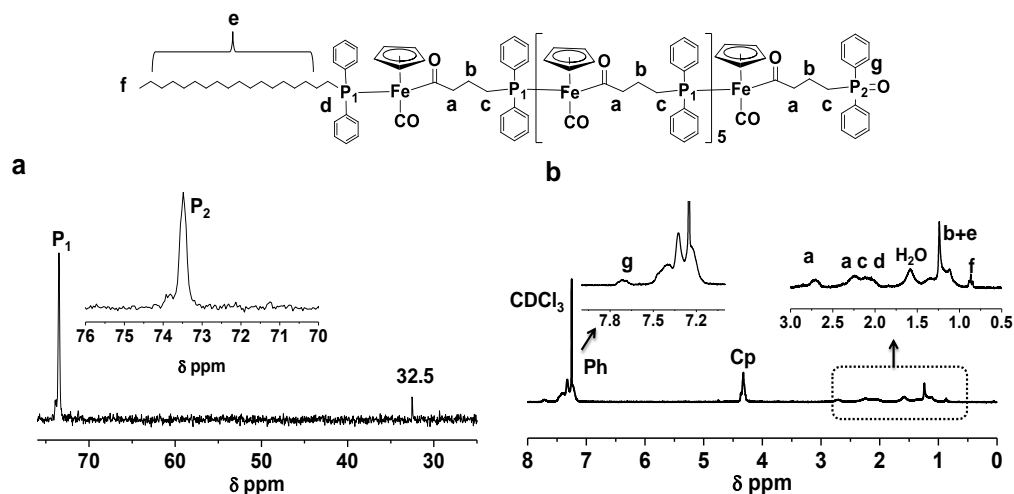
Figure 4.3 (a) ^{31}P NMR and (b) ^{1}H NMR spectra for Ph_2PC18 functionalized PFpP amphiphiles in $CDCl_3$.

^{13}C NMR spectroscopy was also used to demonstrate that the amphiphiles were prepared. The spectrum of PFpP-PPh$_2$C6 is shown in Figure 4.4. The chemical shift for the acyl group appears at 274 ppm, and the signal due to the terminal CO is at 220 ppm.[19] The resonance signals at 132-127 ppm and 86-84 ppm are attributed to the carbons from the phenyl group and the Cp ring, respectively.[19] The resonances for the alkyl spacer in PFpP appears at 20, 29 and 66 ppm, as indicated in the spectrum.[18] The rest of the upfield signals can be attributed to the alkyl segments of the amphiphilies. To be specific, the peaks at 13.7 ppm, 21.7 ppm and 30.5 ppm are due to the methyl group, the four carbons in the middle of alkyl part and the carbon α to phosphorus, respectively.[19]
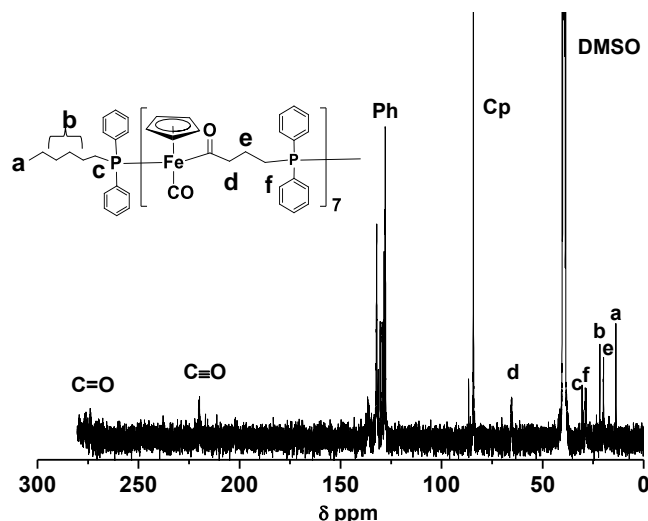
Figure 4.4 ^{13}C NMR spectrum for PFpP-PPh$_2$C6 in DMSO-d_6.

The amphiphiles were further characterized using FT-IR spectroscopy to verify the occurrence of end group MIR. As shown in Figure 4.5a, the peaks at 1910 cm^{-1} and 1600 cm^{-1} represent the terminal and the acyl CO groups in the main chain of PFpP, respectively. The two terminal CO groups in the Fp end group of PFpP stretch symmetrically and anti-symmetrically, resulting in two additional absorption frequencies at 2000 cm^{-1} and 1939 cm^{-1}.[20] After the Fp

end group was coupled with PPh_2Cn (n = 6, 10, 18) *via* MIR, these two peaks due to Fp end groups disappeared, because the resulting terminal and acyl CO have the same absorption frequency as the other CO groups in PFpP appearing at 1910 and 1600 cm^{-1}. However, we still see a weak peak at 2010 cm^{-1} for all the PFpP amphiphiles prepared (Figure 4.5a). It is therefore questionable whether or not all the Fp end groups reacted. In order to clarify this, we performed IR analysis of $[\eta^5$-$C_5H_5]Fe(CO)(PPh_3)[(C(O)(CH_2)_5CH_3]$ (FpC6), which has a coordination structure similar to the junction unit of the prepared PFpP amphiphiles.[21] The FT-IR spectrum for FpC6 crystal is illustrated in Figure 4.5 (b). As shown in Figure 4.5 (b), in addition to the two absorptions corresponding to terminal and acyl CO at 1909 cm^{-1} and 1614 cm^{-1}, a weak absorption at a higher wavenumber is also clearly observed. Therefore, we may conclude that the peak at 2010 cm^{-1} is not associated with unreacted Fp group, although we are not able to precisely assign this absorption band.
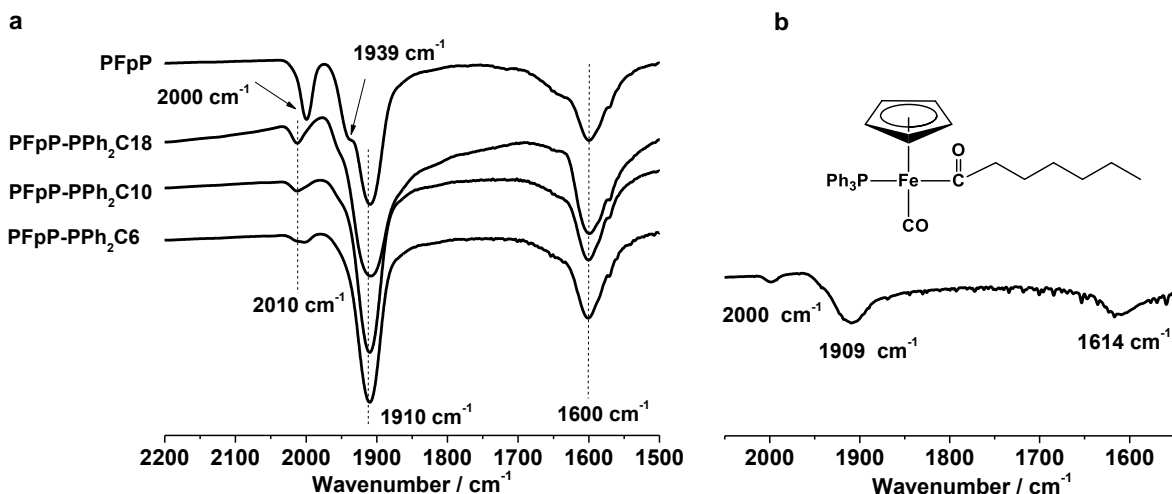
Figure 4.5 FT-IR partial spectra for (a) PFpP oligomer with DP_n = 7, PFpP-PPh$_2$C18, PFpP-PPh$_2$C10 and PFpP-PPh$_2$C6; (b) $[\eta^5$-C$_5$H$_5]$Fe(CO)(PPh$_3$)[(C(O)(CH$_2$)$_5$CH$_3$] crystals.

4.2.3 Amphiphilic nature of PFpP-PPh$_2$Cn

The amphiphilic nature of the prepared molecules was tested by adding hexane to THF

solutions of PFpP-PPh$_2$Cn. As shown in Figure 4.6, when 0.6 mL, 1.0 mL and 2.0 mL hexane

was added to 0.1 mg/mL (1.0 mL) PFpP-PPh$_2$C6, PFpP-PPh$_2$C10 and PFpP-PPh$_2$C18,

respectively, the intensity of the scattered light abruptly increased, indicating the formation of

aggregates. Critical hexane content (CHC) to induce the aggregation of PFpP-PPh$_2$Cn with n = 6,

10, 18 was 37.5, 50.0 and 66.7 % by volume, respectively.
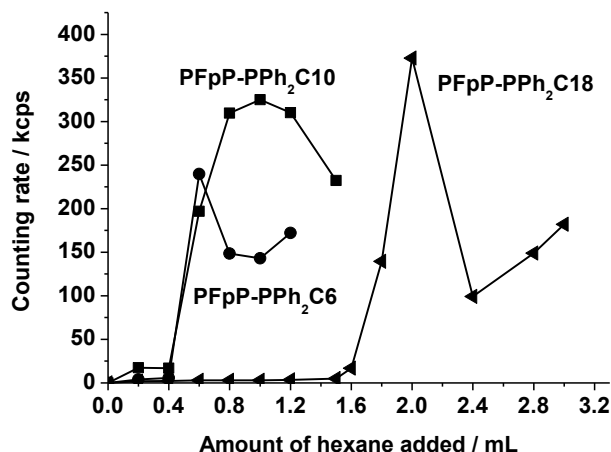
Figure 4.6 Plot of counting rate as a function of the amount of added hexane to 1.0 mL 0.1

mg/mL THF solution.

DLS measurements for the aggregates formed at the critical amount of hexane were

performed. As shown in Figure 4.7, nanoparticles with D$_h$ ranging from 199 nm to 260 nm were

obtained. However, all the aggregates show a high PDI. Beyond the CHC, the polydispersity of

the aggregates became high and a precipitate was observed for all the samples after the solutions

were left for three days. Further work using longer alkyl chains to stabilize the colloids in the

self-assembly studies will be performed.

93
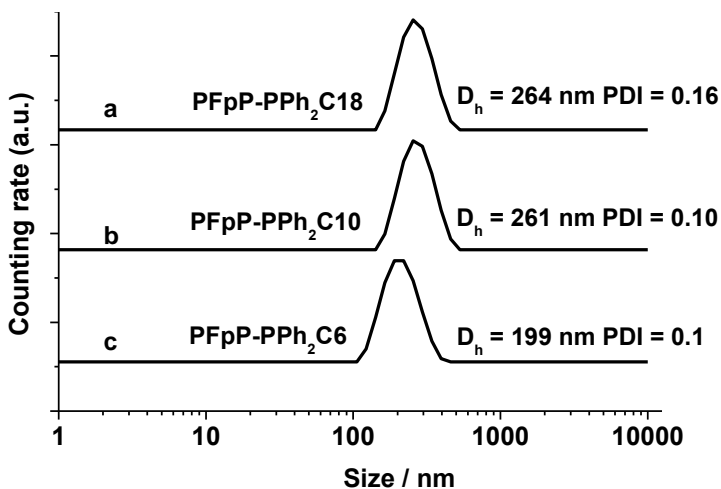
Figure 4.7 DLS results of (a) PFpP-PPh$_2$C6 in 0.6 mL hexane / 1.0 mL THF; (b) PFpP-PPh$_2$C6 in 1.0 mL hexane / 1.0 mL THF and (c) PFpP-PPh$_2$C18 in 2.0 mL hexane / 1.0 mL THF.

4.3 Conclusions

A series of PFpP amphiphiles, PFpP-PPh$_2$Cn (n = 6, 10, 18), were synthesized *via* migration insertion reaction (MIR) of the Fp end groups in PFpP oligomers in the presence of PPh$_2$Cn (n = 6, 10, 18). The resulting amphiphiles were characterized using ^{1}H NMR, ^{31}P NMR, ^{13}C NMR and FT-IR spectroscopies. This work opens up a new synthetic route for the synthesis of metal-carbonyl amphiphiles. The self-assembly behavior of the amphiphiles will be studied in further work, which may have promising applications in colloids for CO delivery,[8] the preparation of magnetic nanoparticles,[9] cell imaging [22] and in bioassay.[23]

Chapter 5. Synthesis of [η^5-Ph$_2$P(CH$_2$)$_3$C$_5$H$_4$]Fe(CO)$_2$[(CH$_2$)$_5$CH$_3$] for Migration Insertion Polymerization (MIP)

5.1 Introduction

As described in Chapter 2 and Chapter 3, CpFe(CO)$_2$(CH$_2$)$_3$PPh$_2$ (FpP) containing Fp and a tethered phosphine group was used as a bifunctional monomer for MIP.[1, 2-5] As a result, a new type of main-chain iron carbonyl macromolecule, PFpP, was generated. Although the resulting polymers are air-stable and soluble in common organic solvents,[1, 5] the synthesis of high molecular weight polymers *via* MIP remains challenging. We have discovered that the phosphine end groups in PFpP oligomers with DP$_n$ = 7 did not react with CpFe(CO)$_2$CH$_3$ (FpMe), suggesting that the reactivity of the phosphine end group is low.[4] This low reactivity could account for the production of low molecular weight macromolecules.[4] Therefore, the design and synthesis of new monomers for MIP is necessary to address this challenge and to investigate MIP. It is well known that the Cp ligands in metal carbonyl derivatives can rotate and reorient.[6, 7] If the phosphine group is tethered on the Cp ring, the rotation and reorientation of the Cp ligand may help increase the flexibility of the polymer chain during metal coordination propagation. Therefore, it is tempting to establish a synthetic approach to prepare a new monomer for MIP, [η^5-Ph$_2$P(CH$_2$)$_3$C$_5$H$_4$]Fe(CO)$_2$(CH$_2$)$_5$CH$_3$ (FpP^{Cp}) with a phosphine group tethered on the Cp ring.

5.2 Experimental

5.2.1 Materials and Instrumentation

All experiments were performed under dry nitrogen atmosphere using standard Schlenk techniques unless otherwise indicated. THF was freshly distilled under nitrogen from Na/benzophenone. Hexane used for precipitation was cooled at -58 $^{\circ}$C before use. 1-Bromohexane, iodomethane, 1-chloro-3-iodopropane, 1,3-diiodopropane, n-BuLi, s-BuLi, $BH_3 \cdot THF$ solution and triphenylphosphine were purchased from Sigma-Aldrich and used as received unless otherwise indicated. $(\eta^5\text{-}C_5H_5)Fe(CO)_2(CH_2)_5CH_3$ (FpC6), $Cl(CH_2)_3PPh_2$ and $NaPPh_2$ were synthesized according to literature.[1, 8]

5.2.2 Nuclear magnetic resonance (NMR) spectroscopy

^1H, ^{31}P and ^{13}C one-dimensional NMR and heteronuclear multiple quantum coherence (HMQC), correlation spectroscopy (COSY) and heteronuclear multiple bond correlation (HMBC) two-dimensional NMR spectroscopies were performed on a Bruker Avance 300 (^1H: 300 MHz, ^{31}P: 120 MHz, ^{13}C: 75 MHz) spectrometer at ambient temperature using appropriate solvents. NMR samples were prepared under an atmosphere of dry nitrogen unless otherwise indicated.

5.2.3 FT-IR

Fourier transform infrared (FT-IR) spectra for FpP^{Cp} and oligo-PFpP^{Cp} solid samples were recorded on a Bruker Tensor 27 spectrophotometer with a resolution of 1 cm^{-1}. Test pellets were prepared by grinding and compressing FpP^{Cp} or oligo-PFpP^{Cp} (2 wt%) in KBr.

5.2.4 Gel permeation chromatography (GPC)

Molecular weights and molecular weight distributions, M_w/M_n, were characterized using GPC analysis at room temperature with THF as eluent at a flow rate of 1.00 mL/min. The Viscotek GPC max unit used was equipped with a VE 2001 GPC, three PolyAnalytik organic mixed bed columns, PAS-103-L, PAS-104-L, and PAS-105-L with dimensions of 8 mm (i.d.)$\times$300 mm (L) each, and a Viscotek triple detector array including refractive index, viscosity and dual-angle light scattering detectors. Polystyrene standards were used as references.

5.2.5 Single crystal X-ray diffraction

Single crystals suitable for X-ray diffraction analysis were mounted onto the tips of glass fibers with thick oil and transferred immediately into a cold nitrogen gas stream in the diffractometer cryostat. X-ray data were collected using Mo Kα radiation at 200 K on a Bruker Kappa APEX II System (Madison, WI, USA).

5.2.6 Mass spectroscopy

Positive ion electrospray was performed with a Thermo Scientific LTQ mass spectrometer. FpP^{Cp} was dissolved in dry MeCN and the solution was infused at 10 µL/min. Spray voltage was 3 kV. The capillary temperature was 275 ^{o}C. Tandem mass spectrometry (MS/MS) was performed for the identification of the ion with m/z of 490. He was used as the collision gas. The normalized collision energy was 25 %.

5.2.7 Metalation and functionalization of the Cp ring in FpC6

FpC6 (0.5 g, 1.91 mmol) was dissolved in 40.0 mL THF and the solution was cooled to -78 ^{o}C using a bath of dry ice and acetone. Then an approximate amount of BuLi (the type and amount of BuLi are indicated in Table 5.1) was added drop-wise to the solution at -78 ^{o}C. After the solution was left to stir for 30 min at -78 ^{o}C, an excess amount of alkyl halide (MeI, Br(CH$_2$)$_5$CH$_3$ or Cl(CH$_2$)$_3$PPh$_2$) in 10.0 mL THF was added drop-wise to the reaction flask at -78 ^{o}C. Afterwards, the cold bath was removed and the solution was allowed to warm to room temperature. The solution was subsequently stirred for 2 h at room temperature. After the reaction, THF was removed under vacuum and degassed n-hexane was added to dissolve the crude product. The hexane solution was passed through a plug of Celite to remove salts. Hexane was then removed under vacuum, yielding a red viscous oil. The crude product was further purified using silica gel chromatography. Hexane was used as eluent to collect the hexane soluble product. Metalation and functionalization of the Cp ring were evaluated using ^{1}H NMR analysis of the final product.

5.2.8 Synthesis of [η^5-(CH$_3$)C$_5$H$_4$]Fe(CO)(PPh$_3$)[C(O)(CH$_2$)$_5$CH$_3$]

To a THF solution (80.0 mL) of [η^5-(CH$_3$)C$_5$H$_4$]Fe(CO)$_2$(CH$_2$)$_5$CH$_3$ (0.5 g, 1.8 mmol), one equivalent of PPh$_3$ was added and the solution was refluxed at 70 ^{o}C for 3 days. Afterwards, the solvent was removed under vacuum and the crude product was purified using silica gel chromatography. Hexane was used as eluent to remove the unreacted [η^5-(CH$_3$)C$_5$H$_4$]Fe(CO)$_2$(CH$_2$)$_5$CH$_3$. Hexane : DCM (3 : 1, v/v) were subsequently used to remove oxidized triphenylphosphine. Finally, the column was flushed with DCM to collect [η^5-

$(CH_3)C_5H_4]Fe(CO)(PPh_3)[C(O)(CH_2)_5CH_3]$. DCM was then removed under vacuum at room temperature, yielding an orange oil. NMR analysis suggested that the targeted $[\eta^5-(CH_3)C_5H_4]Fe(CO)(PPh_3)[C(O)(CH_2)_5CH_3]$ was prepared, but contaminated with a side product, $[\eta^5-C_5H_5]Fe(CO)(PPh_3)[C(O)(CH_2)_5CH_3]$. The generation of the side product was due to the impurity of the starting material, $[\eta^5-(CH_3)C_5H_4]Fe(CO)_2(CH_2)_5CH_3$, which was contaminated with $[\eta^5-C_5H_5]Fe(CO)_2(CH_2)_5CH_3$.

5.2.9 Synthesis of $I(CH_2)_3PPh_2 \cdot BH_3$

$I(CH_2)_3I$ (6.3 g, 21.3 mmol) was dissolved in 40.0 mL THF and the solution was cooled to -78 ^{o}C using a bath of dry ice and acetone. $NaPPh_2$ in THF (26.0 mL, 0.5 mol/L) was added drop-wise to the above solution at -78 ^{o}C. Afterwards, the cold bath was removed and the solution was allowed to gradually warm to room temperature. After the solution was stirred overnight under N_2, one equivalent of BH_3 in THF solution was added at 0 ^{o}C. After the solution was stirred for 2 h at room temperature, 60.0 mL of water was added to the THF solution. DCM was then used to extract $I(CH_2)_3PPh_2 \cdot BH_3$. This extraction was performed three times. All DCM phases were combined and the solvents were removed under vacuum, yielding a white powder. The resulting white powder was found to be partially soluble in hexane. The hexane insoluble fraction was collected *via* filtration and subsequently dried under vacuum. NMR analysis indicated that the hexane soluble material was not the targeted $I(CH_2)_3PPh_2 \cdot BH_3$, because the resonance signal due to the phenyl group was very weak. The hexane insoluble material was further purified using silica gel chromatography. DCM was used as eluent to remove the oxidized $I(CH_2)_3PPh_2$. The NMR analysis suggested that $I(CH_2)_3PPh_2 \cdot BH_3$ was produced, but it

was not pure.

5.2.10 Synthesis of [η^5-Cl(CH$_2$)$_3$C$_5$H$_4$]Fe(CO)$_2$(CH$_2$)$_5$CH$_3$

FpC6 (0.5 g, 1.9 mmol) was dissolved in 40.0 mL THF, then the solution was cooled to -78 ^{o}C using a bath of dry ice and acetone. s-BuLi (1.2 equivalents) was then added drop-wise at -78 ^{o}C. The resulting solution was stirred at -78 ^{o}C for 30 min. Afterwards, 1-chloro-3-iodopropane (1.5 equivalents relatively to FpC6) was added drop-wise at -78 ^{o}C. At the end of the addition, the cold bath was removed. The reaction mixture was allowed to warm to room temperature and stirred for 1.5 h. Afterwards, the THF was removed under vacuum, yielding a brown oil. The crude product was dissolved in a small amount of hexane and passed through a plug of Celite to remove LiI. The resulting solution was concentrated and passed through a silica gel column using hexane as eluent. The unreacted 1-chloro-3-iodopropane was eluted first and a yellow band was then collected. The solvent was finally removed under vacuum, yielding a yellow oil. ^{1}H NMR (CDCl$_3$): 7.4-7.3 ppm (10H, C$_6$$H$$_5$), 4.6 ppm (2H, C$_5$$H$$_4$), 4.5 ppm (2H, C$_5$$H$$_4$), 3.6 ppm (2H, C$H$$_2$Cl), 2.40 ppm (2H, C$H$$_2C_5H_4$), 1.9 ppm (2H, C$_5H_4CH_2CH$$_2CH_2$), 1.56-1.2 ppm (d, 10H, Fe(C$H$$_2$)$_5$), 0.87 ppm (s, 3H, Fe(CH$_2$)$_5$C$H$$_3$).

5.2.11 Synthesis of [η^5-Ph$_2$P(CH$_2$)$_3$C$_5$H$_4$]Fe(CO)$_2$[(CH$_2$)$_5$CH$_3$]

To a THF (20.0 mL) solution of [η^5-Cl(CH$_2$)$_3$C$_5$H$_4$]Fe(CO)$_2$(CH$_2$)$_5$CH$_3$ (634.0 mg, 1.46 mmol), a THF solution of NaPPh$_2$ (6.0 mL, 0.5 mol/L) was added drop-wise at 0 ^{o}C. After addition, the ice bath was removed and the solution was allowed to warm to room temperature. After it was stirred for 2 h, 2.0 mL degassed methanol was added drop-wise to react with the excess of NaPPh$_2$. The resulting solution was first passed through a Celite column, followed by

a silica gel column using hexane/DCM (3 : 1, v/v) as eluent to collect the yellow band. The solvent was subsequently removed under vacuum, yielding a yellow oil (300.0 mg, 47 %). ^{31}P NMR (CDCl$_3$): -15 ppm. ^{1}H NMR (CDCl$_3$): 7.5-7.0 ppm (b, 10H, C$_6$$\textbf{\textit{H}}$$_5$), 4.6 ppm (s, 2H, C$_5$$\textbf{\textit{H}}$$_4$), 4.5 ppm (s, 2H, C$_5$$\textbf{\textit{H}}$$_4$), 2.3 ppm (t, 2H, C$\textbf{\textit{H}}$$_2PPh_2$), 2.0 ppm (t, 2H, C$\textbf{\textit{H}}$$_2C_5H_4$), 1.6 ppm (t, 2H, CH$_2C\textbf{\textit{H}}$$_2CH_2PPh_2$), 1.56-1.0 ppm (d, 10H, Fe(C$\textbf{\textit{H}}$$_2$)$_5$), 0.87 ppm (s, 3H, Fe(CH$_2$)$_5$C$\textbf{\textit{H}}$$_3$).

5.2.12 Bulk polymerization of [η^5-Ph$_2$P(CH$_2$)$_3$C$_5$H$_4$]Fe(CO)$_2$[(CH$_2$)$_5$CH$_3$] at 105 ^{o}C

Polymerization of [η^5-Ph$_2$P(CH$_2$)$_3$C$_5$H$_4$]Fe(CO)$_2$[(CH$_2$)$_5$CH$_3$] (500.0 mg, 1.02 mmol) was carried out in bulk at 105 ^{o}C for 20 h. After the polymerization, the crude product was dissolved in a minimum amount of THF (ca. 5.0 mL) and then precipitated in hexane (200.0 mL) which had been cooled to -58 ^{o}C. This precipitation procedure was repeated three times. The precipitate was collected *via* filtration and dried under vacuum overnight at room temperature, yielding a yellow powder (250 mg, 50 %). FT-IR: 1997 cm^{-1}, 1906 cm^{-1} (terminal CO group); 1601 cm^{-1} (migrated CO group). ^{31}P NMR (C$_6$D$_6$): 73 ppm. ^{1}H NMR (C$_6$D$_6$): 7.8-7.0 ppm (b, 10H, C$_6$$\textbf{\textit{H}}$$_6$), 4.2-3.8 ppm (m, 4H, C$_5$$\textbf{\textit{H}}$$_4$), 3.0 ppm (s, 1H, C$\textbf{\textit{H}}$$_2$(CO)), 2.9 ppm (s, 1H, C$\textbf{\textit{H}}$$_2$(CO)), 2.6-2.3 ppm (b, 2H, C$\textbf{\textit{H}}$$_2$Ph), 2.3-2.1 ppm (s, 2H, CpCH$_2$C$\textbf{\textit{H}}$$_2CH_2$), 1.8-1.5 ppm (b, 2H, CpC$\textbf{\textit{H}}$$_2CH_2CH_2$), 1.5-1.2 ppm (s, 8H, CH$_2$(CO)(C$\textbf{\textit{H}}$$_2$)$_4$), 1.0-0.9 ppm (s, 3H, C$\textbf{\textit{H}}$$_3$). ^{13}C NMR (C$_6D_6$): 273 ppm ($\textbf{\textit{C}}$=O), 220 ppm ($\textbf{\textit{C}}$≡O), 82 ppm (s, $\textbf{\textit{C}}$$_5H_4$), 84 ppm (s, $\textbf{\textit{C}}$$_5H_4$), 87 (s, $\textbf{\textit{C}}$$_5H_4$), 102 ppm (s, $\textbf{\textit{C}}$$_5H_4$), 67 ppm (s, (CO)$\textbf{\textit{C}}H_2$), 32.4 ppm (s, CH$_2$($\textbf{\textit{C}}H_2$)$_4CH_3$), 29.7 ppm (b, CH$_2$$\textbf{\textit{C}}H_2CH_2Ph, CH_2CH_2$$\textbf{\textit{C}}H_2Ph, CH_2$($\textbf{\textit{C}}H_2$)$_4CH_3$), 26.5 ppm (s, CH$_2$($\textbf{\textit{C}}H_2$)$_4CH_3$), 26.1 ppm (s, $\textbf{\textit{C}}$H$_2$CH$_2$CH$_2$Ph), 23.1 ppm (s, CH$_2$($\textbf{\textit{C}}$H$_2$)$_4$CH$_3$), 14.4 ppm (s, CH$_2$(CH$_2$)$_4$$\textbf{\textit{C}}H_3$).

5.3 Results and Discussion

In order to prepare $[\eta^5\text{-}Ph_2P(CH_2)_3C_5H_4]Fe(CO)_2[(CH_2)_5CH_3]$ (FpP^{Cp}), $[\eta^5\text{-}C_5H_5]Fe(CO)_2(CH_2)_5CH_3$ (FpC6) was first metalated using BuLi, generating the FpC6 anion (Scheme 5.1).
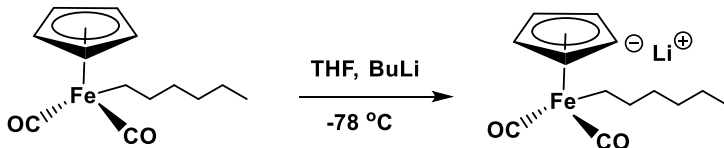
Scheme 5.1 Metalation of FpC6 using BuLi.

Two routes were investigated to prepare FpP^{Cp} (Scheme 5.2). In route 1, $Ph_2P(CH_2)_3X$ (X represents a halogen) was first prepared, and reacted with the FpC6 anion; In route 2, the FpC6 anion was first reacted with $X(CH_2)_3X$ (X represents a halogen) to produce $[\eta^5\text{-}X(CH_2)_3C_5H_4]Fe(CO)_2(CH_2)_5CH_3$. Diphenylphosphine was then introduced on the Cp ring *via* the reaction of $[\eta^5\text{-}X(CH_2)_3C_5H_4]Fe(CO)_2(CH_2)_5CH_3$ with NaPPh$_2$.
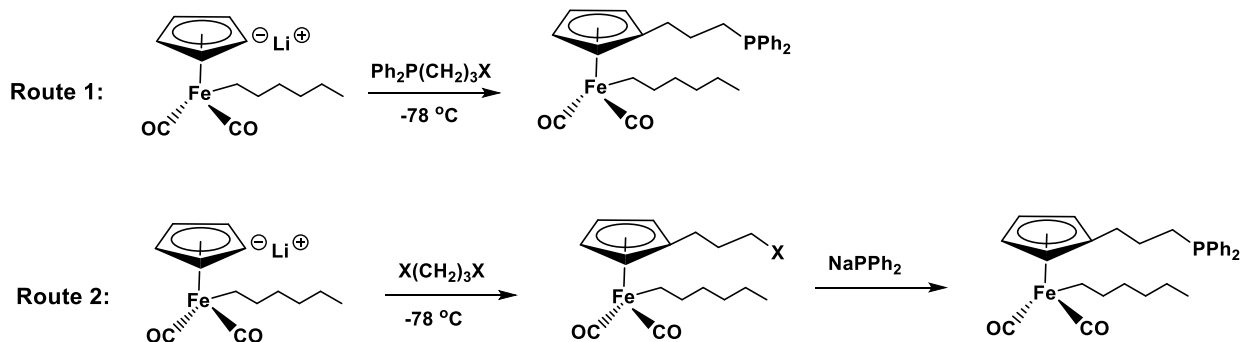
Scheme 5.2 Synthesis of $[\eta^5\text{-}Ph_2P(CH_2)_3C_5H_4]Fe(CO)_2(CH_2)_5CH_3$.

5.3.1 Conditions for the metalation reaction of the Cp ring in FpC6

Although metalation of the Cp ring in $[\eta^5\text{-}C_5H_4]Fe(CO)_2Ph^9$ (FpPh) and $[\eta^5\text{-}C_5H_4]Fe(CO)_2Me^{10}$ (FpMe) has been reported, the metalation of the Cp ring in FpC6 has not

yet been attempted. Also, it was reported that the metalation of the Cp ligands in metal carbonyl complexes can be affected by many parameters such as the temperature and the type of butyllithium used.[11] Therefore, we first explored this reaction using either n-BuLi or s-BuLi. The resulting anions were subsequently reacted with alkyl halide (Cl(CH$_2$)$_3$PPh$_2$, Br(CH$_2$)$_5$CH$_3$, MeI). The corresponding reaction scheme is illustrated in Scheme 5.3.
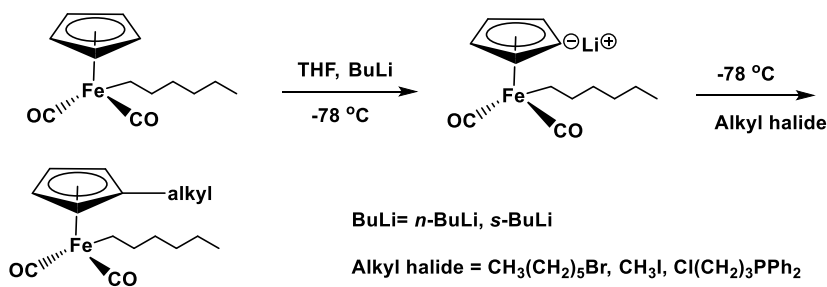
Scheme 5.3 Metalation and functionalization of the Cp ring in FpC6.

The experimental results are summarized in Table 5.1. When FpC6 was first treated with one equivalent of n-BuLi, followed by the addition of MeI, ^{1}H NMR analysis of the final product indicated that FpC6 had not reacted (Entry 1 in Table 5.1). It has been reported that three equivalents of n-BuLi were required to metalate FpPh, and that the metalated FpPh can react with EtBr or MeI, resulting in methyl or ethyl group functionalized Cp rings.[9] Therefore, we treated FpC6 with three equivalents of n-BuLi before the addition of MeI. The ^{1}H NMR analysis of the final product revealed that only 27 mole% of the starting FpC6 reacted (Entry 2 in Table 5.1). The above experiments suggest that even though n-BuLi could deprotonate the Cp ring in FpC6, the conversion is low. Therefore, more reactive s-BuLi was selected for the metalation reaction and Br(CH$_2$)$_5$CH$_3$ was used for Cp functionalization. The ^{1}H NMR results implied that FpC6 was not functionalized when one equivalent of s-BuLi was used (Entry 3 in Table 5.1). In contrast, when MeI was used, ^{1}H NMR analysis revealed that 96.3 mole% of FpC6 reacted and a

methyl group was introduced on the Cp ring (Entry 4 in Table 5.1). However, there was still a small amount of unreacted FpC6, and it could not be fully reacted even after the additions of three equivalents of s-BuLi to the system. Attempts to separate the unreacted FpC6 from $[\eta^5\text{-CH}_3\text{C}_5\text{H}_4]\text{Fe(CO)}_2(\text{CH}_2)_5\text{CH}_3$ *via* silica gel chromatography did not succeed. Nevertheless, this set of experiments indicates that the metalation of the Cp ring can be achieved using *s*-BuLi, and that iodide compounds can be used for a subsequent Cp functionalization.

Table 5.1 Metalation and functionalization of the Cp ligand in FpC6[a]

Entry	Type and amount of BuLi	Type of halide	Reaction results[b]
1	1 equivalent of *n*-BuLi	MeI	No reaction
2	3 equivalents of *n*-BuLi	MeI	27 mole % FpC6 reacted
3	1 equivalent of *s*-BuLi	$Br(CH_2)_5CH_3$	No reaction
4	1 equivalent of *s*-BuLi	MeI	96.3 mole % FpC6 reacted
5	3 equivalents of *n*-BuLi	$Cl(CH_2)_3PPh_2$	5-membered ring generated

[a] Metalation performed at -78 $^{\circ}$C for 0.5 h. Alkyhalides added at -78 $^{\circ}$C and the solution then warmed to room temperature. Reaction solution left for 2 h longer at room temperature under stirring. [b] ^{1}H NMR spectrum used to evaluate the reaction.

When FpC6 was treated with three equivalents of *n*-BuLi, followed by the addition of $Cl(CH_2)_3PPh_2$, ^{31}P NMR analysis of the reaction mixture showed a major peak at 109 ppm

(Figure 5.1). The yield for this reaction was 70 %. After purification, a single crystal suitable for X-ray diffraction was obtained (Figure 5.1). The X-ray diffraction result indicated that the product was the 5-membered ring **1** and previously discussed in Chapter 2, as shown in Figure 5.1.
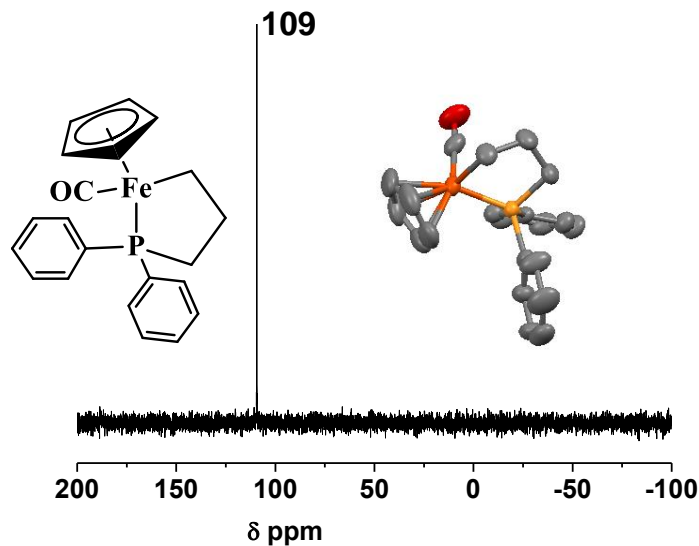
Figure 5.1 ^{31}P NMR spectrum (in CDCl$_3$) and single crystal structure with thermal ellipsoids (50 % probability level) of the 5-membered ring **1** generated from the reaction of FpC6 with Cl(CH$_2$)$_3$PPh$_3$ in the presence of three equivalents of *n*-BuLi.

We know that it takes 7 days to convert CpFe(CO)$_2$(CH$_2$)$_3$PPh$_2$ (FpP) into the 5-membered ring **1** *via* CO release, as discussed in Chapter 2,[3] while in this experiment, it only took 30 min. We assume that this acceleration of the reaction was due to *n*-BuLi. In order to test this idea, one equivalent of *n*-BuLi was used for the reaction. The ^{31}P NMR spectrum of the reaction mixture, after stirring for 30 min, was compared with that produced using three equivalents of *n*-BuLi. As shown in Figure 5.2a, when one equivalent of *n*-BuLi was used, a strong peak at -15 ppm due to the unreacted Cl(CH$_2$)$_3$PPh$_2$ was observed. In contrast, when three equivalents of *n*-BuLi were used (Figure 5.2b), the intensity of the peak at -15 ppm was much weaker as compared to that in

Figure 5.2a when one equivalent of *n*-BuLi was used, indicating that the conversion of

$Cl(CH_2)_3PPh_2$ into the 5-membered ring was significantly enhanced when three equivalents of

n-BuLi were used. Further research is required to understand the mechanism of this reaction.
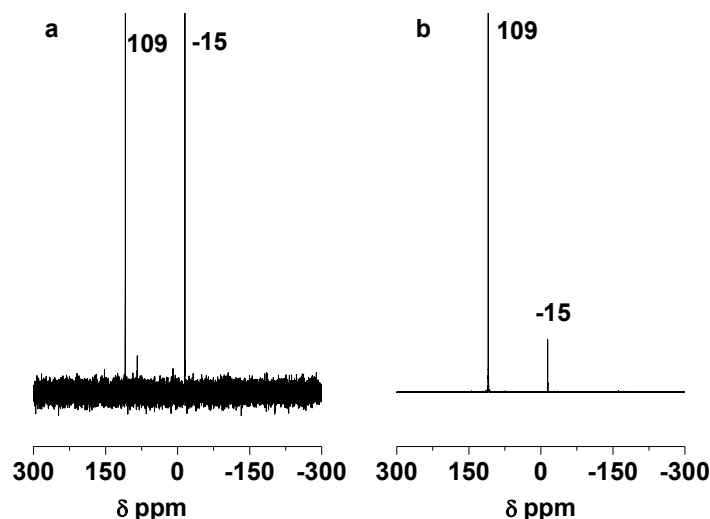
Figure 5.2 ^{31}P NMR spectra for the reaction mixture of metalation and functionalization of

FpC6 in the presence of $Cl(CH_2)_3PPh_2$ using (a) one equivalent and (b) three equivalents of

n-BuLi.

Our preliminary investigation suggests that FpC6 can be metalated using one equivalent of

s-BuLi, and functionalized using MeI (Scheme 5.3). The resulting Cp functionalized products

were characterized in detail. The ^{1}H NMR spectrum for $[\eta^5\text{-}C_5H_4CH_3]Fe(CO)_2(CH_2)_5CH_3$ is

shown in Figure 5.3. The chemical shift due to the methyl group in the hexyl chain is at 0.9-0.7

ppm (a in Figure 5.3), and the resonance signals at 1.5-1.2 ppm are attributed to the protons

from the five CH_2 in the hexyl group (b in Figure 5.3). The chemical shift for the CH_3 connected

to the Cp ring is at 1.9 ppm[9] (c in Figure 5.3). The integration ratio for the peaks at 0.8 ppm (a),

1.5- 1.2 ppm (b) and 1.9 ppm (c) is 3 : 10 : 3.1, which is close to the expected values for the

proposed structure. In addition, three peaks at 4.7 ppm, 4.6 ppm and 4.5 ppm corresponding to

the protons from the Cp ring are observed. The small peak at 4.7 ppm can be assigned to the Cp ring in the unreacted FpC6.[8] The resonance signals at 4.6 and 4.5 ppm are attributed to the Cp protons in $[\eta^5\text{-}CH_3C_5H_4]Fe(CO)_2(CH_2)_5CH_3$.[9] The integration ratio for the peaks at 4.6 ppm and 4.5 ppm is 1 : 1, which is in agreement with the proposed structure. Furthermore, by comparing the intensities for the signals at 4.6 ppm and 4.5 ppm with that at 4.7 ppm, we can estimate that 11.0 mole% of FpC6 were unreacted. Nevertheless, ^{1}H NMR analysis confirms that the metalation and functionalization of the Cp ring in FpC6 is possible.
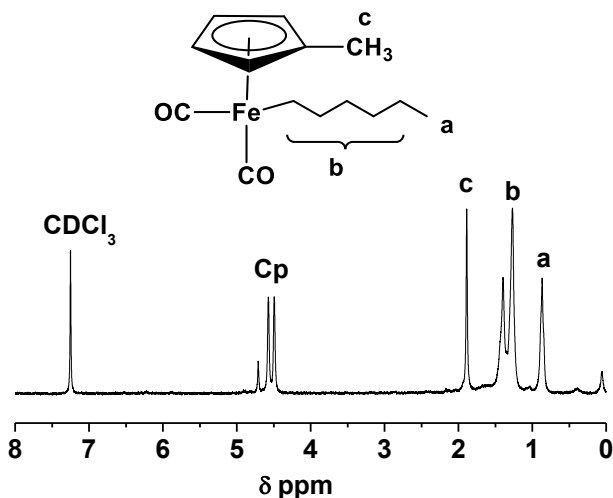
Figure 5.3 ^{1}H NMR spectrum for $[\eta^5\text{-}CH_3C_5H_4]Fe(CO)_2(CH_2)_5CH_3$ in CDCl$_3$.

The migration insertion reaction of $[\eta^5\text{-}CH_3C_5H_4]Fe(CO)_2(CH_2)_5CH_3$ was performed in the presence of PPh$_3$ in THF at 70 °C. The ^{31}P NMR spectrum of the product shows a peak at 77 ppm, suggesting the occurrence of the migration insertion reaction and the production of $[\eta^5\text{-}CH_3C_5H_4]Fe(CO)(PPh_3)[C(O)(CH_2)_5CH_3]$[8] (Figure 5.4a). The ^{1}H NMR spectrum shows a peak at 1.9 ppm, which is assigned to the CH$_3$ on the Cp ring[9] (a in Figure 5.4b). The chemical shifts at 2.9 and 2.5 ppm are attributed to the two protons α to the acyl CO (b in Figure 5.4b). The resonance signals due to the four CH$_2$ and the CH$_3$ in the hexyl chain appear at 1.5-1.2 ppm (c in Figure 5.4b) and 0.9-0.7 ppm (d in Figure 5.4b), respectively.[12] The integration ratio of CpC*H*$_3$:

COCH_2: (CH_2)$_4$: (CH$_2$)$_5$CH_3 is 3 : 2 : 10 : 4, which is close to the theoretical values. In addition, five peaks at 4.4-4.0 ppm are observed for the Cp protons. The upfield shift of the signals due to the Cp ring in [η^5-CH$_3$C$_5$H$_4$]Fe(CO)$_2$(CH$_2$)$_5$CH$_3$ suggests that migration insertion reaction has occurred.[1] The chemical shift at 4.4 ppm may arise from the MIR of FpC6.[8] The four peaks at 4.3, 4.2, 4.15 and 4.0 ppm are attributed to the four protons in the Cp ring from [η^5-CH$_3$C$_5$H$_4$]Fe(CO)(PPh$_3$)[C(O)(CH$_2$)$_5$CH$_3$]. The integration ratio of the four peaks (4.3, 4.2, 4.15, 4.0 ppm) to the peak at 4.4 ppm suggests that the product is contaminated with 15.0 mole% of side product generated by the MIR of FpC6.
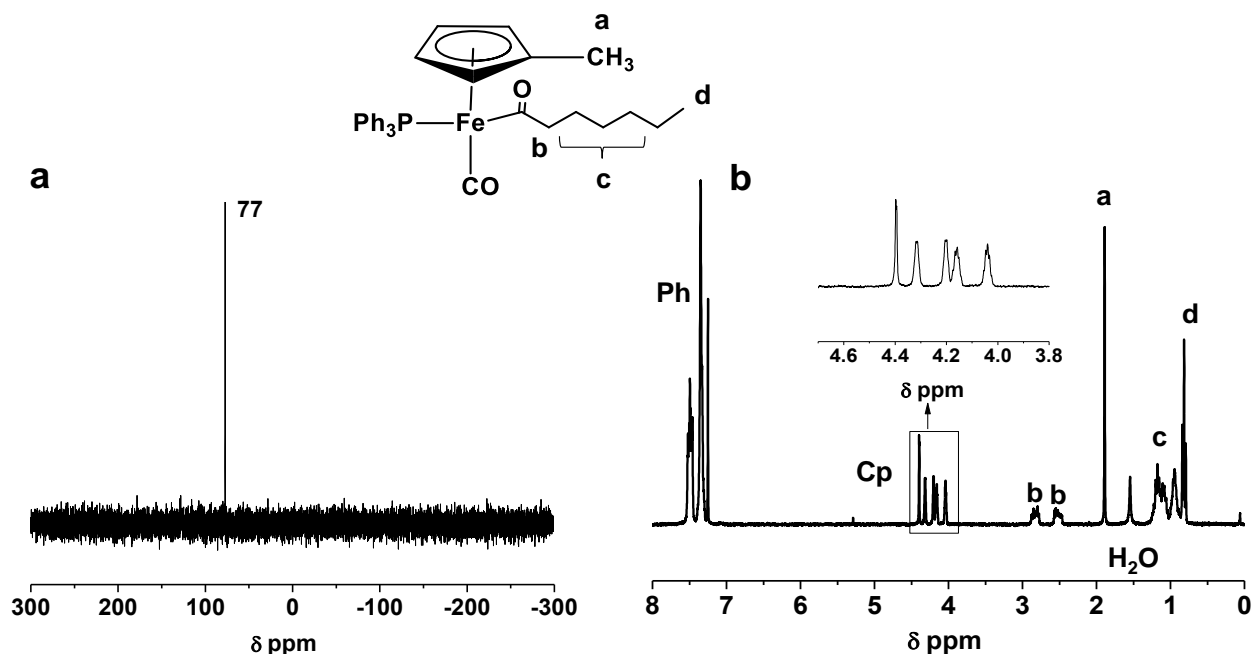
Figure 5.4 (a) ^{31}P NMR and (b) ^{1}H NMR spectra for [η^5-CH$_3$C$_5$H$_4$]Fe(PPh$_3$)(CO)[C(O)(CH$_2$)$_5$CH$_3$] in CDCl$_3$.

5.3.2 Synthesis of I(CH$_2$)$_3$PPh$_2$

Following the above investigation, we intended to prepare I(CH$_2$)$_3$PPh$_2$ to target the proposed molecules *via* route 1 (Scheme 5.2). NaPPh$_2$ was reacted with an excess of I(CH$_2$)$_3$I at -78 °C. In

order to remove unreacted $I(CH_2)_3I$, the crude product was heated at 110 ^{o}C for 5 h under vacuum. However, the ^{31}P NMR spectrum of the final product reveals a single peak at 28 ppm due to the formation of quaternized phosphine[13] (Figure 5.5).
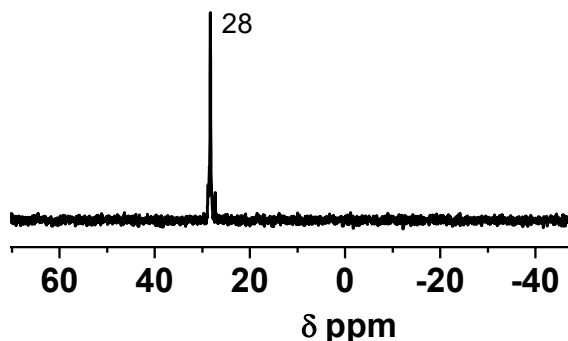
Figure 5.5 ^{31}P NMR spectrum for the reaction mixture of $NaPPh_2$ and $I(CH_2)_3I$ in THF after heating at 110 ^{o}C for 5 h.

In order to avoid the quaternization reaction, protection of the phosphine ligand using BH_3 was attempted[14] (Scheme 5.4). $BH_3 \cdot THF$ was added to the reaction solution before heating for the purification.
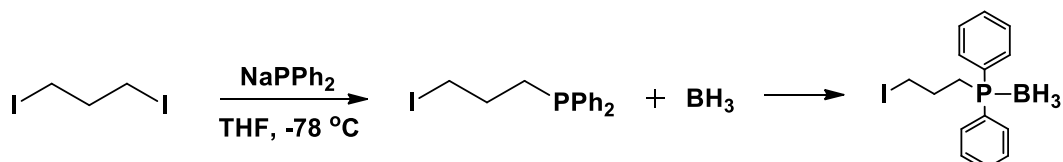
Scheme 5.4 Synthesis of phosphine borane complex $I(CH_2)_3PPh_2 \cdot BH_3$.

Figure 5.6 illustrates the ^{31}P NMR spectra for the reaction mixture before and after the addition of $BH_3 \cdot THF$. A major peak at 17 ppm due to the coordination of phosphine and BH_3 is observed.[15]
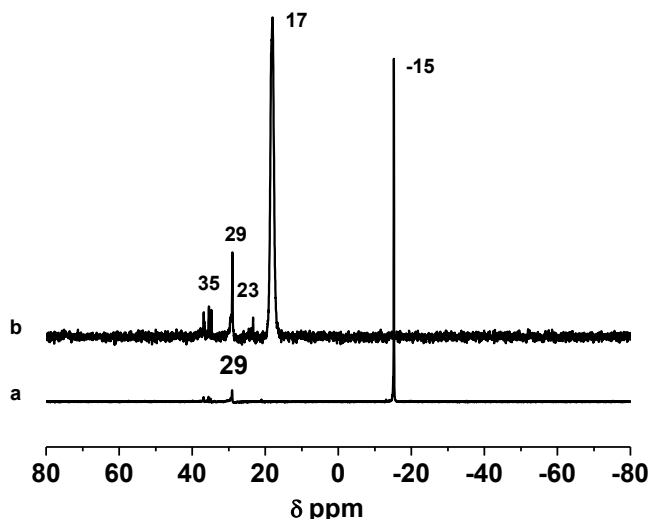
Figure 5.6 ^{31}P NMR spectra for reaction mixture of NaPPh$_2$ and I(CH$_2$)$_3$I in THF (a) before and (b) after addition of BH$_3$·THF.

After purification, a single peak at 18 ppm was observed in the ^{31}P NMR spectrum (Figure 5.7a). In the ^{1}H NMR spectrum (Figure 5.7b), the peaks at 7.8-7.2 ppm are attributed to the phenyl groups. The chemical shift due to the CH$_2$ adjacent to I appears at 3.2 ppm (a in Figure 5.7b). The resonance signals at 2.2 ppm are assigned to the middle CH$_2$ in the propyl spacer (b in Figure 5.7b) and the signal at 1.8 ppm corresponds to the CH$_2$ next to phosphorus (c in Figure 5.7b). The broad peak at 1.2-0.6 ppm is due to the protons from BH$_3$. The integration ratio of ***Ph*** : CH$_2$***CH$_2$***CH$_2$: B***H$_3$*** is 10 : 2 : 3, which matches the targeted structure. However, the integration ratio of I***CH$_2$*** : ***CH$_2$***PPh$_2$: ***Ph*** is 0.6 : 1 : 10. As compared to the theoretical value of 2 : 2 : 10, the experimental NMR intensities for I***CH$_2$*** and ***CH$_2$***PPh$_2$ are too low, suggesting that I(CH$_2$)$_3$PPh$_2$·BH$_3$ is not pure.
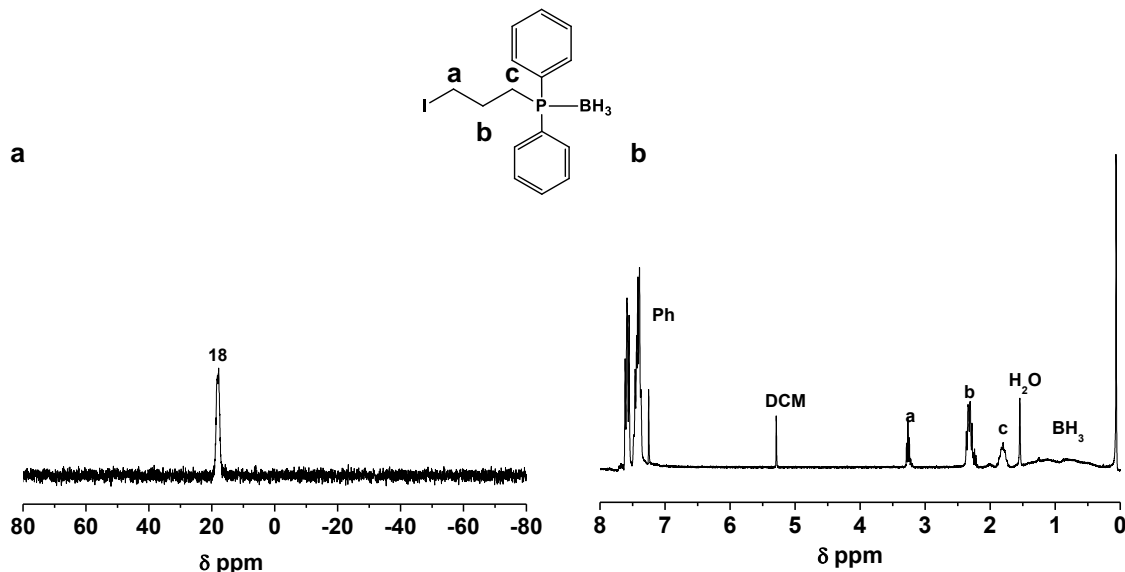
Figure 5.7 (a) ^{31}P NMR and (b) ^{1}H NMR spectra for $I(CH_2)_3PPh_2 \cdot BH_3$ in $CDCl_3$.

5.3.3 Synthesis of $[\eta^5\text{-Cl}(CH_2)_3C_5H_4]Fe(CO)_2(CH_2)_5CH_3$
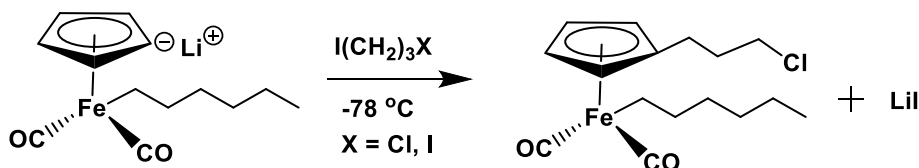
Scheme 5.5 Synthesis of $[\eta^5\text{-Cl}(CH_2)_3C_5H_4]Fe(CO)_2(CH_2)_5CH_3$.

As discussed above, the synthesis of $I(CH_2)_3PPh_2 \cdot BH_3$ was not successful. In order to get around this problem, synthetic route 2 was attempted. Two propyl dihalides, 1,3-diiodopropane and 1-chloro-3-iodopropane, were selected to react with the FpC6 anion. ^{1}H NMR analysis suggests that, when 1,3-diiodopropane was used, $[\eta^5\text{-IC}_5H_4]Fe(CO)_2(CH_2)_5CH_3$ was generated. As illustrated in the ^{1}H NMR spectrum (Figure 5.8), the signals at 4.9 and 4.8 ppm are attributed to the protons in the Cp ring. The resonance signals due to the CH_2 and the CH_3 in the hexyl group appear at 1.8-1.0 ppm (b in Figure 5.8) and 0.9-0.6 ppm (a in Figure 5.8), respectively. The integration ratio of Cp : b : a is 4 : 11 : 3, which is close to the theoretical value.
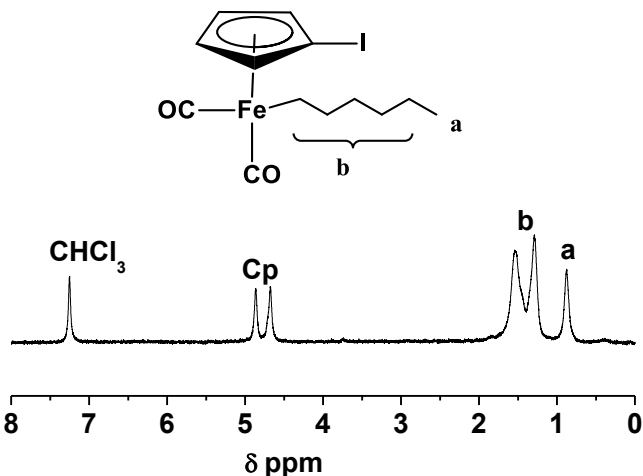
Figure 5.8 ^{1}H NMR spectrum for $[\eta^5\text{-IC}_5\text{H}_4]\text{Fe(CO)}_2(\text{CH}_2)_5\text{CH}_3$ in CDCl$_3$.

In contrast, when 1-chloro-3-iodopropane was reacted with the FpC6 anion, the targeted molecule $([\eta^5\text{-Cl(CH}_2)_3\text{C}_5\text{H}_4]\text{Fe(CO)}_2(\text{CH}_2)_5\text{CH}_3)$ with a chloropropyl group connected to the Cp ring was obtained (Scheme 5.5). The ^{1}H NMR spectrum for $[\eta^5\text{-Cl(CH}_2)_3\text{C}_5\text{H}_4]\text{Fe(CO)}_2(\text{CH}_2)_5\text{CH}_3)$ in CDCl$_3$ (Figure 5.9) reveals two peaks at 4.6 ppm and 4.5 ppm due to the protons from the Cp ring. The triplet peak at 2.4 ppm and multiplet peak at 1.9 ppm are assigned to the CH$_2$ α (a in Figure 5.9) and β (b in Figure 5.9) to the Cp ring, respectively. The chemical shift due to the CH$_2$ connected to Cl appears at 3.6 ppm (c in Figure 5.9). Furthermore, the chemical shifts at 1.56-1.2 ppm are attributed to the CH$_2$ from the hexyl group (d in Figure 5.9), and the chemical shift due to the CH$_3$ in the hexyl group appears at 0.87 ppm (e in Figure 5.9). The integration ratio of Ph : Cp : a : b : c : d : e is 10 : 4 : 2 : 2 : 2 : 10 : 3, which matches the targeted structure. Therefore, the NMR results suggest that $[\eta^5\text{-Cl(CH}_2)_3\text{C}_5\text{H}_4]\text{Fe(CO)}_2(\text{CH}_2)_5\text{CH}_3$ was obtained.
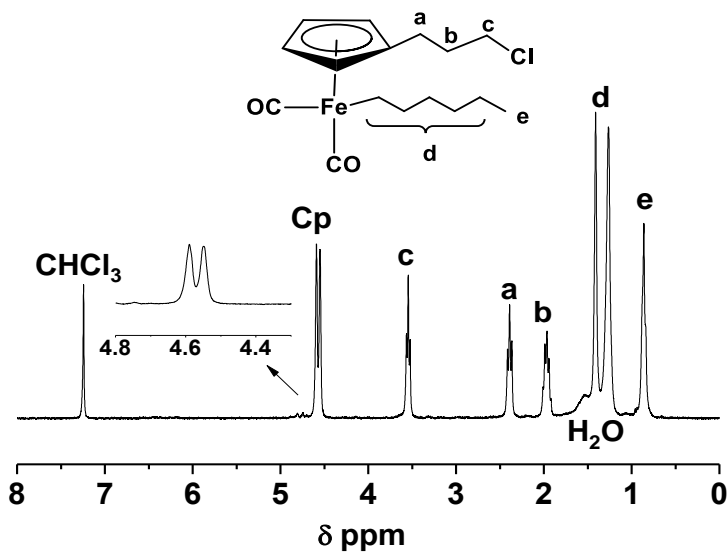
Figure 5.9 ^{1}H NMR spectrum for $[\eta^5\text{-Cl(CH}_2)_3C_5H_4]Fe(CO)_2(CH_2)_5CH_3$ in CDCl$_3$.

5.3.4 Synthesis of $[\eta^5\text{-Ph}_2P(CH_2)_3C_5H_4]Fe(CO)_2(CH_2)_5CH_3$
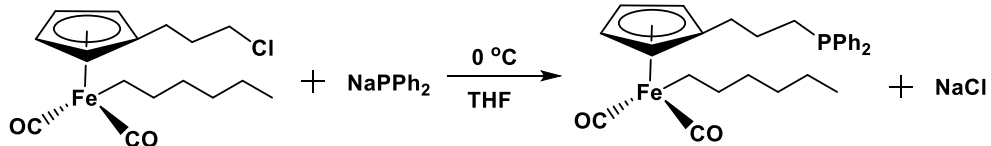
Scheme 5.6 Synthesis of $[\eta^5\text{-Ph}_2P(CH_2)_3C_5H_4]Fe(CO)_2(CH_2)_5CH_3$ (FpP^{Cp}).

FpP^{Cp}, with a phosphine group tethered on the Cp ring, was synthesized *via* the reaction of $[\eta^5\text{-Cl(CH}_2)_3C_5H_4]Fe(CO)_2(CH_2)_5CH_3$ with NaPPh$_2$. After purification, FpP^{Cp} was characterized using NMR and FT-IR spectroscopies. The ^{31}P NMR spectrum shows a single peak at -15 ppm, indicating the presence of phosphine[1] (Figure 5.10a). The IR spectrum for $[\eta^5\text{-Ph}_2P(CH_2)_3C_5H_4]Fe(CO)_2(CH_2)_5CH_3$ reveals two absorption bands at 1997 cm^{-1} and 1935 cm^{-1} (Figure 5.10b), which are the absorptions characteristic for the terminal carbonyl groups in Fp derivatives.[1]
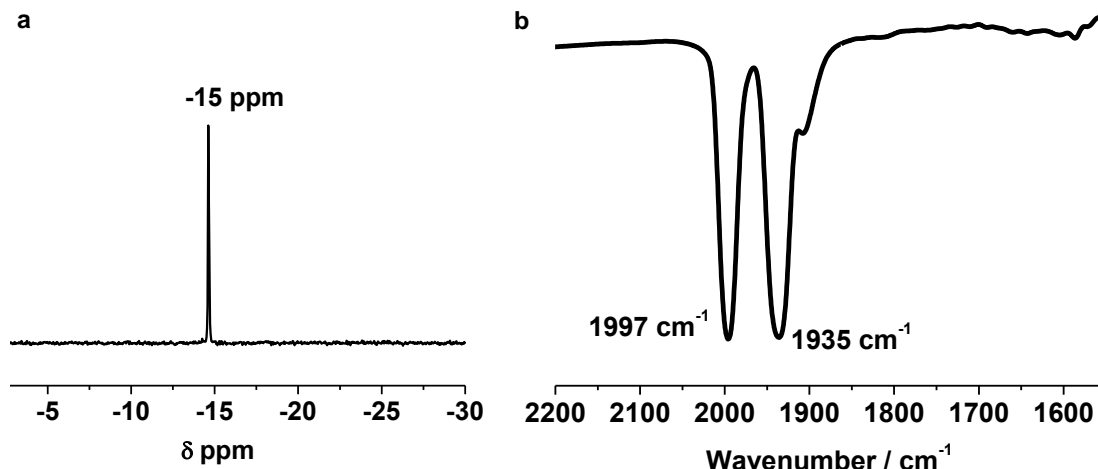
Figure 5.10 (a) ^{31}P NMR (in CDCl$_3$) spectrum and (b) partial FT-IR spectrum for
[η^5-Ph$_2$P(CH$_2$)$_3$C$_5$H$_4$]Fe(CO)$_2$(CH$_2$)$_5$CH$_3$.

FpP^{Cp} was also analyzed using ^{1}H NMR spectroscopy. As illustrated in Figure 5.11, the peaks

at 4.6 and 4.5 ppm are attributed to the protons in the Cp ring and the chemical shifts at 7.5-7.0

ppm are assigned to the phenyl groups. The resonance signals due to the CH$_2$ α (a in Figure 5.11)

and β (b in Figure 5.12) to the Cp ring appear at 2.1-2.0 ppm and 1.7-1.5 ppm, respectively. The

peaks at 2.4-2.2 ppm are caused by the CH$_2$ coordinated to the phosphorus atom (c in Figure

5.11). The proton integration indicates that a ratio of Ph : Cp : a : b : c is 10 : 5 : 2 : 2 : 2, which

matches the theoretical values. The chemical shifts due to the methylene group in the hexyl

group (d in Figure 5.11) are 1.5-1.0 ppm, and that due to the methyl group from the hexyl group

is 0.87 ppm (e in Figure 5.11). The ratio of Ph : d : e as calculated from the proton integration is

10 : 10 : 2, which matches the targeted structure.

114
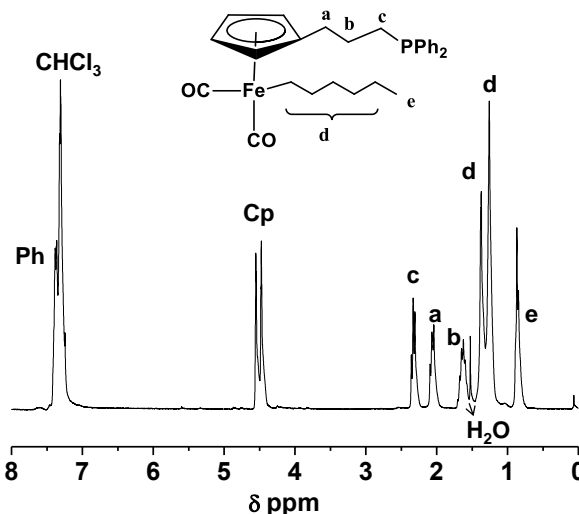
Figure 5.11 ^{1}H NMR spectrum for [η^5-Ph$_2$P(CH$_2$)$_3$C$_5$H$_4$]Fe(CO)$_2$(CH$_2$)$_5$CH$_3$ in CDCl$_3$.

Two-dimensional ^{1}H-^{1}H COSY was utilized to verify the peak assignment. As illustrated in Figure 5.12, a cross peak is observed for the peaks at 2.1-2.0 ppm (a in Figure 5.12) and 1.7-1.5 ppm (b in Figure 5.12), indicating that a and b are adjacent to each other. A second cross peak is also observed for the peaks at 1.7-1.5 ppm (b in Figure 5.12) and 2.4-2.2 ppm (c in Figure 5.12), suggesting that b and c are connected. However, no cross peak is observed for the signals at 2.4-2.2 ppm (c in Figure 5.12) and 2.1-2.0 ppm (a in Figure 5.12), suggesting that a and c are separated. A third cross peak is observed for the chemical shifts at 1.45-1.0 (d in Figure 5.12) ppm and 0.87 ppm (e in Figure 5.12), because the methyl group (e in Figure 5.12) in the hexyl chain is connected to the CH$_2$ (d in Figure 5.12). The ^{1}H-^{1}H COSY results therefore confirm the assignment for the peaks in the ^{1}H NMR spectrum for FpP^{Cp} (Figure 5.11).

115
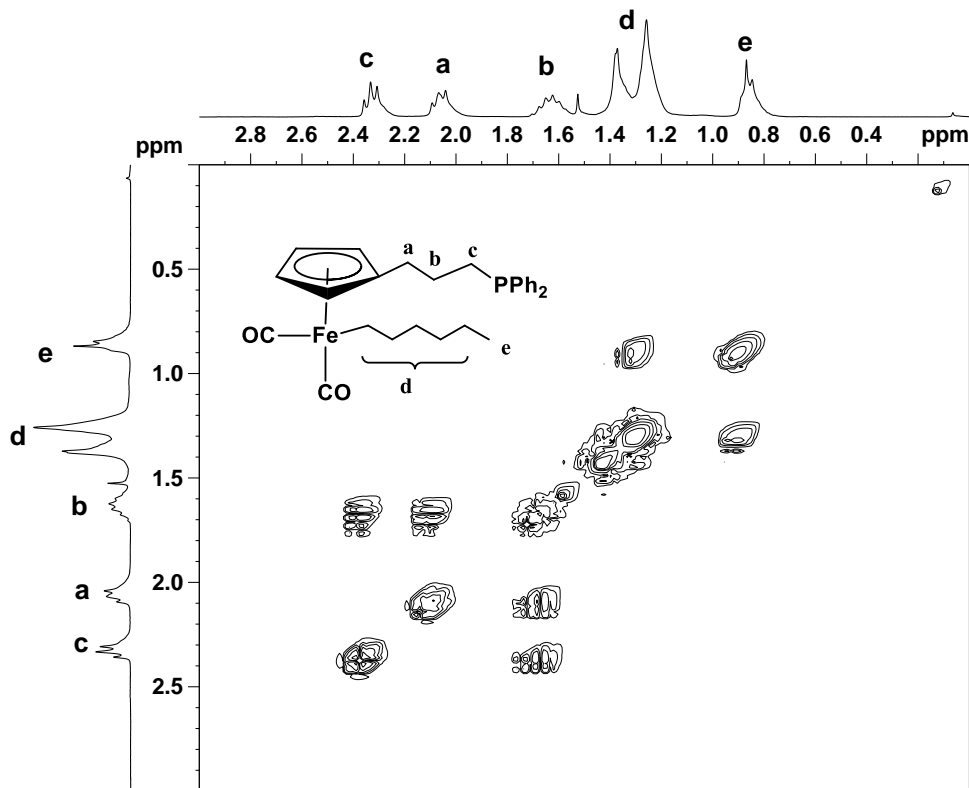
Figure 5.12 ^{1}H-^{1}H COSY NMR spectrum for $[\eta^5\text{-}Ph_2P(CH_2)_3C_5H_4]Fe(CO)_2(CH_2)_5CH_3$ in CDCl$_3$.

The mass of FpP^{Cp} was determined using electrospray ionization (ESI) mass spectroscopy, which shows an ion with m/z of 490 (Figure S5.2). This m/z can be interpreted as the [M+H]$^+$ ion from the targeted FpP^{Cp}. MS/MS analysis indicated that the fragmentation pathway of this ion with m/z of 490 followed by the loss of carbonyl and (CH$_2$)$_5$CH$_3$ groups (Figure S5.3), which matched the chemical structure of FpP^{Cp}.

5.3.5 Polymerization of $[\eta^5\text{-}Ph_2P(CH_2)_3C_5H_4]Fe(CO)_2(CH_2)_5CH_3$

Bulk polymerization of FpP^{Cp} was performed at 105 ^{o}C. During the polymerization, we observed that the viscosity of the system dramatically increased within a short period of time, and that the originally orange oil-like monomer gradually changed to a transparent reddish-

brown solid. After 20 h, the polymerization was terminated by cooling the reaction flask to room temperature. THF was added to dissolve the crude product, generating a clear red solution. Afterwards, the THF solution was added drop-wise to cold hexane, yielding a yellow precipitate. The yellow precipitate was first analyzed using GPC, which revealed that oligomeric species with a M_n of 4200 g/mol and a PDI of 1.73 were produced (Figure 5.13).
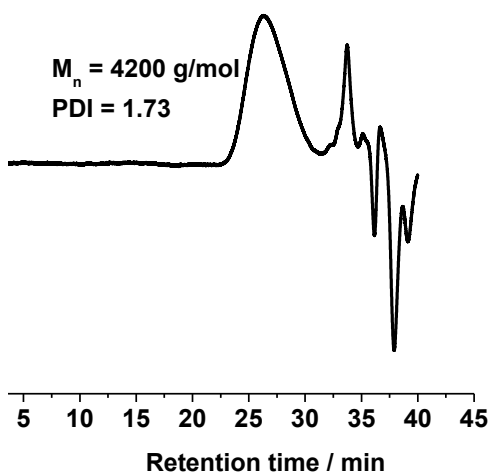
Figure 5.13 GPC curve for oligo-PFpP^{Cp}.

The resulting oligo-PFpP^{Cp} was further analyzed using IR and NMR spectroscopies. As shown in Figure 5.14, the absorption frequency at 1601 cm^{-1}, which is characteristic for the migrated CO, is observed in the IR spectrum. In the ^{31}P NMR spectrum, a single peak at 73 ppm due to the coordinated phosphorus is observed (Figure 5.14b). Therefore, both IR and ^{31}P NMR analyses suggest that the MIR occurred.[1]
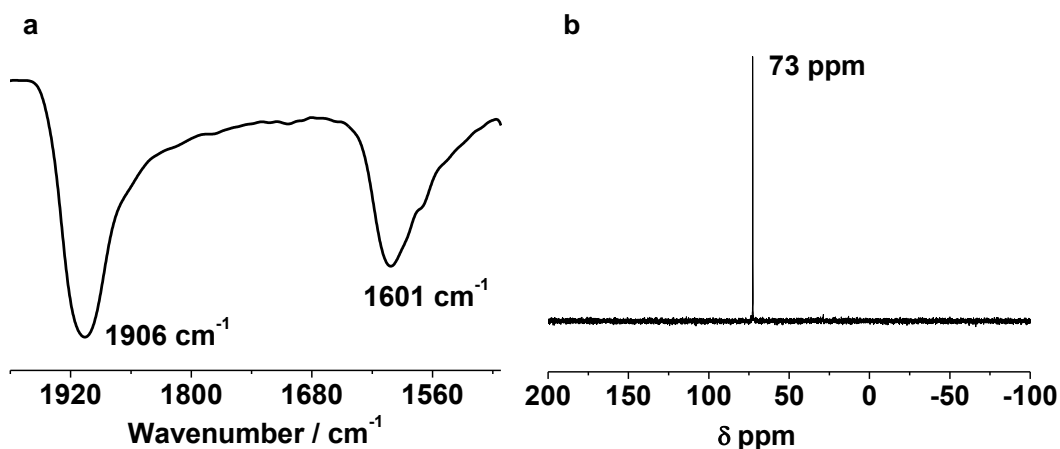
Figure 5.14 (a) Partial FT-IR spectrum and (b) ^{31}P NMR spectrum for oligo-PFpP^{Cp} in C_6D_6.

Oligo-PFpP^{Cp} was also analyzed by ^{1}H NMR spectroscopy (Figure 5.15). The peaks at 7.8-7.0 ppm are attributed to the phenyl groups. The resonance signals due to the protons from the Cp ring appear at 4.2-3.8 ppm. The upfield shift of the Cp protons in the oligo-PFpP^{Cp} confirms the occurrence of the MIR. The peaks at 3.0 and 2.9 ppm (d in Figure 5.15) are assigned to the two diastereotopic protons from the CH_2 α to the acyl group. The peaks at 1.5-1.2 ppm (e in Figure 5.15) and 1.0-0.9 ppm (f in Figure 5.15) are assigned to the CH_2 and the CH_3 in the hexyl group, respectively. The integration ratio of Cp : d : e : f is 4 : 2 : 7.6 : 3.2, which matches the targeted structure. The chemical shift due to the hydrogens from CH_2 connected to the Cp ring is at 1.8-1.5 ppm (a in Figure 5.15), while the chemical shift due to hydrogens from the CH_2 α to the phosphorus appears at 2.6-2.3 ppm (c in Figure 5.15). The peak at 2.3-2.1 ppm (b in Figure 5.15) is assigned to the middle CH_2 in the propyl spacer on the Cp ring. The integration ratio of a : b : c is 2 : 2 : 3, which is close to the theoretical value.
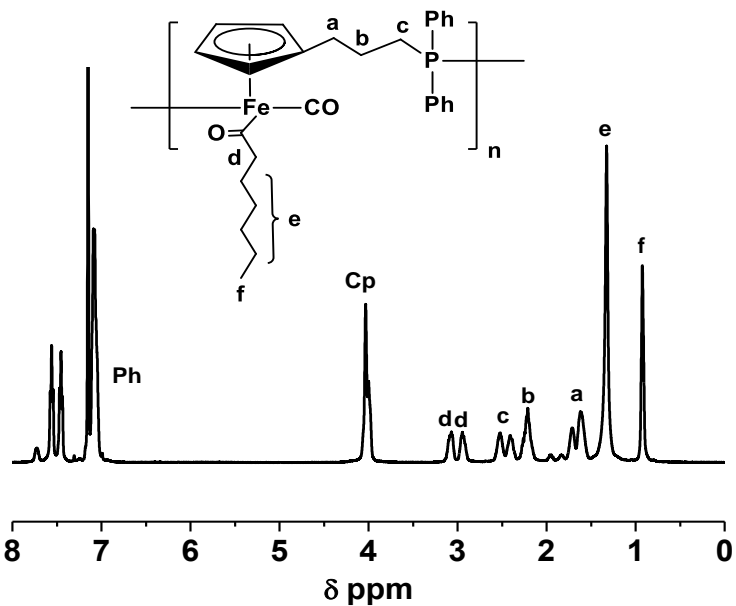
Figure 5.15 ^{1}H NMR spectrum for oligo-PFpP[Cp] in C_6D_6.

The chemical structure of oligo-PFpP[Cp] was further analyzed using ^{13}C NMR spectroscopy. The chemical shift at 220 ppm is characteristic for the terminal carbonyl group.[1] The weak resonance signal at 273 ppm is attributed to the acyl CO. In order to clarify that the signal at 273 ppm is indeed a resonance signal rather than baseline noise, ^{1}H-^{13}C HMBC 2D NMR spectroscopy (HMBC: Heteronuclear Multiple Bond Correlation) of oligo-PFpP[Cp], which can be used to determine long range C-H connectivity,[16] was performed. As illustrated in Figure 5.16 (b), the protons with chemical shifts at 3.0 and 2.9 ppm, due to the two diastereotopic protons connected to the acyl CO group (d in Figure 5.16), correlate to the peak at 273 ppm in ^{13}C NMR. The appearance of these two cross peaks confirms that the peak at 273 ppm is indeed the chemical shift for the acyl CO group. In addition, we observe that the chemical shifts at 4.2-3.8 ppm due to the protons in the Cp ring strongly correlate to the peaks at 82, 84, 87 and 102 ppm in the ^{13}C NMR spectrum, suggesting that these carbons are very close to the protons in the Cp ring. As the chemical shifts in the region of 82-102 ppm in the ^{13}C NMR spectrum usually

119

associated with aromatic carbons, these peaks can be assigned to the carbons on the Cp ring.
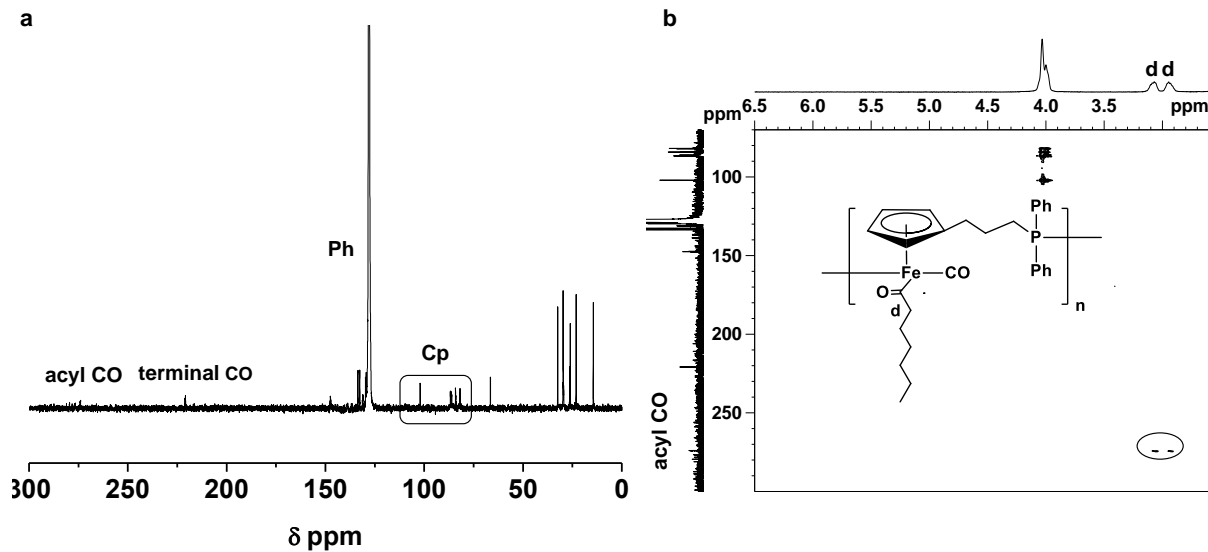
Figure 5.16 (a) ^{13}C NMR spectrum and (b) HMBC 2D NMR spectrum for oligo-PFpP^{Cp} in C$_6$D$_6$.

^{13}C-^{1}H HMQC 2D NMR spectroscopy (HMQC: Heteronuclear Multiple Quantum Coherence) was performed in order to precisely assign the carbons from the Cp ring, the propyl spacer and the hexyl group. As illustrated in Figure 5.17, the chemical shifts at 87, 84 and 82 ppm in the ^{13}C NMR spectrum correlate to the peak at 4.2-3.8 ppm due to Cp ring in the ^{1}H NMR, indicating that these three peaks are due to the three carbons in the Cp ring. Another peak at 102 ppm is observed but with no cross peak in the correlation map. This peak can be assigned to the carbon in the Cp ring connected to the alkyl group, because there is no proton on this carbon. HMBC 2D NMR spectrum (Figure 5.16b) also supports this assignment. The correlation map shows that the signal at 67 ppm is connected to the two protons from C(O)CH$_2$. Therefore, this chemical shift at 67 ppm (d in Figure 5.17) is assigned to the carbon in the CH$_2$ α to the acyl CO. According to the correlation map, chemical shifts for other carbons are assigned as follows: the resonance signal at 26.1 ppm (a in Figure 5.17) is attributed to the carbon α to the Cp ring. The

chemical shifts due to the carbon β to the Cp ring and the carbon connected to the phosphorus

atom overlapped and appear at 29.7 ppm (b, c in Figure 5.17). The peak at 14.4 ppm (f in Figure

5.17) is assigned to the CH_3 in the hexyl group. The chemical shifts due to the four CH_2 in the

middle of the hexyl group appear at 32.4, 29.7, 26.5 and 23.1 ppm (e in Figure 5.17).
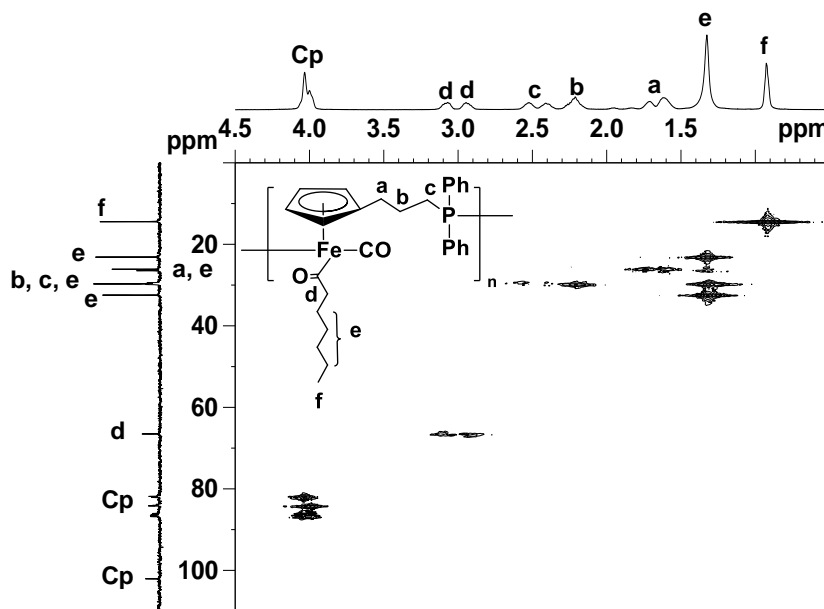
Figure 5.17 ^{1}H-^{13}C HMQC 2D NMR spectrum for oligo-PFpP^{Cp} in C_6D_6.

5.4 Conclusions

The Cp ligand in FpC6 was metalated using *s*-BuLi and subsequently reacted with MeI or

$Cl(CH_2)_3I$ for the functionalization of the Cp ring. These reactions were used for the synthesis of

$[\eta^5$-Ph$_2$P(CH$_2$)$_3$C$_5$H$_4$]Fe(CO)$_2$(CH$_2$)$_5$CH$_3$ (FpP^{Cp}) with a phosphine group tethered on the Cp

ring. The resulting FpP^{Cp} was characterized using FT-IR, ^{1}H NMR, ^{31}P NMR and ^{1}H-^{1}H 2D

COSY NMR spectroscopy. Migration insertion polymerization of FpP^{Cp} was attempted in bulk

at 105 ^{o}C, generating oligo-PFpP^{Cp} with a M_n of 4200 g/mol as determined by GPC analysis.

The chemical structure of the oligo-PFpP^{Cp} was confirmed using a number of characterization

techniques including FT-IR, ^{1}H NMR, ^{31}P NMR, ^{13}C NMR spectroscopies, and the HMBC and

HMQC 2D NMR techniques.

Chapter 6. Hydration of Hydrophobic Iron-Carbonyl Homopolymers *via* Water-Carbonyl Interaction (WCI): Creation of Uniform Organometallic Aqueous Vesicles with Exceptionally High Encapsulation Capacity

6.1 Introduction

The hydration of carbonyl groups is crucial for many biological events including protein folding[1] and enzymatic catalysis.[2] Water-carbonyl interaction (WCI) has therefore become an important research topic for molecular biology.[3, 4] Synthetic macromolecules containing carbonyl groups, e.g., poly(methyl methacrylate),[5] poly(dimethylaminoethyl methacrylate),[6] poly(N-isopropylacrylamide),[7] often exhibit peculiar solution behaviour, which may be related to WCI as illustrated by FT-IR analysis.[8] Therefore, it is tempting to explore how we may harness WCI as a supramolecular driving force for the creation of assemblies with defined nanostructures.

The micellization of macromolecules, including block copolymers and homopolymers,[9-13] driven by various forces such as amphiphilicity,[14] crystallization,[15] hydrogen bonding[16] and electrostatic interactions[17] has been intensively studied[18-20] and has evolved to the level of precise synthesis and architecture design.[15, 21] WCI, however, has not been considered as a topic for macromolecule self-assembly. Chemists explore molecular physics and the natural world by creating new molecules. We have developed a polymerization technique, namely migration insertion polymerization (MIP),[22,23] which allows the step-growth of $CpFe(CO)_2(CH_2)_3PPh_2$

(FpP) *via* migration insertion reactions (MIRs), resulting in a group of iron carbonyl polymers (PFpP) (Figure 6.1a).[22, 23] PFpP is hydrophobic and contains both terminal and acyl CO groups. The acyl COs are highly polarized with strong electronegative charges on the oxygen elements, as speculated in previous literature (Figure 6.1b).[24, 25] These highly polarized COs may exert a stronger WCI as compared to those observed for organic carbonyl polymers, e.g., PMMA,[5] and may act as a driving force for aqueous self-assembly of hydrophobic PFpP homopolymers.

In this Chapter, we report that hydrophobic PFpP is able to self-assemble into stable colloidal vesicles with a narrow size distribution in water. The hydration of carbonyl groups *via* WCI was identified as a driving force for the assembly. The vesicular morphology was confirmed by light scattering, TEM, AFM and encapsulation experiments. Particularly, PFpP vesicles were able to encapsulate hydrophilic molecules with extremely high encapsulation efficiency (EE) and loading capacity (LC).
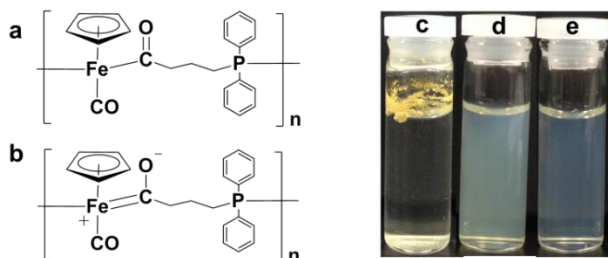
Figure 6.1 (a) Chemical structure of PFpP; (b) PFpP resonance structure; (c) Hydrophobic PFpP floating on water; (d) PFpP colloids in water at polymer concentration of 0.1 mg/mL and (e) 0.05 mg/mL. Note: The degree of polymerization was $DP_n = 20$.

6.2 Experimental

6.2.1 Materials and Instrumentation

Sodium (Na), 1-bromo-3-chloropropane, potassium (K), cyclopentadienyl iron dicarbonyl dimer (Fp$_2$), benzophenone and poly(ethylene glycol) (2000 g/mol) were purchased from Sigma-Aldrich. Calcein and chlorodiphenylphosphine were purchased from Tokyo Chemical Industry (TCI). All the chemicals were used as received unless otherwise indicated. THF was freshly distilled under nitrogen from Na/benzophenone. Hexane was purged with dry nitrogen prior to use. Toluene was dried using molecular sieves before use.

6.2.2 Zeta-potential

A Malvern Zetasizer nano ZS instrument was used for zeta potential measurement. The zeta-potential of PFpP colloidal solutions was measured at 25 $^{\circ}$C with 20 repeated measurements. The zeta-potential of PFpP in dry THF was performed on the same instrument equipped with a dip cell at 25 $^{\circ}$C. The experiment was conducted with 10 repeated measurements.

6.2.3 FT-IR

Fourier transform infrared spectroscopy (FT-IR) spectra for PFpP solid samples were recorded on a Bruker Tensor 27 spectrophotometer with a resolution of 1 cm^{-1}. Test pellets were prepared by grinding and compressing PFpP (2 wt%) in KBr; FT-IR of PFpP in dry THF solution was performed on the same instrument in attenuated total reflectance (ATR) mode using the Pike MIRacle accessory equipped with a germanium crystal (Pike Technology). For PFpP in THF/water solution, THF solution of PFpP (20.0 mg/mL) was first prepared by dissolving PFpP

(60.0 mg) in dry THF (3.0 mL). A certain amount of water was then added to the solution. The solutions were then examined using ReactIR IC10 with a SiComp ATR crystal.

6.2.4 Surface tension

A tensiometer Data Physics DCAT 21 system was used for surface tension measurements. Pure water was measured prior to the measurement of PFpP colloidal solutions with varied concentrations.

6.2.5 Dynamic light scattering and static light scattering

Dynamic light scattering (DLS) was carried out at 25 ^{o}C using a Malvern Zetasizer Nano90. Multiangle DLS and static light scattering (SLS) were carried out using a Brookhaven Laser Light Scattering System with a BI-200 SM goniometer. A vertically polarized helium−neon diode laser with wavelength of 636 nm was used as the light source. All the samples were freshly prepared and directly used for the measurements at 25 ^{o}C, at a series of angles between 60 ^{o}and 150 ^{o}at 15 ^{o}intervals. Toluene was used as the reference for the Rayleigh ratio.

6.2.6 Transmission electron microscopy

Transmission electron microscopy (TEM) images were recorded using a number of TEM microscopes, including a low voltage (5 kV) electron transmittance microscope LVEM5 Benchtop (TEM-STEM-SEM) (Delong), a Philips CM10 electron microscope (60 kV) and a Zeiss Libra 200 MC (200 kV). TEM samples were prepared by placing a drop of solution onto a carbon-coated copper grid. Excess solution was subsequently removed using a piece of filter paper, and the grid was dried at ambient temperature.

6.2.7 Cryo-transmission electron microscopy

Cryo-TEM images were obtained using a high voltage (200 kV) field emission FEI Tecnai G2 F20 cryo-TEM microscope. Cryo-TEM samples were prepared by applying 5.0 μL of PFpP colloidal solution (0.1 mg/mL) onto a glow discharged copper grid with holey carbon film (Quantifoil Multi A), and blotted with filter paper. The grid was then quickly plunged into liquid ethane and transferred under liquid nitrogen to a Gatan 914 cryo-holder and viewed at -179 °C.

6.2.8 Atomic force microscopy

Atomic force microscopy (AFM) experiments were conducted on Nanoscope MultiModeTM AFM microscope using a conical AFM tip with a spring constant of 40 N/m, resonance frequency of 300 kHz and tip radius of 8 nm. The samples were prepared as follows: Three drops of aqueous colloid were placed on a freshly cleaved mica substrate; excess solution was subsequently removed with a piece of filter paper or *via* spin-coating for 45 s. The substrates were then dried at ambient temperature.

6.2.9 Nuclear magnetic resonance (NMR) spectroscopy

^{1}H, ^{31}P, and ^{13}C NMR spectra were obtained using a Bruker Avance 300 (^{1}H: 300 MHz; ^{31}P: 120 MHz; ^{13}C:75 MHz) spectrometer at ambient temperature. For the experiments using THF-d_8 and THF-d_8/D_2O as solvents, a NMR sample was first prepared by dissolving 20.0 mg of PFpP in 1.0 mL THF-d_8. After the measurement, 0.1 mL of D_2O was added to the THF-d_8 solution.

6.2.10 Gel permeation chromatography (GPC)

Molecular weights and molecular weight distributions, M_w/M_n, were characterized using GPC analysis at room temperature with THF as eluent at a flow rate of 1.00 mL/min. The Viscotek GPC max unit used was equipped with a VE 2001 GPC, three PolyAnalytik organic mixed bed columns, PAS-103-L, PAS-104-L, and PAS-105-*L* with dimensions of 8 mm (i.d.)×300 mm (L)

each, and a Viscotek triple detector array, including refractive index, viscosity, and dual-angle light scattering detectors. Polystyrene standards were used as references.

6.2.11 UV-vis spectroscopy

UV-vis absorption spectra for water solutions of calcein were recorded using a Varian (Carey 100 Bio) UV-vis spectrophotometer. Water was used as blank. A quartz cuvette with a path length of 1 cm was used. The absorption intensity at wavelength of 495.6 nm was plotted against the solution concentration, yielding to a straight line. The slope of the line determined the molar extinction coefficient of the calcein solutions.

6.2.12 Synthesis of PFpP

The synthesis and characterization of PFpP were described in Chapter 2 and Chapter 3.

6.2.13 Colloid preparation

Different amounts of PFpPs were dissolved in 1.00 mL THF, yielding clear yellow solutions. The solutions were then filtered through PTFE membranes with a pore size of 0.22 μm. To these THF solutions, 10.00 mL of deionized water was injected. THF was subsequently removed *via* N_2 bubbling for 1 h.

6.2.14 Photoluminescence of PFpP colloids in the presence of pyrene

A stock solution of pyrene in acetone at a concentration of 4.96 $\times 10^{-6}$ mol/L was first prepared, and then 1.00 mL of this acetone solution was added to a vial. Upon the evaporation of acetone, 10.00 mL PFpP aqueous solution (0.005 mg/mL) was added to the vial which was shaken for 30 min. The steady state fluorescence spectra were then recorded using a Photo Technology International LS-100 steady-state fluorometer equipped with a continuous xenon

lamp. The solution was excited at 338 nm. Pure pyrene solution in water was measured as a control. The fluorescence decay profiles were obtained using a time-correlated single photo counter from IBH Ltd. using a NanoLED 340 nm diode as the excitation source. The sample was excited at 338 nm and the emission wavelength was set at 375 nm.

6.2.15 Preparation of saturated calcein THF solution

Calcein (3.0 mg) was dissolved into THF (15.0 mL), and this solution was subsequently centrifuged to remove insoluble materials. In order to determine the concentration of the saturated solution, 1.0 mL of the solution was added to a vial, and the THF was subsequently evaporated with N_2 flow. Water (10.0 mL) was then added to dissolve the calcein in the vial. UV-vis measurement of the water solution was performed, yielding an absorption of 0.15 (Figure 6.17). The calcein concentration (c) in the water solution can therefore be calculated as follows:

$$A = \varepsilon l c$$

A is the absorption, ε is the molar extinction coefficient, l is the length of cell used for the measurement (1.0 cm), c is the solution concentration.

$$0.15 = 89556 \text{ L mol}^{-1}\text{cm}^{-1} \times 1 \text{ cm} \times c$$

$$c = 1.67 \times 10^{-6} \text{ mol L}^{-1}$$

Therefore, the concentration of calcein in THF saturated solution was:

$$c^* = \frac{1.67 \times 10^{-6} \text{ mol L}^{-1} \times 10.0 \text{ mL}}{1.0 \text{ mL}} = 1.67 \times 10^{-5} \text{ mol L}^{-1}$$

6.2.16 Encapsulation of calcein *via* nano-precipitation of PFpP

1.0 mL of the saturated calcein THF solution (1.67×10^{-5} mol/L, see above calculation) was used to dissolve 1.0 mg of PFpP. To the resulting PFpP solution, 10.0 mL water was injected

with stirring. THF was subsequently removed *via* N_2 bubbling for 1.5 h. In a control experiment, 10.0 mL water was quickly added to a calcein saturated THF solution (1.0 mL) without PFpP, followed by N_2 bubbling to remove THF. A mixed solution of PFpP colloids and calcein was also prepared as follows: PFpP aqueous colloids (0.10 mg/mL) were added to a vial containing calcein dried from 1.00 mL of calcein saturated THF solution. The resulting solution was then shaken for 1.5 h before characterization. The three prepared solutions were characterized using DLS, UV-vis, fluorescence spectroscopy and thin layer chromatography (TLC) using water as eluent.

6.2.17 Encapsulation of PEG *via* nano-precipitation of PFpP

A predetermined amount of PEG was dissolved in 1.00 mL THF solution of PFpP (1.00 mg/mL). 5.00 mL D_2O was injected to the vial under stirring and THF was subsequently removed *via* N_2 bubbling for 2.5 h. After the procedure, D_2O was added to compensate for the loss of D_2O during N_2 bubbling. The amount of D_2O was determined by weight. In control experiments, the same amount of PEG was directly dissolved in 5.00 mL D_2O. The prepared solutions were characterized using ^{1}H NMR; the encapsulation efficiency (EE) and loading capacity (LC) were then calculated using the following equations:

$$\text{Encapsulation efficiency (EE)} = \frac{I_{3.57} - I'_{3.57}}{I_{3.57}} \times 100\ \% \quad (1)$$

$I_{3.57}$ and $I'_{3.57}$ represent the integration area for the peak at 3.57 ppm due to PEG in D_2O in the absence and presence of PFpP, respectively.

$$\text{Loading capacity (LC)} = \frac{m_{PEG} \times EE}{m_{PFpP}} \times 100\ \% \quad (2)$$

m_{PEG} and m_{PFpP} represent the mass of PEG and PFpP (1.00 mg) used for the experiments, respectively.

In order to verify the calculations based on ^{1}H NMR spectra, PFpP colloidal solutions

prepared in the presence of PEG were transferred to dialysis tubes with a cut-off molecular

weight of 14,000 g/mol and dialyzed against either D_2O or H_2O to remove unencapsulated PEG.

When D_2O was used, the solution in the dialysis tube was analyzed by ^{1}H NMR, the results of

which indicated that free PEG could be removed. After dialysis, the materials in the dialysis tube

were recycled *via* freeze-drying. The mass of the encapsulated PEG was subsequently calculated

either by ^{1}H NMR analysis of the recovered solids in $CDCl_3$ or by gravimetry and used for EE

and LC calculation. The results obtained from these two methods are similar to those calculated

from equation (1) and (2).

The error on the calculated encapsulation efficiency and loading capacity was

determined from equations (3) and (4).

$$\% \text{ Error (EE)} = \frac{|Theoretical\ value\ of\ EE - Experimental\ value\ of\ EE|}{Theoretical\ value\ of\ EE} \quad (3)$$

$$\% \text{ Error (LC)} = \frac{|Theoretical\ value\ of\ LC - Experimental\ value\ of\ LC|}{Theoretical\ value\ of\ LC} \quad (4)$$

The theoretical values of EE and LC were calculated by comparing the $I'_{3.57} : I'_{4.6}$ in

Figure 6.23b with $I_{3.57} : I_{4.67}$ obtained by the fitting line in Figure 6.23a inset (Y = 0.12X)

6.2.18 Cell viability (MTT) Study

In a typical MTT assay, 60 wells in a 96-well plate were seeded with HeLa cells at a well

concentration of 5000 cells/well. The cells are incubated overnight with 100 µL Dulbeco's

Modified Eagle Medium (DMEM) at 37 ^{o}C with 5 % CO_2. Initial PFpP colloids with

concentration of 0.10 mg/mL were prepared and were filtered on a membrane to remove bacteria. PFpP colloidal samples with different concentrations were prepared by mixing the colloids with varying amounts of medium and were added to the well. One of the wells in each row was reserved as a control experiment in which no PFpP colloidal sample was added. All the samples were incubated overnight. On the second day, the PFpP sample-medium mixture was removed and replaced with 100 μL of fresh mediums, followed by the addition of 25 μL of MTT reagents. This was left to incubate for 2 h. After the incubation, cell lysate was added to break the cell walls and release the purple formazan. The wells which were mixed with lysate were incubated for an additional 4 h. Finally, the plate was removed and the absorbance of the formazan (at 570 nm) was measured using a SpectraMax M3 microplate reader. Cell viability was normalized to that of the HeLa cells cultured in the normal cell media.

The microscopic experiment of the HeLa cells after treatment with PFpP colloid was achieved as follows: First, the HeLa cells were incubated overnight with 100 μL of Dulbeco's Modified Eagle Medium (DMEM) at 37 ^{o}C with 5 % CO_2. On the second day, the cells were washed two times with PBS, which involved removal of the old medium and the addition of 100 μL of fresh medium. After that, PFpP colloids with concentration of 0.05 mg/mL were added to the well. The sample was then incubated for 4 h. Then the image of the HeLa cells was obtained using a fluorescence microscope (Eclipse Ti-S, Nikon Instruments Inc., Melville, NY) with a CCD camera (Qimaging Retiga 2000R Fast 1394).

6.3 Results and Discussion

6.3.1 PFpP colloidal Solution

PFpP[22, 23] is soluble in organic solvents, e.g., THF, but insoluble in water. As shown in Figure 6.1c, hydrophobic PFpPs float on water. However, when we quickly inject water into a THF solution of PFpPs followed by N_2 bubbling to remove the THF, the polymer is uniformly dispersed in the solution. Figures 6.1d, e illustrate aqueous solutions of PFpPs with various concentrations. Both solutions show a blue tint, suggesting that colloids are formed.[19] In contrast, if water is slowly added to the THF solution of PFpP, the resulting colloids are not uniform and less colloidally stable (Figure S6.1).

Table 6.1 illustrates the results of DLS and zeta-potential measurements for a number of colloids prepared using PFpP with various molecular weights and concentrations. As shown in the table, colloids with a low PDI were obtained regardless of the molecular weight of the PFpPs (entries 1-3 in Table 6.1). The effect of concentration on the self-assembly was investigated for the same sample with $DP_n = 20$ (entries 3-7 in Table 6.1). As shown in the table, when the concentration was reduced from 0.10 mg/mL to 0.00625 mg/mL, the R_h of the colloids decreased from 77 to 42 nm, correspondingly. Meanwhile, the PDI of the aggregates increases, indicating that the size distribution of the aggregates broadened.

Table 6.1 Aqueous self-assembly of PFpPs with various molecular weights and concentrations

Entry	DP_n[a]	Micelle concentration (mg/mL)	R_h (nm)	PDI	Avg. Zeta-potential (mV)	Standard deviation(mV)
1	7[b]	0.10	68.8	0.004	-37.6	8.9
2	63[c]	0.10	62.0	0.025	-44.8	9.2
3	20[d]	0.10	77.0	0.03	-46.3	9.1
4	20	0.05	73.5	0.035	-44.5	8.9
5	20	0.025	61.3	0.086	-44.9	9.0
6	20	0.0125	50.4	0.135	-44.9	8.0
7	20	0.00625	42.2	0.214	-43.7	10.0

[a] Degree of polymerization [b] PDI = 1.21 [c] PDI = 1.73 [d] PDI = 1.35.

Zeta-potential measurements revealed that all colloids had ζ-potentials between -37.6 and -46.3 mV (Table 6.1), i.e. that the surface of the colloids was negatively charged. The colloidal stability therefore can be explained by electrostatic repulsion. It has been reported that the IR absorption frequency for the acyl CO in $CpFePR_3(CO)COCH_3$ appears at 1590-1625 cm^{-1}.[26] This value is much lower than that for the dicarbonyl Fp acyl analogue ($CpFe(CO)_2COCH_3$), which is at 1655 cm^{-1}.[26] This comparison prompted a hypothesis that phosphine-coordinated Fp acyl derivatives might possess a resonance structure with a highly polarized acyl CO group as shown in Figure 6.1b.[24, 26] Our zeta potential experiments (Table 6.1) support this speculation. It is worthy nothing that, for PFpP in the solid state and in pure THF solution, we also observed a low frequency band for the acyl CO at 1604 cm^{-1}, as shown in Figure 6.2.
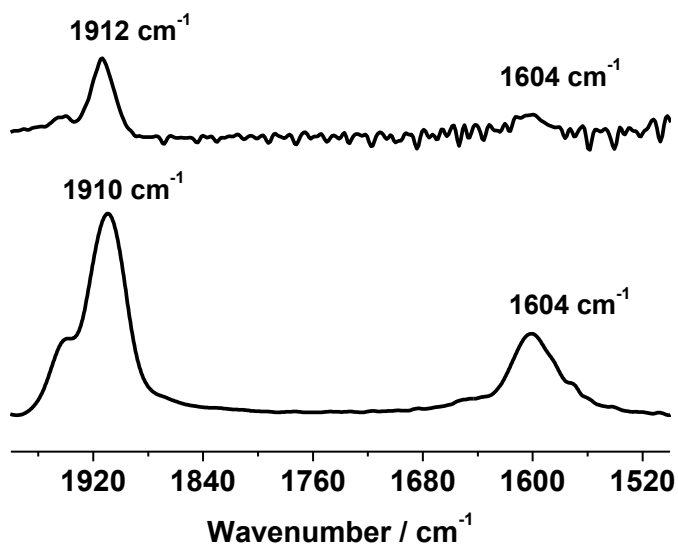
Figure 6.2 (a) FT-IR spectra for PFpP powder and (b) ATR FT-IR for PFpP in dry THF (20.0 mg/mL).

The FT-IR results therefore support that the acyl CO is indeed polarized and that the polymers may possess a resonance structure with a negative charges on oxygen as speculated in previous literature.[24, 26] Colloidal stability of the solution was investigated *via* monitoring the R_h of the colloids as a function of time, and these results are illustrated in Figure 6.3. As shown in the figure, the resulting colloids are stable and maintain their same size over time.
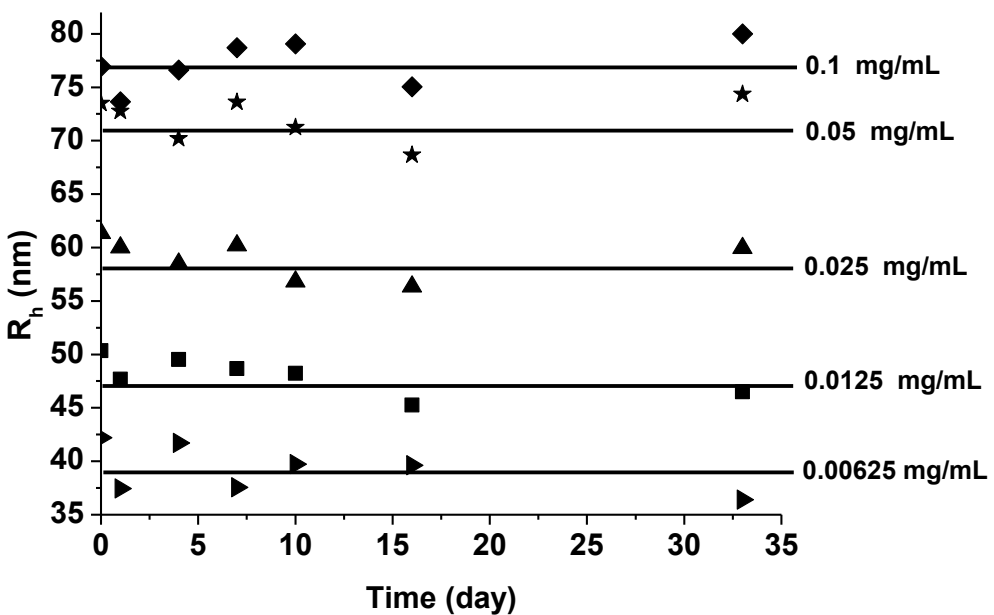
Figure 6.3 R_h of PFpP colloids in water as a function of aging time.

^{31}P and ^{1}H NMR spectroscopy analysis of the materials recycled from the PFpP colloidal solution left for over one month was performed. As shown in Figure 6.4, the ^{31}P NMR spectrum for the materials exhibits two peaks at 73.2 and 35.5 ppm, which are attributed to the main-chain coordinated phosphorus and the oxidized phosphorus end groups, respectively. No additional phosphorus signals appear, indicating no degradation. In the ^{1}H NMR spectrum, the integration ratio for the signals corresponding to the phenyl protons (7.6-7.1 ppm) to that for the Cp protons (4.3 ppm) is 2.2, close to the theoretical value of 2. The integration of the signals for the Cp ring in the main chain and end group ($I_{4.3}/I_{4.5}$) was compared for end group analysis. This calculation revealed that the degree of polymerization was 20, indicating that there was no degradation of the polymer.
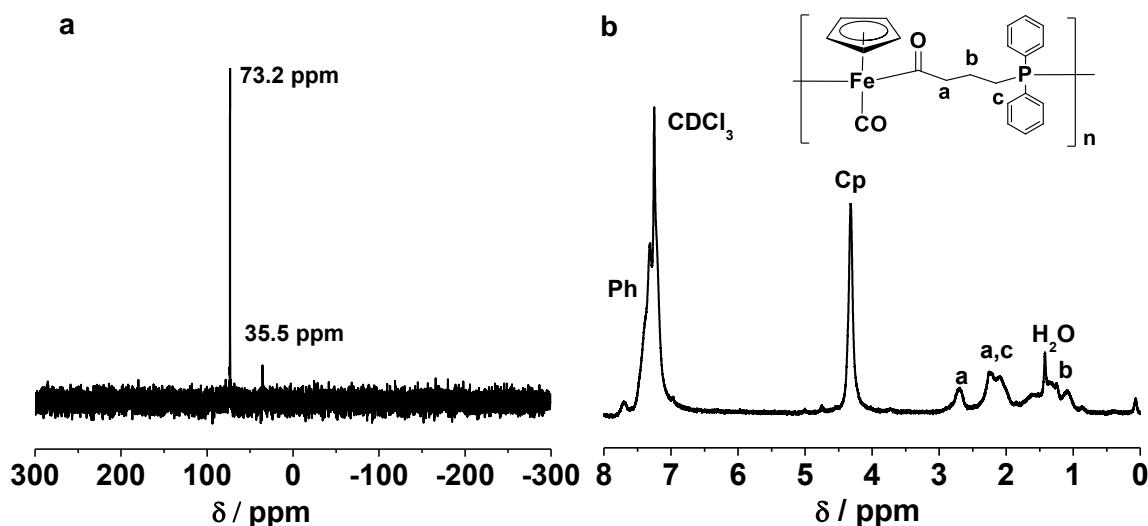
Figure 6.4 (a) ^{31}P NMR spectrum and (b) ^{1}H NMR spectrum for PFpP in CDCl$_3$. The polymers were recovered from their aqueous solution *via* freeze-drying.

GPC measurements were also performed for the PFpP recovered from the aqueous solution was also performed. As shown in Figure 6.5, the molecular weight of the recovered material was 8100 g/mol with a PDI of 1.35, which is similar to the starting PFpP (8200 g/mol). This GPC experiment also confirms that there was no degradation of the polymers.
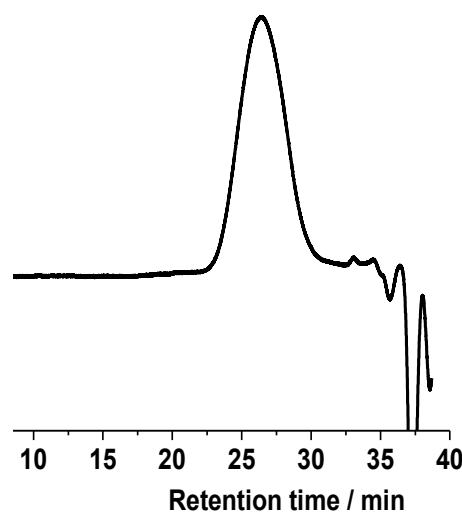
Figure 6.5 GPC curve for PFpPs recovered from their aqueous solution *via* freeze-drying.

6.3.2 Non-amphiphilic character of PFpP

The surface tension of water solutions of PFpP as a function of concentration was measured. As shown in Figure 6.6, there was no discernible drop in surface tension for the solutions at the different concentrations. At 1.25×10^{-5} mol/L (0.10 mg/ml), the PFpP solution clearly displayed a bluish tint (inset in Figure 6.6), indicating that PFpP colloids were formed. The surface tension remained at ca. 72.30 mN/m, close to pure water (71.99 mN/m at 25 $^{\circ}$C).[27] This experiment indicates that hydrophobic PFpPs, as a novel class of building blocks for aqueous colloids, cannot be classified as a classical amphiphile, [28] as these are typically surface active. This idea is supported by the ^{1}H NMR spectrum of the colloids in D_2O. As shown in Figure 6.7, the ^{1}H NMR spectrum for the colloids in D_2O shows no signals corresponding to PFpP. The peak at 4.70 ppm is due to residual H_2O in D_2O, suggesting that PFpPs have no hydrophilic fragments.
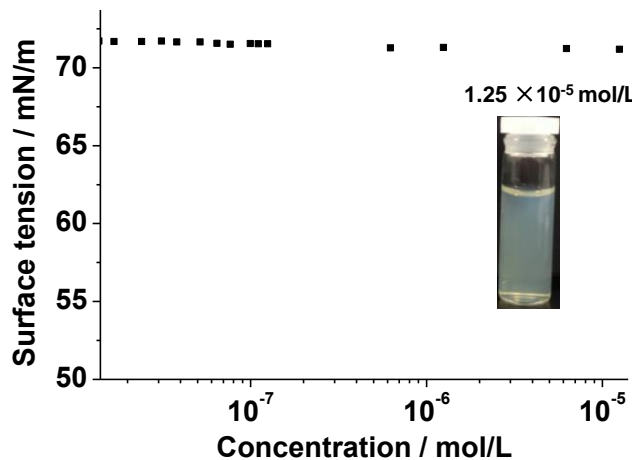
Figure 6.6 Surface tension of water solutions of PFpP as a function of concentration. The inset is a photograph of an aqueous PFpP solution (1.25×10^{-5} mol/L).
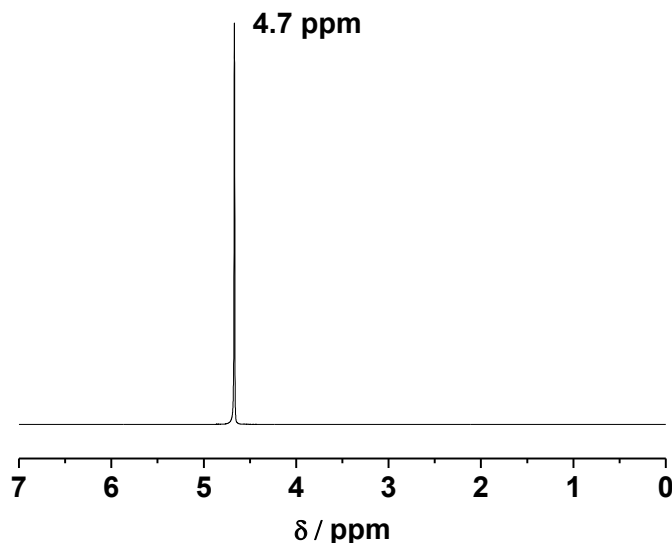
Figure 6.7 ^{1}H NMR spectrum for PFpP colloid in D_2O (0.1 mg/mL).

The hydrophobicity of PFpP colloids was further confirmed using pyrene fluorescence measurement. When PFpP colloids were mixed with pyrene, the fluorescence intensity for the solution was substantially weakened as compared to the intensity of the pure pyrene solution in water. This suggests that pyrene molecules were partially adsorbed by hydrophobic PFpP and their fluorescence was quenched. The detected fluorescence signal emitted from the remaining pyrene in water had a ratio of I_1/I_3 1.7, similar to that of pyrene in pure water (1.8). Moreover, the fluorescence lifetime of the remaining pyrene was 132 ns (inset in Figure 6.8), which is also similar to pyrene in water.
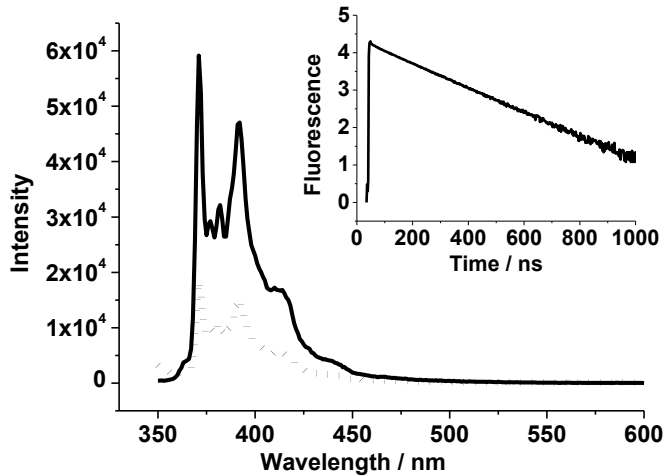
Figure 6.8 Emission spectra for pyrene in water (solid line) and in 0.005 mg/mL PFpP aqueous solution (dotted line). The inset is the pyrene fluorescence decay (excited at 338 nm) measured for the latter solution. The fluorescence lifetime for pyrene in the solution was 132 ns.

6.3.3 PFpP hydration *via* water carbonyl interaction (WCI)

FT-IR, due to its sensitivity to CO, was employed for the investigation of WCI. Figure 6.9 illustrates the IR spectra for PFpP obtained in THF solution with increasing amounts of water. As shown in the figure, PFpP (2 wt%) in 3.00 mL pure THF solution shows one absorption band at 1914 cm^{-1} corresponding to the terminal CO, and the peak at 1603 cm^{-1} is attributed to the acyl CO (*a* in Figure 6.9). When 0.36 mL water was added, the absorption at 1650 cm^{-1} due to water (H-O-H scissor bending)[29] swamped the signal due to the acyl CO (*b* in Figure 6.9). Upon further addition of water, the intensity for the acyl CO absorption (1599 cm^{-1}) was actually enhanced and became visible (*c, d* in Figure 6.9). After a large amount of water (15.00 mL) was introduced into the system, the absorption frequencies for both terminal and acyl COs shifted by 4 cm^{-1} toward lower wavenumbers, suggesting that all the CO groups were hydrated (*d* in Figure 6.9) as a result of WCI.[30] It is interesting that the absorption intensities for both CO signals are

enhanced ca. 10-fold while the concentration of the polymers actually decreased by 6-fold as a result of water addition (a and d in Figure 6.9). Water-enhanced IR absorption of CO groups by 4-5 fold was reported previously,[31, 32] and was explained by an enhanced extinction coefficient[31] resulting from water-induced polarization of the CO groups.[33] The intensity enhancement observed in our experiment is much larger and in the range of surface-enhanced infrared absorption (SEIRA),[34] so negatively charged dielectric PFpP aggregates may also yield a locally enhanced electric field contributing to the observed phenomenon.[35] The detailed mechanism for the enhancement requires further study, but the IR investigation supports that WCI plays a crucial role in driving the self-assembly of hydrophobic PFpPs in water.
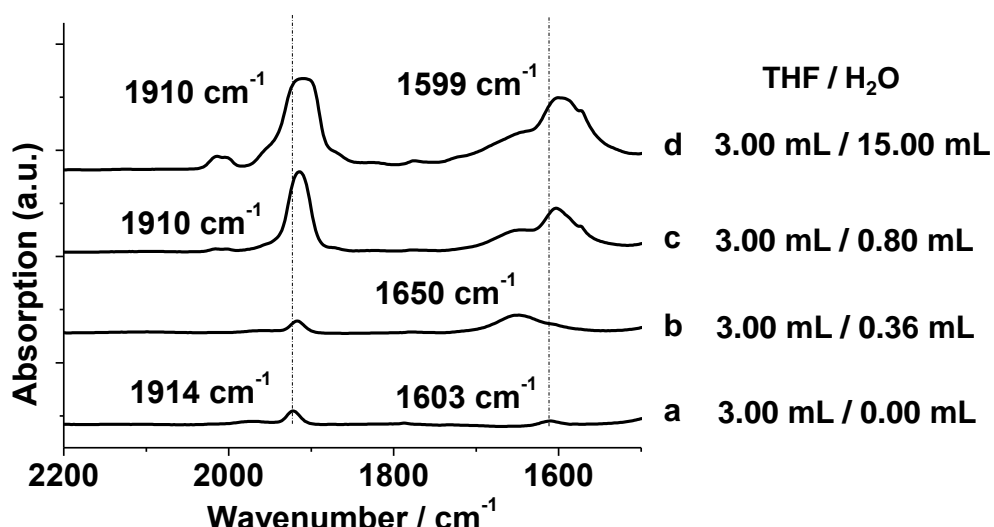
Figure 6.9 In situ FT-IR spectra for PFpP in THF (3.00 mL, 2 wt%) with (a) 0.00 mL; (b) 0.36 mL; (c) 0.80 mL; (d) 15.00 mL water.

The ^{1}H and ^{13}C NMR spectra for PFpP in pure THF-d_8 and THF-d_8/D$_2$O mixed solvents were compared in an attempt to identify hydration effects. No obvious shift for the signals due to PFpP was observed (Figure S6.2 and S6.3), suggesting that the techniques are not sensitive enough. However, ^{31}P NMR spectroscopy, due to its higher sensitivity and broader range of

chemical shifts, is able to detect the spectroscopic difference upon the addition of water to a THF solution of PFpP. As shown in Figure 6.10, an upfield shift of the resonance signal due to the coordinated phosphorus and a downfield shift for the signal due to the oxidized phosphorus chain end were observed as a result of water addition, supporting the occurrence of PFpP hydration.
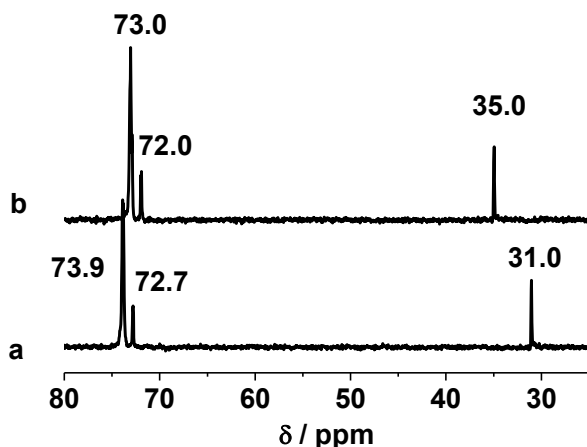
Figure 6.10 ^{31}P NMR spectra for PFpP in THF-d_8 (20.00 mg/mL) (a) without and (b) with 0.10 mL D_2O.

6.3.4 Morphology of PFpP colloids

The morphology of the colloids was investigated *via* a combination of DLS and SLS (static light scattering) analysis. Following multiangle DLS experiments, the decay rates, Γ, were plotted against the square of the scattering vectors, q^2, for two solutions with respective concentrations of 0.009 mg/mL and 0.006 mg/mL (Figure 6.11a and Figure S6.4a). The diffusion coefficients for the two colloids derived from Figure 6.11a and Figure S6.4a were 5.938×10^{-12} and 5.944×10^{-12} cm^2/s, respectively. Based on the Stokes-Einstein equation, the effective R_h for the colloids were 41.11 and 41.07 nm, respectively. Multiangle SLS experiments

for the same samples were used to generate Berry plots, where the scattered intensity, $(I^{-1})^{1/2}$, is

plotted as a function of q^2, (Figure 6.11b and Figure S6.4b). As approximated from the plots, the

R_g (radius of gyration) for the two colloids were 40.0 and 43.9 nm, respectively. The shape

factors of R_g/R_h were therefore calculated to be 0.98 and 1.06, respectively, suggesting that the

two colloids were vesicles.[36]
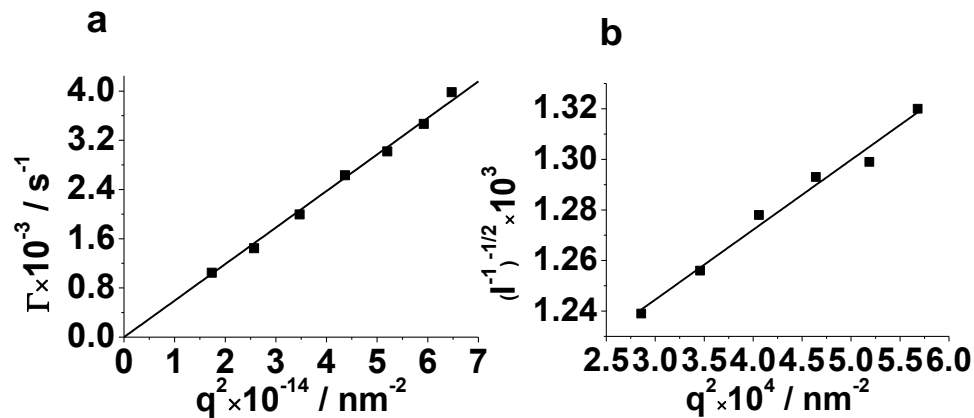
Figure 6.11 (a) DLS data as a function of scattering angle and (b) Berry plot obtained from SLS.

The PFpP concentration was 0.009 mg/mL.

The morphology of PFpP colloids was further verified using a number of TEM techniques.

Using a low voltage (5 kV) benchtop TEM, spherical particles were observed with diameters of

ca. 60 nm (Figure 6.12). As compared to the D_h (hydrodynamic diameter) of 106 nm measured

using DLS, there appears to be significant shrinkage due to drying.
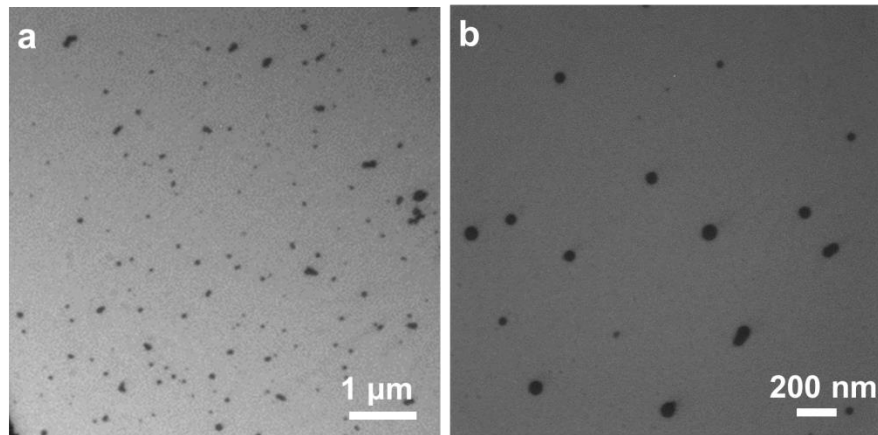
Figure 6.12 TEM images of PFpP vesicles obtained from low voltage benchtop TEM.

When TEM with a high voltage electron beam (60 kV or 200 kV) was used, particles with a relatively darker periphery were observed, suggesting that the spherical nanoparticles were indeed vesicles (Figure 6.13 a, b and c).[37] As shown in Figure 6.13 b, the thickness of the darker periphery was ca. 4.0 nm, suggesting that the walls of the vesicles are very thin. This feature explains the weak contrast for the circumference of the particles relatively to the inner domains (Figure 6.13b), and that no distinguishable contrast was observed for the images obtained from the low voltage TEM (Figure 6.13a). TEM was also performed in the dark-field mode. As shown in Figure 6.13c, the vesicles were bright, indicating strong electron scattering, which is reasonable because the building blocks, PFpPs, contain iron.
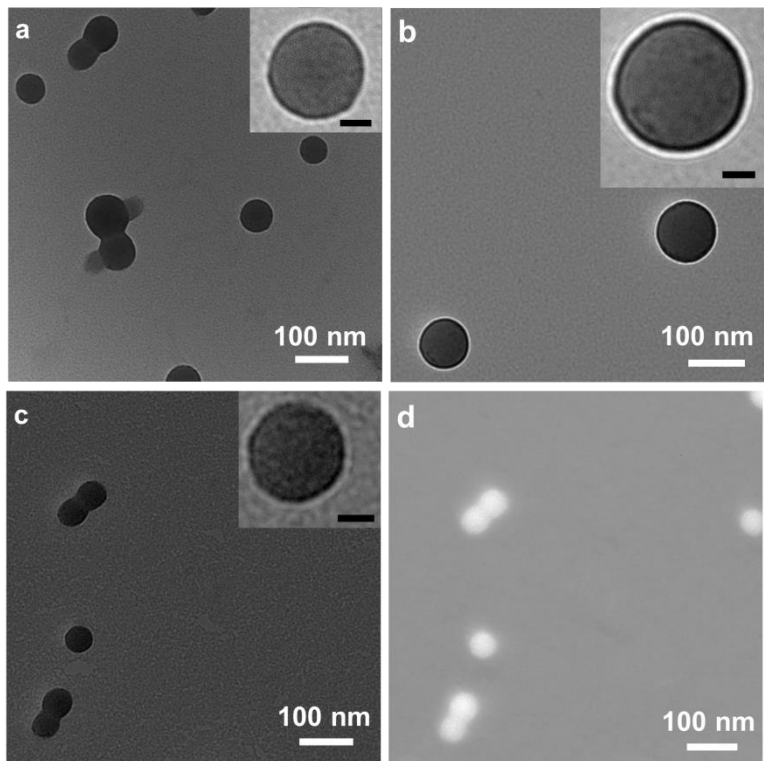
Figure 6.13 TEM images for PFpP vesicles obtained from (a, b) 60 kV TEM; (c) 200 kV TEM with transmission mode; (d) 200 kV TEM with bright-field mode. The concentration of PFpP was 0.1 mg/mL). The scale bar for the insets in a, b and c is 20 nm.

To further demonstrate that particles are formed in water, cryo-TEM was performed. Samples at two concentrations were examined and the images obtained were provided in Figure 6.14a and b. Nanoparticles with a diameter of ca. 95 nm were observed for both samples, close to DLS results (D_h = 106 nm). The particles in Figure 6.14a show slight elongation, suggesting that the vesicles with thin walls are prone to deformation upon vitrification of the water. Despite the low contrast, darker peripheries are discernible for the particles. The thickness of the periphery was around 3.0 nm, slightly thinner as compared to that estimated from Figure 6.14b. Although the estimation of vesicle membrane thickness from TEM images is commonly achieved in research,[37] experimental error cannot be avoided. Particularly for thin membrane PFpP vesicles.

The precise value for the thickness is a matter of further characterization using other techniques, e.g., small-angle X-ray scattering.[38]
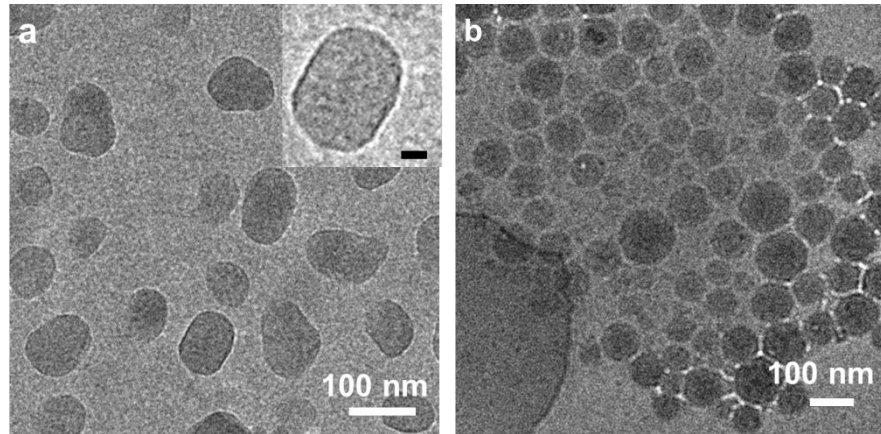
Figure 6.14 Cryo-TEM images for PFpP vesicles with concentration of (a) 0.1 mg/mL; (b) 0.05 mg/mL. (Scale bar for the insets in Figure a is 20 nm)

AFM analysis of the PFpP colloids dried from their aqueous solutions was also performed in the tapping mode. The phase image is displayed in Figure 6.15a, and section analyses of the height image are displayed in Figures 6.15b and 6.15c. These indicate that the diameter for the particles was ca. 113 nm, which is comparable with the DLS results (D_h = 106 nm). Their height is only ca. 27 nm however (Figure 6.15c), with a diameter-to-height ratio of ca. 4.0. This ratio suggests that these PFpP particles adopt a spherical 'cap' topology, in agreement with the model for the deformation of a vesicle bound to a planar surface.[39] It is noteworthy that PFpP vesicles are relatively rigid as compared to polymersomes assembled from block copolymers.[40, 41] For example, although the membrane for poly(ε-caprolactone)-b-poly[2-(methacryloyloxy)ethyl phosphorylcholine] (PCL-b-PMPC) vesicles (ca. 20.0 nm) was much thicker than that for PFpP (ca. 3.0-4.0 nm) estimated from TEM, the height of the PCL-b-PMPC particles from AFM analysis was only ca. 3.0 nm.[40]
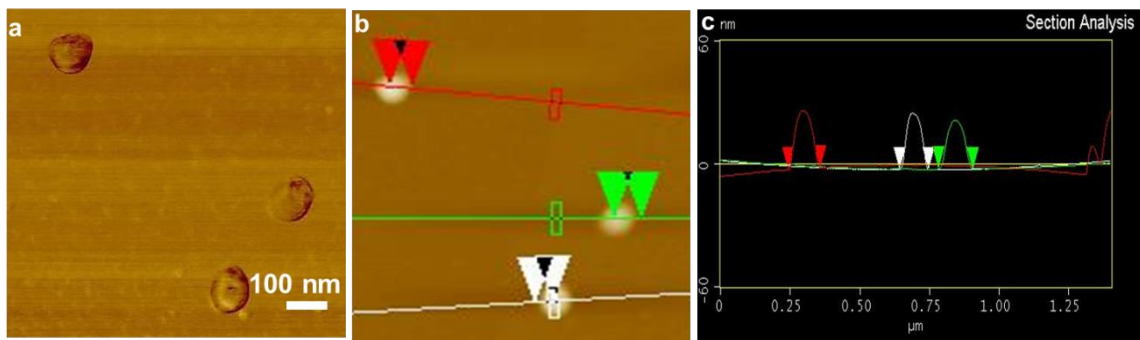
Figure 6.15 AFM images for PFpP colloids dried from their aqueous solutions (0.10 mg/mL) in (a) phase contrast mode, (b) height mode, and (c) corresponding height profile along the scan lines. The sample was prepared by spin coating of a PFpP colloidal solution on a freshly cleaved mica substrate.

6.3.5 Encapsulation of hydrophilic molecules in PFpP colloids

The encapsulation capability of PFpP aqueous vesicles was first explored using calcein, a self-quenching hydrophilic fluorescent dye. Using nano-precipitation,[42] the dye molecules were enclosed by preparing the PFpP colloidal solution in the presence of calcein. DLS characterization indicated that the colloids had R_h = 77 nm with PDI of 0.06 (Figure 6.16). This value is similar to PFpP colloids prepared in the absence of calcein, and therefore suggests that the presence of calcein does not affect self-assembly.
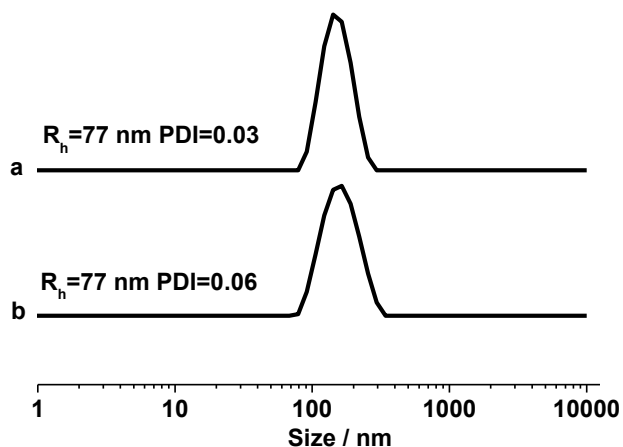
Figure 6.16 (a) DLS results for PFpP colloids (0.1 mg/mL) and (b) PFpP colloids (0.1 mg/mL) with calcein encapsulated.

The presence of calcein in the colloids was also verified using UV-vis spectroscopy. As shown in Figure 6.17, an absorption peak at 495 nm arising from calcein was observed.
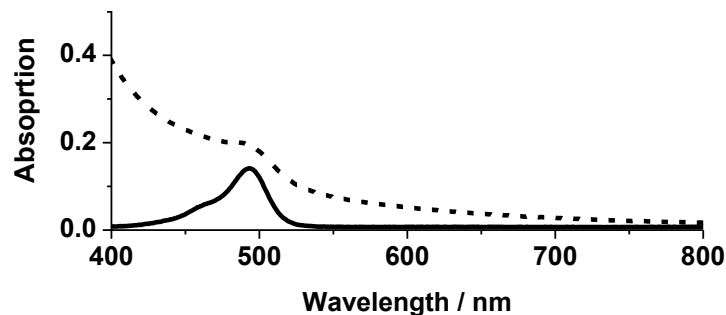
Figure 6.17 UV-vis absorption of free calcein in water (solid line) and PFpP colloid prepared in the presence of calcein (dashed line).

Fluorescence experiments for the colloids with enclosed calcein were performed. It is striking that the solution displayed almost no fluorescence emission (Figure 6.18b), suggesting that there were no free dye molecules in the solution. In other words, the calcein molecules were fully encapsulated and their fluorescence was quenched. To verify this, thin layer chromatography (TLC) experiments using water as eluent was performed. Water eluent can push calcein to the solvent front (image ⅰ in Figure 6.18a) and separate the dye molecules from PFpP if calcein

and separately prepared PFpP colloids were merely mixed together (image ⅱ in Figure 6.18a).

For the PFpP colloids with calcein enclosed *via* nano-precipitation (image ⅲ in Figure 6.18a),

no calcein spot is detected, which confirmed that the PFpP vesicles were able to enclose

hydrophilic calcein with a high encapsulation efficiency (EE). Based on the weight ratio of

calcein and PFpP used in the experiments, the loading capacity (LC) was ca. 1.0 wt%.
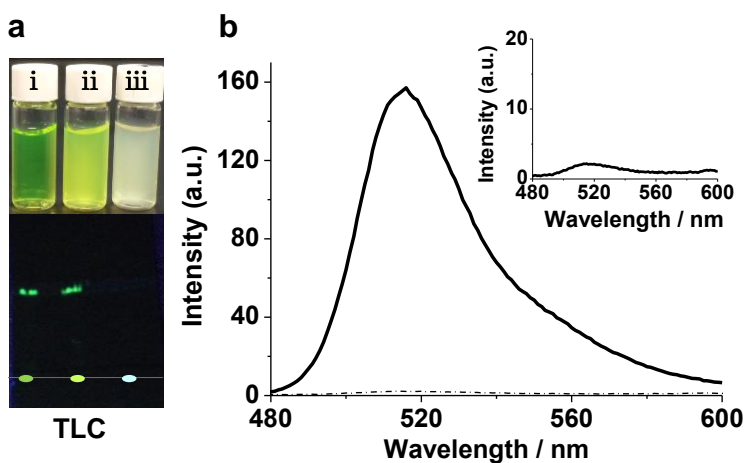
Figure 6.18 (a) Photographs for solutions and TLC results for free calcein in water (ⅰ); PFpP

colloids mixed with calcein (ⅱ); and PFpP colloids prepared in the presence of calcein (ⅲ). (b)

Emission spectra for calcein in water (solid curve) and encapsulated by PFpP (0.10 mg/mL)

(dash curve). The inset is the enlargement of the emission spectrum for PFpP colloids with

encapsulated calcein.

To explore the LC potential of PFpP vesicles for hydrophilic molecules *via* nano-precipitation,

a guest molecule with a high solubility in both THF and water was required, such as

poly(ethylene glycol) (PEG). PFpP (1.00 mg) colloids were first prepared in the presence of

5.00 and 100.00 mg of PEG, and subsequently characterized using TEM and DLS. For the

sample with a relatively small amount of PEG (5.00 mg), DLS revealed that D_h of the colloids

was 110 nm. A spherical morphology with a diameter of ca. 60 nm was observed from the TEM

image (Figure 6.19a), which is similar to the empty PFpP vesicles (Figure 6.13b). The shrinkage of the colloids upon drying accounts for the discrepancy in the estimated diameters as discussed above. The darker periphery can also be observed by carefully examining the spherical particles (inset in Figure 6.19a), although it is not obvious as compared to the empty PFpP vesicles (Figure 6.13b). In contrast, when a PFpP (1.00 mg) colloidal solution was prepared in the presence of a larger amount of PEG (100.0 mg), the D_h was determined to be 121 nm by DLS and 120 nm from the TEM image (Figure 6.19b). The similarity between the D_h from DLS and TEM suggests that there is no obvious shrinkage of the colloids upon drying, and can be reasonably explained due to the encapsulation of PEG. We also measured the zeta-potential for the PFpP colloids prepared in the presence of PEG (100 mg), which was determined to be -42.6 mV, similar to the empty PFpP colloids (Table 6.1). We can therefore rule out the possibility of PEG adsorption on the surface of the PFpP colloids.

To further verify the occurrence of encapsulation, AFM analysis was performed. As shown in Figure 6.20, phase imaging shows obvious contrast in softness as compared to Figure 6.15a for empty PFpP colloids. This contrast may be caused by the location of the PEG molecules within the PFpP vesicles in the dry state. Height analysis of the image (Figure 6.20b and 6.20c) reveals that the height for the colloids is ca. 63 nm. The diameter-to-height ratio is 1.80, much smaller than that for the empty PFpP vesicles (ca. 4.00). It is reasonable that the vesicles be less deformed when they are filled with guest molecules. Therefore, the combination of TEM, zeta-potential and AFM measurement supports that PEG encapsulation occurred. In an attempt to encapsulate 200 mg of PEG into 1.0 mg PFpP vesicles, PEG-encapsulated PFpP spherical colloids were also

obtained. The diameters for the colloids in solution and in the dry state were the same, but larger than when less PEG was encapsulated (Figure S6.6).
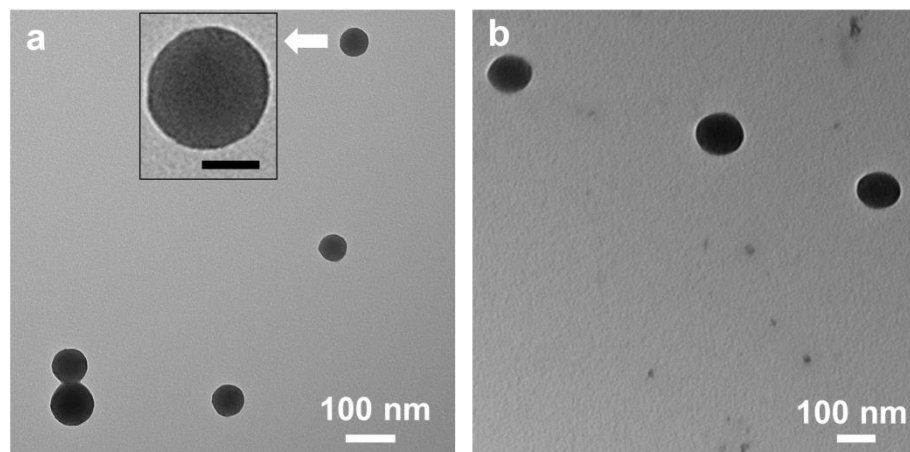
Figure 6.19 TEM images for PFpP (1.0 mg) colloids prepared in the presence of (a) 5.0 mg of PEG and (b) 200.0 mg of PEG. The scale bar for the inset is 30 nm. The TEM samples were prepared from PFpP colloidal solutions in which unencapsulated PEG was removed *via* dialysis.
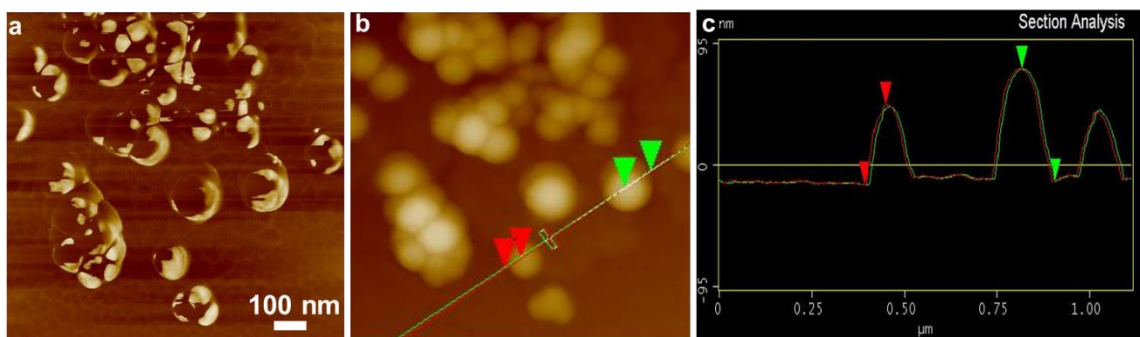
Figure 6.20 AFM images for PFpP colloids dried from aqueous solutions (0.1 mg/mL) in (a) phase contrast mode, (b) height mode, and (c) corresponding height profile along the scan lines. The sample was prepared by drying a drop of PFpP colloidal solution on a freshly cleaved mica substrate.

In order to quantify EE and LC, a NMR technique was explored to estimate the percentage of encapsulated and unencapsulated PEG. Instead of H_2O, D_2O was used as a solvent for the

nano-precipitation. The ^{1}H NMR spectrum for pure PEG in D_2O, as illustrated in Figure 6.21a, shows a peak at 4.67 ppm due to residual H_2O in D_2O, and a peak at 3.57 ppm due to PEG. The integration ratio for these two peaks ($I_{3.57}$: $I_{4.67}$) proportionally increases with the concentration of PEG (inset in Figure 6.21a), suggesting that the signal due to the residual H_2O can be used as an internal standard for the mass estimation of PEG in D_2O. Figure 6.21b displays the spectra for PFpP colloidal solutions prepared in the presence of PEG. The concentrations of PEG used for the experiments were the same as in the corresponding spectra in Figure 6.21a. As shown in Figure 6.21b, no signal corresponding to PFpP was observed as expected (Figure 6.7) and the intensity of the signals due to PEG (3.57 ppm) relatively to H_2O (4.67 ppm) was relatively weak as compared with Figure 6.21a, suggesting that a fraction of PEG molecules was encapsulated and showed no NMR signal. If it is true that the signal at 3.57 ppm in Figure 6.21b is due to unencapsulated PEG, the EE and LC can then be calculated by comparing the integration ratio of $I'_{3.57}$: $I'_{4.6}$ in Figure 6.21b with the ratio of $I_{3.57}$: $I_{4.67}$ in Figure 6.21a.
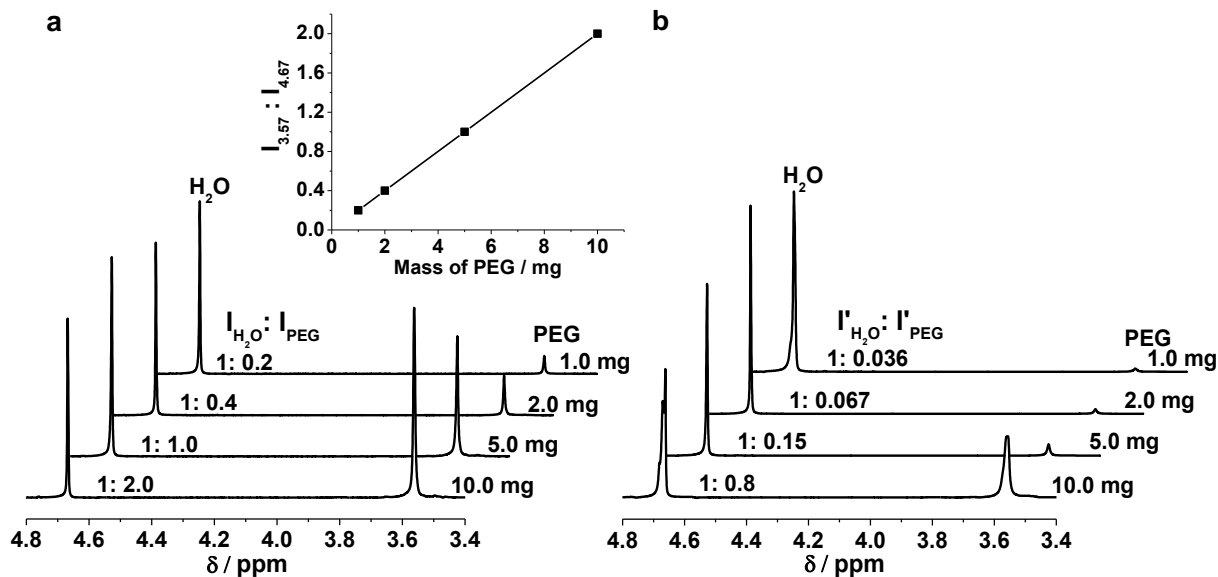
Figure 6.21 (a) ^{1}H NMR spectra for PEG in D$_2$O at various concentrations (the inset is a plot of the integration ratio of I$_{3.57}$: I$_{4.67}$ as a function of the mass of PEG); (b) ^{1}H NMR spectra for PFpP colloids prepared in the presence of various amount of PEG in D$_2$O.

To confirm that encapsulated PEG produced no NMR signal, the solution of PFpP prepared in the presence of 5.0 mg PEG was dialyzed against D$_2$O for 5 days. After dialysis, the NMR spectrum (Figure 6.22a) showed no signal at 3.57 ppm, suggesting that the unencapsulated PEG had been removed. The resulting PFpP colloids were freeze-dried and the recovered solids were dissolved in CDCl$_3$, a good solvent for both PFpP and PEG, for NMR analysis. As shown in Figure 6.22b, the signal at 3.57 ppm appears clearly, indicating that PEG has been released due to the disassembly of PFpP aggregates in CDCl$_3$. The Cp signal representing PFpP appears at 4.3 ppm. The integration ratio for the signals due to PEG and Cp is 30 : 1. Based on this ratio and the amount of PFpP used for the experiment, the mass of encapsulated PEG can be calculated using the following equation:

$$\left\{\frac{Mass_{PEG} \times DP_{PEG} \times 4}{M_{n,PEG}}\right\} \bigg/ \left\{\frac{Mass_{PFpP} \times DP_{PFpP} \times 5}{M_{n,PFpP}}\right\} = 30\!:\!1$$

DP_{PEG} is the degree of polymerization of PEG, which is 45.

$M_{n,PEG}$ is the number average molecular weight of PEG, which is 2000 g/mol.

$Mass_{PFpP}$ is the mass of PFpP used for the encapsulation of PEG, which is 1.0 mg.

DP_{PFpP} is the degree of polymerization of PFpP, which is 20.

$M_{n,PFpP}$ is the number average molecular weight of PFpP, which is 8000 g/mol.

The mass of encapsulated PEG can be calculated to be 4.17 mg. This value is close to that calculated from Figure 6.21 (4.25 mg), by comparing the ratio of $I'_{3.57}$: $I'_{4.6}$ (in the colloidal solution before dialysis, Figure 6.21b) with $I_{3.57}$: $I_{4.67}$ (in the PEG solution without PFpP, Figure 6.21a). This experiment demonstrates that the encapsulated PEG shows no NMR signal. This NMR technique was further verified *via* gravimetric analysis of a PFpP colloidal solution prepared in the presence of 200 mg PEG. The colloidal solution was first dialyzed against water to remove unencapsulated PEG, then the encapsulated PEG was recovered *via* freeze-drying. The mass of encapsulated PEG was found to be 102 mg, which is close to the value estimated from the NMR calculation (115 mg). Therefore, it is confirmed that the EE and LC for PFpP encapsulation *via* nano-precipitation can be calculated by ^{1}H NMR analysis as shown in Figure 6.21.
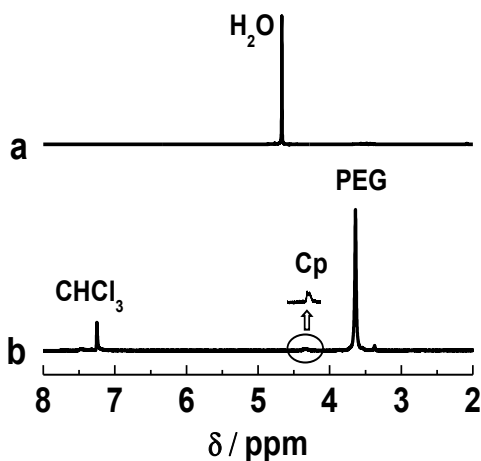
Figure 6.22 (a) ^{1}H NMR spectrum for PFpP (1.0 mg) colloids prepared in the presence of PEG (5.0 mg) and subsequently dialyzed against D_2O; (b) ^{1}H NMR spectrum for PFpP and encapsulated PEG in in CDCl$_3$, The sample was recovered from the dialyzed PFpP colloids *via* freeze-drying.

Attempts to encapsulate larger amounts of PEG were also made. The ^{1}H NMR spectrum for D_2O solutions with various amount of PEG and PFpP colloidal solutions, prepared in the presence of different amounts of PEG in D_2O, are illustrated in Figure 6.23a and Figure 6.23b, respectively. As shown in Figure 6.23a, when PEG was dissolved in D_2O, two peaks at 4.67 ppm and 3.57 ppm were observed. The peak at 4.67 ppm was due to H_2O in D_2O and the peak at 3.57 ppm was attributed to PEG. The ratio of $I_{3.57} : I_{4.67}$ displays a linear relationship with the mass of PEG. This result indicates that the residual H_2O in D_2O can be used as an internal reference for the estimation of the mass of PEG in D_2O. When PFpP colloids were prepared in the presence of various amounts of PEG, the two peaks at 4.67 ppm and 3.57ppm were still observed (Figure 6.23b). However, the integration ratio of $I'_{3.57} : I'_{4.6}$ in Figure 6.23b was smaller as compared to $I_{3.57} : I_{4.6}$ in Figure 6.23a, due to the encapsulation of PEG molecules in the PFpP vesicles. Therefore, the encapsulation efficiency (EE) and loading capacity (LC) can be

155

calculated by comparing the ratio of $I'_{3.57}$: $I'_{4.6}$ (Figure 6.23b) with $I_{3.57}$: $I_{4.67}$ (Figure 6.23a) as illustrated in Figure 6.24.
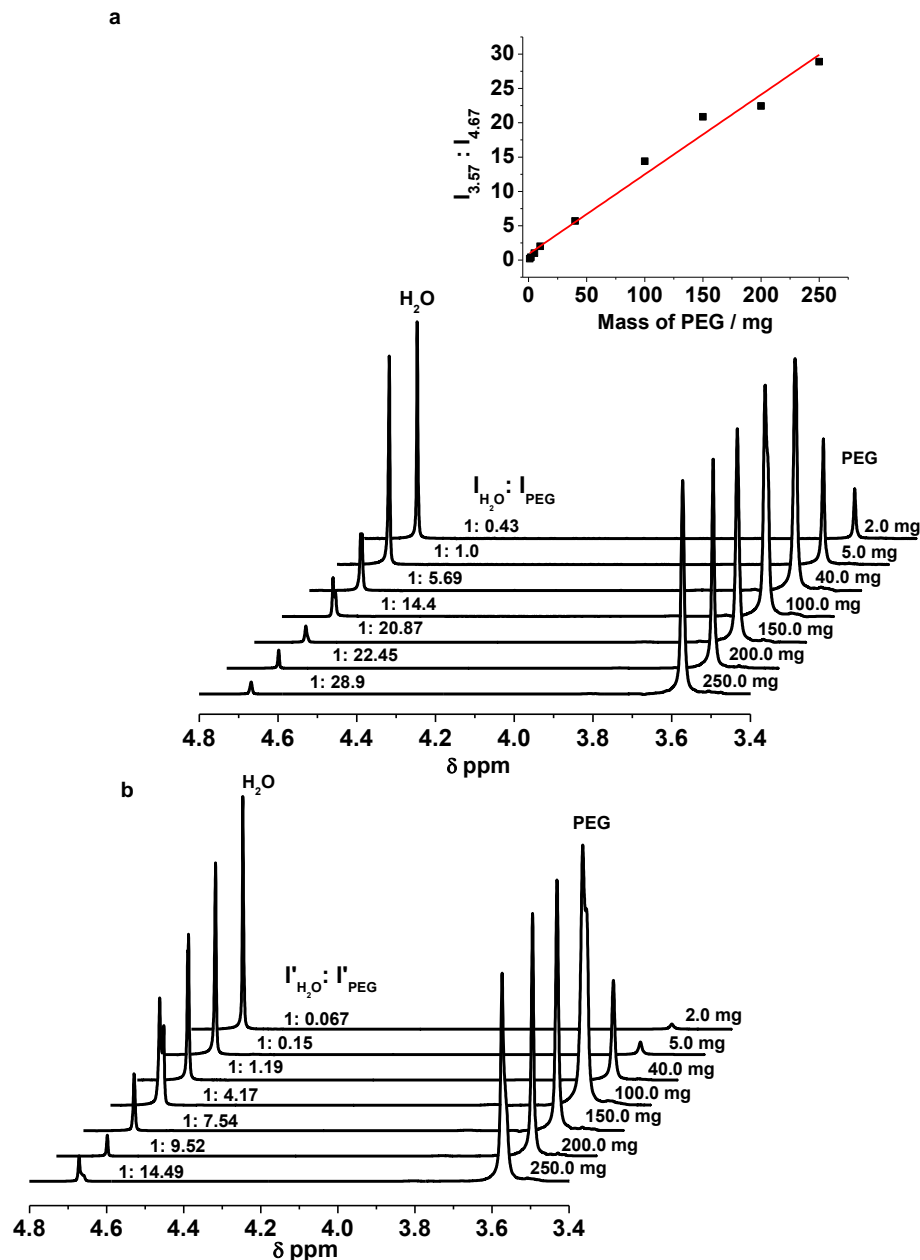
Figure 6.23 (a) ^{1}H NMR spectra for PEG in D_2O with various concentrations and (b) ^{1}H NMR spectra for PFpP (1.0 mg) colloids prepared in the presence of various amount of PEG in D_2O.

As shown in the Figure, when the PEG/PFpP ratio is relatively low, the EE is extremely high (Figure 6.24). For example, for the colloids prepared in the presence of 5.0 mg PEG, the EE was 85 % and LC was 425 %. By increasing the ratio of PEG/PFpP, EE slightly dropped but still

remained at a fairly high level (greater than 50 wt%). Particularly, PFpP vesicles have exceptionally high LC. For the solution prepared from 1.0 mg PFpP in the presence of 250 mg PEG, LC can reach 12450 wt% by comparing the mass ratio of the encapsulated PEG and the PFpP. In other words, 1.0 mg PFpP can enclose 124.5 mg PEG.
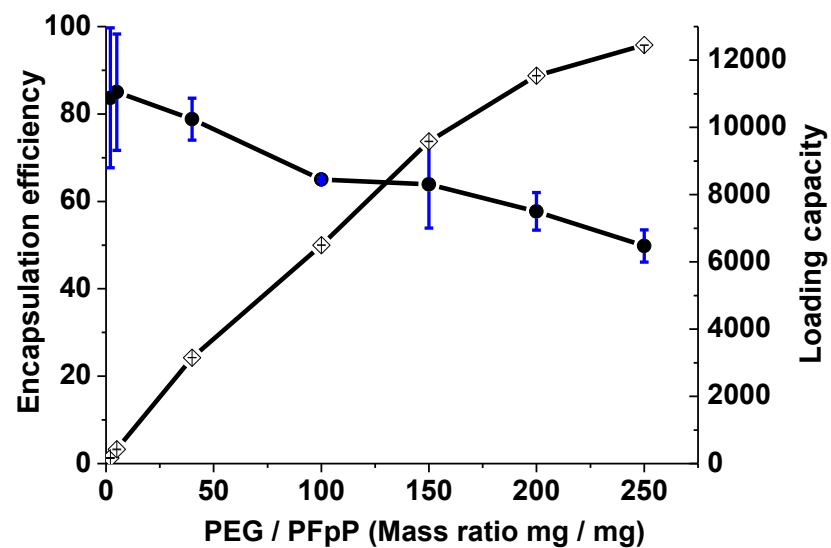

Figure 6.24 Encapsulation efficiency (●) and loading capacity (◇) of PEG in PFpP vesicles *via* nano-precipitation of PFpP (1.0 mg) in the presence of various amounts of PEG.

It is noteworthy that the encapsulation of hydrophilic molecules *via* nano-precipitation using amphiphilic molecules is not efficient, and this remains an unresolved challenge.[43] For example, the EE for the vesicles assembled from amphiphilic block copolymers was only ca. 6.0 % in a number of recent reports,[44-46] and the LC could reach up to ca. 74 %.[45] Other complicated encapsulation techniques, e.g., oil/water emulsion,[43] ionic complexation[47] are currently used if high EE and LC are required. Our discovery therefore represents a significant breakthrough for the encapsulation of hydrophilic molecules *via* nano-precipitation. This success can be attributed

to the hydrophobic nature and non-surface activity of PFpP, which will be investigated in detail in our future work.

Since the biomedical area is a major field for vesicle applications, preliminary cell viability tests using the MTT assay were performed. As shown in Figure 6.25, the colloids exhibit negligible toxicity to HeLa cells at various concentrations. The average cell viability was above 90 %. Optical microscopic view of HeLa cells after treating with PFpP colloids (Figure 6.25b) also showed that the HeLa cells were alive, which indicates good biocompatibility of the PFpP colloids with the cells. Therefore, the high encapsulation capacity, non-toxicity and uniformity in size make PFpP vesicles promising for biomedical application.
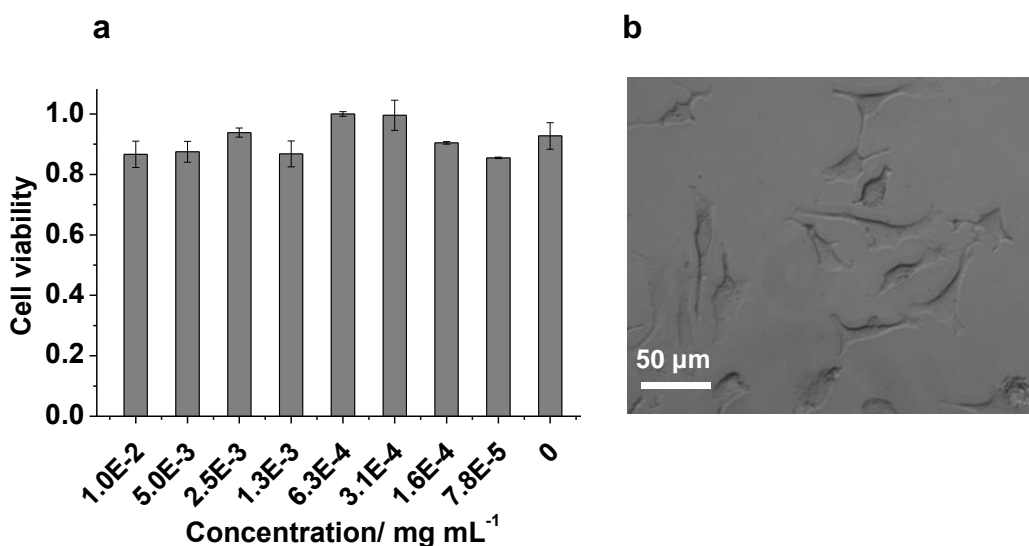

Figure 6.25 (a) Cell viability as a function of PFpP concentration measured using MTT assay and (b) Optical microscopic view of HeLa cell after treatment with PFpP colloids (0.05 mg/mL).

6.4 Conclusions

In summary, we discovered that hydrophobic metal carbonyl macromolecules, PFpPs, can be hydrated and subsequently self-assemble in water into uniform vesicles. IR and NMR analysis indicates that WCI is responsible for the assembly. The vesicles are able to encapsulate hydrophilic molecules, e.g., calcein and PEG, with exceptionally high EE and LC for PEG up to 85 and 12450 wt%, respectively. This discovery resolves a long-standing challenge remaining in nano-precipitation for the encapsulation of hydrophilic molecules.[43] This work establishes the concept that hydrophobic macromolecules can be used as building blocks for aqueous self-assembly *via* hydration forces. Further exploration of this concept offers possibilities for novel functional materials and understanding of related biological systems.[1-3]

Chapter 7. Summary

Migration insertion polymerization (MIP) has been developed, resulting in two examples of main-chain metal carbonyl organometallic macromolecules. Self-assembly of the resulting macromolecules has been explored.

$CpFe(CO)_2(CH_2)_3PPh_2$ (FpP), containing cyclopentadienylironcarbonyl (Fp) and phosphine groups, was synthesized and characterized. Solution polymerization of FpPs resulted in PFpP oligomers with $DP_n = 11$, cyclic molecules and THF-insoluble material (Chapter 2).

Bulk polymerization of FpP was performed, resulting in THF-soluble macromolecules without cyclics, and THF-insoluble material. Relatively high molecular weight PFpP was synthesized at 105 ^{o}C in the presence of DMSO. TGA revealed that the resulting polymers are thermally stable up to 180 ^{o}C, and DSC results showed that the resulting polymers have a T_g of 99 ^{o}C (Chapter 3).

A series of alkyldiphenylphosphine-functionalized PFpP were synthesized by taking advantage of the reactivity of the Fp end group in PFpP oligomers. Prolonged reaction time and excess amounts of alkyldiphenylphosphine were required to overcome the steric effects of the alkyldiphenylphosphine group(Chapter 4).

Metalation and functionalization of the Cp ligand in FpC6 was performed, resulting in $[\eta^5\text{-}Ph_2P(CH_2)_3C_5H_4]Fe(CO)_2(CH_2)_5CH_3$, FpP^{Cp}, with a phosphine group tethered on the Cp ring. Bulk polymerization of FpP^{Cp} at 105 ^{o}C produced oligo-$PFpP^{Cp}$ with M_n of 4200 g/mol (Chapter 5).

The PFpP homopolymer is able to self-assemble into uniform and stable vesicles in water.

Water carbonyl interactions are responsible for the stability of the colloids. The encapsulation of

hydrophilic molecules, including calcein and PEG, within the PFpP vesicles was achieved with

high encapsulation capacity (Chapter 6).

Chapter 8. Suggestions for Future Work

8.1 Synthesis of new monomers with less hindered phosphine ligands or non-iron metal centers for migration insertion polymerization

As discussed in Chapter 3, the reactivity of the phosphine end group gradually dropped during the polymerization, which is probably a reason why low molecular weight polymers were produced. Therefore, the synthesis of monomers with less sterically hindered phosphine ligands would be desired. For example, monomers with two methyl groups on the phosphines can be synthesized and used for migration insertion polymerization as shown in Scheme 8.1.
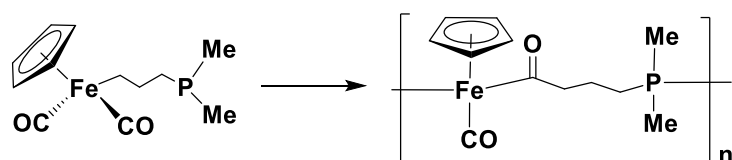
Scheme 8.1 Synthesis and migration insertion polymerization of FpP with two methyl groups on phosphine.

On the other hand, it would also be interesting to synthesize non-iron metal carbonyl organometallic monomers (Scheme 8.2) and to investigate their polymerization behavior.
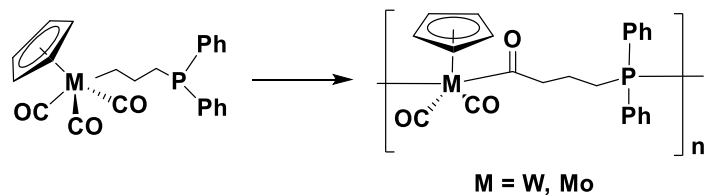

Scheme 8.2 Synthesis and migration insertion polymerization of monomers with non-iron metal centers.

8.2 Electrochemical properties of FpPs and their cyclic and polymeric molecules

The redox properties of metal-containing polymers have been applied to the fabrication of redox-responsive materials[1] or as a trigger for drug release.[2] It would be necessary to study the reduction and oxidation as well as reversibility of PFpP. Meanwhile, it would be also interesting to compare the electrochemical properties PFpPs with monomers and cyclic molecules, which would help us to understand structure dependent electrochemical properties.

8.3 Lewis acid catalyzed migration insertion polymerization

It is well known that Lewis acids such as $AlBr_3$ can coordinate to metal carbonyl compounds, e.g., $(\eta^5\text{-}C_5H_5)Fe(CO)_2CH_3$ to produce acyl derivatives,[3] as shown in Scheme 8.3. Due to the formation of Lewis acid adducts a rapid alkyl migration was achieved.[3]
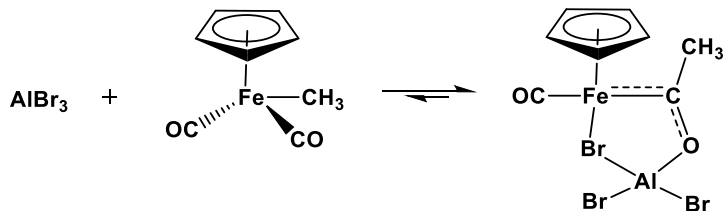
**Scheme 8.3** Coordination of $(\eta^5\text{-}C_5H_5)Fe(CO)_2CH_3$ with $AlBr_3$.

It would therefore be interesting to investigate the coordination of FpP with Lewis acids and the effect of Lewis acids on the migration insertion polymerization of FpPs. The coordination of Lewis acids with $(\eta^5\text{-}C_5H_5)Fe(CO)_2CH_3$ or $(\eta^5\text{-}C_5H_5)Fe(CO)_2(CH_2)_5CH_3$ can be studied first using FT-IR and ^1H NMR spectroscopies. Then the complexation of $AlBr_3$ and $AlCl_3$ with FpPs can be investigated.

163

8.4 Synthesis of block copolymers using migration insertion reaction

In addition to the synthesis of organometallic monomers for migration insertion polymerization, the migration insertion reaction can also be used to prepare block copolymers *via* end group coupling reactions of two homopolymers with Fp and phosphine groups, respectively. One example for the synthesis of a PMMA-*b*-PEG diblock copolymer using migration insertion reaction is illustrated in Scheme 8.4.
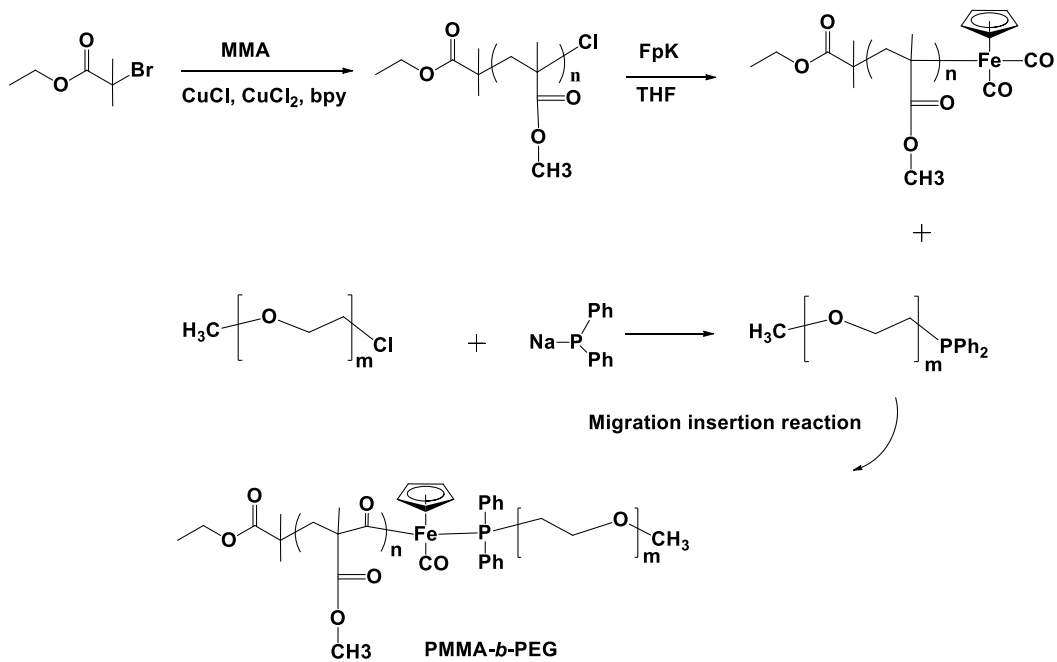
Scheme 8.4 Synthesis of PMMA-*b*-PEG diblock copolymer *via* migration insertion reaction.

Chapter 2 Supporting information
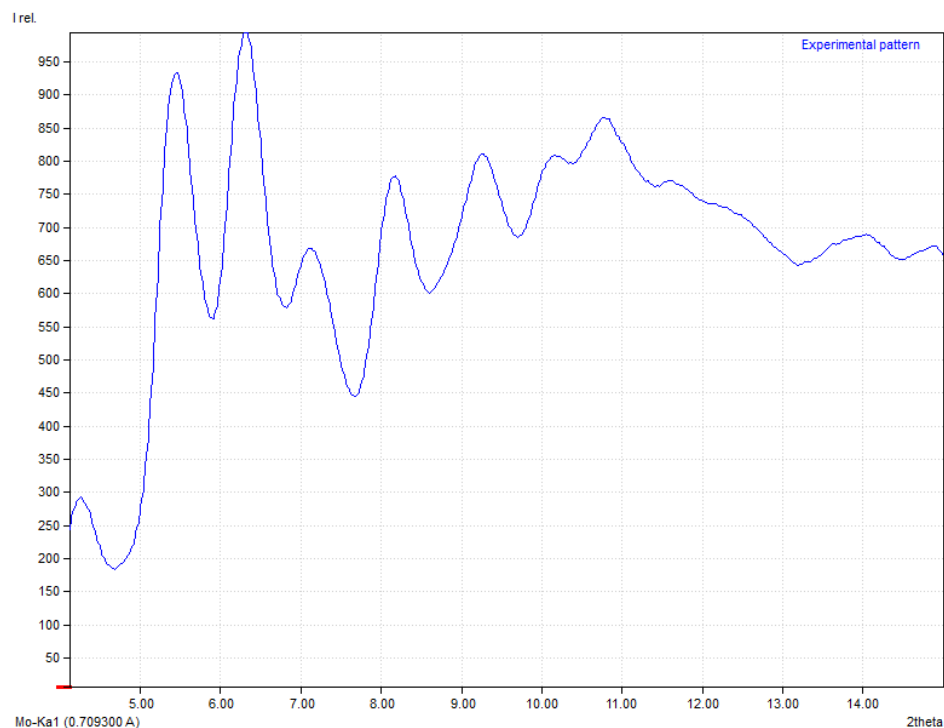
Figure S2.1 Powder X-ray diffraction pattern for the insoluble materials produced from solution MIP of FpP.

Table S2.1 Summary of crystal data and structure refinement for FpP, 5-membered ring and

6-membered ring

	FpP	5-membered ring	6-membered ring
Empirical Formula	$C_{22}H_{21}O_2PFe$	$C_{21}H_{21}OPFe$	$C_{22}H_{21}O_2PFe$
Formula Weight	404.21	376.20 g/mol	404.21 g/mol
Temperature	296(2) K	200(2) K	296(2) K
Wavelength	0.71073 Å	0.71073 Å	0.71073 Å
Crystal System	Monoclinic	Monoclinic	Monoclinic
Space Group	$P2_1/c$	$P2_1/c$	$P2_1/c$
A	8.6898(2) Å	16.2810(8) Å	10.3890(4) Å
B	24.7491(7) Å	7.8128(4) Å	12.5243(3) Å
C	10.1917(3) Å	15.0261(7) Å	14.4003(4) Å
A	90 °	90°	90°
B	110.519(2) °	110.433(2)°	94.592(2)°
Γ	90 °	90°	90°
Volume	2052.81(10) Å^3	1791.06(15) Å^3	1867.68(10) Å^3
Z, calculated Density	4, 1.308 g/cm^3	4, 1.395 g/cm^3	4, 1.438 g/cm^3
Absorption Coefficient	0.824 mm^{-1}	0.935 mm^{-1}	0.906 mm^{-1}
F(000)	840	784	840
θ range for data collection	2.29 to 28.00 °	1.33 to 28.00°	1.97 to 28.00°
Reflections collected /unique	34800/4972[R(int)=0.0648]	38882/4310[R$_{(int)}$= 0.0201]	20942/4424[R$_{(int)}$= 0.0211]
Completeness to θ = 28.00	100.0 %	99.7 %	98.1 %
Refinement method	Full-matrix least-squares on F^2	Full-matrix least-squares on F^2	Full-matrix least-squares on F^2
Data / restraints / parameters	4972 / 0 / 235	4310 / 0 / 217	4424 / 0 / 236
Goodness-of-fit on F^2	1.054	1.065	1.306
Final R indices [I>2σ(I)]	R1=0.0436,wR2= 0.0787	R1=0.0219, wR2 = 0.0576	R1=0.0248,wR2=0.0674
R indices (all data)	R1= 0.0938, wR2 = 0.0950	R1= 0.0249, wR2 = 0.0621	R1 =0.0309, wR2 = 0.0799
Largest diff. peak and hole	0.334 and -0.182 e.Å^{-3}	0.307 and -0.199 e.Å^{-3}	0.282 and -0.199 e.Å^{-3}

Table S2.2 Comparison of bond angles and distances between FpP and other Fp derivative

Bond angles and distances	FpP	$[(\eta^5\text{-}C_5H_5)Fe(CO)_2]_2(CH_2)_4$
C(6)-Fe-C(7)	93.64(14)	95
C(6)-Fe-C(8)	85.84(12)	86
C(7)-Fe-C(8)	87.29(12)	88
Fe-C8	2.066(3)	2.08
C8-C9	1.520(3)	1.54

Table S2.3 Selected torsion angles for 5-membered ring

Number	Atom1	Atom2	Atom3	Atom4	Torsion angle
1	C8	Fe1	P1	C10	-16.28(6)
2	P1	Fe1	C8	C9	39.4(1)
3	Fe1	P1	C10	C9	-6.6(1)
4	Fe1	C8	C9	C10	-54.2(1)
5	C8	C9	C10	P1	35.8(1)

Table S2.4 Selected torsion angles for 6-membered ring

| Number	Atom1	Atom2	Atom3	Atom4	Torsion angle
1	P13	Fe1	C1	C2	55.6(1)
2	C1	Fe1	P13	C4	-47.54(8)
3	Fe1	C1	C2	C3	-69.4(2)
4	C1	C2	C3	C4	65.6(2)
5	C2	C3	C4	P13	-61.7(2)
6	C3	C4	P13	Fe1	58.5(1)

Chapter 4 Supporting information
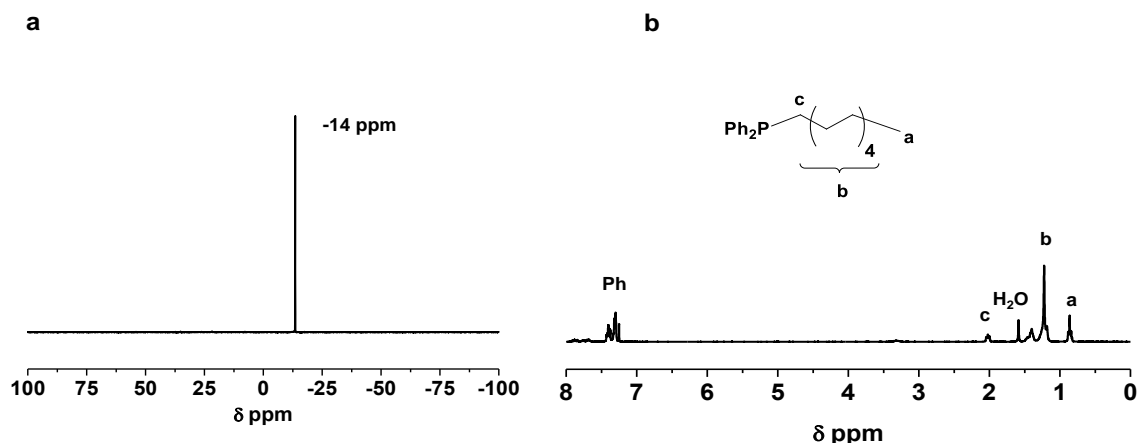
**Figure S4.1** (a) ^{31}P NMR spectrum and (b) ^{1}H NMR spectrum for Ph$_2$PC10 in CDCl$_3$.
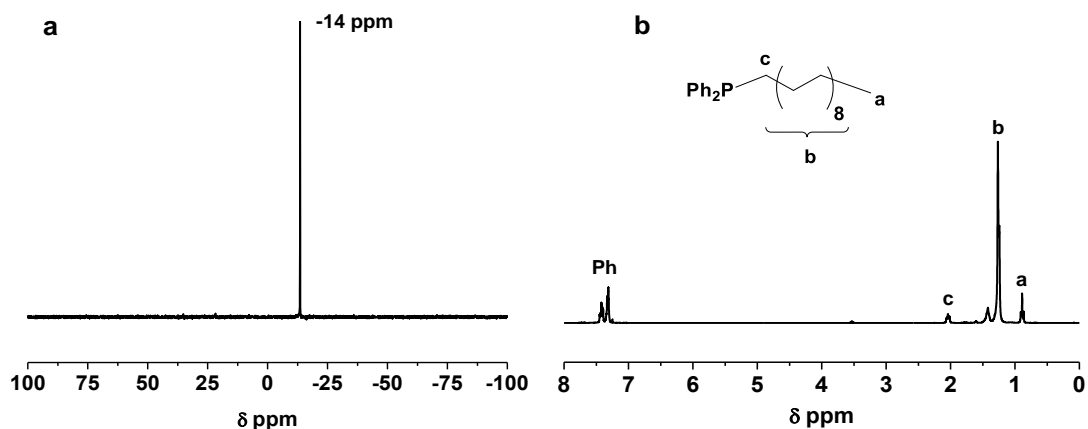
**Figure S4.2** (a) ^{31}P NMR spectrum and (b) ^{1}H NMR spectrum for Ph$_2$PC18 in CDCl$_3$.
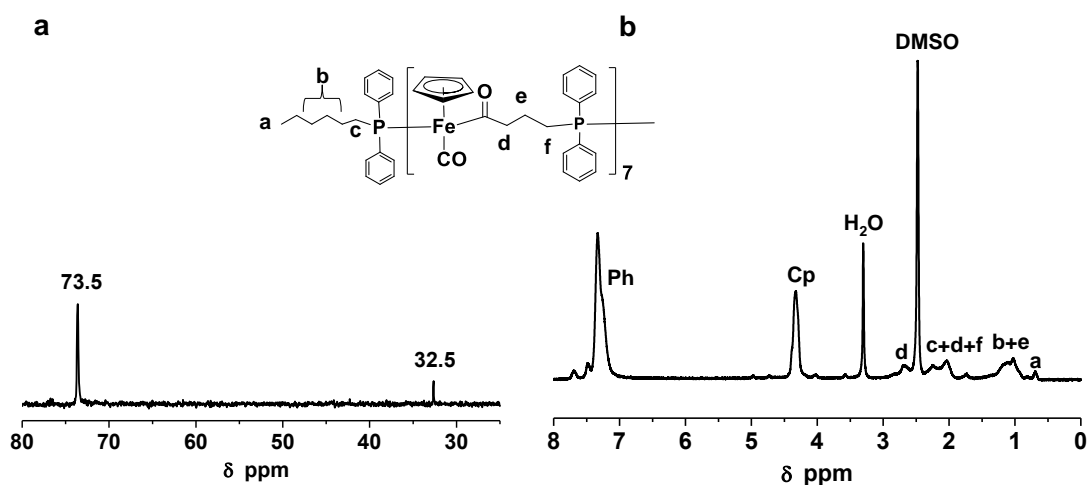
Figure S4.3 (a) ^{31}P NMR spectrum and (b) ^{1}H NMR spectrum for PFpP-PPh$_2$C6 in DMSO-d_6.
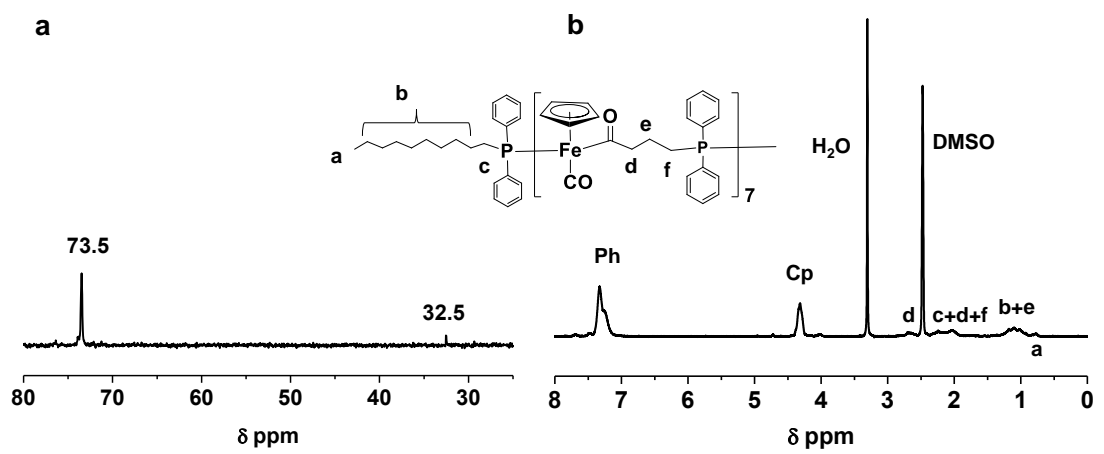
Figure S4.4 (a) ^{31}P NMR spectrum and (b) ^{1}H NMR spectrum for PFpP-PPh$_2$C10 in DMSO-d_6.

# Chapter 5 Supporting information
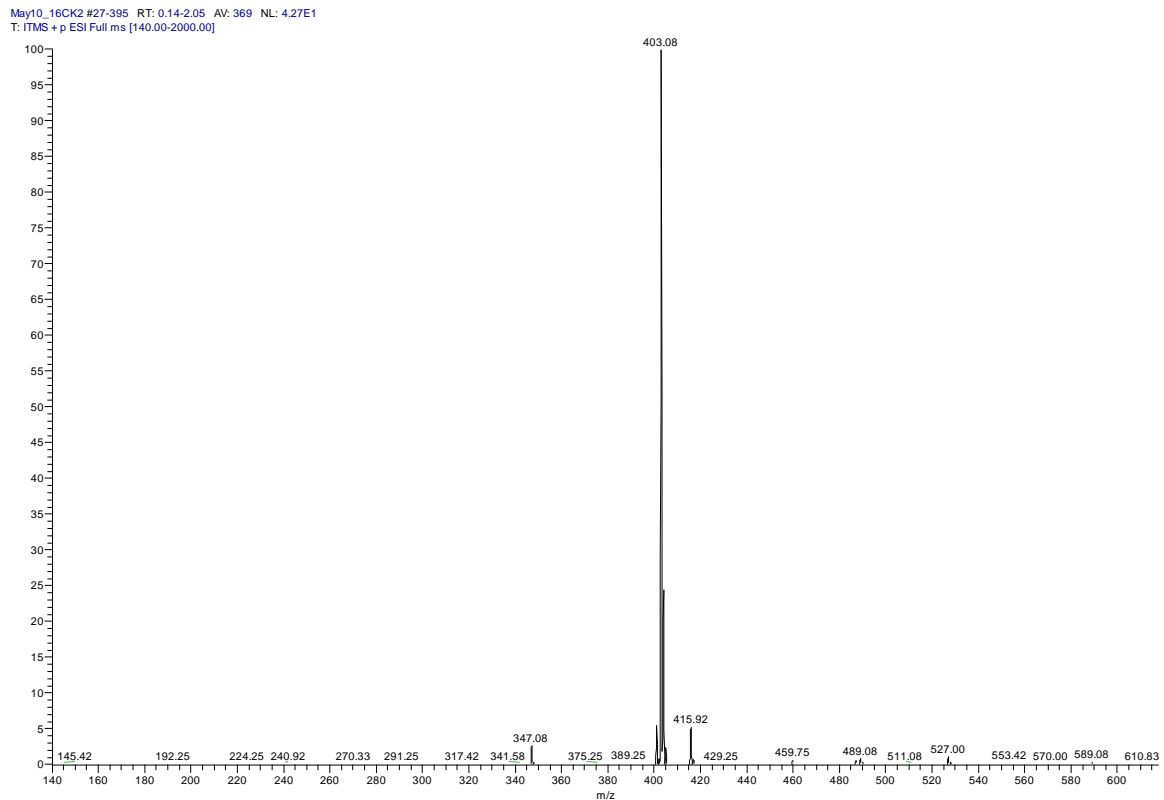
Figure S5.1 Electrospray ionization (ESI) mass spectrum for FpP^{Cp}.

The spectrum shows a strong signal for the ion with mass to charge (m/z) of 403. This peak does not come from the background and is smaller than the mass of FpP^{Cp}. The appearance of this peak is probably caused by the instability of FpP^{Cp}, which generates a fragment that is easy to be ionized.

170
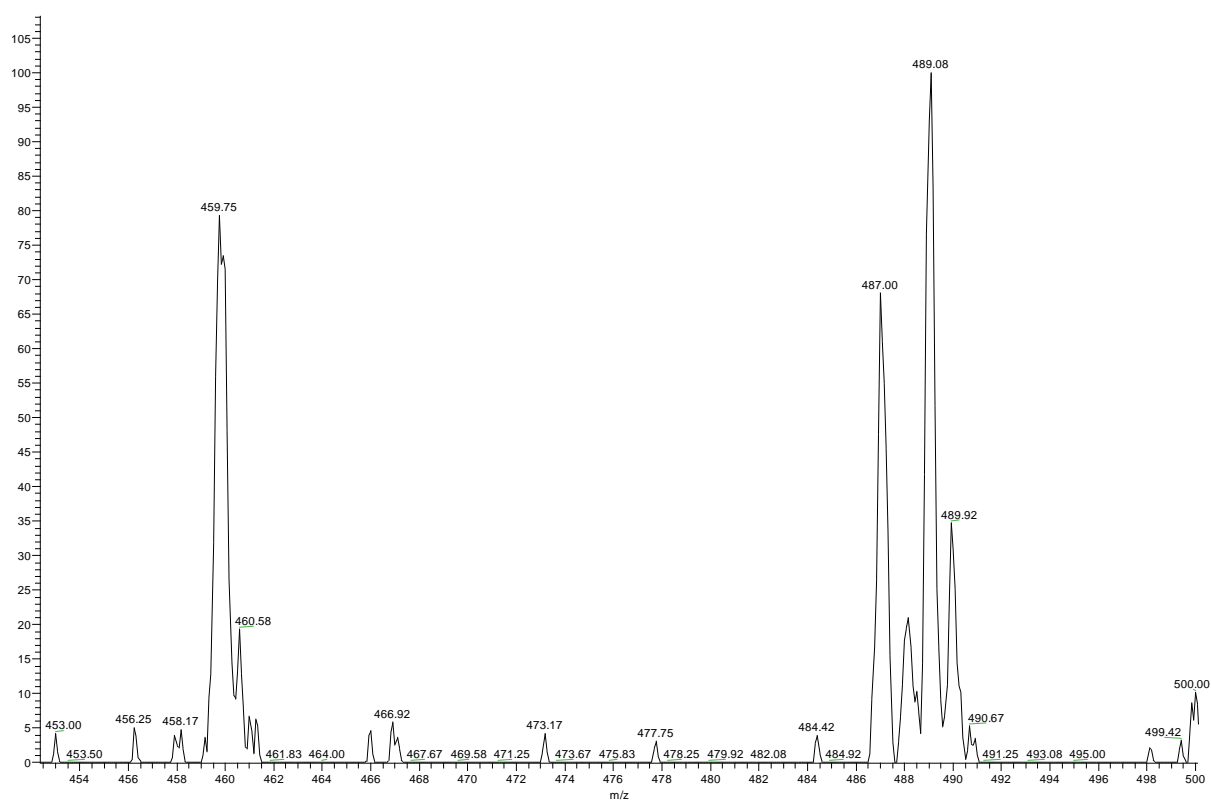
Figure S5.2 Enlarged electrospray ionization (ESI) mass spectrum for FpP^{Cp}.
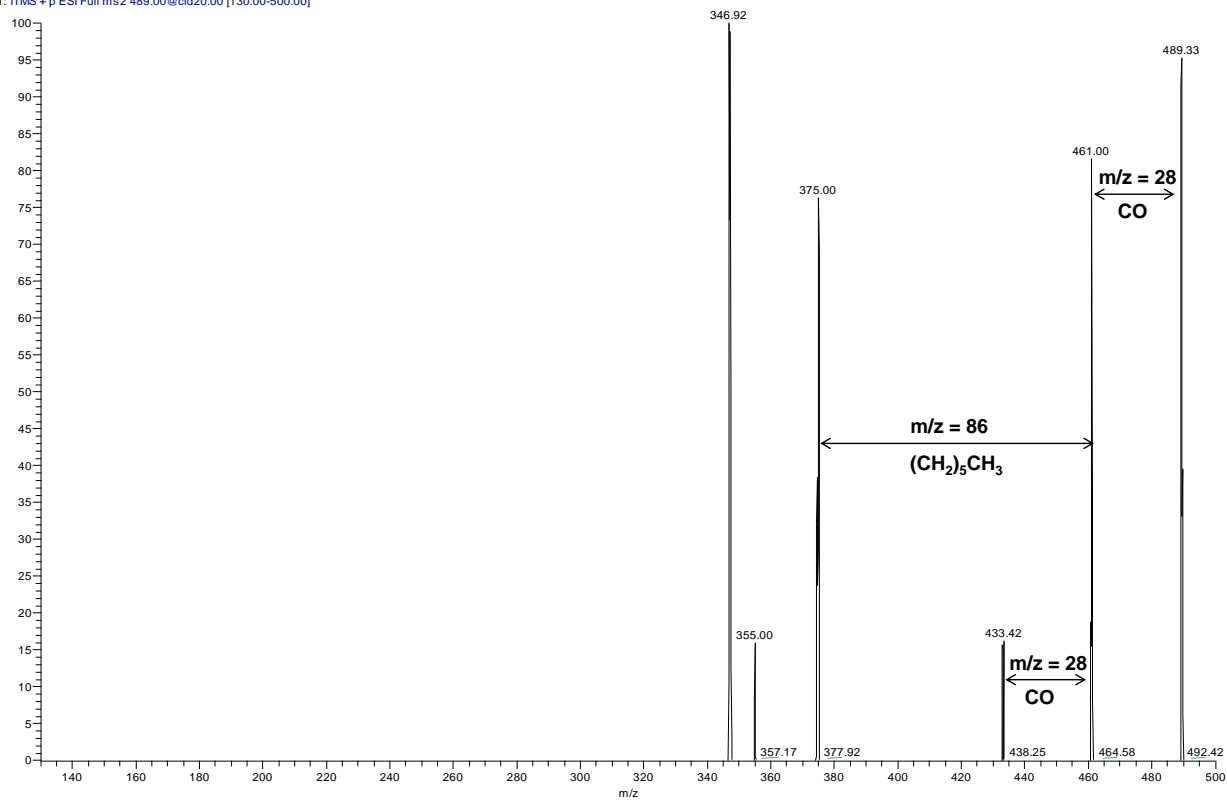
Figure S5.3 Electrospray ionization (ESI) MS/MS spectrum for FpP^{Cp}.

Chapter 6 Supporting information
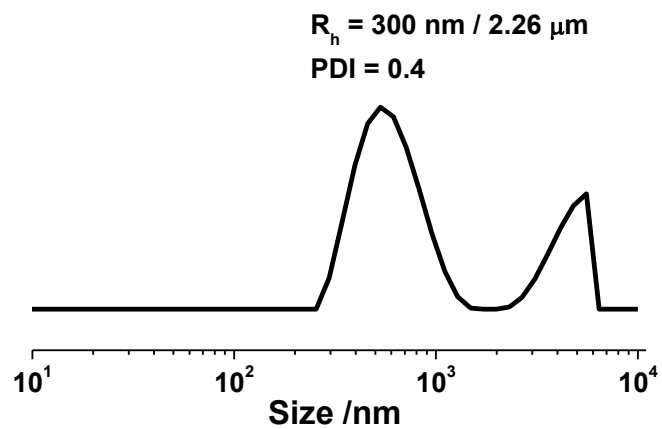
Figure S6.1 DLS analysis of PFpP colloids prepared by slow addition of water in PFpP THF solution, followed by N_2 bubbling to remove THF.
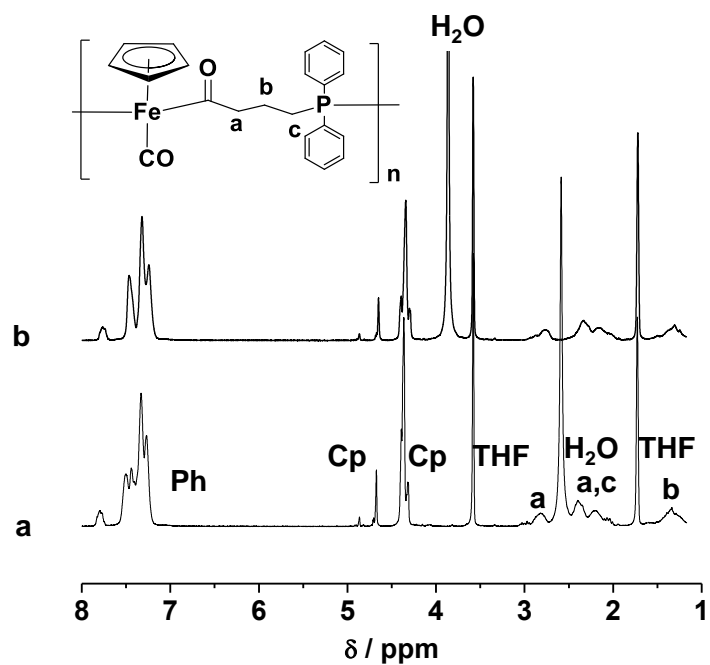
**Figure S6.2** ^{1}H NMR spectra for PFpP in THF-d_8 (20.00 mg/mL) (a) without and (b) with D_2O (0.10 mL).
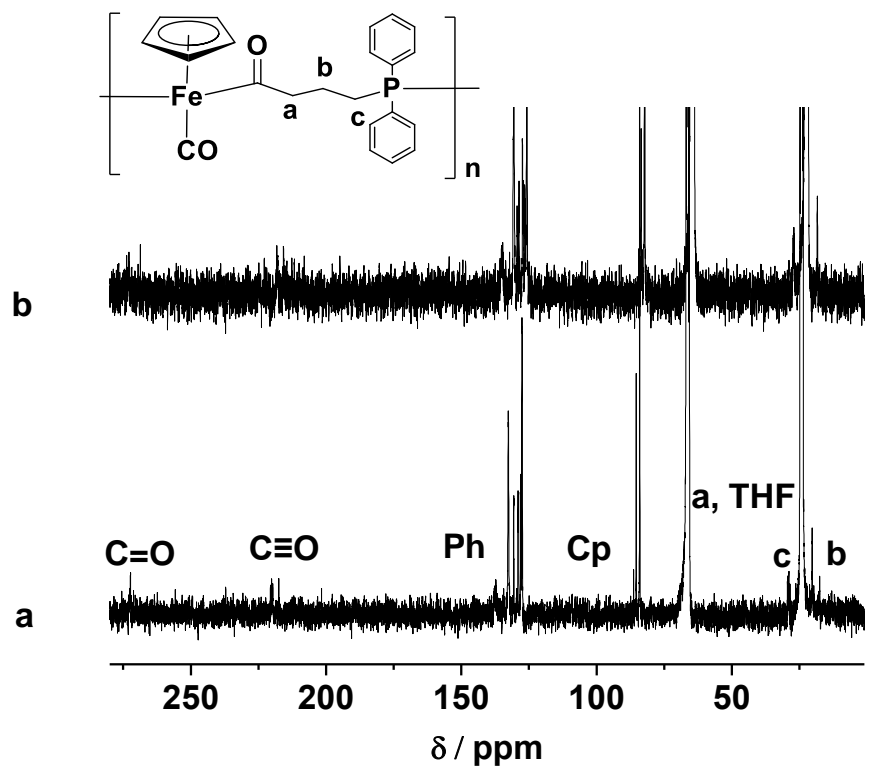
Figure S6.3 ^{13}C NMR spectra for PFpP in THF-d_8 (20.00 mg/mL) (a) without and (b) with 0.10

mL D_2O.
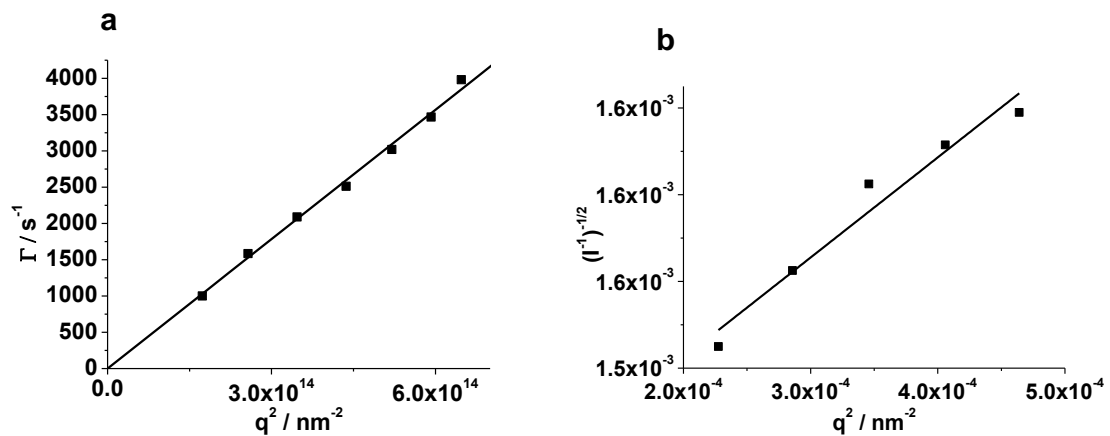
Figure S6.4 (a) DLS data as a function of scattering angle and (b) Berry plot for PFpP colloids

(0.006 mg/mL) derived from multiple angle SLS measurements ($R_g/R_h = 1.06$).
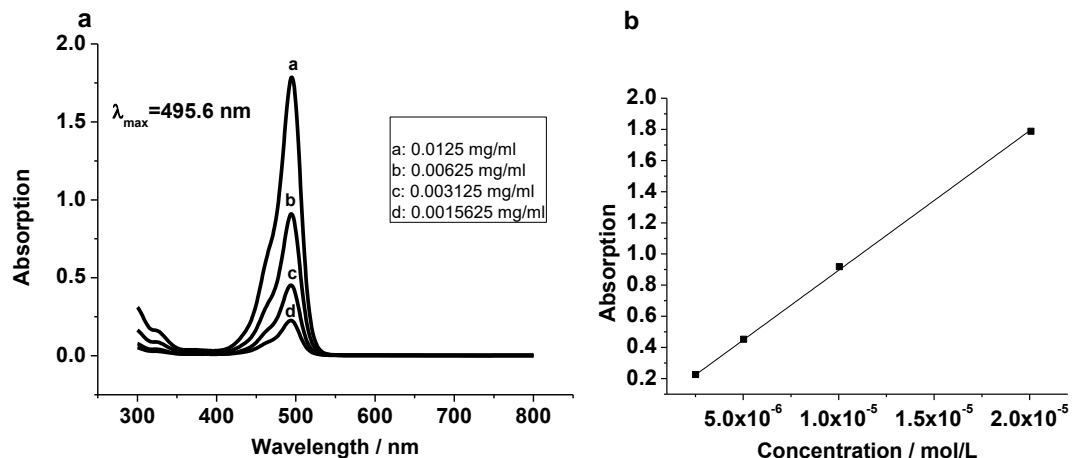
Figure S6.5 (a) UV-vis absorption spectra for calcein in H$_2$O at various concentrations and (b) plot of the absorption at 495.6 nm as a function of solution concentration (ε = 89556 L mol^{-1} cm^{-1}).
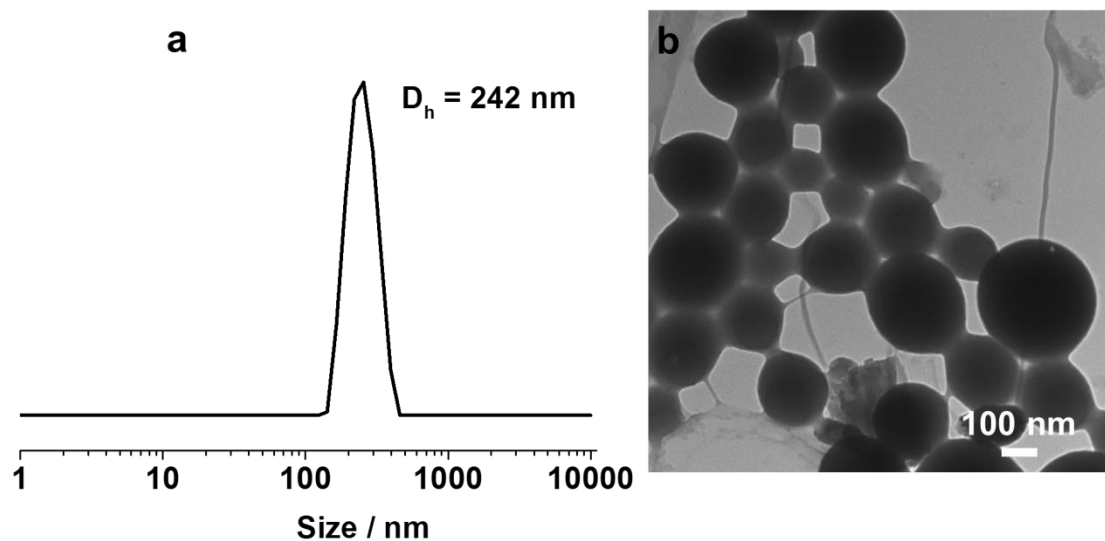
Figure S6.6 (a) DLS results and (b) TEM images for PFpP colloidal solution prepared in the presence of 200 mg PEG after the removal of unencapsulated PEG by dialysis.

175

References

Chapter 1

1. Wong, W.-Y.; Wang, X.-Z.; He, Z.; Djurisic, A. B.; Yip, C.-T.; Cheung, K.-Y.; Wang, H.; Mak, C. S. K.; Chan, W.-K. *Nat. Mater.* **2007,** 6, (7), 521-527.

2. Burnworth, M.; Tang, L.; Kumpfer, J. R.; Duncan, A. J.; Beyer, F. L.; Fiore, G. L.; Rowan, S. J.; Weder, C. *Nature* **2011,** 472, (7343), 334-337.

3. Arsenault, A. C.; Míguez, H.; Kitaev, V.; Ozin, G. A.; Manners, I. *Adv. Mater.* **2003,** 15, (6), 503-507.

4. Baldwin, M. G.; Johnson, K. E. *J. Polym. Sci., Part A: Polym. Chem.* **1967,** 5, (8), 2091-2098.

5. Aso, C.; Kunitake, T.; Nakashima, T. *Die Makromol. Chem.* **1969,** 124, (1), 232-240.

6. Nuyken, O.; Burkhardt, V.; Hübsch, C. *Macromol. Chem. Phys.* **1997,** 198, (11), 3353-3363.

7. Zotti, G.; Zecchin, S.; Schiavon, G.; Berlin, A.; Pagani, G.; Canavesi, A. *Chem. Mater.* **1995,** 7, (12), 2309-2315.

8. Albagli, D.; Bazan, G.; Wrighton, M. S.; Schrock, R. R. *J. Am. Chem. Soc.* **1992,** 114, (11), 4150-4158.

9. Dragutan, I.; Dragutan, V.; Fischer, H. *J. Inorg. Organomet. Polym.* **2008,** 18, (3), 311-324.

10. Hardy, C. G.; Ren, L.; Tamboue, T. C.; Tang, C. *J. Polym. Sci., Part A: Polym. Chem.* **2011,** 49, (6), 1409-1420.

11. Herfurth, C.; Voll, D.; Buller, J.; Weiss, J.; Barner-Kowollik, C.; Laschewsky, A. *J. Polym. Sci., Part A: Polym. Chem.* **2012,** 50, (1), 108-118.

12. Hardy, C. G.; Zhang, J.; Yan, Y.; Ren, L.; Tang, C. *Prog. Polym. Sci.* **2014,** 39, (10),

1742-1796.

13. Ren, L.; Hardy, C. G.; Tang, C. *J. Am. Chem. Soc.* **2010,** 132, (26), 8874-8875.

14. Lin, W.; Zheng, Y.; Zhang, J.; Wan, X. *Macromolecules* **2011,** 44, (13), 5146-5154.

15. Zhang, J.; Ren, L.; Hardy, C. G.; Tang, C. *Macromolecules* **2012,** 45, (17), 6857-6863.

16. Ren, L.; Zhang, J.; Bai, X.; Hardy, C. G.; Shimizu, K. D.; Tang, C. *Chem. Sci.* **2012,** 3, (2), 580-583.

17. Willis, T. C.; Sheats, J. E. *J. Polym. Sci., Part A: Polym. Chem.* **1984,** 22, (5), 1077-1084.

18. Allcock, H. R.; Lavin, K. D.; Riding, G. H. *Macromolecules* **1985,** 18, (6), 1340-1345.

19. Buchmeiser, M.; Schrock, R. R. *Macromolecules* **1995,** 28, (19), 6642-6649.

20. Rasenberg; H. US. Patent 3, 053, 1969.

21. Foucher, D. A.; Tang, B. Z.; Manners, I. *J. Am. Chem. Soc.* **1992,** 114, (15), 6246-6248.

22. Fischer, A. B.; Kinney, J. B.; Staley, R. H.; Wrighton, M. S. *J. Am. Chem. Soc.* **1979,** 101, (22), 6501-6506.

23. Pudelski, J. K.; Rulkens, R.; Foucher, D. A.; Lough, A. J.; MacDonald, P. M.; Manners, I. *Macromolecules* **1995,** 28, (22), 7301-7308.

24. Rulkens, R.; Ni, Y.; Manners, I. *J. Am. Chem. Soc.* **1994,** 116, (26), 12121-12122.

25. Temple, K.; Jäkle, F.; Sheridan, J. B.; Manners, I. *J. Am. Chem. Soc.* **2001,** 123, (7), 1355-1364.

26. Ni, Y.; Rulkens, R.; Pudelski, J. K.; Manners, I. *Macromol. Rapid Commun.* **1995,** 16, (9), 637-641.

27. Tanabe, M.; Manners, I. *J. Am. Chem. Soc.* **2004,** 126, (37), 11434-11435.

28. Tanabe, M.; Vandermeulen, G. W. M.; Chan, W. Y.; Cyr, P. W.; Vanderark, L.; Rider, D. A.;

Manners, I. *Nat. Mater.* **2006,** 5, (6), 467-470.

29. Herbert, D. E.; Gilroy, J. B.; Chan, W. Y.; Chabanne, L.; Staubitz, A.; Lough, A. J.; Manners, I. *J. Am. Chem. Soc.* **2009,** 131, (41), 14958-14968.

30. Nelson, J. M.; Lough, A. J.; Manners, I. *Angew. Chem. Int. Ed.* **1994,** 33, (9), 989-991.

31. Berenbaum, A.; Manners, I. *Dalton Trans.* **2004**, (14), 2057-2058.

32. Ieong, N. S.; Manners, I. *Macromol. Chem. Phys.* **2009,** 210, (13-14), 1080-1086.

33. Baljak, S.; Russell, A. D.; Binding, S. C.; Haddow, M. F.; O'Hare, D.; Manners, I. *J. Am. Chem. Soc.* **2014,** 136, (16), 5864-5867.

34. Spessard, G. O.; Miessler, G. L., *Organometallic chemistry*. Oxford University Press: 2010.

35. Douglas, B. E. **1982**.

36. Apodaca, P.; Kumar, M.; Cervantes-Lee, F.; Sharma, H. K.; Pannell, K. H. *Organometallics* **2008,** 27, (13), 3136-3141.

37. Jennings, D.; Brady, S.; Shultz, G.; Zakharov, L.; Tyler, D. *Polym. Bull.* **2012,** 68, (9), 2243-2254.

38. K.Saha, A.; Hossain, M. M. *J. Organomet. Chem.* **1993,** 445, (1–2), 137-141.

39. Martin, K.; Dotson, M.; Litterer, M.; Hanks, T. W.; Veas, C. *Synthetic Metals* **1996,** 78, (2), 161-168.

40. Martin, K. F.; Hanks, T. W. *Organometallics* **1997,** 16, (22), 4857-4860.

41. Mapolie, S. F.; Mavunkal, I. J.; Moss, J. R.; Smith, G. S. *Appl. Organomet. Chem.* **2002,** 16, (6), 307-314.

42. Morisaki, Y.; Chen, H.; Chujo, Y. *Polym. Bull.* **2002,** 48, (3), 243-249.

43. Al-Badri, Z. M.; Tew, G. N. *Macromolecules* **2008,** 41, (12), 4173-4179.

44. Al-Badri, Z. M.; Maddikeri, R. R.; Zha, Y.; Thaker, H. D.; Dobriyal, P.; Shunmugam, R.; Russell, T. P.; Tew, G. N. *Nat. Commun.* **2011,** 2, 482.

45. Pittman Jr, C. U.; Felis, R. F. *J. Organomet. Chem.* **1974,** 72, (3), 399-413.

46. Allcock, H. R.; Mang, M. N.; McDonnell, G. S.; Parvez, M. *Macromolecules* **1987,** 20, (9), 2060-2067.

47. Ohshita, J.; Yamashita, A.; Hiraoka, T.; Shinpo, A.; Kunai, A.; Ishikawa, M. *Macromolecules* **1997,** 30, (6), 1540-1549.

48. Ram ŕez-Oliva, E.; Cuadrado, I.; Casado, C. M.; Losada, J.; Alonso, B. *J. Organomet. Chem.* **2006,** 691, (6), 1131-1137.

49. Chan, W. Y.; Clendenning, S. B.; Berenbaum, A.; Lough, A. J.; Aouba, S.; Ruda, H. E.; Manners, I. *J. Am. Chem. Soc.* **2005,** 127, (6), 1765-1772.

50. M înea, L. A.; Sessions, L. B.; Ericson, K. D.; Glueck, D. S.; Grubbs, R. B. *Macromolecules* **2004,** 37, (24), 8967-8972.

51. Hasegawa, U.; van der Vlies, A. J.; Simeoni, E.; Wandrey, C.; Hubbell, J. A. *J. Am. Chem. Soc.* **2010,** 132, (51), 18273-18280.

52. Shultz, G.; Tyler, D. *J. Inorg. Organomet. Polym.* **2009,** 19, (4), 423-435.

53. Bevin, C. D.; David, R. T., Factors Controlling the Rate of Photodegradation in Polymers. In *Degradable Polymers and Materials: Principles and Practice (2nd Edition)*, American Chemical Society: 2012; Vol. 1114, pp 73-84.

54. Nieckarz, G. F.; Tyler, D. R. *Inorganica. Chimica. Acta.* **1996,** 242, (1–2), 303-310.

55. Tyler, D. R. *Coord. Chem. Rev.* **2003,** 246, (1–2), 291-303.

56. Moran, M.; Pascual, M. C.; Cuadrado, I.; Losada, J. *Organometallics* **1993,** 12, (3), 811-822.

57. Tenhaeff, S. C.; Tyler, D. R. *Organometallics* **1991,** 10, (4), 1116-1123.

58. Tyler, D. R., Mechanistic Aspects of the Photodegradation of Polymers Containing Metal–Metal Bonds along Their Backbones. In *Macromolecules Containing Metal and Metal-Like Elements*, Abd-El-Aziz, A. S.; Carraher, C. E.; Pittman, C. U. and Zeldin, M. (eds), wiley: Hoboken, NJ, USA. 2005: pp 77-109.

59. Brady, S.; Shultz, G.; Tyler, D. *J. Inorg. Organomet. Polym.* **2010,** 20, (3), 511-518.

60. Brady, S.; Tyler, D. *J. Inorg. Organomet. Polym.* **2013,** 23, (1), 158-166.

61. Br äse, S.; Gil, C.; Knepper, K.; Zimmermann, V. *Angew. Chem. Int. Ed.* **2005,** 44, (33), 5188-5240.

62. Shultz, G.; Berryman, O.; Zakharov, L.; Tyler, D. *J. Inorg. Organomet. Polym.* **2008,** 18, (1), 149-154.

63. Shultz, G. V.; Zakharov, L. N.; Tyler, D. R. *Macromolecules* **2008,** 41, (15), 5555-5558.

64. Shultz, G. V.; Zemke, J. M.; Tyler, D. R. *Macromolecules* **2009,** 42, (20), 7644-7649.

65. Sutthasupa, S.; Shiotsuki, M.; Sanda, F. *Polym. J.* **2010,** 42, (12), 905-915.

66. Gilbertson, J.; Weakley, T. J. R.; Han, F.; Wolcott, J.; Tyler, D. *J. Inorg. Organomet. Polym.* **2005,** 15, (4), 439-446.

67. Sharma, H. K.; Cervantes-Lee, F.; Pannell, K. H. *J. Am. Chem. Soc.* **2004,** 126, (5), 1326-1327.

68. Kumar, M.; Metta-Magana, A. J.; Sharma, H. K.; Pannell, K. H. *Dalton Trans.* **2010,** 39, (30), 7125-7131.

69. Sharma, H. K.; Pannell, K. H. *Chem. Commun.* **2004**, (22), 2556-2557.

70. Braunschweig, H.; Dellermann, T.; Dewhurst, R. D.; Mies, J.; Radacki, K.;

Stellwag-Konertz, S.; Vargas, A. *Organometallics* **2014,** 33, (7), 1536-1539.

71. Clendenning, S. B.; Aouba, S.; Rayat, M. S.; Grozea, D.; Sorge, J. B.; Brodersen, P. M.; Sodhi, R. N. S.; Lu, Z. H.; Yip, C. M.; Freeman, M. R.; Ruda, H. E.; Manners, I. *Adv. Mater.* **2004,** 16, (3), 215-219.

72. Cheng, A. Y.; Clendenning, S. B.; Yang, G.; Lu, Z.-H.; Yip, C. M.; Manners, I. *Chem. Commun.* **2004**, (7), 780-781.

Chapter 2

1. Manners, I., *Synthetic Metal containing polymers*. wiely, 2004.

2. Whittell, G. R.; Hager, M. D.; Schubert, U. S.; Manners, I. *Nat. Mater.* **2011,** 10, (3), 176-188.

3. Wang, X.; McHale, R. *Macromol. Rapid Commun.* **2010,** 31, (4), 331-350.

4. Ramanathan, M.; Tseng, Y. C.; Ariga, K.; Darling, S. B. *J. Mater. Chem. C* **2013,** 1, (11), 2080-2091.

5. Abd-El-Aziz, A. S.; Strohm, E. A. *Polymer* **2012,** 53, (22), 4879-4921.

6. Wong, W.-Y.; Wang, X.-Z.; He, Z.; Djurisic, A. B.; Yip, C.-T.; Cheung, K.-Y.; Wang, H.; Mak, C. S. K.; Chan, W.-K. *Nat. Mater.* **2007,** 6, (7), 521-527.

7. Arsenault, A. C.; M ǵuez, H.; Kitaev, V.; Ozin, G. A.; Manners, I. *Adv. Mater.* **2003,** 15, (6), 503-507.

8. Dong, Q.; Li, G.; Ho, C.-L.; Faisal, M.; Leung, C.-W.; Pong, P. W.-T.; Liu, K.; Tang, B.-Z.; Manners, I.; Wong, W.-Y. *Adv. Mater.* **2012,** 24, (8), 1034-1040.

9. Zha, Y.; Disabb-Miller, M. L.; Johnson, Z. D.; Hickner, M. A.; Tew, G. N. *J. Am. Chem. Soc.* **2012,** 134, (10), 4493-4496.

10. Zha, Y.; Thaker, H. D.; Maddikeri, R. R.; Gido, S. P.; Tuominen, M. T.; Tew, G. N. *J. Am. Chem. Soc.* **2012,** 134, (35), 14534-14541.

11. Kishimura, A.; Yamashita, T.; Yamaguchi, K.; Aida, T. *Nat. Mater.* **2005,** 4, (7), 546-549.

12. He, F.; Gadt, T.; Manners, I.; Winnik, M. A. *J. Am. Chem. Soc.* **2011,** 133, (23), 9095-9103.

13. Ma, Y.; Dong, W.-F.; Hempenius, M. A.; Mohwald, H.; Vancso, G. J. *Nat. Mater.* **2006,** 5, (9), 724-729.

14. Hasegawa, U.; van der Vlies, A. J.; Simeoni, E.; Wandrey, C.; Hubbell, J. A. *J. Am. Chem.*

Soc. **2010,** 132, (51), 18273-18280.

15. Burnworth, M.; Tang, L.; Kumpfer, J. R.; Duncan, A. J.; Beyer, F. L.; Fiore, G. L.; Rowan, S. J.; Weder, C. *Nature* **2011,** 472, (7343), 334-U230.

16. Wang, X.; Guerin, G.; Wang, H.; Wang, Y.; Manners, I.; Winnik, M. A. *Science* **2007,** 317, (5838), 644-647.

17. Mapolie, S. F.; Moss, J. R.; Smith, G. S. *Appl. Organomet. Chem.* **1998,** 12, (12), 801-807.

18. Sharma, H. K.; Cervantes-Lee, F.; Pannell, K. H. *J. Am. Chem. Soc.* **2004,** 126, (5), 1326-1327.

19. Zhang, J.; Ren, L.; Hardy, C. G.; Tang, C. *Macromolecules* **2012,** 45, (17), 6857-6863.

20. Chadha, P.; Ragogna, P. J. *Chem. Commun.* **2011,** 47, (18), 5301-5303.

21. Tonhauser, C.; Alkan, A.; Schomer, M.; Dingels, C.; Ritz, S.; Mailander, V.; Frey, H.; Wurm, F. R. *Macromolecules* **2013,** 46, (3), 647-655.

22. Jennings, D. M.; Brady, S. E.; Shultz, G. V.; Zakharov, L. N.; Tyler, D. R. *Polym. Bull.* **2012,** 68, (9), 2243-2254.

23. Miles, D.; Burrow, T.; Lough, A.; Foucher, D. *J. Inorg. Organomet. Polym. Mater.* **2010,** 20, (3), 544-553.

24. Gladysz, J. A. *Organometallics* **2011,** 30, (1), 1-4.

25. Green, M.; Westlake, D. J. *J. Chem. Soc. A.* **1971**, (2), 367-371.

26. Bibler, J. P.; Wojcicki, A. *Inorg. Chem.* **1966,** 5, (5), 889-892.

27. Plotkin, J. S.; Shore, S. G. *Inorg. Chem.* **1981,** 20, (1), 284-285.

28. Scharrer, E.; Brookhart, M. *J. Organomet. Chem.* **1995,** 497, (1-2), 61-71.

29. Emeran, A.; Gafoor, M. A.; Goslett, J. K. I.; Liao, Y. H.; Pimble, L.; Moss, J. R. *J.*

Organomet. Chem. **1991,** 405, (2), 237-246.

30. Davies, S. G.; Dordorhedgecock, I. M.; Sutton, K. H.; Whittaker, M. *J. Am. Chem. Soc.* **1987,** 109, (19), 5711-5719.

31. Pope, L.; Sommerville, P.; Laing, M.; Hindson, K. J.; Moss, J. R. *J. Organomet. Chem.* **1976,** 112, (3), 309-324.

32. Kumar, M.; Metta-Magana, A. J.; Sharma, H. K.; Pannell, K. H. *Dalton Trans.* **2010,** 39, (30), 7125-7131.

33. Quin, L. D., *A guide to organophosphorous chemistry*. A John Wiley & Sons, Inc., Publication: 2000; p 394.

34. Wedge, T. J.; Herzog, A.; Huertas, R.; Lee, M. W.; Knobler, C. B.; Hawthorne, M. F. *Organometallics* **2004,** 23, (3), 482-489.

35. Davies, S. G.; Dordorhedgecock, I. M.; Sutton, K. H.; Whittaker, M. *J. Organomet. Chem.* **1987,** 320, (2), C19-C22.

36. Liu, H. Y.; Eriks, K.; Giering, W. P.; Prock, A. *Acta Crystallogr., Sect. C: Cryst. Struct. Commun.* **1992,** 48, 433-436.

37. Ashby, M. T.; Enemark, J. H. *Organometallics* **1987,** 6, (6), 1318-1323.

38. Liu, L. K.; Luh, L. S. *Organometallics* **1994,** 13, (7), 2816-2824.

39. Wang, X. S.; Cao, K.; Liu, Y. B.; Tsang, B.; Liew, S. *J. Am. Chem. Soc.* **2013,** 135, (9), 3399-3402.

Chapter 3

1. Piper, T. S.; Wilkinson, G. . *J. Inorg. Nucl. Chem.* **1956,** 3, (2), 104-124.

2. Wang, X. S.; Cao, K.; Liu, Y. B.; Tsang, B.; Liew, S. *J. Am. Chem. Soc.* **2013,** 135, (9), 3399-3402.

3. Green, M.; Westlake, D. *J. Chem. Soc. A* **1971**, 367-371.

4. Cao, K.; Tsang, B.; Liu, Y.; Chelladural, D.; Power, W. P.; Wang, X. *Organometallics* **2014,** 33, (2), 531-539.

5. Nicholas, K.; Raghu, S.; Rosenblum, M. *J. Organomet. Chem.* **1974,** 78, (1), 133-137.

6. Adeyemi, O. G.; Coville, N. J. *Organometallics* **2003,** 22, (11), 2284-2290.

7. Seuring, J.; Agarwal, S. *Macromol. Rapid Commun.* **2012,** 33, (22), 1898-1920.

8. Carrasco, S.; Canalejas-Tejero, V.; Navarro-Villoslada, F.; Barrios, C. A.; Moreno-Bondi, M. C. *J. Mater. Chem. C* **2014,** 2, (8), 1400-1403.

9. Jochum, F. D.; Theato, P. *Chem. Soc. Rev.* **2013,** 42, (17), 7468-7483.

Chapter 4

1. Bhattacharya, S.; Kumari, N. *Coord. Chem. Rev.* **2009,** 253, (17–18), 2133-2149.

2. Wang, X.; McHale, R. *Macromol. Rapid Commun.* **2010,** 31, (4), 331-350.

3. Ren, L.; Hardy, C. G.; Tang, C. *J. Am. Chem. Soc.* **2010,** 132, (26), 8874-8875.

4. Parera, E.; Comelles, F.; Barnadas, R.; Suades, J. *Chem. Commun.* **2011,** 47, (15), 4460-4462.

5. Wang, X.; Guerin, G.; Wang, H.; Wang, Y.; Manners, I.; Winnik, M. A. *Science* **2007,** 317, (5838), 644-647.

6. Yan, Q.; Yuan, J.; Cai, Z.; Xin, Y.; Kang, Y.; Yin, Y. *J. Am. Chem. Soc.* **2010,** 132, (27), 9268-9270.

7. Gohy, J.-F.; Lohmeijer, B. G. G.; Schubert, U. S. *Macromolecules* **2002,** 35, (12), 4560-4563.

8. Hasegawa, U.; van der Vlies, A. J.; Simeoni, E.; Wandrey, C.; Hubbell, J. A. *J. Am. Chem. Soc.* **2010,** 132, (51), 18273-18280.

9. Al-Badri, Z. M.; Maddikeri, R. R.; Zha, Y.; Thaker, H. D.; Dobriyal, P.; Shunmugam, R.; Russell, T. P.; Tew, G. N. *Nat. Commun.* **2011,** 2, 482.

10. Wang, X.; Cao, K.; Liu, Y.; Tsang, B.; Liew, S. *J. Am. Chem. Soc.* **2013,** 135, (9), 3399-3402.

11. Cao, K.; Ward, J.; Amos, R. C.; Jeong, M. G.; Kim, K. T.; Gauthier, M.; Foucher, D.; Wang, X. *Chem. Commun.* **2014,** 50, (70), 10062-10065.

12. Davies, J. A.; Mierzwiak, J. G.; Syed, R. *J. Coord. Chem.* **1988,** 17, (1), 25-43.

13. Green, M.; Westlake, D. J. *J. Chem. Soc. A* **1971**, (0), 367-371.

14. Cotton, J. D.; Markwell, R. D. *Organometallics* **1985,** 4, (5), 937-939.

15. Cotton, J. D.; Markwell, R. D. *Inorg. Chim. Acta.* **1982,** 63, 13-16.

16. Cotton, J. D.; Crisp, G. T.; Latif, L. *Inorg. Chim. Acta.* **1981,** 47, 171-176.

17. Shortt, A. B.; Durham, L. J.; Mosher, H. S. *J. Org. Chem.* **1983,** 48, (18), 3125-3126.

18. Cao, K.; Tsang, B.; Liu, Y.; Chelladural, D.; Power, W. P.; Wang, X. *Organometallics* **2014,** 33, (2), 531-539.

19. Kumar, M.; Metta-Magana, A. J.; Sharma, H. K.; Pannell, K. H. *Dalton Trans.* **2010,** 39, (30), 7125-7131.

20. Ginzburg, A. G.; Lokshin, B. V.; Setkina, V. N.; Kursanov, D. N. *J. Organomet. Chem.* **1973,** 55, (2), 357-361.

21. Lanigan, N.; Assoud, A.; Wang, X. *ACS Macro Letters* **2014,** 3, (12), 1281-1285.

22. Kong, K. V.; Lam, Z.; Goh, W. D.; Leong, W. K.; Olivo, M. *Angew. Chem. Int. Ed.* **2012,** 51, (39), 9796-9799.

23. Policar, C.; Waern, J. B.; Plamont, M.-A.; Clède, S.; Mayet, C.; Prazeres, R.; Ortega, J.-M.; Vessières, A.; Dazzi, A. *Angew. Chem. Int. Ed.* **2011,** 50, (4), 860-864.

Chapter 5

1. Wang, X.; Cao, K.; Liu, Y.; Tsang, B.; Liew, S. *J. Am. Chem. Soc.* **2013,** 135, (9), 3399-3402.

2. Cao, K.; Murshid, N.; Li, L.; Lopez, A.; Tam, K. C.; Wang, X. *Macromolecules* **2015**.

3. Cao, K.; Tsang, B.; Liu, Y.; Chelladural, D.; Power, W. P.; Wang, X. *Organometallics* **2014,** 33, (2), 531-539.

4. Cao, K.; Ward, J.; Amos, R. C.; Jeong, M. G.; Kim, K. T.; Gauthier, M.; Foucher, D.; Wang, X. *Chem. Commun.* **2014,** 50, (70), 10062-10065.

5. Liu, J.; Cao, K.; Nayyar, B.; Tian, X.; Wang, X. *Poly. Chem.* **2014,** 5, (23), 6702-6709.

6. Aime, S.; Cordero, L.; Gobetto, R.; Szalontai, G. *Spectrochim. Acta, Part A* **1993,** 49, (9), 1307-1314.

7. Gilson, D. F. R.; Gomez, G.; Butler, I. S.; Fitzpatrick, P. J. *Can. J. Chem.* **1983,** 61, (4), 737-742.

8. Lanigan, N.; Assoud, A.; Wang, X. *ACS Macro Letters* **2014,** 3, (12), 1281-1285.

9. Orlova, T. Y.; Setkina, V. N.; Sizoi, V. F.; Kursanov, D. N. *J. Organomet. Chem.* **1983,** 252, (2), 201-204.

10. Stille, J. K.; Smith, C.; Anderson, O. P.; Miller, M. M. *Organometallics* **1989,** 8, (4), 1040-1047.

11. Orlova, T. Y.; Nekrasov, Y. S. *Ref. J. Chem.* **2013,** 3, (1), 95-116.

12. Kumar, M.; Metta-Magana, A. J.; Sharma, H. K.; Pannell, K. H. *Dalton Trans.* **2010,** 39, (30), 7125-7131.

13. Grim, S. O.; C. Barth, R. *J. Organomet. Chem.* **1975,** 94, (3), 327-332.

14. Brisset, H.; Gourdel, Y.; Pellon, P.; Le Corre, M. *Tetrahedron Lett.* **1993,** 34, (28),

4523-4526.

15. Pellon, P.; Brule, E.; Bellec, N.; Chamontin, K.; Lorcy, D. *J. Chem. Soc., Perkin Trans.* **2000**, (24), 4409-4412.

16. Mekky, A. E. M.; Saleh, T. S.; Al-Bogami, A. S. *Tetrahedron* **2013,** 69, (33), 6787-6798.

Chapter 6

1. Makhatadze, G. I.; Privalov, P. L. *J. Mol. Biol.* **1993,** 232, (2), 639-659.

2. Hamilton, J. A.; Small, D. M. *Natl. Acad. Sci.* **1981,** 78, (11), 6878-6882.

3. Brewer, S. H.; Tang, Y. F.; Vu, D. M.; Gnanakaran, S.; Raeigh, D. P.; Dyer, R. B. *Biochemistry* **2012,** 51, (26), 5293-5299.

4. Chandra, A. K.; Zeegers-Huyskens, T. *J. Comput. Chem.* **2012,** 33, (11), 1131-1141.

5. Cowie, J. M. G.; Mohsin, M. A.; McEwen, I. J. *Polymer* **1987,** 28, (9), 1569-1572.

6. Wang, X. S.; Winnik, M. A.; Manners, I. *Macromolecules* **2005,** 38, (5), 1928-1935.

7. Winnik, F. M.; Ringsdorf, H.; Venzmer, J. *Macromolecules* **1990,** 23, (8), 2415-2416.

8. Tu, C.-W.; Kuo, S.-W. *J. Polym. Res.* **2014,** 21, (6), 1-8.

9. Zhu, Y.; Liu, L.; Du, J. *Macromolecules* **2012,** 46, (1), 194-203.

10. Arumugam, S.; Vutukuri, D. R.; Thayumanavan, S.; Ramamurthy, V. *J. Am. Chem. Soc.* **2005,** 127, (38), 13200-13206.

11. Basu, S.; Vutukuri, D. R.; Thayumanavan, S. *J. Am. Chem. Soc.* **2005,** 127, (48), 16794-16795.

12. Savariar, E. N.; Aathimanikandan, S. V.; Thayumanavan, S. *J. Am. Chem. Soc.* **2006,** 128, (50), 16224-16230.

13. Kale, T. S.; Klaikherd, A.; Popere, B.; Thayumanavan, S. *Langmuir* **2009,** 25, (17), 9660-9670.

14. Discher, D. E.; Eisenberg, A. *Science* **2002,** 297, (5583), 967-973.

15. Wang, X.; Guerin, G.; Wang, H.; Wang, Y.; Manners, I.; Winnik, M. A. *Science* **2007,** 317, (5838), 644-647.

16. Yan, X.; Liu, G.; Hu, J.; Willson, C. G. *Macromolecules* **2006,** 39, (5), 1906-1912.

17. Kishimura, A. *Polym. J.* **2013,** 45, (9), 892-897.

18. Cameron, N. S.; Corbierre, M. K.; Eisenberg, A. *Can. J. Chem.* **1999,** 77, (8), 1311-1326.

19. Hayward, R. C.; Pochan, D. J. *Macromolecules* **2010,** 43, (8), 3577-3584.

20. Qian, J.; Zhang, M.; Manners, I.; Winnik, M. A. *Trends. Biotechnol.* **2010,** 28, (2), 84-92.

21. Rupar, P. A.; Chabanne, L.; Winnik, M. A.; Manners, I. *Science* **2012,** 337, (6094), 559-562.

22. Wang, X.; Cao, K.; Liu, Y.; Tsang, B.; Liew, S. *J. Am. Chem. Soc.* **2013,** 135, (9), 3399-3402.

23. Cao, K.; Tsang, B.; Liu, Y.; Chelladural, D.; Power, W. P.; Wang, X. *Organometallics* **2014,** 33, (2), 531-539.

24. King, R. B. *J. Am. Chem. Soc.* **1963,** 85, (13), 1918-1922.

25. Green, M. L. H.; Hurley, C. R. *J. Organomet. Chem.* **1967,** 10, (1), 188-&.

26. Bibler, J. P.; Wojcicki, A. *Inorg. Chem.* **1966,** 5, (5), 889-892.

27. Pallas, N. R.; Harrison, Y. *Colloids Surf.* **1990,** 43, (2), 169-194.

28. Menger, F. M.; Galloway, A. L.; Chlebowski, M. E. *Langmuir* **2005,** 21, (20), 9010-9012.

29. Imoto, S.; Xantheas, S. S.; Saito, S. *J. Chem. Phys.* **2013,** 138, (5), -.

30. Mukherjee, S.; Chowdhury, P.; Gai, F. *J. Phys. Chem. B* **2007,** 111, (17), 4596-4602.

31. Ebbesen, S. D.; Mojet, B. L.; Lefferts, L. *J. Catal.* **2007,** 246, (1), 66-73.

32. Ebbesen, S. D.; Mojet, B. L.; Lefferts, L. *Langmuir* **2006,** 22, (3), 1079-1085.

33. Nakashima, N.; Yamada, N.; Kunitake, T.; Umemura, J.; Takenaka, T. *J. Phys. Chem.* **1986,** 90, (15), 3374-3377.

34. Aroca, R. F.; Ross, D. J.; Domingo, C. *Appl. Spectrosc.* **2004,** 58, (11), 324A-338A.

35. Anderson, M. S. *Appl. Phys. Lett.* **2003,** 83, (14), 2964-2966.

36. Peng, H.; Chen, D.; Jiang, M. *Langmuir* **2003,** 19, (26), 10989-10992.

37. Bermudez, H.; Brannan, A. K.; Hammer, D. A.; Bates, F. S.; Discher, D. E. *Macromolecules* **2002,** 35, (21), 8203-8208.

38. Battaglia, G.; Ryan, A. J. *J. Am. Chem. Soc.* **2005,** 127, (24), 8757-8764.

39. Seifert, U.; Lipowsky, R. *Phys. Rev. A* **1990,** 42, (8), 4768-4771.

40. Du, J.; Armes, S. P. *Langmuir* **2009,** 25, (16), 9564-9570.

41. Liu, Q.; Chen, J.; Du, J. *Biomacromolecules* **2014,** 15, (8), 3072-3082.

42. Hocine, S.; Cui, D.; Rager, M.-N.; Di Cicco, A.; Liu, J.-M.; Wdzieczak-Bakala, J.; Brûlet, A.; Li, M.-H. *Langmuir* **2013,** 29, (5), 1356-1369.

43. Vrignaud, S.; Benoit, J.-P.; Saulnier, P. *Biomaterials* **2011,** 32, (33), 8593-8604.

44. Das, S.; Sharma, D. K.; Chakrabarty, S.; Chowdhury, A.; Sen Gupta, S. *Langmuir* **2015,** 31, (11), 3402-3412.

45. Jia, L.; Cui, D.; Bignon, J.; Di Cicco, A.; Wdzieczak-Bakala, J.; Liu, J.; Li, M.-H. *Biomacromolecules* **2014,** 15, (6), 2206-2217.

46. Barichello, J. M.; Morishita, M.; Takayama, K.; Nagai, T. *Drug Dev. Ind. Pharm.* **1999,** 25, (4), 471-476.

47. Akhlaghi, S.; Berry, R.; Tam, K. *AAPS PharmSciTech* **2015,** 16, (2), 306-314.

Chapter 8

1. Hempenius, M. A.; Cirmi, C.; Savio, F. L.; Song, J.; Vancso, G. J. *Macromol. Rapid Commun.* **2010,** 31, (9-10), 772-783.

2. Liu, L.; Rui, L.; Gao, Y.; Zhang, W. *Poly. Chem.* **2015,** 6, (10), 1817-1829.

3. Butts, S. B.; Strauss, S. H.; Holt, E. M.; Stimson, R. E.; Alcock, N. W.; Shriver, D. F. *J. Am. Chem. Soc.* **1980,** 102, (15), 5093-5100.

List of Publications

(1) **Cao, K**.; Wang, X.S. Macromolecular Rapid Communications. 2016, 37, 246-250

(2) **Cao, K**.; Murshid, N.; Li, L.; Lopez, A., Tam, K. C.; Wang, X. Macromolecules. 2015, 48, 7968-7977

(3) **Cao, K**.; Murshid, N.; Wang, X. Macromolecular Rapid Communications. 2015, 36, 586-596

(4) Zhang, J.; **Cao, K**.; Wang, X.; Cui, B. Chemical Communications. 2015, 51, 17592-17595

(5) **Cao, K**.; Tsang, B.; Liu, Y.; Chelladural, D.; Power, W. P.; Wang, X. Organometallics 2014, 33, 531-539

(6) **Cao, K**.; Ward, J.; Wang, X. Chemical Communications, 2014, 50(70), 10062-10065

(7) Liu, J.; **Cao, K**.; Nayyar, B.; Tian, X.; Wang, X. Polymer Chemistry. 2014, 5(23), 6702-6709

(8) Wang, X..; **Cao, K**.; Liu, Y. B.; Tsang, B.; Liew, S. J. Am. Chem. Soc. 2013, 135, 3399-3402

Permissions

The thesis contains material which was reprinted (adapted) with permision from the following

publications:

Copyright Clearance Center — RightsLink

Home	Account Info	Help

Title: Synthesis of Main-Chain Metal Carbonyl Organometallic Macromolecules (MCMCOMs)
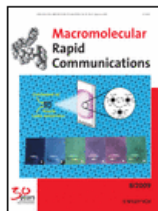
Author: Kai Cao,Nimer Murshid,Xiaosong Wang

Publication: Macromolecular Rapid Communications

Publisher: John Wiley and Sons

Date: Jan 13, 2015

© 2015 WILEY-VCH Verlag GmbH & Co. KGaA, Weinheim

Logged in as:
Kai Cao
Account #:
3000841043

LOGOUT

Order Completed

Thank you for your order.

This Agreement between Kai Cao ("You") and John Wiley and Sons ("John Wiley and Sons") consists of your license details and the terms and conditions provided by John Wiley and Sons and Copyright Clearance Center.

Your confirmation email will contain your order number for future reference.